Issue No. 237 October 2003

NEWSLETTER

BARC

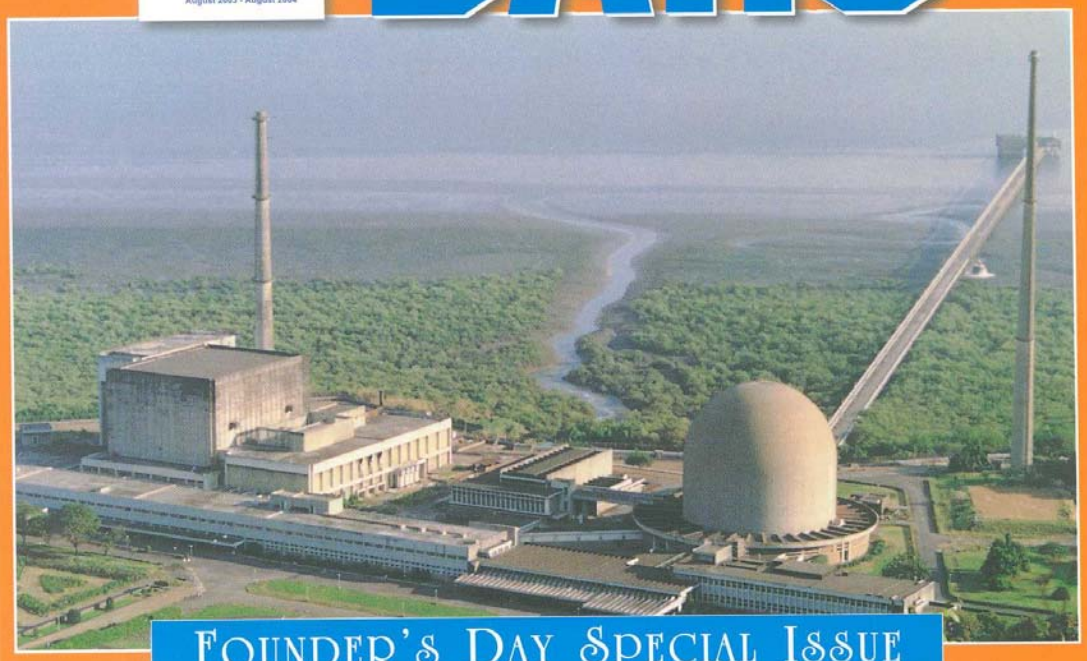

Founder's Day Special Issue

Bhabha Atomic Research Centre

Femtoscience: Exploring the Ultrafast Dynamics of Molecular Processes

Dipak K. Palit
Radiation Chemistry & Chemical Dynamics Division
Bhabha Atomic Research Centre

Abstract

In the course of photo and radiation chemical processes, reactants are converted into products with the possibility of various transition states and transient intermediates on the reaction pathway. The properties of these transient intermediate species are central to the reaction and determine its rate, selectivity and the course of the reaction. Lifetimes of these intermediates vary from a few tens of a femtosecond to a few picoseconds. Development of high power femtosecond lasers has made possible investigation of these processes in real time. Ultrafast transient absorption spectroscopic techniques developed in our laboratory have enabled us to investigate the intra and intermolecular processes undergone by the excited states and the other intermediate species produced following optical excitation of a solute molecule in condensed phase with femtosecond time resolution. In this talk, we discuss briefly the results of our studies on the excited state dynamics and photophysical and photochemical processes in some model molecules in solution.

Introduction

FEMTOSCIENCE IS THE BRANCH OF science, which uses the femtosecond lasers as tools. This branch of science has been developed only recently after the invention of the high power femtosecond laser systems. Now, the first question is: what is a f*emtosecond?* Technically, 1 femtosecond (fs) = 10^{-15} s. However, for those, who have the difficulties to visualize the shortness of this time scale, to say non-technically, if light can travel from here to the moon in 1 s, in 50 fs it can't even travel the width of a human hair. The next question is: What femtosecond lasers can deliver? Combination of 'mode-locking' pulse generation and 'Chirped Pulse Amplification' techniques have produced the shortest pulse of 0.65 fs duration, and the biggest pulse of 10^{15}W or 10^{22} W/cm^2 of energy. These short duration lasers have made possible applications of femtosecond lasers in physics (for example, ultrafast spectroscopy of materials, non-linear optics, plasma physics and particle accelerators, are among a few of many applications), biology, surgery, material processing, imaging (such as multiphoton confocal imaging, optical coherence tomography, T-ray imaging etc.) and in many other fields of science and engineering.

However, our interest in femtosecond lasers has been in investigation of molecular processes with femtosecond time resolution. Exploring phenomena on an ever-shorter time scale in the race against time, femtosecond time resolution is the ultimate achievement for studies of fundamental dynamics of the chemical bond. This field is known as 'femtochemistry'. Femtochemistry has become a well established field of science and its importance has been recognized by awarding the 1999 Nobel Prize to Prof. Ahmed Zewail of the California Institute of Technolgy, USA, who has pioneered this area of research. The importance of femtochemistry is evident from his own recognition: "....knowledge of the mechanisms of chemical reactions is also important for our ability to control the reactions. A desired chemical reaction is often accompanied by a series of unwanted,

competing reactions that lead to a mixture of products and hence the need for separation and cleansing. If the reaction can be controlled by initiating reactivity in selected bonds, this could be avoided……". We should also recognize the important fact that many of the natural processes take place with awesome rapidity and often complete within a few hundred femtoseconds. For example, in vision process, photoisomerization of retinal chromophore is complete within 200 fs. In photosynthetic reaction centre, electron moves about 20 angstrom distance in 3 ps.

Femtochemistry is concerned with the very act of the molecular motions that brings about chemistry. With femtosecond lasers, it is now possible to record the snapshots of chemical reactions with sub-angstrom resolution. A chemical reaction can be reduced to a number of elementary reactions – breaking and forming of chemical bonds, energy transfer within and between molecules, electron transfer, proton or hydrogen atom transfer etc. Understanding a chemical reaction at the atomic level not only requires a description of the reactants and products but also a description of the medium or surroundings, in which the reaction takes place, as well as understanding of the interactions between the reacting system and the surroundings. Now it is possible to characterize the '*transition state*', which determines the course of a reaction. It is not only possible to observe the molecular processes in real time, but also possible to control them at one's will.

Why femtosecond lasers have been considered as attractive tools for studying dynamics of chemical reactions? Of course, for high peak power apart from short duration! Each laser pulse of 50 fs duration and 1 miliJoule energy dumps about 2 x 10^{12} W or 2 teraWatt power onto the material. This generates high nonlinear effects in the material and makes possible to generate laser beams of different colors from the single source and these laser beams are perfectly synchronized in time. Hence, it is suitable for pump-probe experiment. During the last few decades, the development of ultrafast lasers has out-spaced the ability to create detectors with comparable time resolution. This mismatch has necessitated the development of techniques based on two or more pulses with a

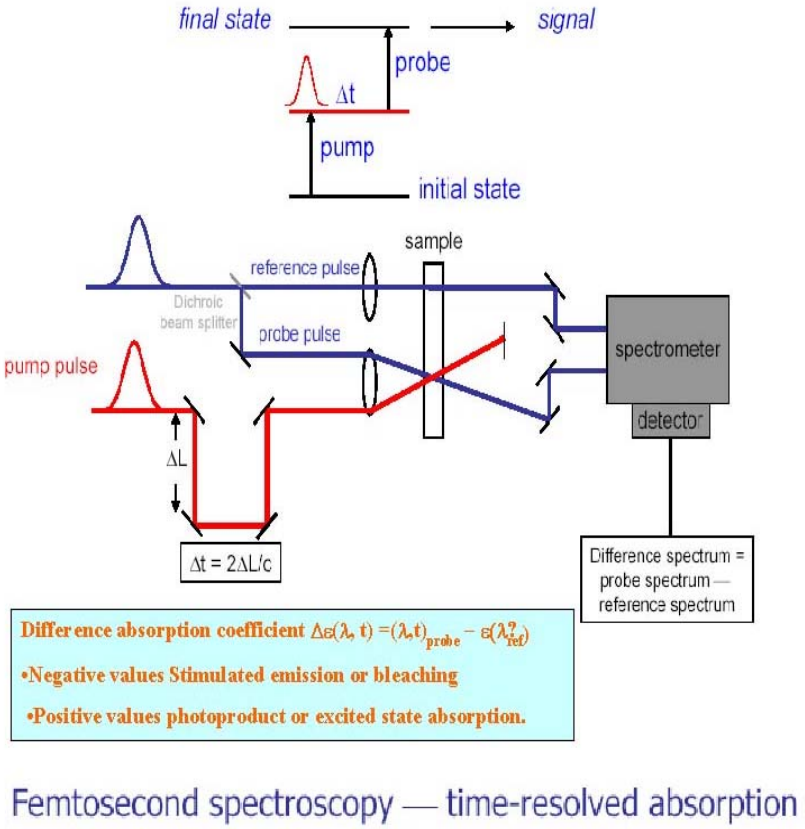

Fig.1 Pump - probe spectroscopy

time resolution that is limited only by the duration of the laser pulses themselves. The most common of these methods capable of initiating a dynamic processes and interrogating its time evolution is known as pump – probe. This technique has been schematically presented in Figure 1.

The pump pulse creates a large population of excited states within short time duration and the probe pulse monitors the evolution of excited states with time delay between the two pulses. Probing can be achieved by monitoring absorption, laser induced fluorescence, ionization, photoelectron detection, resonance Raman etc. Changing the length of the path of either of them by introducing a high precession linear motion translation stage controls the delay between the two pulses. Remembering the fact that light travels only 1 micron distance in 3.3 fs, the linear motion stage should have the resolution of about 0.1 micron to achieve the delay of a few femtosecond between the two pulses. Figure 2 displays schematics of the laser system used in our laboratory for tunable pump - tunable probe transient absorption spectroscopy.

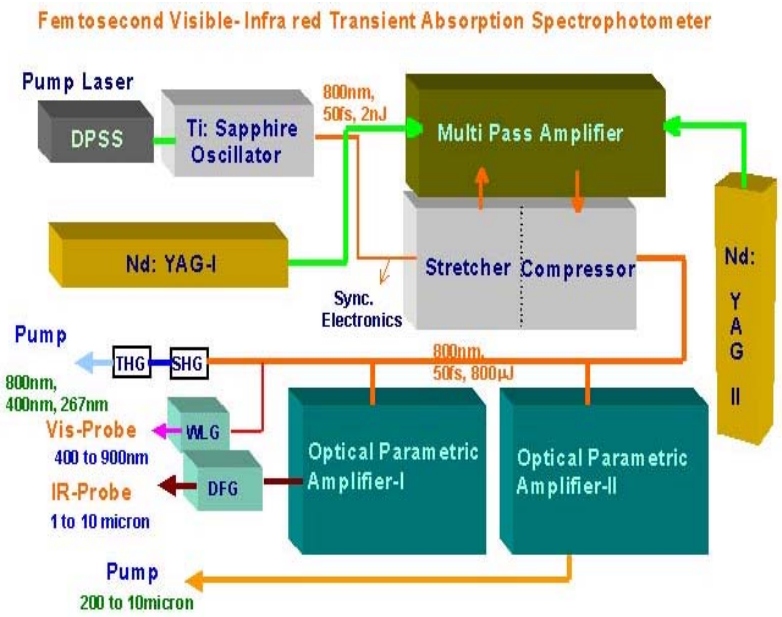

Fig.2 Laser system for tunable pump and tunable probe transient absorption spectroscopy

Dynamics of Chemical Bond-Breaking Process in Solution

Two important and fundamental questions in chemistry are: what is the time required to break a chemical bond in a photo-dissociation process and how the energy supplied to the molecule is partitioned between the fragments and the different kinds of motions of the fragments, such as kinetic, rotational and vibrational? Here, we discuss an example of the laser induced bond-breaking process – the photodissociation dynamics of mercuric iodide (HgI_2) in ethanol solution (eq. 1).

$$HgI_2 \xrightarrow{h\nu,330nm} HgI^* \rightarrow HgI^{\#} + I \quad \text{.....(1)}$$

When HgI_2 is excited by 330 nm light to one of its dissociative higher electronic excited state (HgI^*), the molecule is dissociated into the fragments, vibrationally hot HgI ($HgI^{\#}$) and I. In this process, the $HgI^{\#}$ fragment is produced in the ground electronic state ($X^{2\ +}$), but with a large amount of excess vibrational energy. The iodine atom is produced in the ground electronic state. The excess vibrational energy in $HgI^{\#}$ is subsequently dissipated to the surrounding solvent bath by external vibrational relaxation (EVR) or vibrational cooling process. Using the transient absorption technique we have been able to follow-up the dynamics of the bond breaking and energy flow process in the photodissociation reaction of HgI_2 in ethanol solution. In our experiment, we have used 330 nm pump and probe pulses in the wavelength range 330 to 700 nm, both the laser pulses having 50 fs duration. However, to be brief, we will discuss only the results

obtained from the experiments using 330 nm pump and 660 nm probe pulses, which we will designate as 330/660 experiments, respectively, to explain the photodissociation and energy flow dynamics in the said process.

Let us make a simple calculation to illustrate the fact that the photodissociation process is really very fast and have a rough estimate of the time taken to break the I-HgI bond in the photodissociation process. The excitation energy due to a single photon of 330 nm wavelength is 33,303 cm^{-1} and the energy required to photodissociate the I-HgI bond is 21,000 cm^{-1}. Hence the energy of recoil with which the fragments are moving away from each other is 9303 cm^{-1}. Hence the velocity of the fragments with which they are getting separated is, $v = (2E_{recoil}/\mu)^{1/2}$ = 2 Km/sec where μ is the reduced mass of the separated fragments. If the bond is said to have broken, when the fragments travel away by about 5Å or 5 x 10^{-13} Km apart from each other, the bond dissociation time is calculated to be about 250 fs.

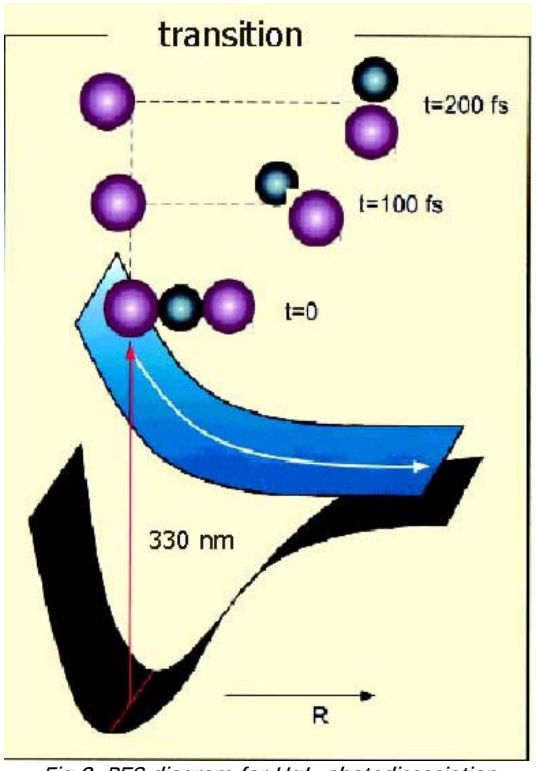

Fig.3 PES diagram for HgI_2 photodissociation

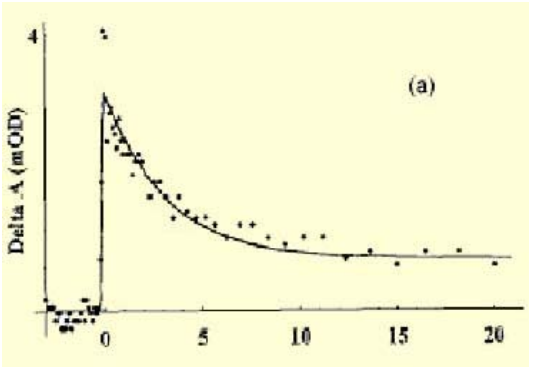

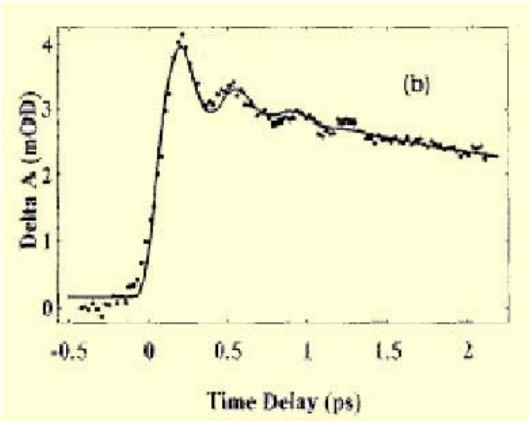

Fig. 4 Temporal profiles for 330/660 experiment on HgI_2 photodissociation reaction

The potential energy surface (PES) diagram for I—HgI bond dissociation dynamics has been depicted in Figure 3. HgI_2 molecule is excited by a 330 nm photon onto a dissociative surface. While traveling on this surface, the molecule undergoes dissociation process completed within 250 fs. The temporal dynamics of the transient absorption recorded in the 330/660 experiment due to photolysis of HgI_2 in ethanol is shown in Figure 4. One of the two most important and interesting features of the temporal dynamics of $HgI^{\#}$, as shown in Figure 3b, is that the absorption signal takes about 250 fs time to attain maximum. This confirms the prediction that the bond-dissociation takes about 250 fs to be completed following excitation. Another feature is an oscillatory component of the signal superimposed on the decay of $HgI^{\#}$. The oscillatory component of the signal persists for a few hundred fs. The total decay dynamics of

$HgI^{\#}$ has been modeled with the response function,

$$OD(t) = A \exp(-t/\tau_A) \cos(\omega t + \pi) + B \exp(-t/\tau_B) \quad (2)$$

A and B are amplitude factors, τ_A the damping time constant for the oscillation amplitude, ω and π are frequency and phase of the oscillatory component and τ_B is the population decay time of the transient species. The best-fit parameters obtained are: A/B = 1.71; τ_A = 330 ± 33 fs; $\omega/2\pi c$ = 89.5 ± 15 cm^{-1}; τ_B = 2.75 ± 0.27 ps. The temporal dynamics as shown in figure 3a is fitted very well to a single exponential function with lifetime of 2.72 ± 0.2 ps. The oscillation of the transient signal shown in Figure 3b arises due to the fact that following photodissociation of HgI_2, $HgI^{\#}$ is created in a coherent superposition of vibrational states, which is popularlry known as '*wave packet*'. The wave packet then oscillates between the classical turning points of the potential energy surface of the ground electronic state of the $HgI^{\#}$ species causing the 660 nm absorption to be tuned in and out of resonance between the ground electronic state and one of its excited state (Figure 5). Using the gas phase PES of HgI, an estimate of the energy content and distribution in the diatomic photoproduct may be ascertained. The fundamental frequency and anharmonicity constant of the stretching vibration, the only mode of Hg— I, are 126 and 1.3 cm^{-1}, respectively. Calculation shows that the beats correspond to a vibrational frequency of *ca* v = 15 and that the observed signal originates mainly from a fragment which is born with *ca* 1700 cm^{-1} of excess (mean) vibrational energy. The remaining photolysis energy (ca 7600 cm^{-1}) must then be distributed among the translational and rotational motions of the fragments as well as the associated solvent motions. The frequency of the wave packet oscillations represents the mean frequency of a distribution of vibrational states determined by the initial conditions. Finally, the overall signal decay with lifetime τ_B, which is 2.7 ps, should be due to solvent induced vibrational relaxation (EVR) process undergone by $HgI^{\#}$.

The phase of the wave packet has been found to be π radian. This result suggests that when Hg—I bond is compressed, the molecule does not absorb at 660 nm. If the Hg — I bond in the nascent product HgI is compressed, such as would occur in a dissociation reaction producing I and HgI from HgI_2 through the asymmetric stretching coordinate (Figure 2), the resulting wave packet would not be detected until it would move to the attractive turning point of the ground state PES. Hence this would yield a phase shift of π for the absorption signal, as observed in Figure 5.

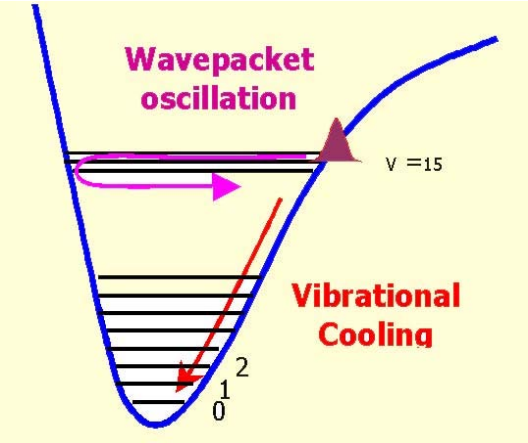

Fig.5 Potential energy surface for HgI

From this study, the following conclusions have been drawn: In photolysis of HgI_2 by 330 nm laser pulses of 50 fs duration, HgI is produced in a coherent superposition of vibrational levels on the ground electronic state. The mean excess vibrational energy corresponds to about 1700 cm^{-1}. This excess vibrational energy is dissipated to the solvent with an average lifetime of about 2.7 ps.

Ultrafast Dynamics of Intramolecular Processes in the Excited States of Some Model Molecules in Condensed Phase

Recently, supramolecules (i.e. large size organic molecules) are being used for various applications, such as in photonics (e.g.

molecular switches, optical data storage devices, optoelectronic devices, sensors, light emitting devices etc.), as well as in solar energy conversion. The photophysical processes responsible for the said actions may be photoinduced electron transfer, proton transfer and / or photoisomerization processes. However, following optical excitation, such a large size molecule in condensed phase, undergoes a numerous number of intra and intermolecular processes, including the desired one important for the said action. Among them two of them are the most important ones, in which the dynamics of interaction of the solute with the surrounding medium play a significant role in determining the fate of the excited state of the solute and hence the rates of photophysical and photochemical processes undergone by it. These processes are: *energy exchange* between the solute and the molecules of the medium via vibrational relaxation or, more specifically, vibrational cooling and *solvation* of the excited state via reorganization of the solvent molecules following intramolecular charge separation in solution. All these processes take place in ultrafast time scale and affect the relaxation dynamics of the electronically excited molecules in condensed phase. We have chosen a few simple model molecules to study the dynamics of these processes, which control the course of the reactions of the excited states in condensed phase.

Conformational relaxation dynamics in the excited state of Benzil

α-Diketones are structurally flexible with respect to the dihedral angle, θ, between the two halves of the molecule, due to low energy barrier. The geometry of the molecule is the result of a balance between the steric effects and resonance stabilization. The later is maximized in all-planar configurations. On the other hand, the steric effects, which arise due to interactions between the carbonyl oxygens and the substituents on the ring atoms (in the case of benzil, these are hydrogen atoms), particularly in ortho positions with respect to the carbonyl groups, never allow the planar configurations to be the most stable ones. Hence, the molecule attains different stable conformations in different electronic states making a compromise between these two factors. As a result, the excited electronic states have very different geometries than that in the ground state (Figure 6).

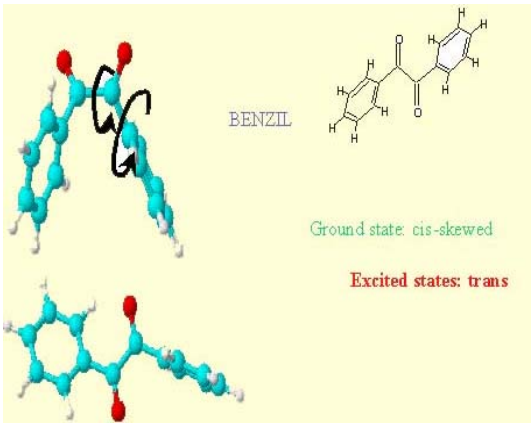

Fig.6 Structure of Benzil

The time resolved absorption spectra of the transients produced due to photoexcitation of benzil in acetonitrile solution by 310 nm laser pulses are shown in Figure 7. In each solvent the time resolved spectra show continuous evolution upto about 200 ps. The transient absorption in the region 540 – 580 nm decays with the rates comparatively faster than that in the bluer region and hence, the width of the spectrum recorded at 200 ps becomes narrower than the one recorded at 0.5 ps in the red region. As a result the peaks of the transient absorption spectra recorded at 200 ps appear at about 527 nm. The decay characteristics of the transient absorption in subpicosecond time domain have been monitored at 570 nm, since the change in absorbance with time has been observed to be maximum at this wavelength. The decay profile along with the fit function obtained by iterative deconvolution analysis using an instrument response function of $sech^2$ functional form having ~0.5 ps FWHM are presented in Figure 7. The inset of this figure, which represents the early time (up to about 15 ps after photo-excitation) dynamics of the

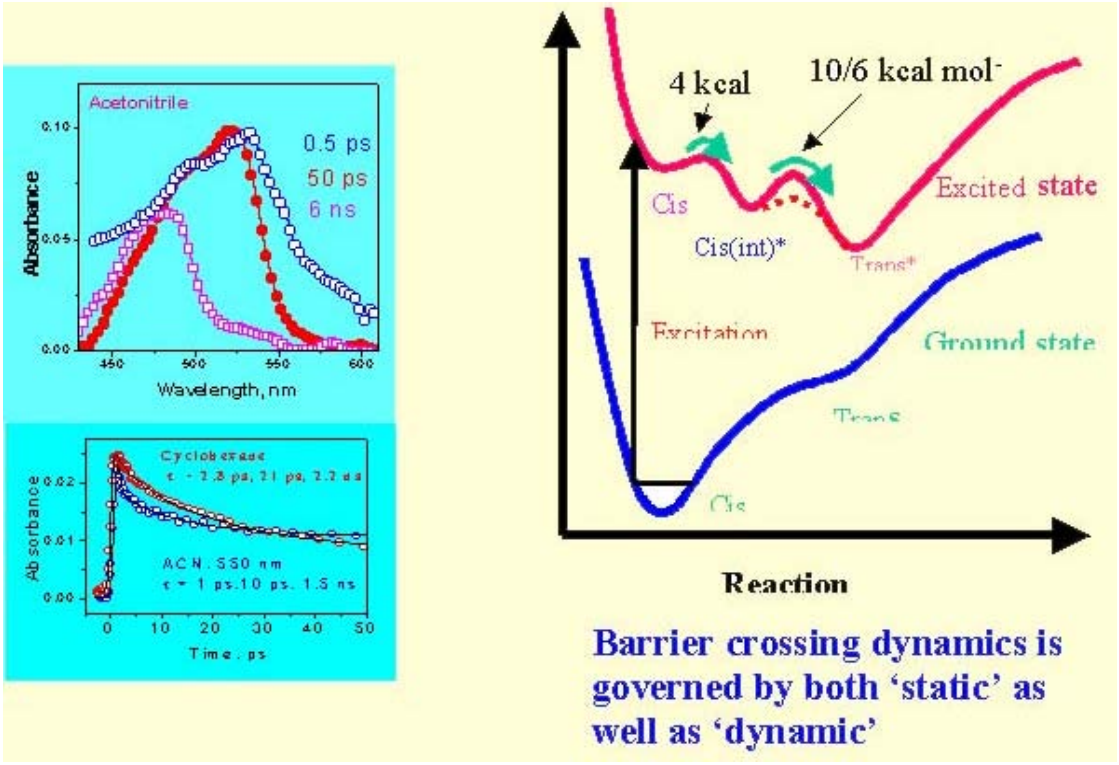

Fig. 7 Results of time resolved absorption study of Benzil and PES diagram for excited state relaxation dynamics

transient species, clearly reveas the non-single-exponential nature of the decay dynamics. The decay dynamics of the transient species have been seen to fit reasonably well with a decay function, which is a sum of at least three exponential terms. Among the three lifetimes, the longest-lived component (about a few hundred picosecond), which represents the residual absorption in this time domain, could be assigned due to the S_1 state having trans planar conformation. The component with the shortest lifetime, τ_1, is assigned to the S_1 state of the cis-skewed form of benzil. The second component with the intermediate lifetime, τ_2, could be assigned to the S_1 state of the meta-stable intermediate conformer. Hence, the change in conformation from the cis-skewed form to the more stable trans planar form in the S_1 state of benzil is associated with crossings of two consecutive energy barriers (Figure 7). The first of the two barriers is due to change of conformation from the cis-skewed to the meta-stable intermediate conformer and the second one is due to conversion of the later to the trans planar form. The two-step relaxation process, each one being associated with finite energy barriers, leads to non-exponential absorption decay kinetics. The rate of crossing of a particular energy barrier during transformation of one form to the other can be correlated with the disappearance of the precursor species. Since the conformational relaxation process should involve the movement of bulky groups in the molecule, say, the rotational motion of the phenyl and the dicarbonyl groups as well as the translational motion of the two phenyl groups, the rate of barrier crossing dynamics is expected to depend strongly on the viscosity of the medium. The present study in different kinds of solvents has clearly revealed two facts. One is

the existence of at least one other intermediate between the two well-known conformers, cis-skewed and trans-planar,, and the other is that the rates of conformational changes are dependent not only on the viscosities but also polarities of the solvents. In polar solvents, the barrier height of the cis(int) to the trans form is reduced significantly. Hence, it becomes evident that in addition to solute - solvent frictional interactions, the solute-solvent dielectric interactions also play an important role in activated barrier crossing dynamics for conformational changes in the S_1 state of benzil. The most obvious effect arising due to polarity is 'static' and involves the solvation of the reactants, products and transition states. Static interactions modify the intramolecular potential energy surfaces and influence the barrier crossing flux. The solvent induced modification of the barrier height overrides the viscous reduction of the flux over the effective barrier. The situation becomes more complicated by the likelihood that the lowering of the barrier in polar solvents is due largely to dynamic solvent polarization, as the conformational changes proceed such that the barrier crossing is actually a time dependent quantity.

In conclusion, conformational relaxation dynamics of benzil in the S_1 state from the cis-skewed to the trans planar form has been established to take place in two steps via the formation of a meta-stable intermediate conformer, the configuration of which probably has the configuration very near to the cis-planar form. The energy barrier for the first step, i.e. conversion of cis-skewed to the meta-stable intermediate is relatively smaller and barrier crossing dynamics is controlled by 'dynamic' or 'frictional' interactions with the solvent and the effect of 'static' interaction is not very significant. The energy barrier for the second step i.e. conversion of the meta-stable conformer to that of trans planar one is relatively higher and the barrier crossing dynamics is mainly controlled by 'static' rather than 'dynamic' interactions with the solvent.

Ultrafast relaxation dynamics in the excited states of dimethylaminobenzo-phenone (DMABP)

For several decades, steady state and time resolved phosphorescence spectroscopy as well as flash photolysis techniques have been used to study the photophysical and photochemical properties of the excited singlet and triplet states of benzophenone (BP) and its numerous kinds of derivatives by different groups.[1-15] Most of these studies have been devoted to unravel the intricacies of the mechanisms of photoreduction reactions undergone by these aromatic carbonyl compounds in presence of hydrogen atom donors. The rate and efficiency of this process have been shown to depend on the nature of hydrogen atom donor as well as the nature of the substituents on the aromatic rings. Here we present our results of our detailed studies on the photophysical properties of 4-dimethylaminobenzophenone (DMABP) using femtosecond transient absorption spectroscopic technique with a special attention to the solvation and conformational relaxation dynamics in the S_1 state of DMABP.

Geometry optimization for the ground state by molecular mechanic calculation shows that the dihedral angle between the two halves of the DMABP molecule consisting of the phenyl and the dimethylamino substituted phenyl groups attached to the carbonyl group is about 54°. Although we could not perform the geometry optimization for the excited ICT state, the geometry optimization for the ICT state formed in the ground state indicate that, in this state, the dihedral angle between the two phenyl moieties of the molecule is about 90°, i.e. the two halves are orthogonal to each other (Figure 8).

Steady state absorption and fluorescence spectroscopic studies of DMABP in different kinds of solvents reveal significant number of informations regarding the dynamics of intramolecular motions in the excited state: 1. a large shift of absorption in polar solvents, indicating that the Franck-Condon state is an

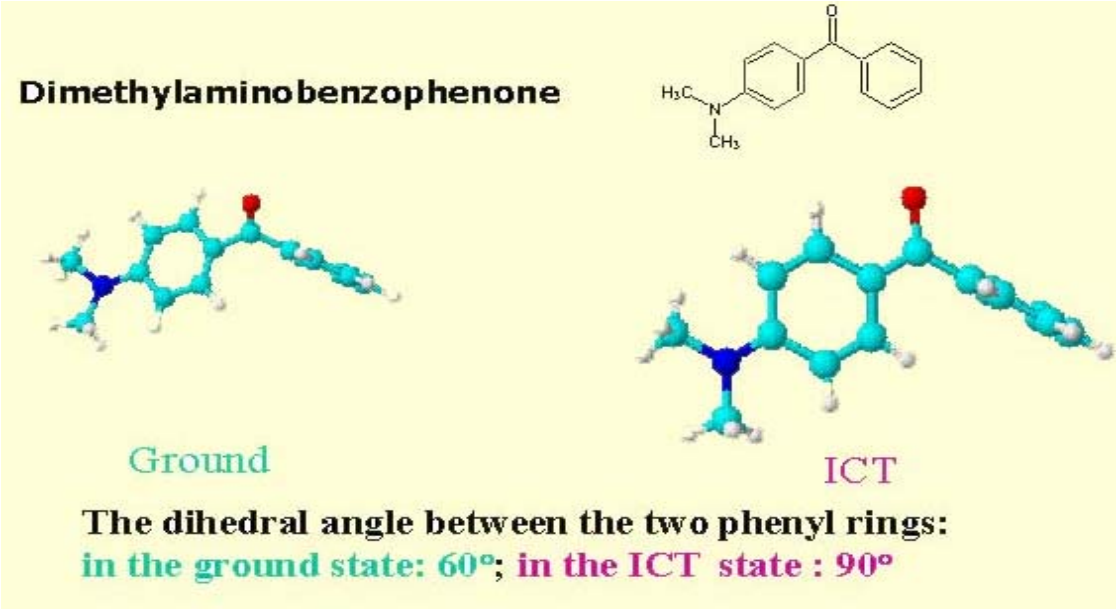

Fig. 8 Structure of DMABP

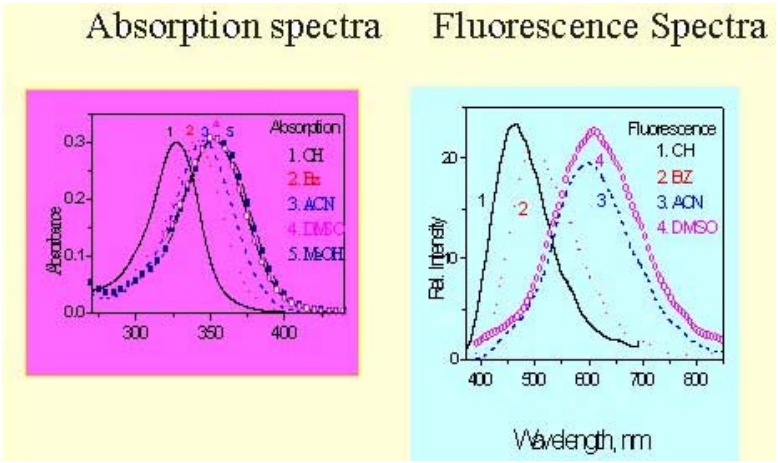

Fig. 9 Steady sate absorption and fluorescence spectra of DMABP

intramolecular charge transfer (ICT) state, 2. large bathochromic shift of fluorescence, indicating that solvation of the ICT state, 3. exceptionally large Stokes shift indicates large change in geometry during elaxation in the excited state, 4. non-fluorescent in rigid matrices, indicating that only the relaxed state is emissive. The difference in dipole moments between those of the fluorescing excited state and the ground state has been determined to be about 6.8 D. This indicates the unsymmetrically charge distributed $\pi\pi^*$ (in non-polar solvents), or the ICT (in polar solvents) character of the S_1 state.

We have studied the early time dynamics of the photophysical processes of DMABP using 400 nm laser pulses of 50 fs duration for excitation and monitoring the transient absorption profile in 470 – 1000 nm wavelength region with about 120 fs time resolution. The temporal profiles have been recorded due to photoexcitation of DMABP in acetonitrile at different wavelengths in 20 nm intervals. A few typical such temporal absorption profiles are shown in Figure 10. The time resolved transient absorption spectra have been constructed using these transient absorption profiles and the same in six time-windows have also been presented in

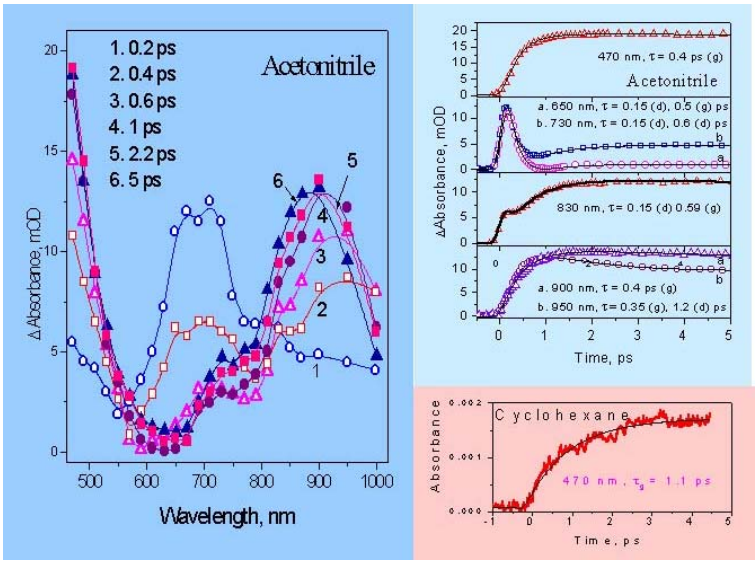

Fig. 10 Results of time resolved absorption study of DHABP

Figure 10. The spectrum constructed for 0.2 ps time-window consists only one major absorption band in 600 – 800 nm wavelength region having maximum at *ca* 670 nm. The transient absorption monitored at different wavelengths in this region grows with instrument limited rise time and then decays in ultrafast time scale with lifetime of about 0.15 ± 0.05 ps. This is followed by a further growth of absorption with a growth lifetime of about 0.55 ± 0.05 ps. The time-resolved transient absorption spectra constructed for the later time-windows reveal the ultrafast decay of the band in 600 – 800 nm region with the concomitant development of the two absorption bands in 470 – 600 nm and 800 –1000 nm wavelength regions. The maximum for the latter band is observed to appear at *ca* 950 nm at 0.4 ps. However, at later time-windows, as the absorbance in this band continues to increase up to 5 ps, the maximum shifts gradually towards the shorter wavelength region and the spectrum constructed at 5 ps show the absorption maximum at *ca* 850 nm. We also observe the growth of the band in 470 - 600 nm region. In 470 – 600 nm wavelength region, we observe only the growth of the transient absorption with growth lifetime of 0.4 ± 0.1 ps. However, the shape of the temporal profiles in 800 – 1000 nm region is sensitive to wavelength. The temporal profiles recorded at 830 nm could be fitted by a function having three exponential terms. Before the decay of the transient species (lifetime is about 0.15 ps), which initially grows with instrument response time (`120 fs), is complete, the absorption due to another species starts growing up to about 5 ps with growth lifetime of about 0.55 ps. The latter decays with longer lifetime, which has been determined to be 160 ps. The temporal absorption profiles at longer wavelengths, e.g. at 900 nm and above, show a single growth component. The growth lifetime this component is wavelength dependent. The growth lifetime increases as the wavelength shifts to shorter wavelength in the 800 – 1000 nm absorption band. However, we also observe the presence of an additional decay component at 950 and 1000 nm following the initial growth of the transient absorption

Following photo-excitation of DMABP, the FC state or the locally excited (LE) state, in which the two halves of the molecule have the initial dihedral angle of about 54°, should undergo twisting, to attain the more stable geometry with the two halves orthogonally oriented with each other. However, in polar solvents, the surrounding solvent dipoles require reorganization and reorientation around the newly created polar S_1 state to attain a new arrangement of solvent dipoles around it, which is known as solvation. Hence, we expect to observe mainly two kinds of relaxation processes following photo-excitation of DMABP: (i) solvation and population spreading in the excited state and (ii) twisting of the phenyl groups. Both of these two processes may be happening simultaneously, immediately after the creation of the excited state. However, in non-polar solvents, solvation process takes a minor role in

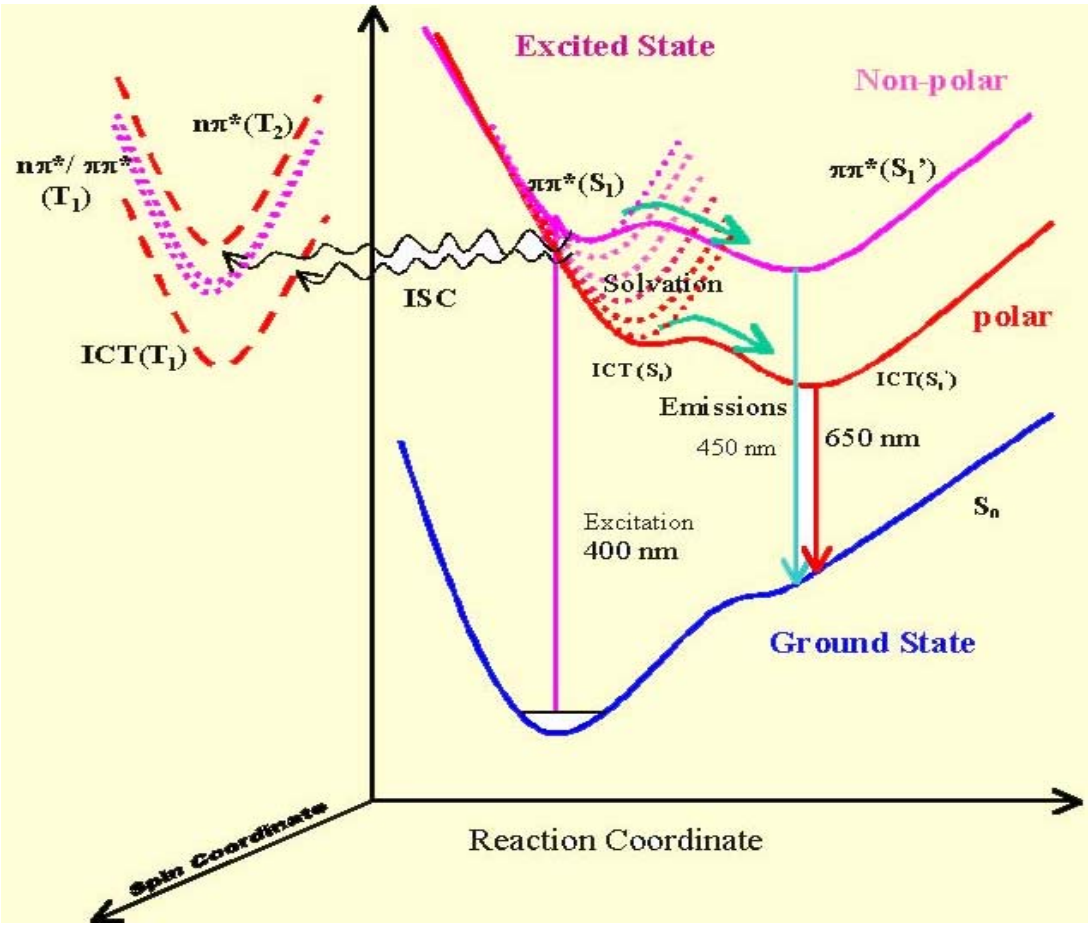

Fig. 11 Potential energy surface for relaxation of the S_1 state of dimethylaminobenzophenone

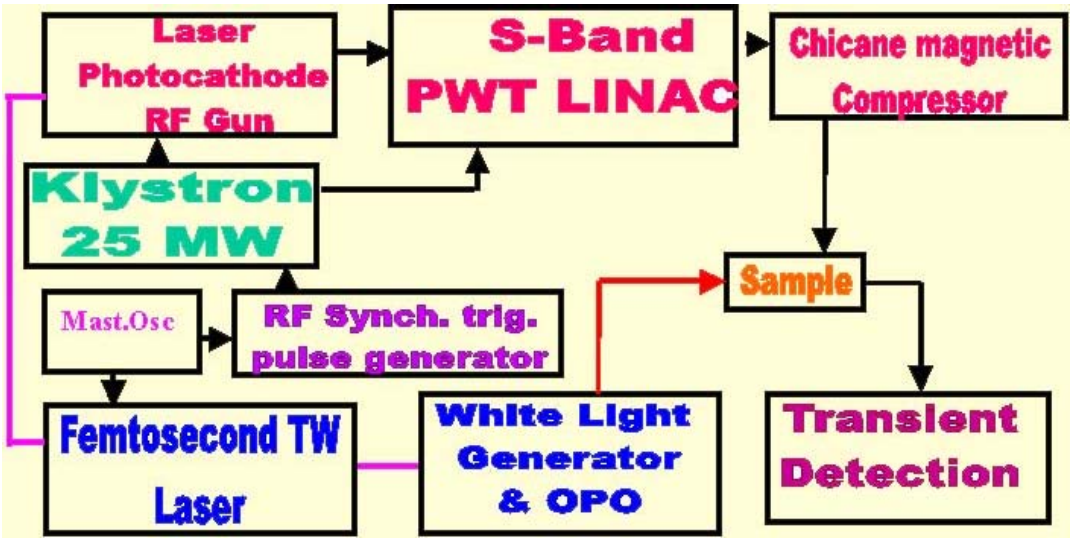

Fig. 12 Laser driven accelerator & subpicosecond pulse radiolysis set up (Proposed)

the relaxation dynamics of the S_1 state. The schematic potential energy surface diagram for the relaxation dynamics of the S_1 state of the DMABP molecule both in non-polar and polar solvents has been presented in Figure 11. In this Figure, we denote the conformationally unrelaxed and relaxed singlet excited states as S_1 and S_1', respectively.

Subpicosecond Pulse Radiolysis Study

So far, our activities have been limited in studying photoinduced chemical reactions in ultrafast (pico and femtosecond) time domain. Also we have been able to study radiation induced chemical reactions in nanosecond tim domain by using electron pulse radiolysis technique. However, in the next *Xth Five year plan project,* we have taken up the task of building *a laser diven sub-picosecond electron accelerator* (schematic diagram of the set up is shown in figure 12*)* to study the short-lived transient intermediate species produced in high energy radiation induced chemical reactions with pico (10^{-12} sec) and sub-picosecond ($<10^{-12}$ sec) time resolution. We like to investigate the following aspects of radiation induced chemical processes using this set-up: a. solvation of excess electrons in polar liquids, b. radiation induced processes in solutes with high concentrations, such as Nuclear Waste, electron mobility in liquids, solids and dense gases, d. slowing down of electrons in *spur* and electron – cation recombination, e. mechanism of hydrogen generation in *LOCA* condition,

Epilogue

Over the years we have developed the transient absorption spectroscopic techniques to study the ultrafast dynamics of molecular processes. We have chosen simple model molecules to understand the dynamics of electron or charge transfer, proton transfer, solvation and conformational relaxation processes. These informations should be useful to design molecular systems, which will be suitable for applications in photonics and solar energy conversion.

Acknowledgement

The author gratefully acknowledges the active contributions of his colleagues, who are the co-authors of the papers referred in the reference section. The author also acknowledges the constant inspiration and support of Dr. J. P. Mittal, Director, Chemistry & Isotope Group, and Dr. T. Mukhejee, Head, Radiation Chemistry &Chemical Dynamics Division, BARC, without which this contribution would not have been possible.

References

1. K. Singh, A. C. Bhasikuttan, D. K. Palit and J. P. Mittal, J. Phys. Chem. A , 2000, **104**, 7002.
2. D. K. Palit et. al *J. Chem. Phys.* ***1993****, 99,* 7273*.*
3. D. K. Palit et. al *Ultrafast Phenomena IX,* ***1994****, 501.*A. K. Singh, D. K. Palit and J. P.
4. Mittal, Res. Chem Intermediates 2001, 27, 125
5. A. C. Bhasikuttan, A. K. Singh, D. K. Palit, A. V. sapre and J. P. Mittal, J. Phys. Chem. A, 1999, 103, 4703.
6. A. C. Bhasikuttan, A. K. Singh, D. K. Palit, A. V. sapre and J. P. Mittal , J. Phys. Chem. A 1998, **102**, 3470.
7. A. K. Singh, D. K. Palit and J. P. Mittal, Chem. Phys. Lett. 360 (2002) 443 – 452.
8. A. K. Singh and Dipak K. Palit**,** Chem. Phys. Lett.357 (2002) 173 -180
9. D. K. Palit, A. K. Singh, A. C. Bhasikuttan and J. P. mittal, J. Phys. Chem. A 105 (2001) 6294.
10. A. K. Singh, G. Ramakrishna, H. N. Ghosh and D. K. Palit, J. Phys. Chem. (communicated).

Dr Dipak Kumar Palit is the recipient of Homi Bhabha Science & Technology Award for the year 2001.

About the author ...

Dr Dipak Kumar Palit *joined the Chemistry Division, BARC, after completion of the one-year orientation course (26th Batch) of BARC Training School. After obtaining his Ph. D. degree from Mumbai University in 1989, he was awarded 'BOYSCAST' Fellowship of DST for his post-doctoral work in the field of Ultrafast Spectroscopy in the University of Pennsylvania, USA. His current interest is to study chemical reaction dynamics in condensed phase using ultrafast lasers and accelerators. He has been conferred the Homi Bhabha Science and Technology Award for the year 2001 for his leading contributions in the field of Ultrafast Spectroscopy and Photo and Radiation Chemistry. He is also the recipient of Rev. Fr. L. M. Yeddanapalli Memorial Award (1999) from the Indian Chemical Society and Bronze Medal (for the year 2001) of Chemical Research Society of India for his significant contribution in this field.*

Remote Repairs of Helium Cover Gas Pipe Flange Joints in CIRUS Pile Block

Anil Bhatnagar and A.V. Kharpate
Reactor Group
Bhabha Atomic Research Centre

Summary

CIRUS IS A 40 MW(TH) HEAVY WATER moderated, light water cooled and natural uranium fuelled research reactor. In order to maintain the purity of heavy water, helium gas is used as cover gas for the heavy water moderator. The helium gas is maintained at a constant pressure of 12" water gauge in the system using a floating shell type gas holder. Normally the helium loss from the system through various pipe joints, through sampling and other day-to-day operations varies from 8 to 10 cuft/day. Helium loss from the system remained steady till year 1990 but gradually increased to 70 cuft/day till year 1996 and then to almost 160 cuft/day in the year 1997. This helium loss further increased to 200 cuft/day after Cirus was shut down for refurbishment in October 1997. This paper gives the details of how the helium leaks were located in Cirus, the design and development effort involved, mock up trials conducted and the remote repairs carried out to reduce the helium loss from the system.

Detection of Leak Location

The detection of leaky locations in helium cover gas system of Cirus was an involved job requiring detailed planning and meticulous site coordination. A step-by-step approach was adopted to locate the leak by sectional isolation of the piping system and pressure testing of each isolated pipe section. This method of pipe testing led to the conclusion that the non-isolable region of the helium piping system, which also included the reactor vessel, was the main source of leakage. Further testing by soap bubble method was carried out on all the helium system pipelines, which could be approached without any site constraints. In addition, helium sniffing using a special sampler and the Veeco MS-17 equipment was carried out above and below the reactor vessel through lattice tube holes to detect any helium leak from reactor vessel and/ or helium piping connected to reactor vessel. Helium sniffing clearly indicated that helium gas was leaking heavily in the 8" gap between the top biological shield and steel thermal shield where eight helium pipe flange joints are located at a depth of 14' from top of the reactor (Fig.1). Further local helium sniffing was carried out around each pipe flange joint and high concentration of helium gas was noticed around these flange joints. These tongue and groove (T&G) type flange joints connect the 2"dia aluminium riser pipes from reactor vessel to the S.S. piping of helium system using Buna –N rubber gaskets (Fig.2 & 3). Out of the eight such pipe flange joints, four pipe joints are connected to a semicircular 3"dia S.S pipe header whereas three pipe joints are connected to another 3"dia. S.S. pipe header. Both these 3"dia S.S. pipe headers are individually embedded in the side concrete biological shield. The remaining one 2"dia aluminium pipe is connected to a 1"dia. S.S pipe thorough flange joint and this pipe also enter the side concrete biological shield (Fig.4).

Selection Basis of Repair Technique

All these eight number of leaking flange joints above the reactor vessel are located deep inside

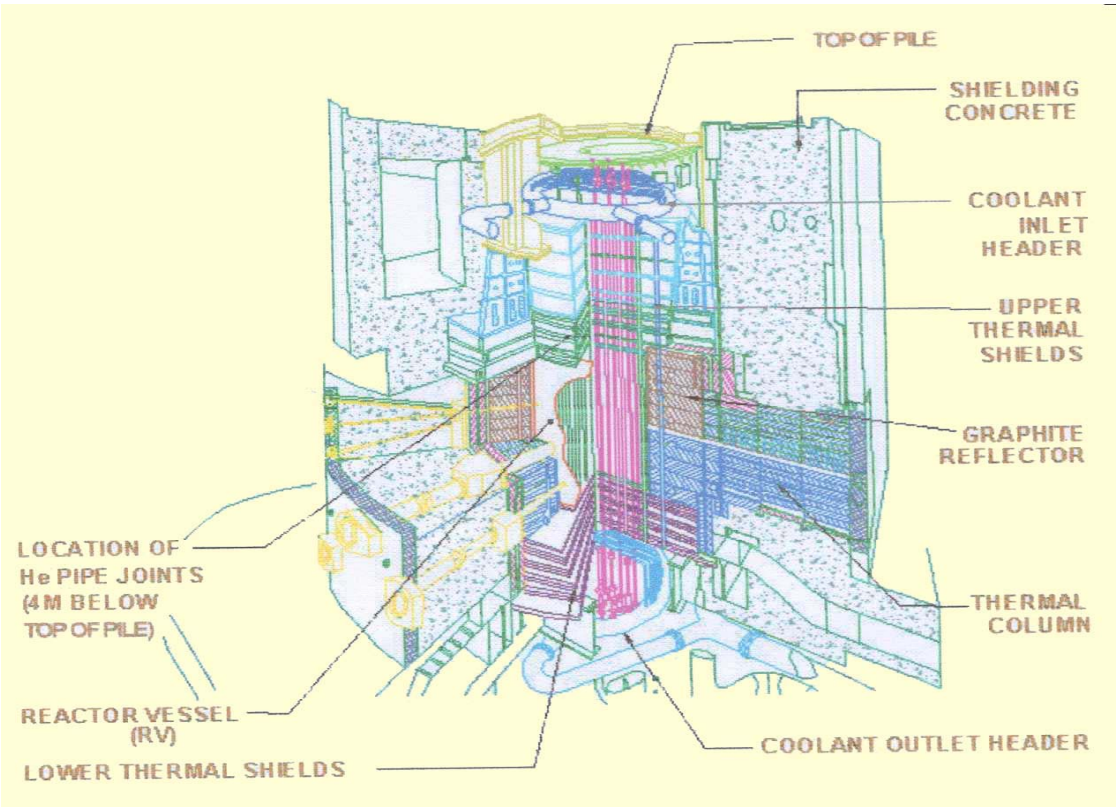

Fig.1 Cirus Reactor structure cross section

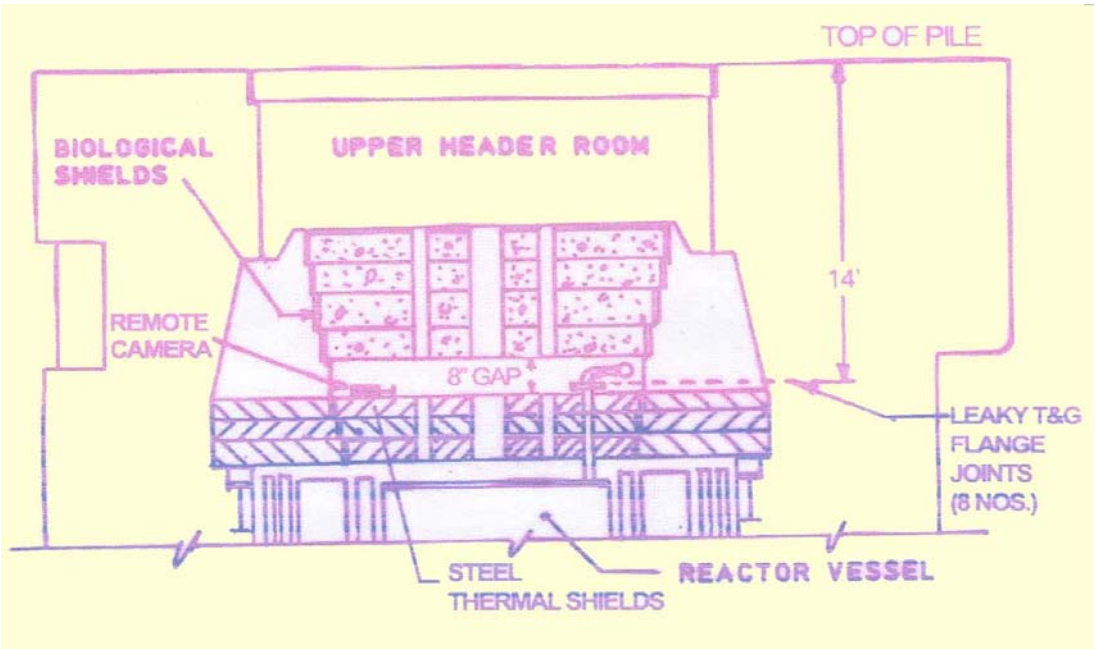

Fig.2 Simplified reactor structure & helium piping above reactor vessel

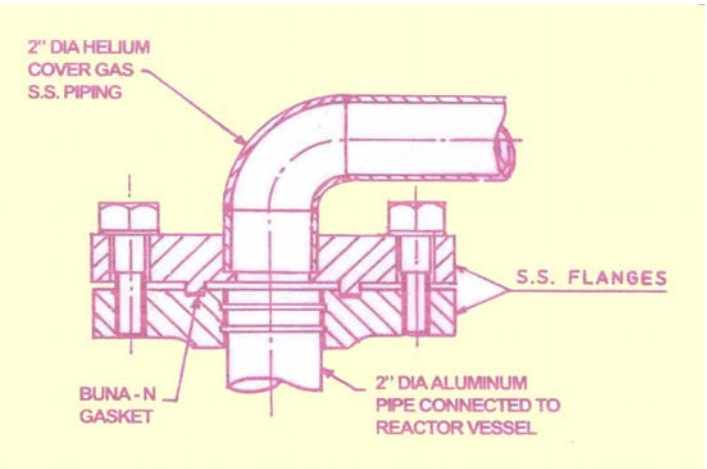

Fig.3 T & G flange joint

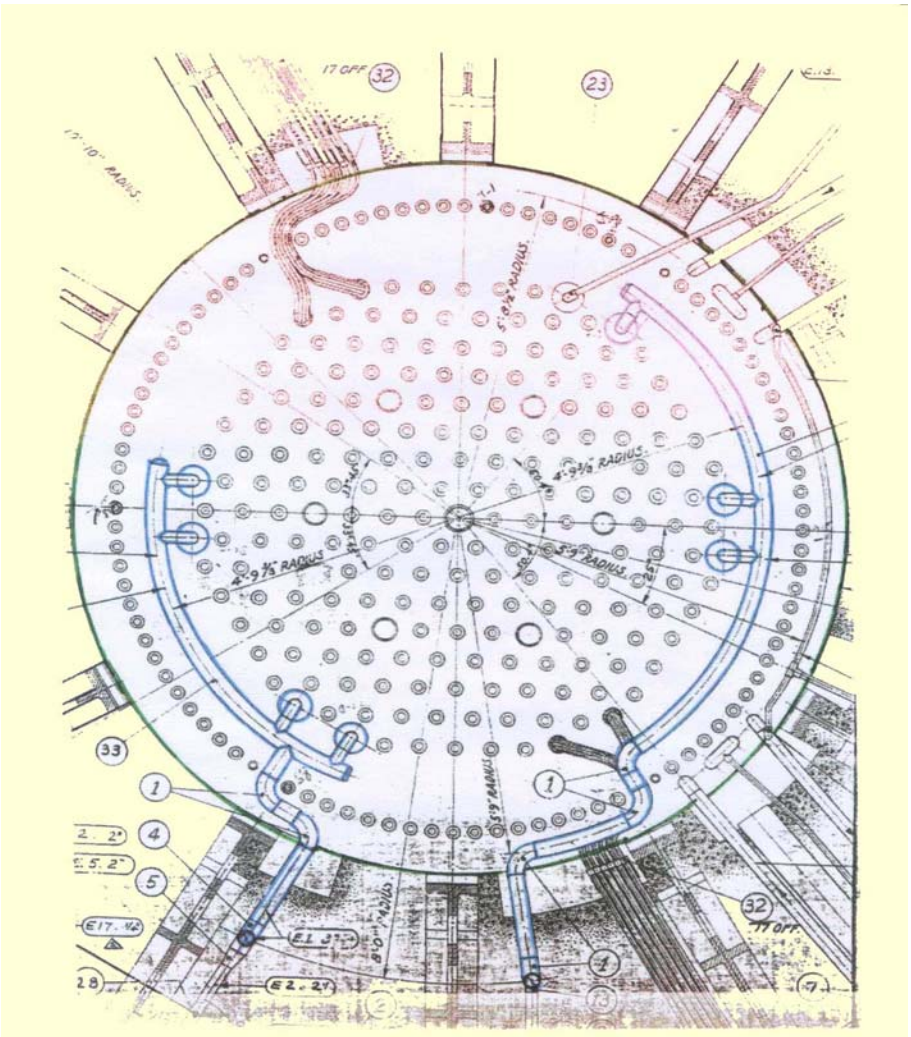

Fig.4 Plan view of cover gas piping at 8" gap location

the reactor structure and cannot be approached directly unless the massive radioactive structural components above the top steel thermal shield are dismantled and removed. The following repair methods were considered:

(A) Remove all the reactor components above the leaky flange joints, replace all eight numbers of leaky flange gaskets and install back all the components.
(B) Remotely repair all the eight number of leaky flange joints from top of reactor without any removal of reactor components.

As far as established maintenance practices are concerned, reactor structure dismantling was the right method (Method A) because all the leaking gaskets could be physically approached and replaced to ensure a leak tight joint. However, dismantling of reactor structure and other components was a massive and complex job, involving dismantling, handling and storage of large radio-active and contaminated components like:

(i) High pressure and High temperature water loop test section used for testing of power reactor fuel.
(ii) Reactor Coolant pipe lines.
(iii) 20"dia Primary coolant inlet header with its 17 cross-headers.
(iv) 200 number of primary coolant inlet valves called Trunnion valves.
(v) 4 inch thick and 13 feet dia support plate called master plate.
(vi) Four numbers of concrete biological shields each 13 feet in dia and each weighing about 20 Tons.

Repairs by method (A) involved working in a highly contaminated and radio active area during removal of radio-active components resulting in high man-rem consumption. Also there were apprehensions that after 40 years of reactor operation various dowels and dowel holes of 4 numbers of 20 Ton biological shields must have got corroded and jammed thereby making their dismantling a very difficult proposition. In addition jamming of some of the corroded components could lead to their breakage while dismantling, which could create difficulties in their reinstallation. Further, each biological shield has nearly 300 lattice holes for lowering/raising of fuel and other irradiation assemblies. These lattice holes are to be aligned very accurately during reinstallation. Any misalignment during reinstallation could render some pile positions unusable, as was the experience at NRX reactor in Canada.

Hence repair of all the above joints by method (A) with many site constraints and with possibility of breakage of any 40 years old radioactive component while dismantling could result in enormous time delays, thus affecting re-commissioning of the reactor. It was, therefore, decided that remote repairs to the tongue and groove joints by method (B) should be attempted.

Design & Development of Remote Repair Technique

Following site constraints were faced while developing the remote repair technique:

(i) All the operations were to be performed from a distance of 14'.
(ii) Vertical gap available around the flanges was only 8". Hence all tool heads had to be less than 8"in length.
(iii) Lattice holes near the leaky 6"OD flange joints were of 2¼"dia only. The 6"dia central hole was nearly 5'away.
(iv) Dimensions of all the eight flange joints varied significantly from each other.
(v) Amount of tightening was to be controlled strictly.

Various alternatives that were considered for remote repairs of the leaky T& G flange joints were as follows:

(a) Tightening of the bolts on the T&G flange joints:
A preliminary design of the tool to be remotely operated from the nearest available lattice position was conceived. As there were four bolts on each T&G flange

joint and as two of these bolts were more than 8" away from the nearest available lattice position, it was felt that designing the tool to provide enough torque transmission for tightening the bolts would be difficult and this alternative was not pursued.

(b) Use of shape memory alloy in a sealing gadget:

This alternative was reviewed with Metallurgy Division. However, during site measurements it was found that the various dimensions of the T&G flanges varied significantly from one T&G joint to other. Further there was severe limitation on the amount of compression to be provided to T&G flanges to avoid undue stress on the reactor vessel and piping. In view of the above, this alternative was also not pursued.

(c) Remote tightening of a split sealing clamps around the T&G joint flanges:

This alternative was finally selected for implementation. The detailed design, development, fabrication and mock-up work carried out on this alternative is described below:

An important observation made during reactor operation was that whenever the reactor was in operation, the helium leak reduced to almost half its value as compared to reactor shut down. This indicated that thermal expansion of pipes during reactor operation brings the T&G flanges close together and makes the joint relatively more leak tight. This also indicated that Buna-N gaskets in T&G joints were still flexible and continued to retain sealing properties. Based on this observation, it was felt that if the T&G flanges could be remotely tightened, it might help in arresting the leak with the old Buna-N gasket itself. Towards this, a special split sealing clamp (SSC) (Fig.5) of innovative design was developed. The special split clamp has tapering surface on the I.D so that when the clamp is tightened over the flanges of the T&G joint, it pushes the T&G flanges closer to each other to compress the Buna-N gasket thus resulting in a good sealing. This clamp was tested on a mock-up station and it could arrest air leak at 20 psig. In the mock-up station very old, broken (in 3 pieces) and irradiated gaskets were also tested and the leak could be easily stopped with less than 5 ft-lb torque applied by clamp tightening. Hence it was decided to develop a remote repair procedure using split sealing clamp. For approach to the leaky flange joints, the largest lattice tube was of 6"dia only and the clamp was bigger in size. Hence the clamp had to be fabricated as a split clamp.

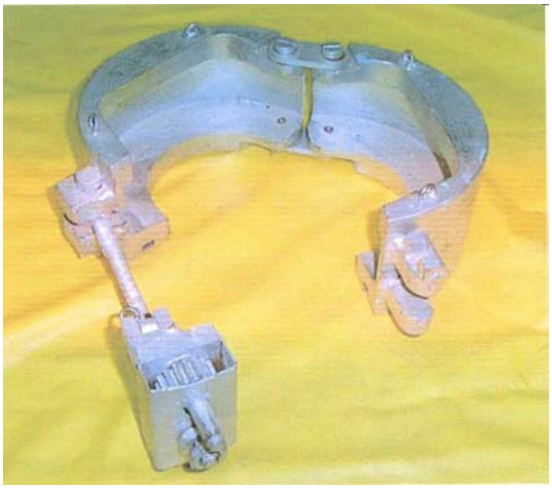

Fig.5 Split sealing clamp

Major Operations Involved in Remote Repair of T&G Flanges

Following were the major operations to be conducted during remote repairs:

(i) Lowering of split sealing clamp through pile lattice hole up to the 8" gap on top of steel thermal shield.
(ii) Horizontal shifting of the clamps up to T&G flange location and fixing the clamp around the leaky flange.

(iii) Remote tightening of the clamps on to each of 8 nos. of T&G flange joints.

The leaky T&G flanges joints are 6”in O.D and are located nearly 5'away from the 6”dia central lattice tube, which is the only largest dia tube through which the split clamp can be lowered. This constraint required horizontal shifting of each clamp to the T&G flange locations. Also the nearest pile hole of 2 ¼” I.D is about 6”away and the 4”dia. hole is about 2'6”away from the T&G joints for any approach for remote repair of the leaky flanges. (Fig.4).

Mock-up Station

In order to develop various tools for remote repair, to calibrate the tools, to establish procedures and train personnel for carrying out the work at site remotely, a full scale mock up station simulating the top portion of the reactor structure including the lattice tubes was erected.

Fig. 6 Clamp fixed around leaky flange

Also one 3”dia semi circular header with two adjacent 2”dia elbows each having a T&G flange joint similar to the one in pile was erected at the mock up station at a depth of about 14' from top of the station. Six nylon ropes of adequate strength were used for vertical lowering, horizontal shifting and fixing of the split sealing clamps around the leaky T&G flange joints. Four of the six nylon ropes were lowered from suitably selected simulated pile lattice holes around the leaky T&G flange into the 8”gap, horizontally shifted in the 8”gap up to the central 6" dia lattice hole and brought through the 6”dia hole up to the top of master plate. These nylon ropes were tied to the hooks provided on the split sealing clamps and the clamps were vertically lowered through 6”pile hole up to 8”gap. These nylon ropes were used for horizontal and vertical manoeuvring of the sealing clamps in the 8” gap and to fix them on the leaky flange joints. For lowering the sealing clamp, manoeuvring and retrieving it, if required, one nylon rope was tied to the swing bolt of the sealing clamp (Fig.6).

Tightening Tool

A tightening tool having a box spanner adapter for the hexagonal tapered spindle on the clamp was designed. This tool was provided with a universal joint for easy alignment of the adaptor with the tightening spindle and a spring loaded telescopic tube arrangement for catering to away movement of the spindle along with the nut during tightening. Power transmission was to be done through a pair of bevel gears attached to the tool. The tool was so designed that it could be lowered vertically through a 2¼”lattice tube and the bevel gears could be engaged by lifting the hinged lower portion of tool to make it horizontal. Tightening heads of different lengths were made for attachment to the tool to permit approach to the clamp from various lattice positions.

Gauging Tool

For finalizing various dimensions of the split clamps, site measurements were taken remotely on all the eight T&G flange joints. A gauging tool was designed and fabricated and separate attachments were made to measure the following site dimensions from a distance of 14':

(i) Total thickness of the T&G flange joint
(ii) Gap between the upper and lower flanges of the joint
(iii) Gap between the top of steel thermal shield and the bottom of bottom flange.

These dimensions were incorporated in the mock up station for conducting the mock up trials and clamp calibration.

Mock-up Trials

Extensive trials for vertical lowering, horizontal shifting and fixing of the split sealing clamp on the tongue and groove flange joint were carried out at the mock up station after installing two video cameras in the 8" gap at a depth of 14' below the top platform and the whole operation was carried out by remote viewing in the video monitors kept on the top platform of mock up station. Special light assemblies were also fabricated and lowered into the 8" gap for proper illumination & viewing. The piping system of mock up station was pressurized with helium to 24"wg i.e. double the reactor helium system pressure and after remote clamping, the joints were checked to be leak free by helium leak testing.

Retrieval of the installed and tightened clamp was also successfully carried out a number of times during mock up trials to meet the eventuality of any rope failure or need to remove clamp for malfunctioning or for any other reason. Suitable ball rollers provided at the bottom of the split sealing clamp ensured that the force required to pull the ropes while horizontal sliding the clamp in the 8" gap from central 6" location to leaky flange T&G joint was less. All the operations and procedures established were checked by the Quality Assurance personnel at the mock up station for approval.

Calibration of Mock-up Station

As the tightening of the split clamps was to be limited in each step, each split clamp was calibrated at mock-up station after adjusting the flange joint at mock up station to suit that particular T&G flange site condition. For each number of turns of tightening nut, the flange compression was measured using dial gauges. A graph was plotted for number of turns of tightening nut v/s. total compression of flange joint. This graph was used for tightening of clamps at site.

Stress Analysis of Piping System due to Clamp Tightening

To measure the stresses developed in aluminium pipes welded to top tube sheet of reactor vessel during tightening of the clamp, the stresses on aluminium pipe at mock up station were measured by Reactor Safety Division, BARC (RSD) during tightening of clamps using strain gauges. The maximum stress measured was found to be less than 50 kg/cm2, which was well within the permissible limit. Further, it was decided to carry out detailed stress analysis on piping system in order to arrive at the maximum permissible compression of the T&G flange joint gasket and also to finalise optimum sequence of flange tightening to minimize the stresses on the pipes/weld joints during tightening.

Tensile properties of irradiated aluminium were earlier measured during ageing studies carried out on reactor vessel. In analysis carried out by RSD no credit was taken for increase in Yield strength and Ultimate tensile strength values due to irradiation. Further, to take care of loss of ductility due to irradiation, the allowable stress was lowered by 25% of that of the irradiated aluminium material.

In order to measure various parameters of irradiated gaskets, Buna – N rubber sheets were procured and irradiated to the estimated total dose received by the T&G joint gaskets. These irradiated gaskets were then compression tested and the test parameters measured were used in the analysis.

A detailed stress analysis by CAESAR-II computer programme was carried out by RSD on the 3" header having four tongue and groove flange joints using the above data, as this combination was subjected to the most severe stress conditions as compared to other piping combinations. The analysis indicated that the T&G flanges joints could be safely compressed up to 0.8 mm on a newly made flange joint. Assuming a normal initial compression of 0.4

mm to achieve flange tightening, as confirmed during various mockup trials, an additional compression of 0.4 mm could be given to all the T&G flange joints on this header. Even for a maximum gasket compression of 0.8 mm, the maximum stresses were within 85% of the allowable value in shear mode for irradiated material.

Similar stress analysis was carried out on the second piping system and the maximum permitted compression was also limited to 0.8 mm and stresses were calculated to be within permissible limits.

Total compression was provided in steps to all the flange joints to ensure uniform tightening thereby reduced stresses on the piping system. It was seen that the stresses increased when only one flange joint was compressed. However once the uniform compression was given to all flanges on the header, the stress values dropped significantly. Therefore, it was also decided that the compression would be given to the flanges in sequential steps.

The sequence of flange tightening was finalized such that the stresses remained at the minimum possible value.

Site Measurements

Site measurements for total thickness of T&G flange joints in pile were taken at three locations 90 deg. apart using the gauging tool. The values varied between 43.5 and 45.4 mm as against the drawing dimension of 44.45 mm with no gasket tightening.

Site measurement of gap between the top of steel thermal shield and lower flange of the T & G flange joint was also done. The distance varied between 29.9 mm and 34.1 mm as against the drawing dimensions of 25 mm necessitating major changes in one of the split clamps.

Site measurement of gap between the top and bottom flanges of the T&G flange joint was also carried out. The readings varied from 2.15 to 3.7 mm. The above two measurements were also carried out at 3 locations 90 deg. apart.

Split Sealing Clamp Lowering and Fixing at Site

For lowering and installing the split sealing clamp around the T&G flange joints, four nylon ropes were lowered from predetermined positions around the flange joints, as per approved procedure established at the mock up station. These ropes were turned around the flange joint in counter clock-wise direction and horizontally shifted in the 8" gap to bring them near 6"dia central lattice hole position and were then brought up to top of pile. These ropes were tied to the clamps at hooks provided on it. Two more ropes were tied to the clamp swing bolt and the locking lever for clamp retrieval if required.

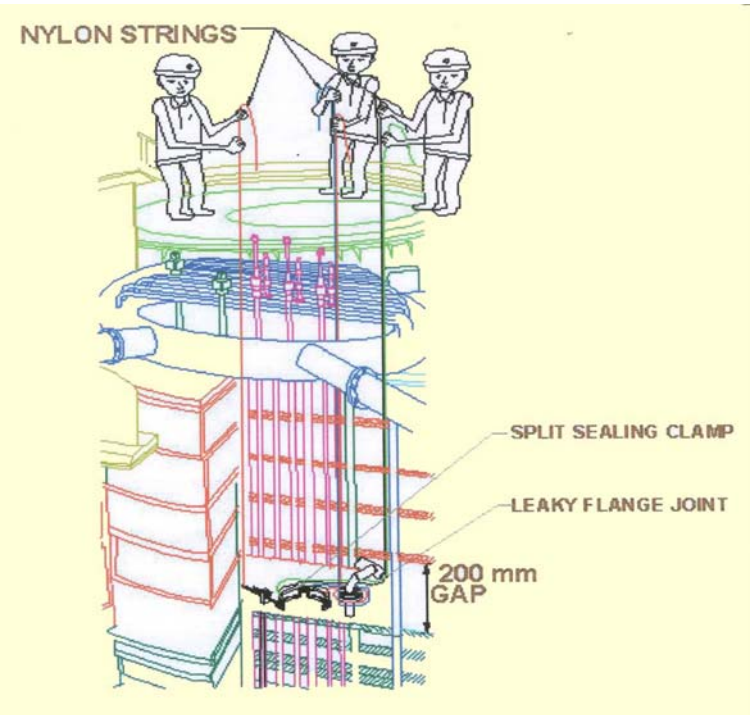

Fig.7 Clamp being manoeuvred around T & G flange joint

Clamp was then lowered through the central lattice hole in the 8" gap, horizontally slid to the flange joint and fixed around the flange joint as per approved procedure (Fig.7). All the remaining seven clamps were likewise lowered and fixed around the flange joints.

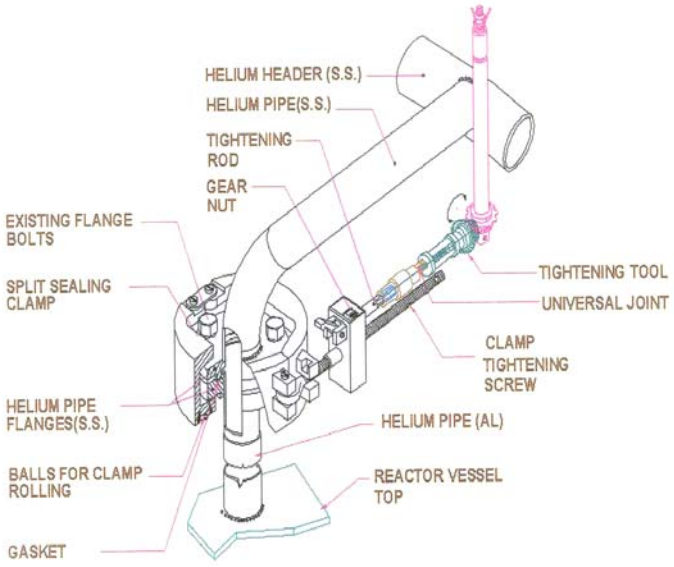

Fig.8 Clamp being tightened with tightening tool

Tightening of the Split Sealing Clamp at Site

For tightening of split sealing clamp on flange joint, tightening tool was lowered from nearby suitable 2¼"dia lattice position and clamp tightening was carried out as per the approved procedure (Fig.8). Tightening was similarly carried out on the remaining seven clamps. The helium leak rate from the system after carrying out this tightening came down to 35 cuft/day.

Conclusion

Helium system leaks, which had risen to as high as 200 cuft/day in year 1998 have been successfully brought down to 35 cuft/day after installation and tightening of split sealing clamps on all the eight tongue and groove flange joints. This leak rate is quite manageable and may come down further during reactor operation due to thermal expansion of piping.

The authors are the recipients of the DAE Technical Excellence Award for the year 2001

About the authors ...

Mr Anil Bhatnagar, *B.E (Mechanical), graduated from 19th Batch of BARC Training School. He joined Cirus reactor operations in 1976 and qualified as Shift Charge Engineer. He later worked as Senior Operations Engineer and was involved in Ageing Studies for in-core components of Cirus Reactor. He subsequently worked in the Design and Planning Section of Cirus and was also involved in scheduling and monitoring of refurbishing activities for Cirus Reactor. He, along with Mr A.V. Kharpate, conceptualized the design and executed remote repair on leaky helium pipe flange joints and leaky inlet coolant pipe of upper aluminium thermal shield in Cirus reactor.*

Mr A.V. Kharpate, *B.E. (Mechanical), graduated from 15th batch of Training School. He joined the fuel handling group of R-5 project (Dhruva Reactor). He was involved in design, development, fabrication, installation & commissioning of underwater spent fuel handling and storage facilities. After commissioning of Dhruva, he was involved in core design and development of a Multipurpose Research Reactor (MPRR). He took over as Maintenance Superintendent (Mechanical) in the year 1994 and since then he is responsible for preventive and break down maintenance of mechanical equipments for safe and reliable operation of the research reactors Dhruva, Cirus & Apsara. He was very actively involved in almost all the refurbishing jobs taken up in Cirus during the recent refurbishing outage. He, along with Mr Anil Bhatnagar, conceptualized the design and executed remote repair on leaky helium pipe flange joints and leaky inlet coolant pipe of upper aluminium thermal shield in Cirus reactor.*

Chemical Decontamination of BWR Nuclear Systems

G. Venkateswaran
Applied Chemistry Division
Bhabha Atomic Research Centre

Abstract

The dilute chemical decontamination (DCD) of Clean-up System of Unit-2 of Tarapur Atomic Power Station was carried out during August 2000 during the 16th refuelling outage of the unit. This was the result of a decade long laboratory cum loop studies, design and indigenous fabrication of components, phase-1 testing without chemicals all of which together finally led to the execution of the actual chemical decontamination of the system. A two-stage three-cycle AP-CEA process developed for stainless steel surfaces, involving an oxidative pre-treatment of the oxide surface using an alkaline permanganate (AP) solution to remove selectively Chromium from the oxide as the first stage and a second stage wherein oxide dissolution was achieved by using a formulation consisting of Citric acid-EDTA-Ascorbic acid (CEA), was employed. Decontamination factors (DFs) ranging from 1.2 to 10 depending on location were obtained. The three regenerative heat exchangers and the two non-regenerative heat exchangers, which are the main pieces of equipment from the surface area consideration, have shown DFs from 3-10. A total of 3.68 Curies comprising mainly of ^{51}Cr radioactivity (97%) along with 3.2 kg of chemical Chromium was removed in the three AP cycles. A total of 8.96 Curies comprising mainly of ^{60}Co along with 6 kg f chemical Iron was removed from the three citric acid washes cum CEA cycles. The spent decontamination solution was successfully treated with a set of ion-exchange columns. A Na^+ form of cation exchange resin (gel type) column was employed for the removal of manganese from the spent pre-treatment solution. A strong acid polystyrene based cation resin column in H^+ form, a strong base polystyrene based anion resin column in OH^- form and a mixed bed column of these resins were employed for the removal of metals and radioactivity from the CEA solution. The manganese-balance done in the system had shown that no Mn was left in the system after decontamination and this is also proved by the continuous operation of the reactor without any radioactivity problem due to ^{56}Mn after the chemical decontamination. The microscopic evaluation of both sensitized and unsensitized stainless steel surfaces had shown no localised attack due to the decontamination process. The uniform corrosion observed on a variety of structural materials except carbon steel was negligible. After this successful campaign, efforts are underway to decontaminate the reactor recirculation system which nearly constitutes a full scale primary system decontamination.

Introduction

ONE OF THE IMPORTANT FACTORS determining the efficient operation of water-cooled nuclear power reactors is the occupational radiation exposure incurred during the reactor operation and maintenance. The structural materials of the primary coolant system, even under optimum water chemistry conditions, generate corrosion products, albeit at minimum levels. These corrosion products which are normally hydrous oxides / hydrated oxides get transported through the core where they undergo neutron activation, a unique phenomenon (applicable only to the nuclear industry) which results in the generation of activated corrosion products (ACPs). Radio nuclides like ^{60}Co (5.27 y), ^{58}Co (72d), ^{54}Mn (278d), ^{59}Fe (45d), ^{51}Cr (27.8d) which have half lives (given in brackets by the side of the

radionuclides) long enough to control the reactor maintenance activities, are normally encountered in these ACPs. When deposition of ACPs occurs on system surfaces, the radiation field around the primary system of the nuclear reactor starts building up. In the case of TAPS BWRs also, it is observed, like that experienced in reactors of that vintage elsewhere, that ^{60}Co controls the radiation fields around the primary coolant system.(1)

Chemical decontamination aims to dissolve these ACP oxides from the system surfaces and remove the resulting solubilized species using the ion-exchange resins. Dilute Chemical Decontamination (DCD) is the most suited method for decontaminating the internals of piping, tubes/shells of heat exchangers, pumps, valves etc., of a reactor. This is because the decontaminating solution can reach the nooks and corners, dissolve out the ACP oxides without causing excessive base metal attack and yield reasonably high DFs (DF is the ratio of initial radioactivity or radiation field on a system surface before decontamination to that existing after decontamination).

The choice of a particular chemical decontamination formulation depends on the type of predominant oxide one encounters on the structural materials present in the system. The requirement for a formulation in the case of BWRs such those at TAPS, employing stainless steel as the major structural material and oxidizing water chemistry in the primary coolant system, is different from the one suited for PHWRs which employ carbon steel as the piping material and follow a reducing water chemistry regime. In the former case the oxide layer formed is really a mixture of oxides such as Cr_2O_3, $FeCr_2O_4$, $Fe_{3-x-y}Cr_xNi_yO_4$ ($x<1$, $y<1$), Fe_3O_4 and Fe_2O_3 unlike the latter case it is essentially Fe_3O_4. While the Cr rich layers such as Cr_2O_3, $FeCr_2O_4$ constitute a thin inner layer, the Ni, Cr substituted magnetite plus the magnetite and the hematitie together constitute the thick outer layer.(2) Thus for BWRs the development of decontamination formulation one must address the effect of Cr content of the oxide in controlling the dissolution of ACP. If the Cr content of the oxide is low, then no pre-treatment step is required and the reductive dissolution formulation can be applied directly. If the Cr content of the oxide is high, then to overcome its negative effect in controlling the oxide solubility in the reductive-complexing formulation, a pre-treatment step needs to be incorporated by which Cr from the oxide is selectively dissolved out. This paper gives a glimpse of the various systematic studies that have gone in the development of a suitable formulation for decontaminating the TAPS BWR sub-system and highlights the results obtained in the actual application of the developed formulation.

Development of the Chemical Process

Coupon experiments

a) *Radioactive coupons employed:* Applied Chemistry Division and TAPS chemical control laboratory were responsible for the development of the decontamination formulation. Test coupons of dimension 26 mm length x 26 mm breadth x 6mm thick with the system oxide were cut from a section of a 100 mm NB AISI-304 piping, removed from the C/U system of Unit-1 of TAPS during the replacement of the regenerative heat exchanger, were employed. Since the pipe line was at the inlet side of the regenerative heat exchanger, the surfaces had developed the oxide under reactor conditions of high temperature (543 K) and pressure (70 kg/cm^2).

b) Formulations employed :

Dissolution stage : Electrolytically prepared tris-picolinato V(II) (called the V^{2+}-LOMI) in the concentration range 4-50 mM was employed on as-such coupons. This formulation in 4 mM concentration was employed in the oxidatively pre-treated coupons. Citric acid-EDTA-Ascorbic acid in the concentration range <2 : <2 :<4 mM was employed on pre-treated coupons.

b.1) Pre-treatment stage: b.1.1) With alkaline permanganate: A 0.3% (19mM) $KMnO_4$ in 1.5%

(375 mM) NaOH for oxidizing the Cr^{3+} in the oxide to yield a soluble CrO_4^{2-} was chosen from the requirements of base material compatibility and the amount of oxidant estimated to be required to solubilize the Cr in the oxide of the Clean-up system. A corrosion rate of $3.8x10^{-3}$ μm/h over a 12 h exposure period was observed for SS-304 in this AP medium without resulting in any specific type of attack. For comparison purposes pre-treatment formulation containing 0.1% $KMnO_4$ in 0.5% NaOH was also tried.

b.1.2) With Permanganic acid: Permanganic acid concentrations of 0.23%(w/v) (19.2 mM) and 0.023% (w/v) (1.9 mM) were employed. opious precipitation of MnO_2 on the oxide surface as well as on the bare stainless steel surfaces was observed. This was not observed with AP solutions. In actual decontamination, deposition of MnO_2 on the oxide bearing SS surface could lead to restricting the Cr leaching from the oxide and affect the efficiency of the decontamination process.

b.1.3) Pre-treatment with H_2O_2: Use of H_2O_2 as an oxidizing agent which gives H_2O and O_2 as the products could be advantageous if it could oxidize the Cr^{3+} in the oxide. A concentration of 2.65% (v/v) i.e., ≈0.8 M was chosen since in the 0.2-1.0 M region H_2O_2 is only mildly corrosive to SS.

Table-1 : Results of decontamination experiments on reactor specimens using V(II) LOMI and CEA dissolution formulations with and without pre-treatment

Expt No. (Coupon No.)	Concentration of formulation (mM)	Temperature (K) – Time of exposure (h)	Deconta-mination Factor (DF)	Remarks
Experiments without pre-treatment with single cycle LOMI [Tris picalinato V(II)]$^-$				
1 (#4)	20	348-363 [4.5]	1.2	DF after single cycle
2 (#3)	20	348-363 [10]	1.2	Fresh coupon, formulation from experiment #1
3 (#4)	20	338-348 [10]	1.0	Coupon from expt.#1, fresh formulation
4 (#10)	20	358-368 [23]	1.3	Fresh coupon, fresh formulation
5 (#1)	5	338-351 [11.5]	1.0	Fresh coupon, fresh formulation
6 (#2)	50	338-343 [18]	1.3	Fresh coupon, fresh formulation
Experiments with 0.3% $KMnO_4$ – 1.5 % NaOH (AP) pre-treatment for 4h at 340 K followed by treatment with LOMI [Tris picalinato V(II)]$^-$ (single cycle)				
7 (#5)	3.3	339-345 [3]	15.4	Fresh coupon, fresh formulation
8 [#20]	4.0	343-353 [2]	4.0	Fresh coupon, fresh formulation
9 [#22]	4.0	359-365 [4]	5.8	Fresh coupon, fresh formulation
10 [#13]	4.0	333-343 [2.6]	2.3	Fresh coupon, fresh formulation

Table contd...

2 cycle AP-LOMI, parameters during 2nd cycle; DF after 2 cycles				
11 [15]	4.0 (0.1%AP)	339-345 [4.0]	4.4	Fresh coupon, fresh formulation
11 [#5]	4.0 (0.3%AP)	337-343 [4.0]	24.6	Fresh formulation
12 [#20]	4.0 (0.3%AP)	333-353 [2.25]	6.9	Fresh formulation
13 [#22]	3.9 (0.3%AP)	359-363 [3.0]	9.2	Fresh formulation
14 [#13]	3.5 (0.3%AP)	348-353 [3.5]	8.1	Fresh formulation
Experiments with $HMnO_4$ pre-treatment followed by V (II).LOMI – single cycle				
15 [#3]	4.0 (pre-treatment with 19.2 mM $HMnO_4$ - 4.8 h)	319-335 [3.3]	2.6	Used coupon, fresh formulation
16 [#1]	4.0 (pre-treatment with 1.9 mM $HMnO_4$ – 4 h)	337-340 [3.2]	1.6	Used coupon, fresh formulation
Experiment with H_2O_2 pre-treatment followed by V(II).LOMI – single cycle				
17 [#16]	4.0	334-343 [2]	1	Fresh coupon, fresh formulation
2 cycle AP-CEA experiments				
18 [#19]	1.3:1.3:1.7 CEA	363-371 [4]	7.7	Fresh coupon, fresh formulation
19 [#10]	1.3:1.3:1.7 CEA	340-345 [4]	4.3	Used coupon, fresh formulation

Table-1 shows the decontamination factors obtained in the coupon experiments with formulations mentioned above. A detailed account of these coupon studies is given elsewhere.[3] The salient findings from the coupon experiments were: a) Decontamination of C/U system surfaces of TAPS required an initial oxidative pre-treatment to remove Cr from the oxide. Without this initial step, even a powerful reductive complexing decontamination formulation such as LOMI was not able to dissolve the oxide and hence did not result in significant DF; b) Among the pre-treatment formulations tried, alkaline permanganate employing 0.3% $KMnO_4$ in 1.5% NaOH was the most effective; c) CEA formulation though gave lesser DFs than those obtained with LOMI formulation, this disadvantage could be overcome with a multicycle approach; further the ease of application of CEA compared to LOMI makes CEA also a favourable candidate formulation; d) Though BWRs operating under normal water chemistry conditions are not expected to contain large amounts of Cr in their oxide surface, the finding in the present work that significant amount of Cr exists on the surfaces of C/U system piping gave a clue to the development of an appropriate methodology for the decontamination of these surfaces.

Loop experiments

Loop decontamination studies were carried on SS-304 system pipe by employing a two cycle AP-LOMI and AP-CEA processes at about 343 K. Fig.1 is a schematic of the decontamination loop established. It employed a circulation tank, a LOMI preparation tank, magnetic sealless centrifugal pump with polypropylene impeller and flexible interconnecting piping. About 500 mm long x 100 mm NB (normial bore) SS pipe cut from the portion of the piping removed during the regenerative heat exchanger replacement in Unit-1 of TAPS was employed. The Initial pre-treatment was done in 0.3%

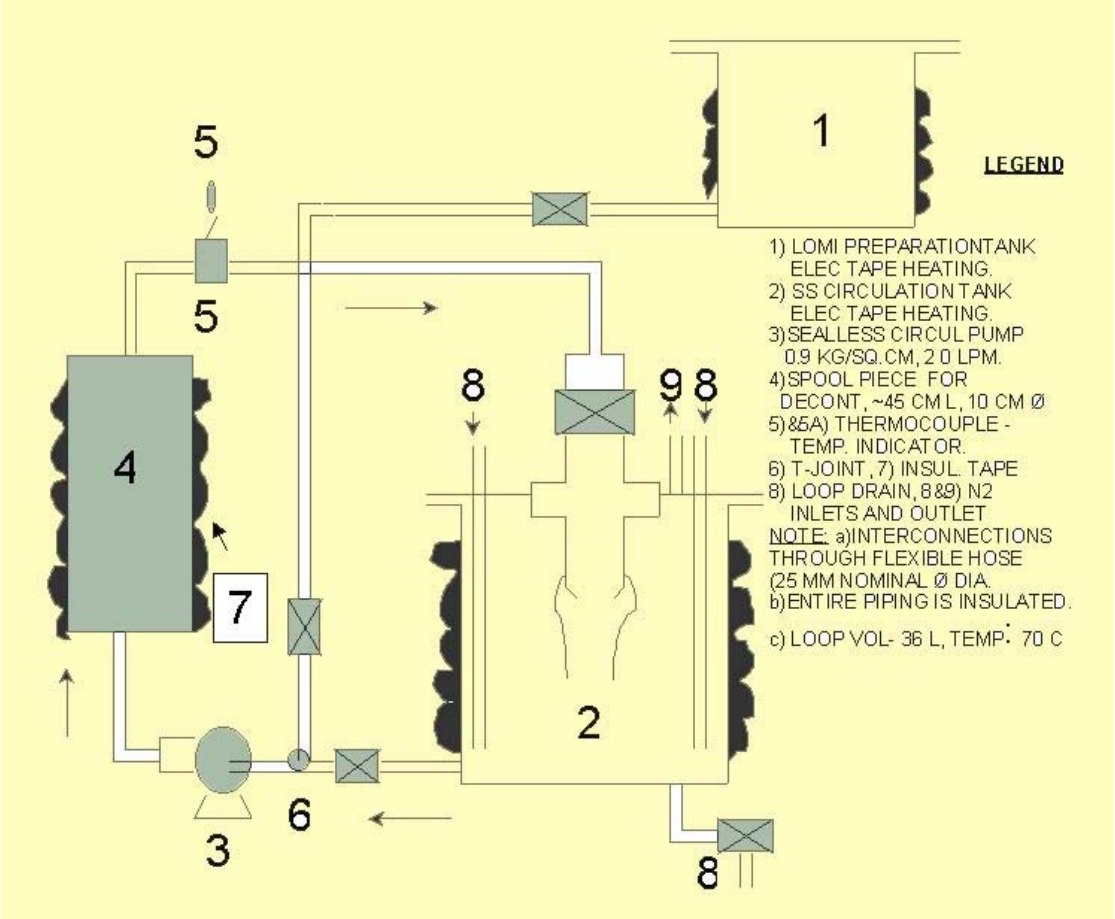

Fig.1 Schematic of spool piece decontamination loop

$KMnO_4$ in 1.5% NaOH for a 4 h period. A 4 mM tris-picolinato V(II) formulation buffered to pH 4.3 was electrolytically (Fig.2 shows the details of the 40 l LOMI electrolysis cell) prepared and employed in on one piece of pipe for 4 h after the pre-treatment. A 2:2:4 mM CEA formulation was employed on a second piece of pipe for 4 h after the pre-treatment step. Waste treatment was done with a mixed bed consisting of a H^+ form of the cation resinand OH^- form of the anion resin. The details of the loop studies are given elsewhere.[4] Fig.3 shows the DFs obtained in the top, middle and bottom portions of the decontamination pipe. The main conclusions from these studies are: a) A two-cycle AP-LOMI gave about 98% removal of radioactivity removal while a two-cycle AP-CEA gave 80% radioactivity removal. The higher efficiency of AP-LOMI process observed was in agreement with the results of laboratory coupon experiments. A specific activity of 7 $\mu Ci/cm^2$ or 5.1 $\mu Ci/mg$ Fe in the oxide and an oxide thickness of 4.7 μm have been computed from these experiments. Effective solidification of AP-LOMI/AP-CEA wastes by employing conventional polystyrene based gel type ion exchangers was demonstrated.

Material Compatibility with the Chosen Formulations

Both unsensitized, furnace sensitized (partially and fully) AISI-304 specimens were employed in the susceptibility-to-intergrannular attack (IGA)

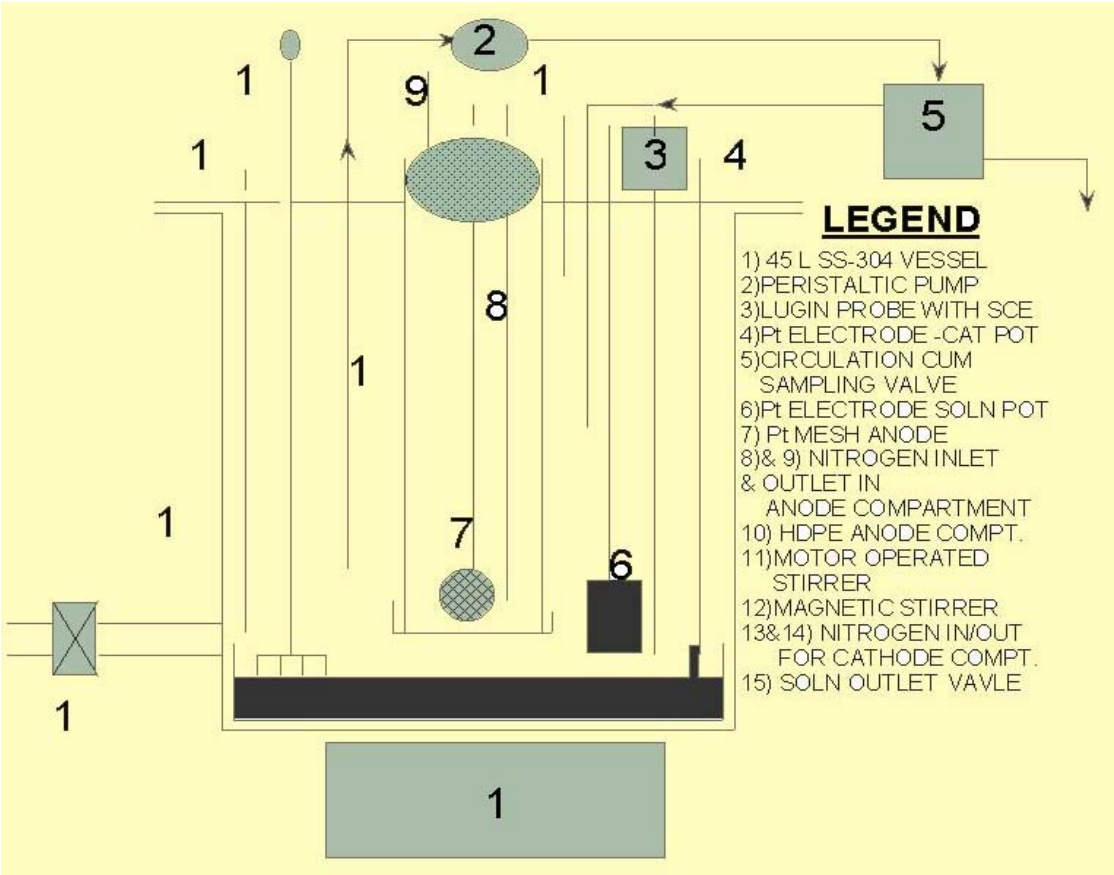

Fig. 2 Stainless steel electrolysis cell for LOMI preparation

studies. The specimens were exposed to a two cycle AP-LOMI and AP-CEA formulations and optical microscopic examinations were carried out. Both personnel from Post-Irradiation Examination Division and Applied Chemistry Division together executed these studies. The details of these studies can be found elsewhere.[6] Table-2 summarizes the results of these studies. It was observed that when LOMI was prepared with less than 10-12 mM free formic acid concentration then there was no susceptibility to intergrannular attack to the sensitized specimens. CEA formulation even with high EDTA and Citric acid concentrations proved benign to the SS surfaces. The behaviour was same in both sensitized and unsensitized specimens.

C/U System Decontamination – Phase 1 Task

The reactor C/U system was chosen for the technology demonstration of the DCD. The C/U system had features of isolation of the reactor so that decontamination chemicals can be prevented from entering the reactor vessel. Further, nearly the whole C/U system is outside the primary containment. In a sub-system decontamination, the first task is to establish a closed loop with the system and then devise a suitable heating methodology. Unlike in a full primary system decontamination of a PHWR where the primary system already exists as a closed loop and operation of the main coolant recirculation pump can heat up the system easily to the required temperatures without requiring any external heat input, the present task of sub-

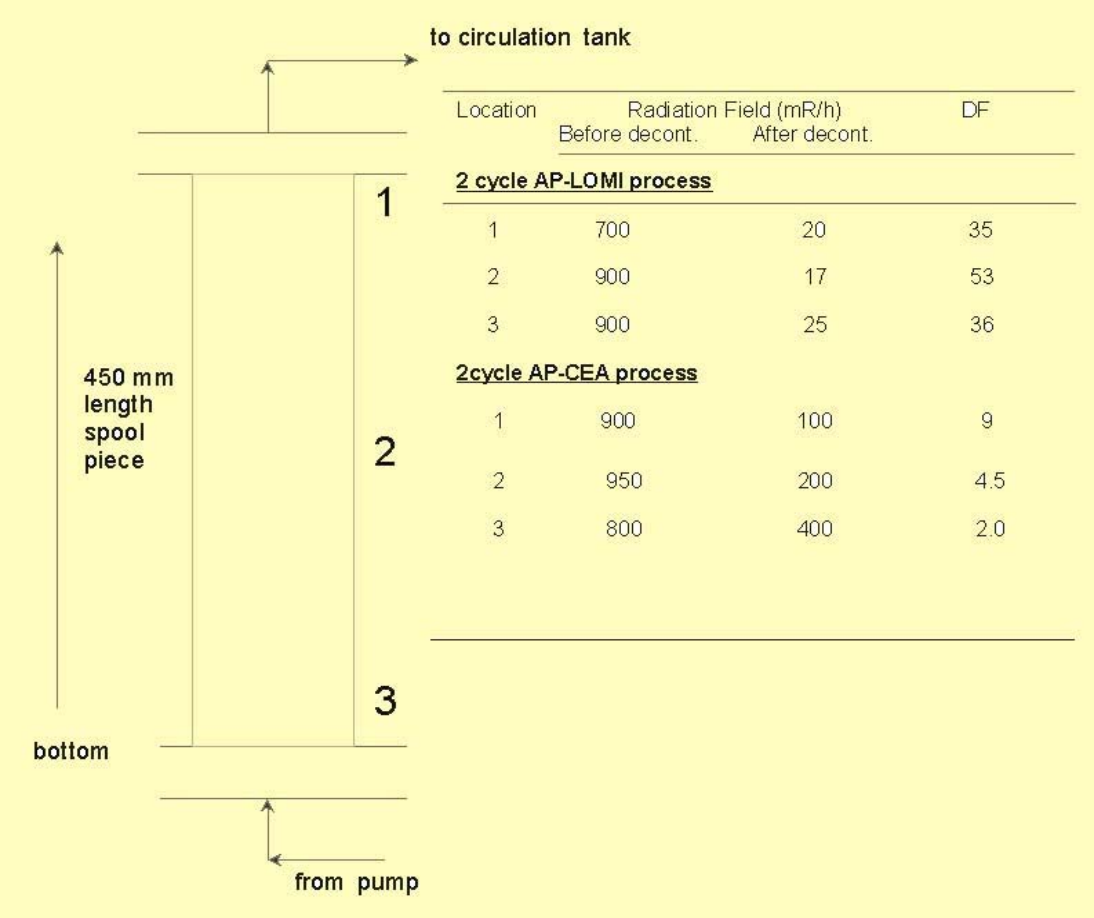

Location	Radiation Field (mR/h) Before decont.	After decont.	DF
2 cycle AP-LOMI process			
1	700	20	35
2	900	17	53
3	900	25	36
2cycle AP-CEA process			
1	900	100	9
2	950	200	4.5
3	800	400	2.0

Fig.3 Decontamination factors obtained in pipe decontaminaton experiments

Table-2 : Microstructural observations made on the sensitized SS-304 before and after exposure to the decontamination formulations

Heat Treatment	Formulation number	Observations under opticalmicroscope	
		Microstructure after heat treatment	Coupon surface after exposure to formulation
Heat treatment at 973 K for 6h	1	Fully sensitized	No selective grain boundary attack, almost uniform corrosion
	2	Fully sensitized	
	3	Fully sensitized	

Formulation 1: Citric acid - 2mM + Na2EDTA-55mM + Ascorbic acid - 4mM, pH 4
Formulation 2: Citric acid - 11mM + Na2EDTA-55mM + Ascorbic acid - 4mM, pH 3.5
Formulation 3: NaV(pic)3 - 4mM + HCOONa - 12mM + free Formic acid - 4mM, free Picolini acid - 12mM, pH4. Note: Exposure to all formulns after an AP pre-treatment

system decontamination requires engineering a suitable external heat input. Further the decontamination efficiency is determined by the control of dissolved oxygen to < 100 ppb level. This is important since under shutdown conditions of the reactor, in which state the reactor decontamination is performed, the reactor water has 5-6 ppm of dissolved oxygen and in a large system such as C/U system (5.3 m^3 water volume) achievability of DO to low levels has to be demonstrated for getting good DFs. An electrode boiler delivering 200 kg/h of steam at a maximum pressure of 10 kg/cm^2 coupled to a half pipe jacketed vessel (called limpet vessel) of 1.5 m^3 volume served as the heat source. In order to bring down the DO level in system water, the ideal choice would have been an expensive deoxygenating plant consisting of different ion-exchange columns, the associated piping and valves and which would probably have to be located outside the reactor building (RB) due to lack of space inside the RB. These requirements were obviated by carrying out engineering scale experiments in the HTL loop in RED which showed that hydrazine dosing to the extent of 5-6 ppm was able to bring down DO levels of water from 3.5 ppm to < 50 ppb in less than 8.5 h time. Hence it was decided to adopt the hydrazine method of deoxygenation. The engineering of the decontamination loop was carried out by RED-BARC, NPCIL head quarters with the functional requirements input provided by ApCD. The phase-1 task was executed by TAPS implementation group with participation from ApCD and RED in September 1998. The achievability of temperature (≈364K) and DO (<100 ppb) were demonstrated in phase-1 task of C/U system decontamination. The details of this task carried are given elsewhere.[5]

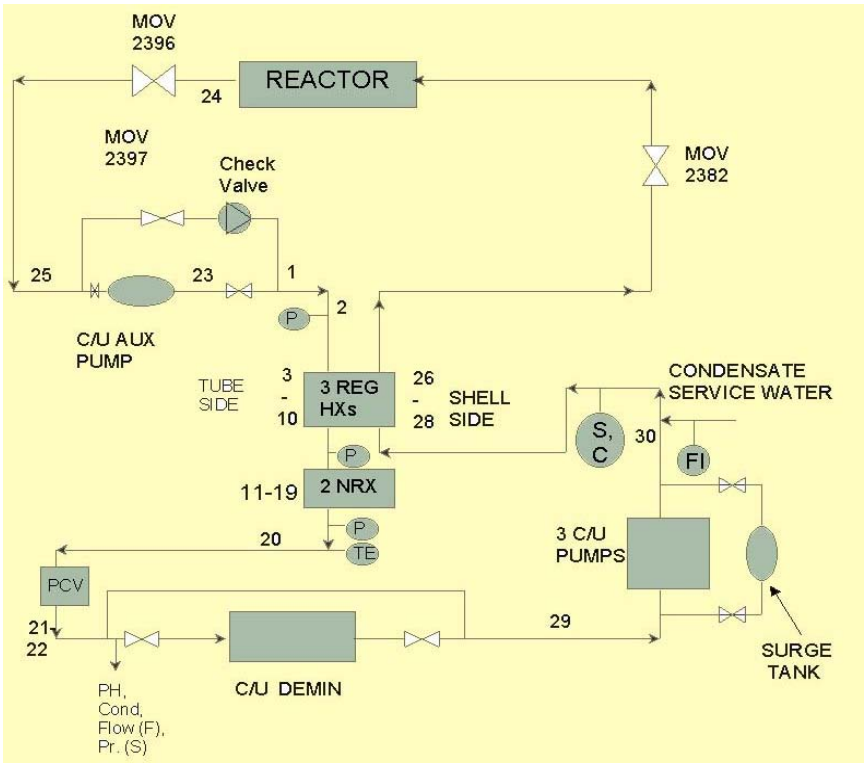

Fig.4 C/U SYSTEM, TAPS (with initially marked points for radiation measurement)

C/U System Decontamination – Phase 2 Task

Fig.4 shows the block diagram of the C/U system. The main C/U pumps, the surge tank and the C/U demineralizer were bypassed and the remaining part of the system was taken up for the chemical decontamination. Connecting the Chemical Addition tank (CAT) (also called the limpet vessel), Corrosion Coupon Autoclave (CCA), external recirculation pump (500 lpm) and the sampling station for on-line DO measurements to the system established the decontamination loop (Fig.5). The electrode boiler (EB) provided the steam for heating the

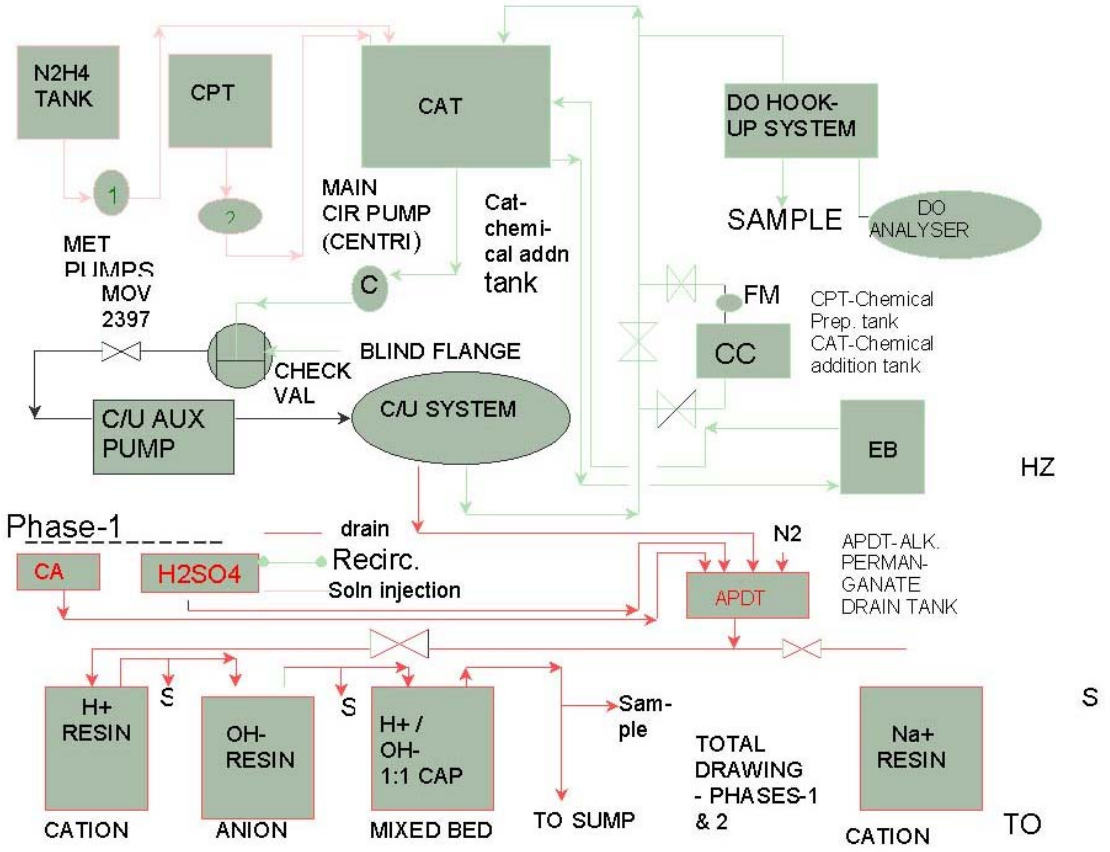

Fig.5 Decontamination loop established with the Clean-up System

system as mentioned earlier. A Chemical Preparation Tank (CPT) and a hydrazine tank were connected to the CAT through separate metering pumps for feeding the chemical solutions to CAT. The spent AP solution from each cycle was drained from the system by the fill and flush method into a 10 m^3 AP drain tank (APDT), neutralized by careful addition of appropriate volumes of concentrated sulphuric acid, the permanganate was reduced with citric acid and resulting Mn^{2+} was sorbed on the Na^+ form of cation resin column. The spent CEA formulation was drained through APDT into a battery of cation, anion and mixed bed columns. The detailed chemistry of the process is described elsewhere.[7] Personnel from ApCD, WSCL (Kalpakkam) & RED apart from the station implementation committee personnel were responsible for executing this task.

Figs 6a & 6b respectively show the Cr chemical concentration buildup in pre-treatment solution and Cr-51 radioactivity concentration buildup in the same solution. Figs. 7a & 7b respectively show the buildup of chemical concentration of Fe buildup and ^{60}Co radioactivity buildup in the dissolution step. The AP oxidative pre-treatment step as envisaged has proved to be very effective in removing Cr from the oxide. A total of 12.25 Ci comprising of 3.65 Ci (3.56 Ci from ^{51}Cr) was removed in 3 AP steps and 8.59 Ci (8.19 Ci from ^{60}Co) was removed by the three Citric acid wash - CEA dissolution cycles. About 6 kg of Fe and 3.2 kg of Cr were dissolved out from the oxide. Figs. 8a & 8b show the DFs obtained at 13 selected locations before and after decontamination. Among the 13 locations, five were in the flow-starved region to observe the flow effects on activity removal. DFs ranging

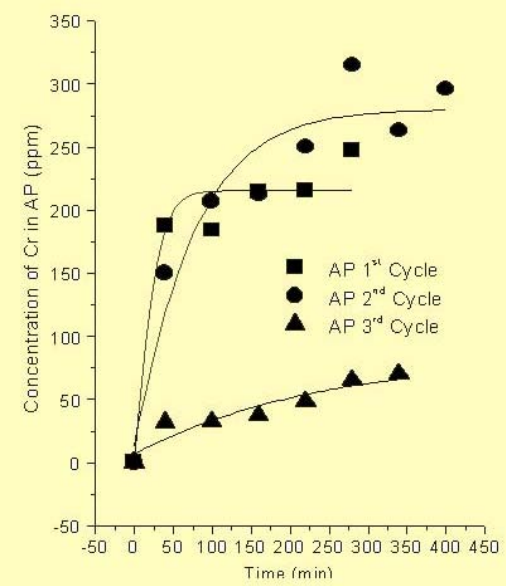

Fig.6a Buildup of Cr concentration in AP during chemical decontamination of C/U system of Unit-2, TAPS

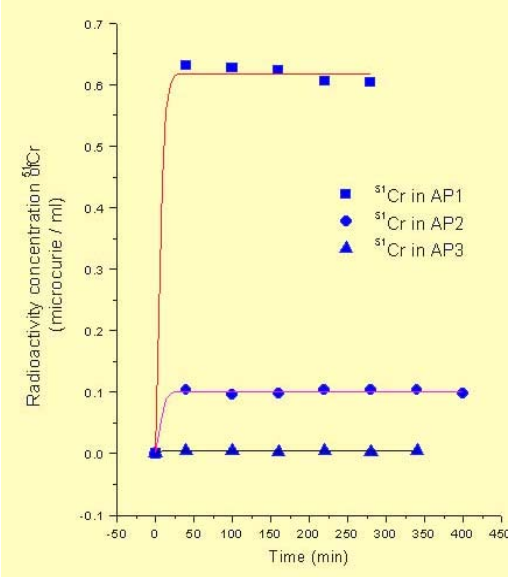

Fig.6 b Buildup of ^{51}Cr in AP solution during chemical decontamination of C/U system of Unit-2, TAPS

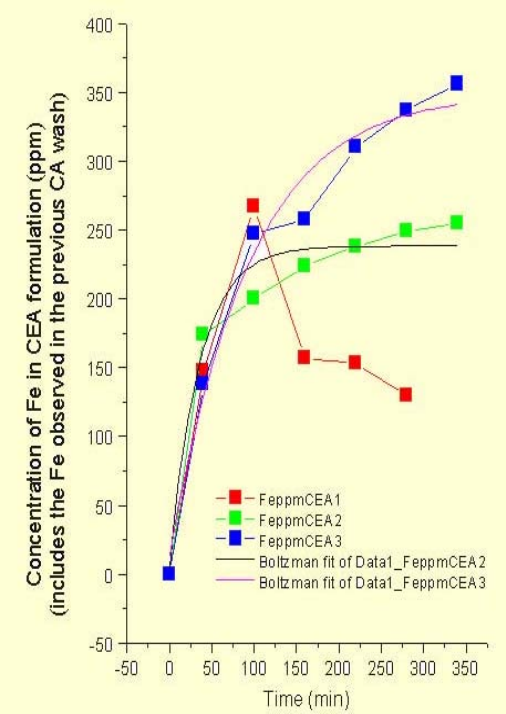

Fig.7a Buildup of Fe concentration in CEA during chemical decontamination of C/U system of Unit-2, APS.

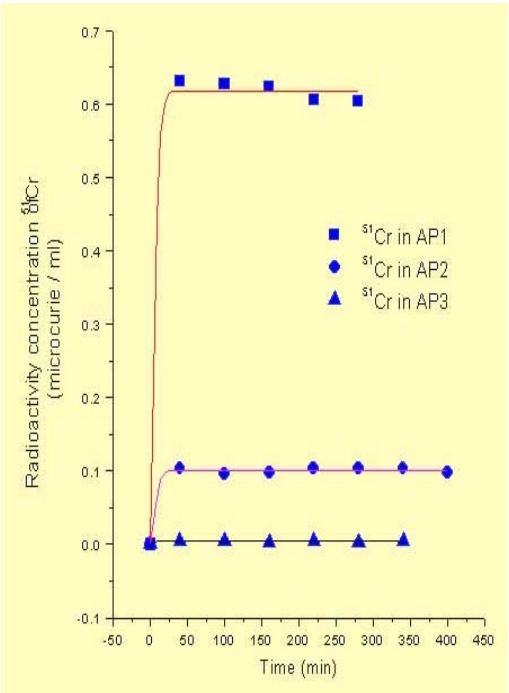

Fig.7b Buildup of ^{60}Co in CEA solution during chemical decontamination of C/U system of Unit-2, TAPS

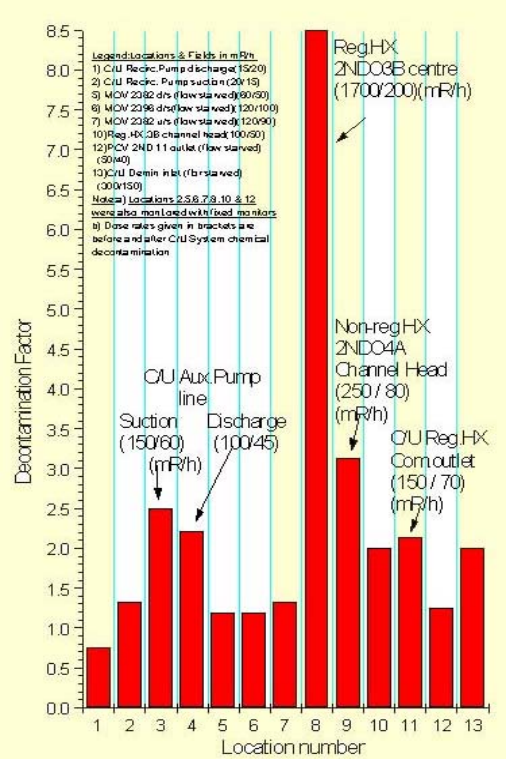

Fig.8a Radiation fields obtained at selected locations before and after C/U system chemical decontamination in Unit-2, TAPS

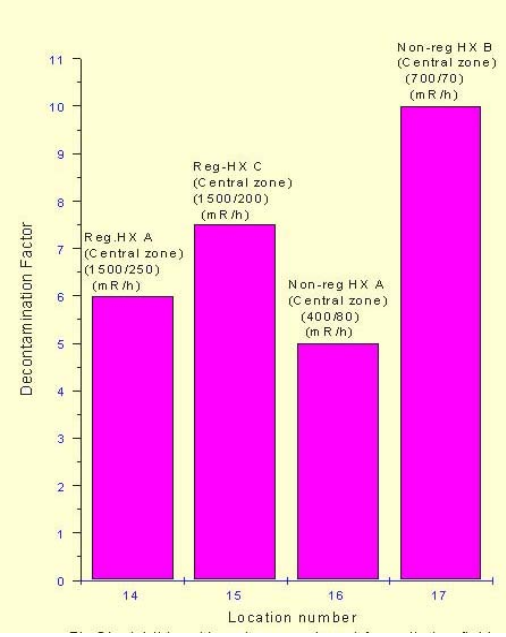

Fig.8b Additional locations monitored for radiation fields before and after C/U system chemical decontamination in Unit-2, TAPS

from 1.2 to 10 were obtained in 12 out 13 locations. The three regenerative and two non-regenerative heat-exchangers which are the major equipment in the system have shown DFs ranging from 5-10. There was a significant (>2) reduction in the heat-exchanger room area background level. The ^{51}Cr radioactivity which did not contribute to dose but contributed significantly to processed radwaste discharges was managed by the co-precipitation route devised during the course of decontamination. Sensitized SS coupons exposed in the corrosion coupon autoclave to the three cycle AP-CEA formulation did not show any susceptibility to IGA attack while uniform corrosion rate observed on SS, Zircaloy, Monel-400 and Incoloy-800 were found to be negligible. Visual observation of the internals of a flow-control valve carried out after chemical decontamination revealed a shining surface without any deposit or colouration. The salient conclusions derived from the sub-system decontamination were: a) the AP-CEA process developed for the decontamination of SS surfaces of TAPS system has proved to be successful; b) the main piece of equipment in the system namely the heat-exchangers have shown high DFs; c) a considerable amount of Cr was present in the oxide which could be efficiently removed in the AP steps; d) the third cycle CEA dissolution step in spite of showing significant Fe in solution did not show any ^{60}Co which indicated that whatever amount of ^{60}Co to be removed from the oxide in the system had been completely removed; e) a methodology to handle ^{51}Cr radioactivity in AP solution had been established and f) the formulation exhibited good material compatibility in actual application.

On-going Studies to Deconta-minate Recirculation System of TAPS

Following the successful execution of chemical decontamination of the C/U system, TAPS/NPCIL has addressed to us the requirement of chemical decontamination of a much larger system as the reactor-recirculation system along with the two secondary steam generators (total solution

volume involved of primary plus secondary systems is 120 m^3). The combination of stainless steel and carbons steel structural materials of this system and its large system volume require tuning of the earlier developed formulation for the C/U system. This is so especially with respect to reduction of waste volumes (both solid and liquid) to be discharged. Based on studies over a period of 3 years now, a multicycle oxidative-reductive entirely acidic formulation has been nearly finalized. The developed process envisages near zero liquid radwaste discharge baring some leaks from the system.

Conclusions

The decontamination studies leading to the execution of C/U system decontamination and the results obtained in the actual system decontamination had shown very good agreement. Some notable observations are 1) TAPS BWRs operating under normal water chemistry conditions require a two stage oxidative-reductive cycle decontamination methodology; 2) Since the major structural material is stainless steel, the oxide dissolution unlike in PHWRs, is not base metal aided and the reduction of Fe^{3+} in the lattice oxide occurs through the solution phase. Hence to achieve a reasonably fast kinetics of dissolution it is important to properly choose the complexing agent which will determine the nature of reductant. Complexing agents like EDTA and NTA adequately satisfy this requirement.

Acknowledgements

The author wishes to acknowledge his colleagues for their participation in the laboratory and loop studies. The executions of phase-1 and phase-2 tasks are teamwork involving a multi-unit, multi-divisional effort. Mainly this involved station, NPCIL headquarters in Mumbai, Applied Chemistry, Reactor Engineering and Post-Irradiation Examination Divisions of BARC. As such the credit for jointly executing phases-1&2 tasks belongs to all these staff. The local implementation committee of TAPS has taken the complete responsibility of erection of the decontamination loops and their efforts are duly acknowledged. A separate detailed report of the C/U system decontamination giving all system chemistry data obtained is being brought out as a BARC report. The author wishes to record his grateful thanks to Director, Chemistry Group, BARC, and Head, Applied Chemistry Division, BARC, for their very keen interest in this work.

References

1. Chemical Decontamination of Clean-up system : Feasibility and Proposal to TAPS – SC & SARCOP, TAPS Report (2000).
2. G.Venkateswaran, “Metal-ion Passivation and Control of Radiation Field Buildup”, Proc. of the National Symposium on Water and Steam Chemistry in Power Plants and Industrial Units, SWASCH-2000, pp20-33, (2000).
3. G.Venkateswaran, A.S.Gokhale, B.Yuvaraju, C.K.Vinay Kumar, P.N.Moorthy, H.N.Kansara and P.M.Wagh, “Coupon Evaluation of LOMI and Citrate Formulations for the Decontamination of the Clean-up System of Tarapur Atomic Power Station (TAPS) BWRs”, Report submitted to TAPS, NPCIL vide letter No.ApCD/0337/NPR/2/217 dated 10-2-1993.
4. G.Venkateswaran and H.N.Kansara, “BWR Pipe Decontamination by LOMI and CEA Formulations”, Technical Report ApCD / 1994 / 01, June 1994.
5. G.Venkateswaran, A.S.Gokhale, M.K.Nema, Ravindra Nath, R.K.Sahu, A.Ramu, H.N.Kansara and T.C.Upadhyaya, “Chemical Decontamination of the Clear-up System of Unit-2 of Tarapur Atomic Power Station – Phase 1 Task”, BARC Report 1999 / I / 011 (1999).
6. G.Venkatewaran, A.S.Gokhale, P.N.Moorthy, S.Kumar, S.M.Sathe and D.N.Sah, Compatibility Studies of Some Nuclear Reactor System Materials in AP/LOMI, AP/CEA, AP and CEA Formulations”, BARC Report I / 013 / 1997.

7. G.Venkateswaran, "Dilute Chemical Decontamination of Clean-up System of Unit-2, TAPS: Chemistry Aspects and Salient Features", BARC News Letter, No.210, pp 1-12, July 2001.

The author is the recipient of the DAE Technical Excellence Award for the year 2001

About the author ...

Gopala Venkateswaran *is a M.Sc. (Madras University), Ph. D in Physical Chemistry (University of Mumbai). He is the graduate from the 14th batch of BARC Training School (1970-71). Currently, he is heading the Reactor System Studies Section of Applied Chemistry Division of BARC. His research experience / interest is in the area of Water Chemistry in Nuclear Reactor Systems. His expertise in this area includes studies on the Chemical decontamination of Nuclear Reactors, Oxide Dissolution, Corrosion and Passivation Aspects of Reactor Structural Surfaces, Ion-exchange Behaviour of Metal Complexes, Bio-remediation of Decontamination Waste, Evoution of Coolant Water Specifications with their technical basis, etc. He has 39 journal publications, 55 conference publications and 16 reports to his credit. He is a member of the Department of Atomic Energy's Committee on Steam and Water Chemistry (COSWAC). He is also the Convener of the Special Group on Water Chemistry constituted to review the water chemistry aspects of the two pressurized water reactors coming up at Kudankulum. He is a recognised M.Sc., / Ph.D guide of the Mumbai University in the field of Physical Chemisty. He has earlier supervised the work of 4 Ph.D. students and 2 M.Sc. students.*

Small-Angle Scattering from Micellar Solutions

Vinod K. Aswal
Solid State Physics Division
Bhabha Atomic Research Centre

Abstract

Micellar solutions are the suspension of the colloidal aggregates of the surfactant molecules in aqueous solutions. The structure (shape and size) and the number density of these aggregates, referred to as micelles, depend on the molecular architecture of the surfactant molecule, presence of additives, and the solution conditions such as temperature, concentration etc. Small-angle scattering is a powerful technique to study the micellar solutions. Depending on the radiation used there are two well-established techniques, namely, small-angle neutron scattering (SANS) and small-angle x-ray scattering (SAXS). These two techniques provide complementary information on the micelles. We have made a combined use of SANS and SAXS to the study of the counterion condensation in ionic micelles.

Introduction

SURFACTANT MOLECULES consist of a polar hydrophilic head group and a long hydrophobic chain connected to the head group. The coexistence of the two opposite types of behavior (hydrophilic and hydrophobic) in the same molecule leads to the self-aggregation of the surfactant molecules when dissolved in water. The aggregates are called as micelles. The typical size of a spherical micelle is about 50 Å and is made up of about 100 surfactant molecules. A schematic representation of a surfactant molecule and a spherical micelle is shown in Figure 1. The micelles are formed by the delicate balance of opposing forces: the attractive tail-tail hydrophobic interaction provides the driving force for the aggregation of the surfactant molecules, while the electrostatic repulsion between the polar head groups limits the size that a micelle can attain. As a result, the characteristics of these aggregates are easily controlled by the small changes in chemical structure of the surfactant molecule and the solution conditions such as concentration, temperature and ionic strength. The aggregates

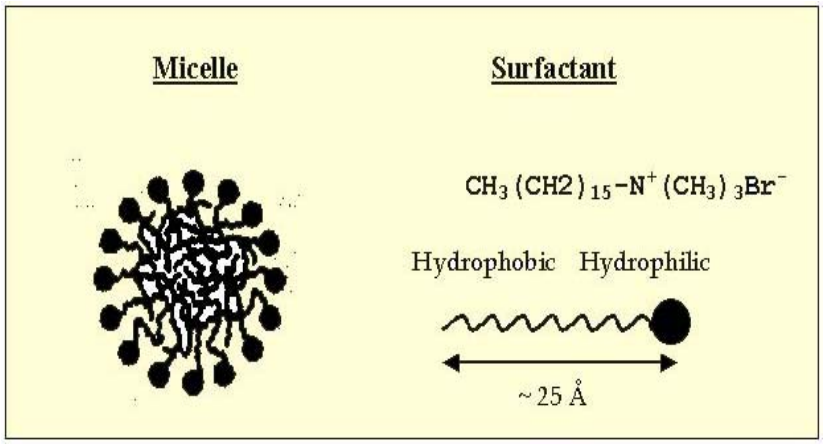

Fig. 1 Schematic of a surfactant molecule and a spherical micelle.

formed are of various types, shapes and sizes such as spherical or ellipsoidal, cylindrical or thread-like micelle, disk-like micelle, membrane and vesicles [1]. The study of formation of these different structures is important as the surfactant solutions are widely used in various household, industrial and research applications.

Surfactant molecules such as cetyltrimethyl-ammonium bromide (CTABr) ionize in aqueous solution and the corresponding micelles are aggregates of CTA^+ ions. The micelle is charged and is called an ionic micelle. The Br^- ions, known as counterions, tend to stay near the CTA^+ micellar surface. The shape, size, fractional charge of the micelle and the intermicellar interaction depend on the nature of these counterions [2]. Since the works of Oosawa [3] and Manning [4], the concept of counterion condensation is widely accepted in the field of linear polyelectrolytes. It has been shown that when the charge density on an infinitely long cylinder is increased beyond a critical value, counterions condense around the cylinder so as to reduce the effective charge density to the critical value. Similar concepts have also been used in colloidal suspensions made of spherical charged colloids [5]. The counterions located at short enough distances from the colloidal surface feel a very strong electrostatic attraction compared with the thermal energy k_BT and these counterions are called as bound to or condensed on the colloid. In ionic micellar solutions, the counterion condensation plays very important role to decide the effective charge on the micelle and hence the formation, structure and interaction of the micelles [6].

The scattering techniques small-angle neutron scattering (SANS) and small-angle x-ray scattering (SAXS) in combination provide a direct method to study the counterion condensation in ionic micelles. While neutron scattering in micellar solutions is from the core of the micelle, x-rays are largely scattered by counterions, especially when the counterion has a large atomic number (e.g. Br^-). The neutron scattering intensity from the counterion distribution is negligible in comparison to that from the core. Thus neutrons see the core of the micelle and x-rays give information relating to the counterion condensation around the micelle [7].

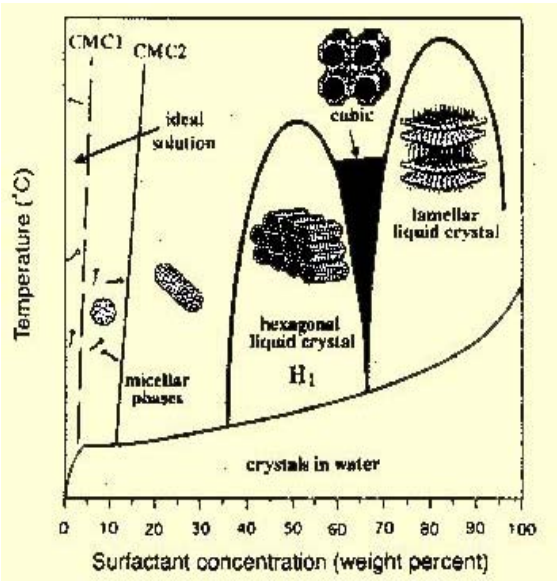

Fig. 2 Phase diagram of ionic surfactant CTABr in water.

Figure 2 shows the phase diagram for ionic surfactant CTABr in water [8]. At low surfactant concentrations, CTABr forms the small spherical micelles. The spherical micelles transform to long rod-like as the concentration is increased. At higher concentrations, different liquid crystalline structures are formed. The above variety of structures in the phase diagram strongly depends on the counterion condensation. Herein, we discuss the small-angle scattering as a method to study the counterion condensation in ionic micelles.

Small-angle Scattering

The small-angle scattering intensity $I(Q)$ as a function of scattering vector Q ($=4\pi\sin\theta/\lambda$, where 2θ is the scattering angle and λ is the wavelength of the incident radiation) for a micellar solution can be expressed as [9]

$$I(Q) = nP(Q)S(Q) \qquad (1)$$

where n is the number density of the particles. $P(Q)$ is the intraparticle structure factor and depends on the shape and size of the particles. $S(Q)$ is the interparticle structure factor and is decided by the spatial distribution of the particles. $P(Q)$ is given by the integral

$$P(Q) = \left| \int (\rho(r)-\rho_s) exp Ii\mathbf{Q}.\mathbf{r})dr \right|^2 \qquad (2)$$

In the simplest case of a monodispersed system of homogeneous particles with a radius R, $P(Q)$ is given by

$$P(Q) = (\rho-\rho_s)^2 V^2 \left[\frac{3J_1(QR)}{QR} \right]^2 \qquad (3)$$

where $V=(4/3)\pi R^3$, ρ_s is the scattering length density of the solvent and ρ is the mean scattering length density of the particle.

The expression for $S(Q)$ depends on the relative positions of the particles. In case of isotropic system, $S(Q)$ can be written as

$$S(Q) = 1 + 4\pi n \int (g(r)-1) \frac{\sin Qr}{Qr} r^2 dr \qquad (4)$$

where $g(r)$ is the radial distribution function. $g(r)$ is the probability of finding another particle at a distance r from a reference particle centered at the origin. The details of $g(r)$ depend on the interaction potential $U(r)$ between the particles. The term $(\rho-\rho_s)^2$ is referred as a contrast factor. The above equations are valid both for the SAXS and the SANS experiments. The contrast factor, however, depends on the radiation used [10]. The values of ρ and ρ_s depend on the chemical composition of the micelle and the solvent and are different for neutrons and x-rays. The differences in ρ values for neutrons and x-rays arise from the fact that while neutrons are scattered by the nucleus of an atom, the x-rays are scattered by the electron clods around the nucleus. It is seen that as one goes across the periodic table, the neutron scattering lengths vary in a random way and the x-ray scattering lengths increase with the atomic number of the atom. For example, unlike x-rays where ρ_s (H_2O) = ρ_s (D_2O), the values of ρ_s changes significantly for neutrons when solvent is changed from H_2O to D_2O. X-rays are scattered more strongly from heavy elements (e.g. Cl^-, Br^- etc.) as compared to light elements such as C, H etc.

Results

Comparison of SANS and SAXS data from ionic micellar solutions

Figure 3 shows the comparison of SANS and SAXS data on 100 mM CTABr micellar solution. Both these data show a correlation peak at Q ~ 0.05 $Å^{-1}$, which is due to peak from the interparticle structure factor $S(Q)$ [11]. The fact that the average distance between the micelles mainly decides position of the correlation peak, it is independent of the radiation used. The peak usually occurs at Q_m ~ $2\pi/d$, where d is the average distance between the micelles and Q_m is the value of Q at the peak position.

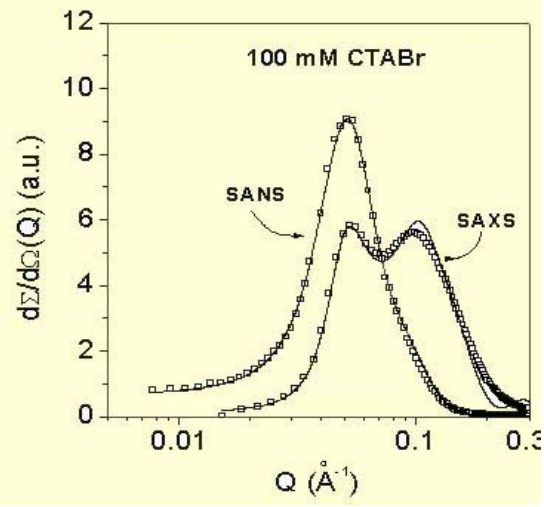

Fig. 3 Comparison of SANS and SAXS data for 100 mM CTABr

The second peak in the SAXS data arises from scattering of shell-like structure of the condensed counterions around the micelles. The analysis of SANS data using Eq. (1) determines the shape and size of the micelles. It is found that the micelles are prolate ellipsoidal with the semimajor axis (a) = 40.2 Å and semiminor axis

(b=c) = 24.0 Å, respectively. The counterion condensation per surfactant molecule on the micelles has the value about 77 %. The above structure and interaction information about the micelles as obtained from SANS is used to fit the SAXS data and the thickness of the condensed counterions around the micelles is obtained as an additional parameter. The calculated value of the thickness over which the Br^- counterions are condensed is 4.2 Å.

Size dependence of the counterions and micelles on the counterion condensation

It has been known that depending on the size of the counterions, the phase diagrams of the similar ionic surfactants have been very different. For example, while the ionic surfactant cetyltrimethylammonium bromide (CTABr) shows sphere to rod-like transition of micelles with the increase in the surfactant concentration, the micelles of cetyltrimethylammonium chloride (CTACl) remain spherical even up to very high surfactant concentrations. This also leads to the different liquid crystalline structures of the surfactants at higher concentrations.

To explain the above differences, Figure 4 shows the comparison of SANS and SAXS data for CTABr and CTACl micellar solutions. SANS suggests the formation of much smaller micelles for CTACl than CTABr [12]. This is explained due to the lower condensation of Cl^- counterions on the micelles. On the other hand, SAXS data suggest that counterions be condensed over larger thickness for CTACl micelles. When surfactant concentration is increased, SANS data show that counterion condensation decreases for CTABr micelles and it remains more or less same for CTACl micelles [13]. In terms of SAXS data, it shows that the counterions maintained to remain over same thickness for CTABr micelles and the thickness increases for CTACl micelles.

Similar results to those of the varying counterions are also obtained when the size of micelles is varied. It is seen from the SANS data that counterion condensation on the ionic micelles increases with the increase in the size of micelle [14]. This is term of SAXS data shows that the counterions get condensed over smaller thickness when the size of micelles is increased.

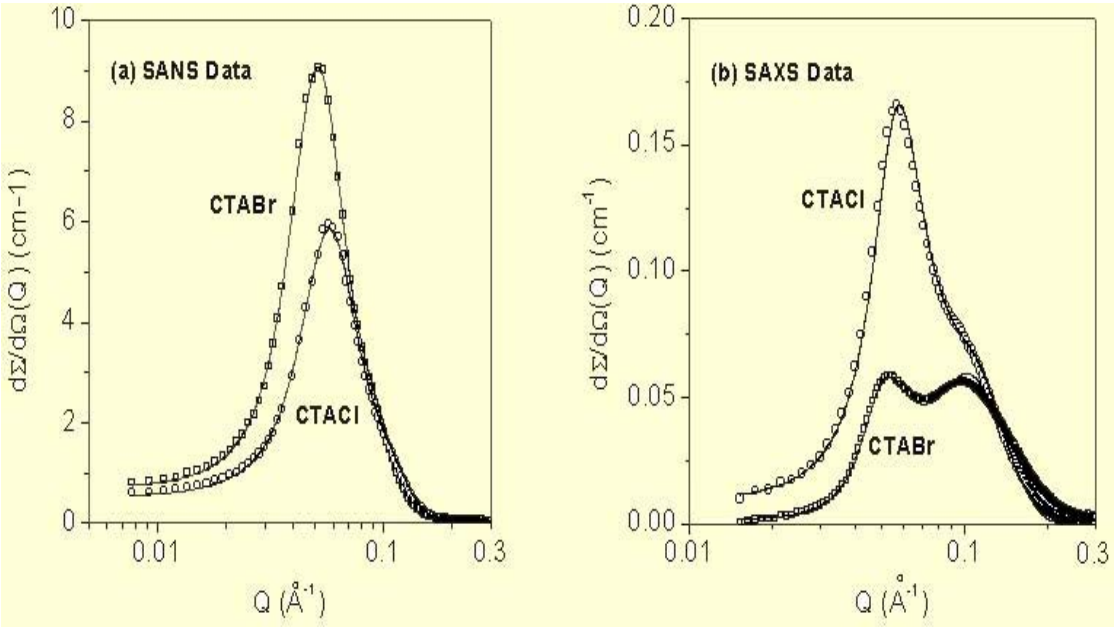

Fig. 4 Comparison of (a) SANS and (b) SAXS data for 100 mM CTABr and CTACl micellar solutions.

Selective counterion condensation in ionic micelles

The effect of addition of salts KBr and KCl to the ionic micellar solutions of cationic surfactant (e.g. CTABr or CTACl) is quite different [15]. In terms of counterion condensation, this suggests the differences in the condensation of Br^- and Cl^- ions that take place on the charged micelles. It is interesting to compare the structure in the equimolar surfactant to salt micellar solutions of CTABr/KCl and CTACl/KBr systems [16]. Figure 5 (a) shows the SANS data from equimolar surfactant to salt CTABr/KCl and CTACl/KBr micellar solutions. These systems have common in them the same number of surfactant CTA^+ ions and as well as Br^- and Cl^- counterions. For comparison, the data from 100 mM CTABr and CTACl micellar solutions without salt are also shown in Figure 5 (a). It is observed that the counterion condensation is more effective in CTACl/KBr than CTABr/KCl. We believe this is due to selective condensation of the counterions around the micelles [16]. In CTABr/KCl, Br^- counterions from the dissociated CTABr molecules are condensed on the CTA^+ charged micelles. The condensation of Cl^- ions of the salt KCl takes place around the condensed Br^- ions. However, in CTACl/KBr, Cl^- counterions of the CTACl molecules are replaced by Br^- ions of the KBr in the micelle. This is expected since Cl^- ions are less effective than Br^- to neutralize the charge on the micelles.

The above SANS results are directly confirmed by the SAXS experiments, where the scattering data depending on the condensed counterions is expected to be different. Figure 5 (b) shows while the SAXS data of CTABr and CTACl are very different the data for CTABr/KCl and CTACl/KBr are quite similar. The small differences in the SANS or SAXS data of CTABr/KCl and CTACl/KBr can be explained in terms of a small fraction of condensed Cl^- counterions in CTACl/KBr, which are not replaced by the Br^- counterions. This provides slightly higher condensation of Cl^- counterions on the micelles of CTACl/KBr than CTABr/KCl, otherwise these two systems have similar counterion condensation of Br^- and Cl^- ions around them.

In summary, small-angle scattering is an ideal method to the study of the micellar solutions. The use of SANS and SAXS provide complementary information on the micelles. The combined experiments of these two techniques have been used to study the counterion condensation in ionic micelles. While neutron scattering in micellar solutions is from the core of the micelle, x-rays are largely scattered by counterions, especially when the counterion has a large atomic number (e.g. Br^-).

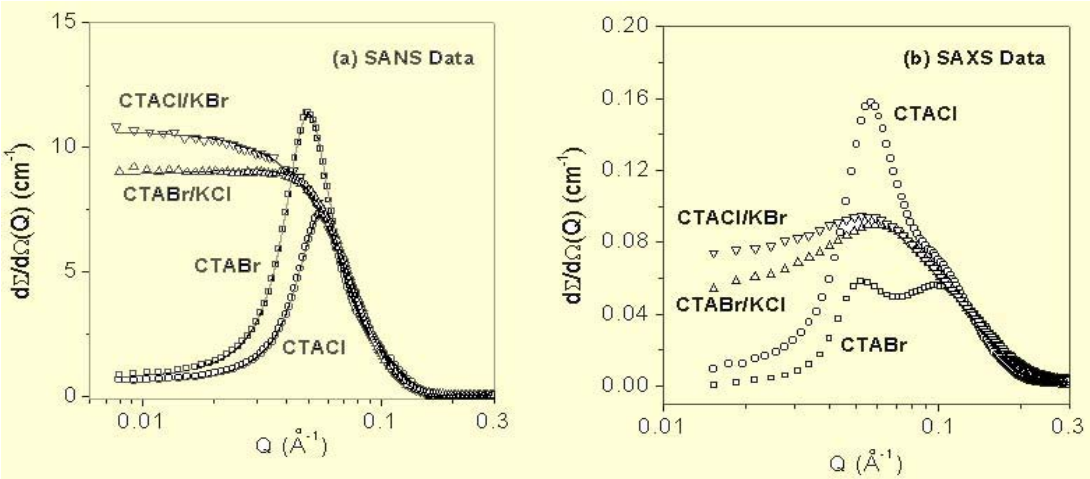

Fig. 5 (a) SANS and (b) SAXS data from equimolar surfactant to salt micellar solutions of CTABr/KCl and CTACl/KBr. For comparison the data from pure CTABr and CTACl micellar solutions are also shown.

Acknowledgement

I would like to thank Dr. P.S. Goyal and Dr. M. Ramanadham for their support and the interest in this work.

References

1. Y. Chevalier, T. Zemb, Rep. Prog. Phys. **53**, 279 (1990).
2. J.N. Israelachvili, *Intermolecular and Surface Forces*, Academic Press, 1992.
3. F. Oosawa, *Polyelectrolytes*, Dekker, New York, 1971.
4. G.S. Manning, J. Chem. Phys. **51**, 924 (1969).
5. L. Belloni, Coll. Surf. A **140**, 227 (1998).
6. V.K. Aswal, P.S. Goyal, P. Thiyagarajan, J. Phys. Chem. **102**, 2469 (1998).
7. C.F. Wu, S.H. Chen, L.B. Shih, J.S. Lin, Phys. Rev. Lett. **61**, 645 (1988).
8. N. Raman, M. Anderson, C. Brinker, Chem. Mater **8**, 1682 (1996).
9. S.H. Chen, T.L. Lin, in: D.L. Price, K. Skold (Eds.), *Methods of Experimental Physics*, vol. 23B, Academic Press, New York, 1987, p. 489.
10. C.G. Windsor, J. Appl. Cryst. **21**, 582 (1988).
11. V.K. Aswal, P.S. Goyal, S. De, S. Bhattacharya, H. Amenitsch, S. Bernstorff, Chem. Phys. Lett. **329**, 336 (2000).
12. V.K. Aswal, P.S. Goyal, Phys. Rev. E **61**, 2947 (2000).
13. V.K. Aswal, P.S. Goyal, Chem. Phys. Lett. **368**, 59 (2003).
14. V.K. Aswal, P.S. Goyal, Chem. Phys. Lett. **364**, 44 (2002).
15. V.K. Aswal, P.S. Goyal, S.V.G. Menon, B.A. Dasannacharya, Physica B **213**, 607 (1995).
16. V.K. Aswal, P.S. Goyal, Phys. Rev. E **67**, 051401 (2003).

The author received the N.S. Satya Murthy Memorial Award for Young Scientists . This award was given by the Indian Physics Association for the year 2001.

About the author ...

Dr. V.K. Aswal, *after obtaining his M.Sc. in Physics from IIT Bombay, joined BARC Training School in 1992 (36th batch). Subsequently, he joined the Solid State Physics Division and has been working in the field of Small-Angle Scattering for instrument development and its applications to the Soft Condensed Matter. He obtained his Ph.D. degree in 1999 from Mumbai University for his work on Small-Angle Neutron from Micellar Solutions. He did his post-doctoral studies as one of the instrument responsible for SANS facility at the Swiss Spallation Neutron Source, Paul Scherrer Institute, Switzerland, during the period 2001-2002. Dr. Aswal was awarded the Homi Bhabha Prize for securing first rank in Physics of the 36th batch of the Training School. He received the Best Ph.D. Thesis Presentation Award of the Indian Physics Association given at the 42nd DAE Solid State Physics Symposium held at Kalpakkam during December 1999. He has also been elected as an Associate of the Indian Academy of Sciences, Bangalore, for the year 2000-2005.*

Photoinduced Dissociative Electron Transfer (PDET)

Sukhendu Nath
Radiation Chemistry & Chemical Dynamics Division
Bhabha Atomic Research Centre

Introduction

PHOTOINDUCED ELECTRON TRANSFER (PET) reactions are one of the most fundamental processes in chemistry and biology. In chemistry, for example, PET is important because it has uncovered simple pathways for the synthesis of novel organic molecules. Products formed by PET could be very reactive and can undergo versatile chemical reactions of mechanistic and synthetic significance. PET is the basis for the development of solar energy storage and conversion systems. Biologists are investigating photosynthesis and electron transport in membrane and respiration systems on the basis of simple PET model.

A PET reaction involves an interaction between a photoexcited electron donor (or acceptor) and a ground state electron acceptor (or donor). Some times the reacting partners also form charge transfer (CT) complexes. On a transfer of electron from the donor to an acceptor, contact ion pair (CIP) is formed, which subsequently produces the solvent separated ion pair (SSIP) due to penetration of the solvent molecules in CIP. With time SSIP dissociates to free ions (FI). As two oppositely charged ions are coupled in CIP and SSIP, there is a strong tendency for these ion pairs to undergo the back electron transfer (BET) giving the reactants back. Different in a PET reactions are shown in the Scheme-1.

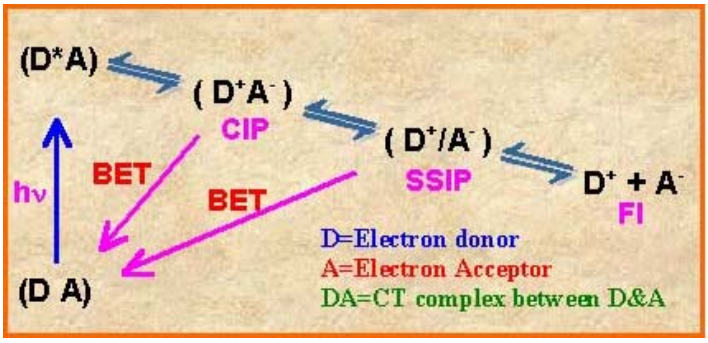

Scheme-1

Thus, BET is an energy wastage process in a PET reaction without giving any net result. For an effective application of ET process, the BET should be minimum. Thus the primary objective of the photochemist is to find ways to minimize the BET processes following ET. In most of the cases, since BET has an appreciable thermodynamic driving force and are quite fast, thus the kinetic suppression of BET often becomes the limiting factor to observe the desired chemistry following the PET process.

Dissociative ET (DET) reactions i.e. ET reactions followed by bond breaking are very promising for this purpose. If an electron donor or an acceptor undergoes cleavage of any of their bonds immediately following the ET, the energy wasting BET process can be prevented. Hence, an increase in the net electron transfer yield, which is the aim of many applications of the ET reactions, can be achieved. A PDET process can be represented by the Scheme-2.

DET processes have extensive applications in daily life. An important application of DET

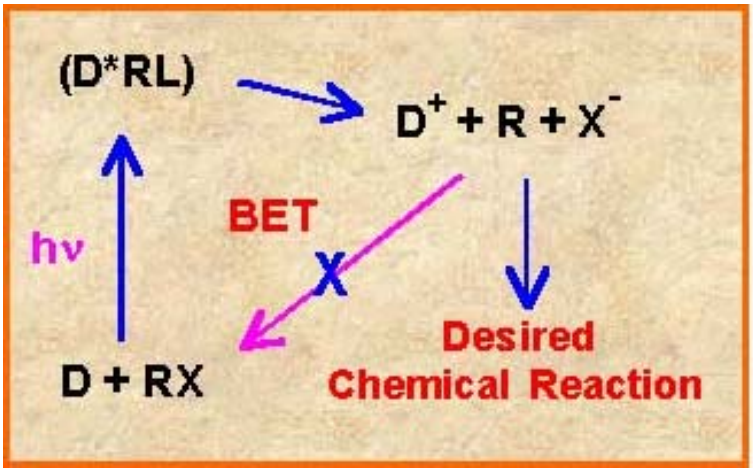

Scheme-2

process is the function of a newly developed antimalarial drug, called artemisinin [1]. This drug, containing a peroxy linkage, accepts an electron from a heme protein of malaria parasite and undergoes scission of the peroxy bond producing a reactive free radical species that subsequently kills the parasite. PDET process is important in fields like, increasing efficiency of solar cell and efficient development of the photographic emulsions [2,3]. This process is also important to understand the DNA strand cleavage [4].

In this article our experimental observation on PDET are elaborated. Before discussing the experimental results on PDET it is more appropriate to make a comparison between classical electron transfer theory proposed by Marcus [5] and dissociative electron transfer theory. This comparison has been given in the following section.

Classical vs. Dissociative ET

Classical theory for the ET, proposed by Marcus [5], is based on the assumption that during the ET there is no breaking or formation of any bond (outer sphere ET) and the potential energies of the reactants (R) and the products (P) can be represented by simple parabolas, as shown in Figure 1.

T takes place when the reactants reach the transition state (TS) via fluctuation in the reaction co-ordinate. This energy is provided by the reorganization energy (λ), which is the sum of two independent terms: (i) solvent reorganization energy (λ_0) and (ii) intramolecular reorganization energy (λ_i).

$$\lambda = \lambda_0 + \lambda_i \qquad (1)$$

Both λ_0 and λ_i are evaluated within the harmonic approximation.

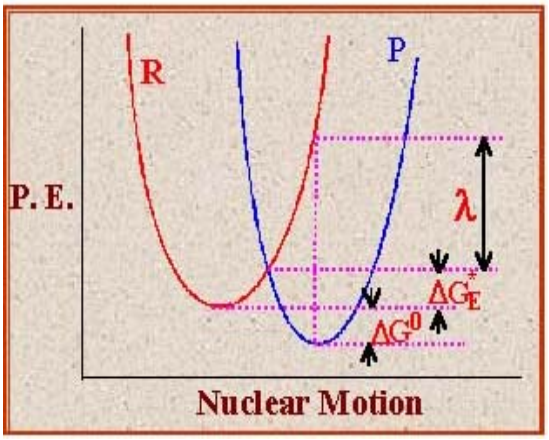

Fig. 1 Potential energy curves for the reactant and product states in an ET reaction. ΔG^0 is the free energy change, ΔG_{ET}^* is the free energy of activation and λ is the reorganization energy.

Minimization of the free energies with respect to the reaction co-ordinate leads to the following quadratic equation for the activation barrier for ET reaction [6].

$$\Delta G_{ET}^* = \Delta G_0^* \left(1 + \frac{\Delta G^0}{4\Delta G_0^*}\right)^2 \qquad (2)$$

Where ΔG^0 is the standard free energy change for the ET reaction, ΔG_0^* is the standard free

energy of activation i.e. the free energy of activation at zero driving force and related to the internal and external reorganization energies by the following expression [7].

$$\Delta G_0^* = \frac{\lambda_0 + \lambda_i}{4} \qquad (3)$$

Marcus theory deals with the outer sphere ET processes where no chemical bonds are formed or broken and the λ is the sum of only two component, λ_i and λ_0. It is expected that the dynamics of the DET process is certainly not governed only by the solvent and intramolecular reorganizations but also by the bond that is being broken. Thus to accommodate the dissociation process, the Marcus ET theory needs to be modified considering the contribution of the bond dissociation energy towards the activation barrier. Such a modified theory, to include DET has been discussed in the following section.

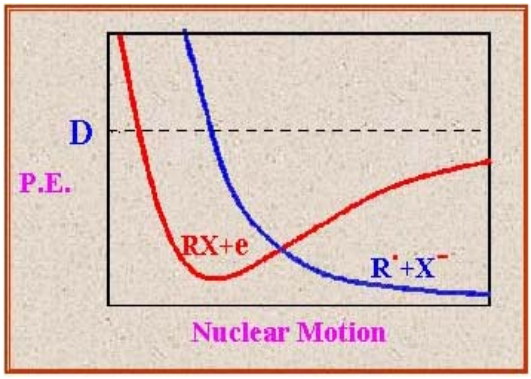

Fig. 2 Morse curve of the reactants and the products corresponding to zero driving force. D is the RX bond dissociation energy.

According to the this theory, the potential energy of the reactants (say RX) and products depends on the stretching of the bond that is being broken besides the fluctuation in solvent and the bonds that are not broken during the reaction. The contributions of the solvents and that from the bonds that are not being broken are treated exactly in the same way as in the Marcus theory. Thus for DET reaction the potential energy of the reactants along the R-X axis is assumed to follow the more realistic Morse curve (see Figure 2) instead of parabolic potential. Potential energy of the product state along the R-X axis is assumed to be purely repulsive in nature and is similar to the repulsive part of the reactant state potential. This assumption is based on the understanding that the repulsive part arises from the interaction between the core nucleus and the outer sphere electrons, which should not be altered significantly in the presence or absence of an additional peripheral electron.

Assuming the potentials for reactant and products as shown in Figure 2, it can be shown that ΔG_0^* follows the similar quadratic relationship as obtained in the Marcus outer sphere ET theory (equation 2) except the standard activation energy follows the Equation 4.

$$\Delta G_0^* = \frac{\lambda_0}{4} + \frac{\lambda_i}{4} + \frac{D_{RX}}{4} \qquad (4)$$

Where D_{RX} is the dissociation energy of the bond being broken during the ET reaction. From the Equation 4 it is evident that the contribution of the bond breaking to the intrinsic barrier is one fourth of the bond dissociation energy.

Experimental Results

We have studied the PDET processes between phenothiazines (PZ) and chloroalkanes (CA) in organic solvents [8-10]. Phenothiazines are very good electron donors, which is also a good psychotropic drugs. Four phenothiazine derivatives (PZ), whose structure is given in Scheme 3, have been used as electron donor. As the four PZ derivatives used have different redox potentials ($E_{1/2}$, see Scheme-3), wide range for free energies for the ET process can be achieved.

Best examples of dissociative fragmentations are found in reductive cleavages of aliphatic carbon-halogen bonds (C-X) where the electron is injected directly into the elongated σ^* bond, which favours a rapid dissociation of the C-X bond. Accordingly in the present study such electron acceptors e.g. chloromethanes, namely

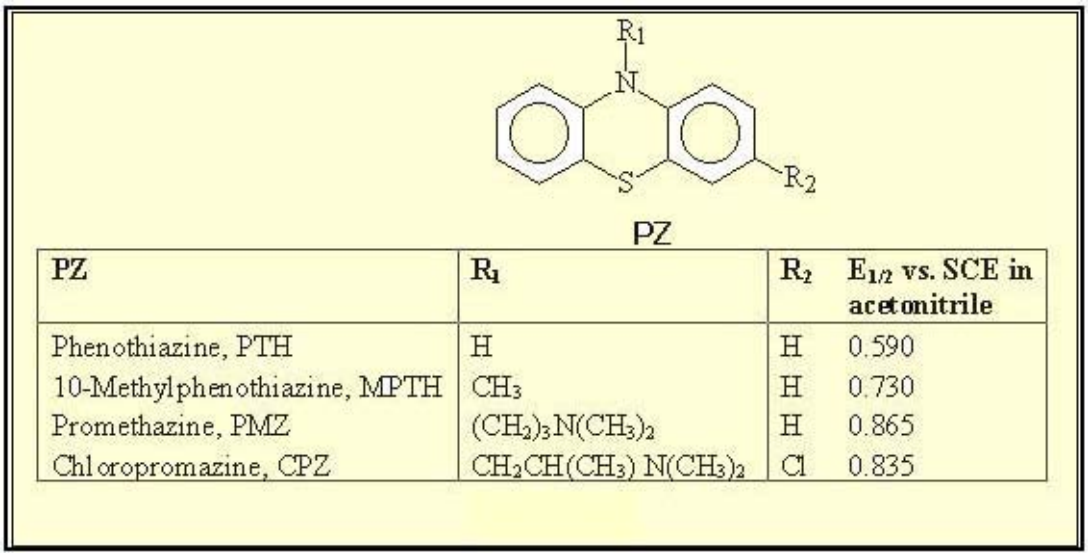

PZ

PZ	R_1	R_2	$E_{1/2}$ vs. SCE in acetonitrile
Phenothiazine, PTH	H	H	0.590
10-Methylphenothiazine, MPTH	CH_3	H	0.730
Promethazine, PMZ	$(CH_2)_3N(CH_3)_2$	H	0.865
Chloropromazine, CPZ	$CH_2CH(CH_3)\ N(CH_3)_2$	Cl	0.835

Scheme-3

carbon tetrachloride and chloroform, have been chosen.

The PZs used in the present work have been found to form weak charge transfer (CT) complexes in their ground state with CA from the changes in their absorption spectra in a number of organic solvents. Figure 3 shows the changes in the absorption spectra of phenothiazine (PTH) in CCl_4 as compared to that in acetonitrile (ACN) solvent.

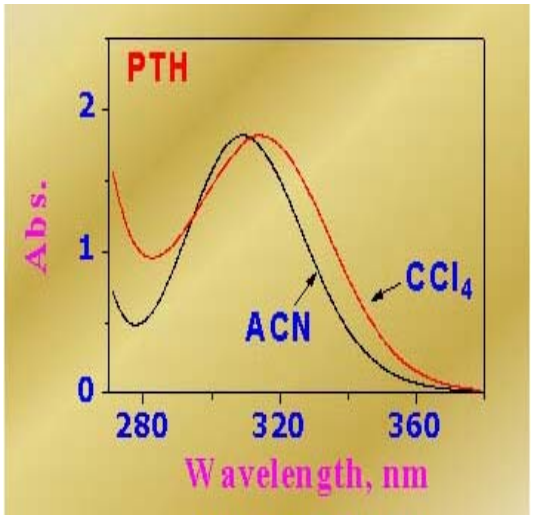

Fig. 3 Ground state absorption spectra of PTH in ACN and CCl_4.

Both steady-state and time-resolved fluorescence studies show that the CA quenches the fluorescence of PZ in all the solvents used. A positive deviation from linear Stern-Volmer relationship in the steady state fluorescence quenching results indicates the presence of static quenching, confirms the presence of ground state complexation as mentioned earlier. Further, it is seen that for strong electron acceptor like CCl_4, a new red shifted emission band appears in less polar solvents like cyclohexane, ethyl acetate, etc., due to exciplex formation. This has been further confirmed from the negative deviation from the linear Stern-Volmer relationship in the time-resolved fluorescence quenching results.

Picosecond transient absorption studies have been carried out in two different situations to understand the details of the CT dynamics and mechanism. In one situation the concentration of CA is kept high to form maximum ground state CT complex. Under such experimental conditions, the laser pulse will excite mainly the ground state CT complex forming the PZ cation radical ($PZ^{\bullet+}$) immediately. Figure 4 shows the picosecond transient absorption spectra of PMZ in ACN at different CCl_4 concentration. Thus the

appearance of the $PZ^{\bullet+}$ on photoexcitation confirms that the interaction between PZ and CA are ET in nature.

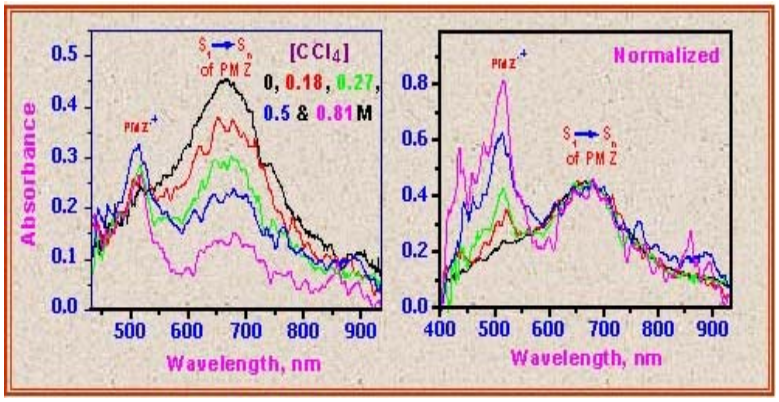

Fig. 4 (A) Picosecond transient absorption spectra, recorded at zero time delay between the pump and probe beam, for PMZ-CCl_4 system in ACN at different concentrations of CCl_4. (B) Spectra in (A) has been normalized at ~660 nm for comparison.

It is evident from the Figure 4, that the absorbance due to the PTH cation radical at ~525 nm increases with the CCl_4 concentration. The results show that the ground state CT complex on photoexcitation undergoes charge separation. As we increase the CCl_4 concentration, extent of ground state complexation is also increases and hence the absorbance of the PTH cation radical also increases.

In another situation the concentration of CA is kept low so that the extent of the ground state complexation is negligible. Under such situation the laser light mainly excites the free PZ molecules giving its excited singlet (S_1) state, which then reacts with CA, resulting in an increase in the absorption of the PZ cation radical with time. This confirms the dynamic ET interaction in the excited state of PZ. These interactions are represented by Scheme 4.

Thus the transient absorption studies shows that the interaction between PZ and CA are electron transfer in nature. Our experimentally measured ET rate constant values have been correlated with those predicted by DET theory and discussed in the following section.

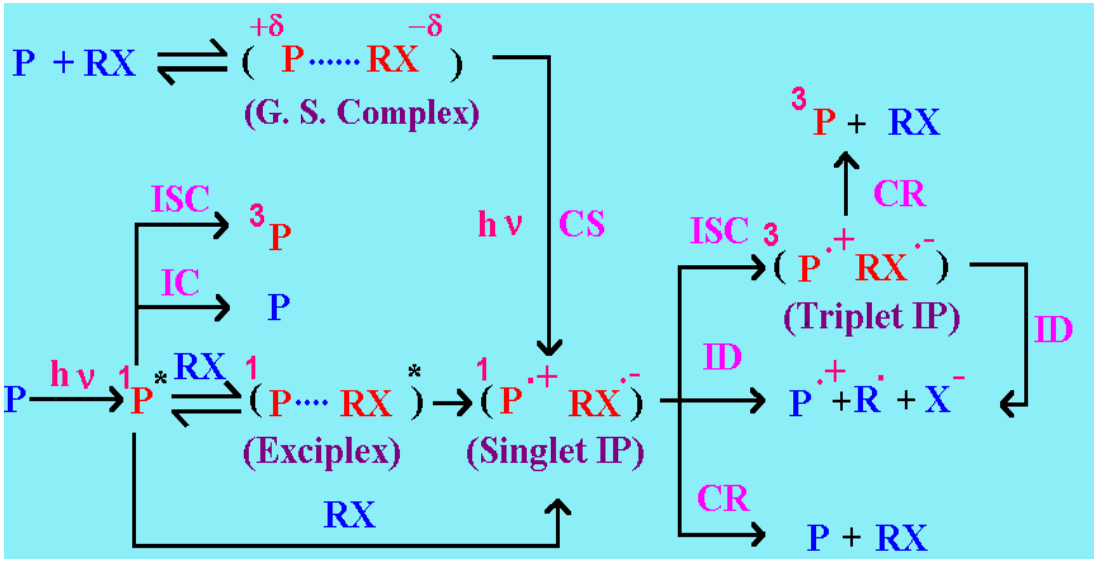

Scheme-4

Theory vs. Experimental Results

Calculation of the driving force for DET process

For the calculation of driving force ($-\Delta G^0$) in case of DET reactions it is more realistic to consider the following irreversible half reaction (Equation 6) for the electron acceptor rather than reversible half reaction used for conventional ET process.

$$RX + e^- \longrightarrow R^{\cdot} + X^- \qquad (6)$$

The standard potential for the above half reaction is calculated from the Equation 7 [11].

$$E(RX/R^{\cdot} + X^-) = E(X/X^-) - BDFE(R-X) \qquad (7)$$

Where BDFE is the bond dissociation free energy for the R-X bond.

The free energy change, ΔG^0, for the reactions is given by Equation 8 [12],

$$\Delta G^0 = E(PZ/PZ^{\cdot +}) - E(RX/R^{\cdot} + X^-) - E_{00} - e^2/\varepsilon r \qquad (8)$$

Where E (PZ/PZ^+) is the oxidation potential of PZs, E_{00} is energy of the singlet excited state (S_1) of PZ and $e^2/\varepsilon_S r$ is the Coulombic energy experienced by the radical ion pair at a transfer distance 'r' in a solvent with the static dielectric constant, ε_S.

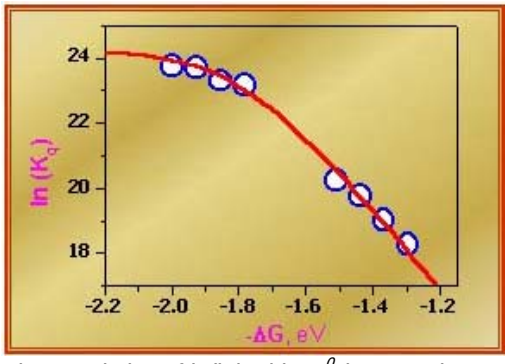

Fig. 5 Variation of ln(k_q) with ΔG^0 in ACN. The solid curve is calculated theoretically.

The experimentally measured values of k_q at different ΔG^0 are correlated according to the DET theory and a fairly good correlation is obtained (see Figure 5).

Mechanism of a DET Process

Dissociative electron transfer processes may follow two distinct mechanisms, stepwise and concerted, and are represented by the following two equations.

Stepwise

$$D + RX \rightleftharpoons [D^+ + RX^-] \longrightarrow D^+ + R^{\cdot} + X^- \qquad (9)$$

Concerted

$$D + RX \longrightarrow D^+ + R^{\cdot} + X^- \qquad (10)$$

Unlike the concerted mechanism, the stepwise mechanism involves the formation of an ion-pair ($[D^+ + RX^-]$) as an intermediate. Whether a given reaction proceeds by a stepwise or concerted mechanism, is an important question in PDET processes. Further, by altering the experimental conditions whether a stepwise ET process can be made to follow a concerted path or vice versa is an exciting proposal.

In PDET process the mechanism is usually determined on the basis of quantum yield measurements, done by end product analysis. A unit quantum yield in a PDET reaction is often been used as an indication of the concerted mechanism and a less than unit quantum yield is indicative of a stepwise process [13]. Recently it is shown that in the case of the PDET reactions, even if the reaction follows the concerted mechanism, the quantum yield need not be unity [14] and the quantum yield for the two step process can also approach unity [15]. Thus proposing the PDET mechanism solely on the basis of the quantum yield measurement may be erroneous. The best approaches for unambiguous assignment of the PDET mechanisms is the monitoring the reaction intermediates, e.g. ion pair formed due to electron transfer, in real time scale. In the

following section, our studies on the PDET reaction using femtosecond laser excitation source (λ_{ex} = 310 nm, pulse width = 300 fs) to understand the mechanistic aspect of the PDET reaction, has been discussed.

Femtosecond Transient Absorption Studies

The transient absorption spectra at zero time delay have been recorded for all four PZ in ACN both in the presence and the absence of CCl_4 (see Figure 6). The concentration of CCl_4 is kept high (~0.5 M) so that the ground state complex formation will be maximum. It is evident from Figure 6 that in the presence of CCl_4, $S_1 \rightarrow S_n$ absorption band (~650 nm) of PZ gets quenched completely and only the absorption due to PZ cation radical ($PZ^{\bullet+}$) remains (spectrum B in Figure 6).

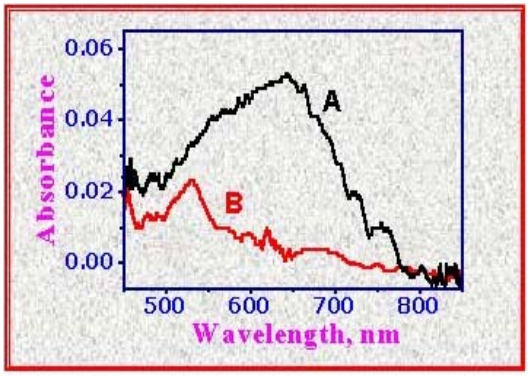

Fig. 6 Transient absorption spectra recorded at zero time delay between the pump and probe pulse for PTH in ACN in the absence of CCl_4 (A) and in the presence of 0.5 M CCl_4 (B).

Figure 7 shows the temporal evolution of $PZ^{\bullet+}$ for PTH and CPZ in ACN in the presence of 0.5 M CCl_4. Temporal characteristics of $PZ^{\bullet+}$ in the presence of CCl_4 for PMZ and MPTH, are very similar to that of CPZ-CCl_4 pair.

From Figure 7 it is seen that the absorbance due to $PTH^{\bullet+}$ shows a fast decay with a decay time

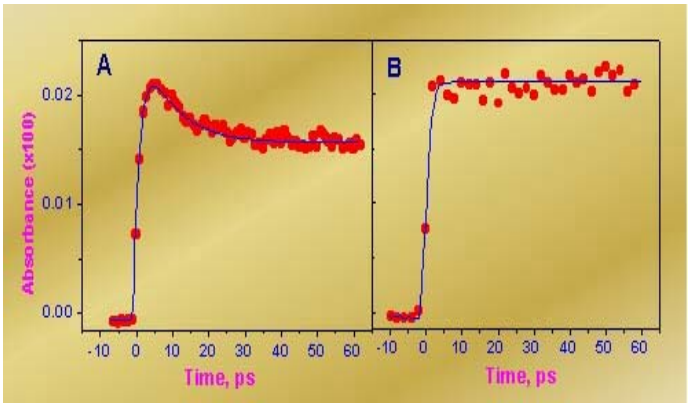

Fig. 7 The kinetic traces recorded in ACN at 530 nm in presence of 0.5 M of CCl_4 for (A) PTH and (B) CPZ.

of 8.5 ps, where as for other PZs, (i.e. CPZ, PMZ and MPTH), the transient absorption due to $PZ^{\bullet+}$ does not show any decay. The fast decay of $PTH^{\bullet+}$ is due to the BET process in the contact ion pair (CIP) produced on charge transfer in the excited CT complex. These processes are depicted in Scheme 5. The CIP can decay by two different channels: i) BET process, by which the $PZ^{\bullet+}$ combines with its geminate radical anion partner, $CCl_4^{\bullet-}$, and is responsible for the fast decay of $PZ^{\bullet+}$. ii) by irreversible dissociation of $CCl_4^{\bullet-}$. The former process will result in the decrease in the absorbance due to $PZ^{\bullet+}$. Thus the decay in the $PTH^{\bullet+}$ absorbance indicates the occurrence of the BET process and also confirms the formation of CIP state. Absence of any decay of cation radical for other three PZs shows the absence of BET process and thus indicates the absence of CIP formation for these three PZ. The results indicate that these PZ follow concerted rather than a stepwise mechanism.

Thus our results indicate that PDET processes for MPTH, CPZ and PMZ follow a concerted mechanism while the stepwise mechanism is operative for PTH.

The observed different reaction mechanisms in

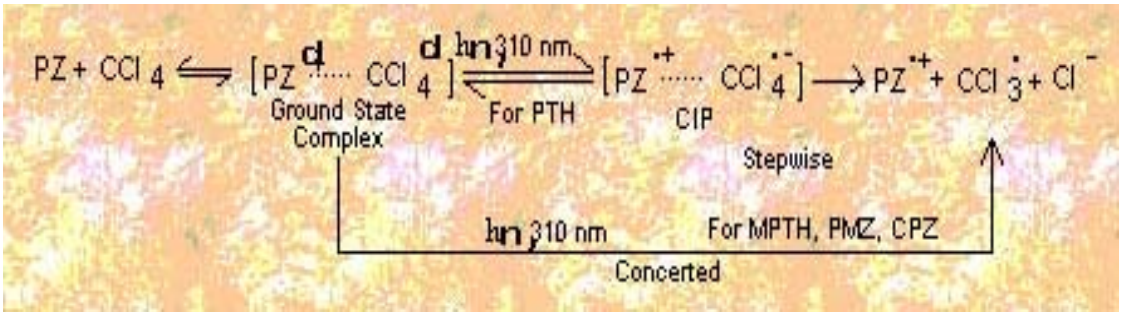

Scheme-5

different PZ can be explained on the basis of the differences in the driving force ($-\Delta G^0$) for the PDET reaction. The effect of change in ΔG^0 on the mechanism of a PDET reaction can be explained by a potential energy diagram shown in Figure 8. The predominance of one mechanism over the other depends on the relative (vertical) position of the potential energy surface (PES) of the reactants and the intermediate (cf. Figure 8). If the minima of these two PES are (vertically) close there is a possibility that the reactant PES can cross the same of the intermediate. In such a case, the reactions pass through an intermediate state and follow a stepwise mechanism. But if the driving force of the reaction decreases, the position of the minimum of the PES of the reactants goes down (vertically), reducing the possibility of crossing of its PES with that of the intermediate. In other words, the energy of the intermediate is so high with respect to the energy of the reactants, that the reaction passing through an intermediate is not favourable. At low enough driving force, the PES of the reactant crosses the PES of the final product directly. In this case the latter is the dissociative PES for CCl_4 [16]. Hence, at lower driving force the concerted mechanism is favoured. Hence for PTH, with higher $-\Delta G^0$ value, the stepwise mechanism operates while for the other PZs, with lower $-\Delta G^0$ values, the concerted mechanism is favoured.

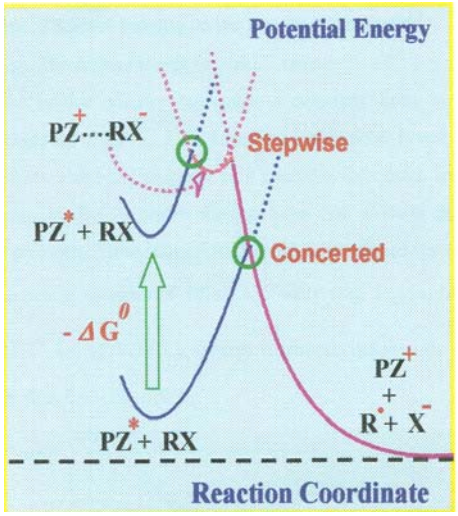

PZ	$-\Delta G^0$, eV
PTH	1.995
MPTH	1.925
PMZ	1.850
CPZ	1.780

Fig. 8 Potential energy diagram for the passage from stepwise to a concerted mechanism as a function of ΔG^0 of the reaction. The transition between stepwise and concerted mechanism takes place on increasing $-\Delta G^0$. Table shows the values of ΔG^0 for the ET reaction between PZ and CCl_4.

Effect of Solvent Polarity on the Reaction Mechanism

The driving forces for the ET reaction ($-\Delta G^0$) is a solvent dependent. Thus a change in the solvent polarity may cause a crossover from one

mechanism to the other. As the products in the present ET reaction are highly polar in nature, a polar solvent will stabilize the products better as compared to a relatively less polar solvent. Thus a more polar medium always provides a higher driving force than a lower polarity solvent for a given donor-acceptor pair. To validate this idea, we have studied the transient spectra and their temporal evolution in solvents of different polarity (ε_S). Figure 9A shows the temporal evolution of $MPTH^{\bullet+}$ for MPTH-CCl_4 system in dimethylsulphoxide (DMSO, $_S$ =46.6) which is more polar than CAN ($_S$ =46.6).

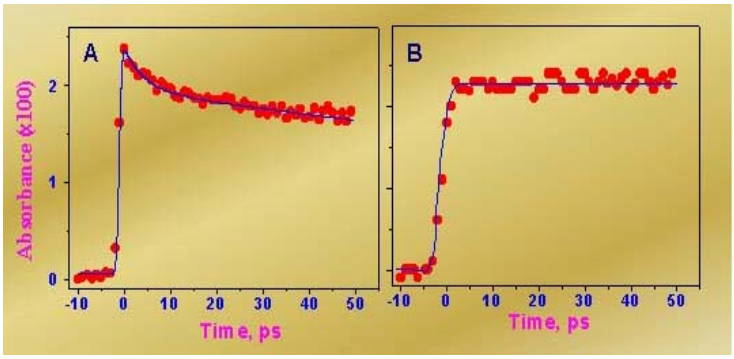

Fig. 9 The kinetic trace recorded at 530 nm for (A) MPTH in DMSO and (B) PTH in 3:2 (v/v) ACN-EA solvent mixture in presence of 0.5 M CCl_4.

It is evident from the Figure 9A that the absorption due to the $MPTH^{\bullet+}$ shows a fast decay as observed for PTH-CCl4 pair in ACN (cf. Figure 7A). Thus it can be concluded that the BET process takes place even for MPTH in a higher polarity solvent. As DMSO is a more polar solvent than ACN, the former can provide more driving force for the ET reaction. The temporal evaluation of $PTH^{\bullet+}$ for PTH-CCl_4 system in ACN-EA (3:2 v/v, EA: Ethyl Acetate, ε_S = 25) mixed solvent, which is less polar than ACN, shows no decay of $PTH^{\bullet+}$ (see Figure 9B). Hence, for PTH in a less polar ACN-EA medium, the BET process, which was clearly taking place in more polar ACN, is now hindered. This clearly shows that in more polar solvent the system follows a stepwise mechanism while in less polar medium the concerted mechanism seems to be operative.Thus the present result demonstrated, for the first time, that an increase in the solvent polarity causes the crossover of PDET reaction mechanism from concerted to stepwise.

Conclusion

Photoinduced dissociative electron processes have been explored in detail using PZ as electron donor and chloroalkanes as electron acceptors. A detailed photochemical kinetic scheme is proposed to explain the observed results for the phenothiazine-chloroalkane systems. A modified Marcus theory applicable for DET processes was applied for the present system studied. Depending on the free energy of the reaction, PZ was found to follow different mechanism in an electron transfer reaction with CCl_4 in acetonitrile. It is demonstrated that the higher driving force for the electron transfer reaction favours the stepwise mechanism while a decrease in the driving force triggers the cross over of mechanism to concerted one. Polarity of the medium plays an important role in determining the mechanism. Higher polarity solvent favours the stepwise mechanism as compared to a less polar medium. The present study shows, for the first time, in contrary to the electrochemical studies, that for a halocarbon like CCl_4, the corresponding anion radical exists for short time and follows a stepwise rather than a concerted mechanism for dissociation.

Acknowledgment

I am grateful to all my coworkers involved in this study. Thanks to Dr. T. Mukherjee, Head, RC&CD Division, BARC for his constant encouragement and support.

References

1. Klayman, D. L. *Science* **1985**, *228*, 1040.
2. Gratzel, M. *Nature* **2001**, *414*, 338.

3. Belloni, J,; Treguer, M.; Remita, H.; Keyzer, R. D. *Nature* **1999**, *402*, 865.
4. Borrows, C. J.; Muller, J. G. *Chem. Rev.* **1998**, *98*, 1109.
5. Marcus, R. A. *J. Chem. Phys.* **1956**, *24*, 966.
6. Marcus, R. A.; Sutin, N. *Biochim. Biophys. Acta* **1985,** *811*, 265.
7. Marcus, R. A. *Annu. Rev. Phys. Chem.* **1964,** *15*, 155.
8. S. Nath**,** H. Pal, D. K. Palit, A. V. Sapre, J. P. Mittal. *J. Phys. Chem. A* **1998,** *102*, 5822.
9. S. Nath, A. V. Sapre *Chem. Phys. Lett.* 2001*, 344*, 138.
10. S. Nath, A. K. Singh, D. K. Palit, A. V. Sapre, J. P. Mittal. *J. Phys. Chem. A* **2001***, 105*, 7151.
11. Andrieux, C. P.; Gorande, A. L.; Saveant, J. M. *J. Am. Chem. Soc*. **1992**, *114*, 6892.
12. Rehm, D.; Weller, A. *Israel J. Chem.* **1970**, *8*, 259.
13. Wang, S.; Saeva, F. D.; Kampmeier, J. A. *J. Am. Chem. Soc.* **1999**, *121*, 4364.
14. Robert, M.; Saveant, J. M. *J. Am. Chem. Soc.* **2000**, *122*, 514.
15. Costentin, C.; Robert, M.; Saveant, J. M. *J. Phys. Chem. A* **2000**, *104*, 7492.
16. Saveant, J. M. *J. Am. Chem. Soc*. **1987**, *109*. 6788.

Dr Sukhendu Nath has been awarded the prestigious Indian National Science Academy (INSA) Young Scientist Medal in Chemical Science in October, 2002.

About the author ...

Dr Sukhendu Nath *obtained his M.Sc (Chemistry) from the University of Burdwan. He joined Chemistry Division, BARC, in 1996 after graduating from the 39th batch of the BARC training school. He received his Ph.D degree from the University of Mumbai in 2002.*

Microwave Processing of Ceramics

A.Ghosh, D.D.Upadhyaya, Ram Prasad and A.K.Suri
Materials Processing Division
Bhabha Atomic Research Centre

Detailed investigations have been undertaken towards harnessing the phenomenon of microwave heating (MWH) for the synthesis and processing of ceramic materials. Its potential has been demonstrated in different variants of ZrO_2, ZTA, Al_2O_3 – SiC composites, HTSC, etc, resulting in rapid densification rate. Similarly for synthesis routes like solution based homogeneous precipitation or solid state reaction in LiO – Ta_2O_5 system, an enhancement in reaction kinetics was achieved. The reduction in processing time thus provided a larger throughput rate. Stabilized zirconia has a large concentration of point defects which makes it an excellent susceptor of microwave energy (above 600^{O}C temperature). Sintering assembly was constructed by modifying 1.5 kW, 2.45 GHz microwave oven. Green samples were placed inside a casket made of alumina and zirconia fiberboards. This was covered with alumina wool (microwave transparent) having low thermal load, for heat containment. To initiate heating, a hybrid mode was adopted using a thin layer of SiC powder as a susceptor. This was found to be essential in minimizing the thermal gradients within the sample. For temperature sensing a shielded R-type thermocouple was used. Samples of 9Y-CSZ and 3Y-TZP were sintered at 1625^{o}C and 1350^{o}C respectively, in microwave furnace. Conventional sintering of the above materials, however, was carried out at 1700^{o}C and 1400^{o}C respectively in resistive heating furnace to achieve comparable density. Microstructural features of 9Y-FSZ show an equiaxed grains (~15 μm) with finely dispersed porosity.

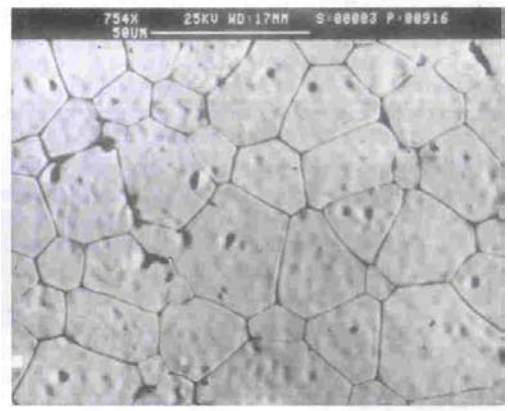

SEM micrographs of mw sintered 9Y-FSZ ceramics

TEM image of microwave sintered 3Y-TZP ceramic

Table 1. Comparative study of conventional (con) and microwave (mw) sintered 3Y-TZP ceramics

Sl. No.	Materials and Sintering Treatment	Bulk Density ($gm.cm^{-3}$)	Hardness H_v (GPa)	Toughness K_{IC} (MPa√m)
1.	3Y-TZP (con)	5.86	6.6	8.7
2.	3Y-TZP (mw)	5.83	8.3	8.6
3.	3Y-TZP + MnO_2 (mw)	5.82	4.5	4.2
4.	3Y-TZP + TiO_2 (mw)	5.77	3.3	4.7

For 3Y-TZP, grains were relatively fine (~100 nm) with a monomodal distribution. The grain boundaries were completely free of amorphous phase indicating that the high purity of the material is retained even after several processing steps.

A combined effect of dielectric heating and the field enhanced mobility during diffusion is manifested in the observed rapid kinetics making the processing cost effective for refractory ceramics systems.

This paper received the Best Paper award of RAMP-2001 held at Chidambaram, Tamil Nadu, during September 7-8, 2001

About the authors ..

Mr Abhijit Ghosh *received his BSc (Tech) in ceramics from University of Calcutta in 1995 and MTech (Ceramics) degree from IT-BHU in 1997 and joined Materials Processing Division, BARC, after completing 6th OCPGE in nuclear science. Since then, he is associated with R&D activity on advanced ceramics, especially structural and electrical ceramics. He is involved in the development of silicon carbide based ceramic, preparation and characterization of nano zirconia based materials, and development of solid oxide fuel cell devices. He has published more than 15 research papers in different journals and conference proceedings.*

Dr D.D.Upadhyaya *joined BARC after completing the orientation course in nuclear science in 1968-69. He earned the Ph.D. degree in physics (1985) and published more than 80 research papers in different journals and conference proceedings. His fields of interest are in structure property correlation in electronic and engineering ceramics, lattice defect-structure characterization, and advanced synthesis and consolidation techniques. He visited Max-Planck Institute, Metals Research, Stuttgart, Germany during 1987-89, under the Indo-German exchange programme.*

Mr Ram Prasad *joined Metallurgy Division in 1963 after completing BARC training school course in 6th batch. He was associated with the ceramic materials development programmes for nearly four decades. His main fields of interest have been electronic and magnetic ceramics, structural ceramics and bioceramics materials in which he has published more than 200 research papers. He retired from BARC on superannuation in Deccember 2002.*

Advanced Oxidation Processes for Treatment of Spent Organic Resins in Nuclear Industry

T.L. Prasad, Smitha Manohar and C. Srinivas
Nuclear Recycle Group
Bhabha Atomic Research Centre

Abstract

The paper presents the feasibility studies on wet air oxidation studies being carried out using the dissolved resin feed having COD value upto 50000 ppm on pilot scale set-up under a pressure upto 20 bars for various durations. This paper also presents comparison of various industrial practices being adopted for treatment of spent resin.

Introduction

THROUGHOUT THE NUCLEAR FUEL CYCLE, Ion exchange processes are used in a number of stages. They are widely used in spent fuel storage pond water treatment and reactor coolant clean up systems. Nuclear power station of 235 Mwe capacity generates around 20 cu.mt of spent ion exchange resin wastes annually [1]. The nuclear grade resins are mainly based on polystyrene type with divinyl benzene cross linking and functionalised with SO_3H for cation resin and $CH_2N^+(CH_3)_3OH^-$ for anion resin. The spent resin from nuclear facilities are usually contaminated with Co^{60} and fission product nuclides such as Cs^{137}.

The processes for waste treatment and conditioning in nuclear power plants are being modified in the light of technical developments [2]. The brief description of the current industrial practices for resin management being adiopted in various countries are mainly of following types.

- Direct Immobalisation in Cement : It is not a completely satisfactory method because of various problems such as setting, swelling and disintegration of the waste form.
- Direct immobalisation in organic matrices : The immobalisation in matrices like bitumen and polymers (polyester, polystyrene) leads to problems of chemical and radiation degradation of the waste form.
- Incineration : Though incineration a very promising technology for organic wastes in general, is not very suitable for spent resins because of the complexity of off-gas treatment and generation of large volumes of secondary aqueous wastes from off-gas treatment

Advanced Oxidation Processes

In recent times, several advanced oxidation processes are emerging as eco-friendly alternatives to incineration. Some of these processes are wet oxidation; photo oxidation and wet air oxidation. These advanced oxidation processes helps in conversion of organic wastes into inorganic form, which is required in order to have a more stable and inert form for final disposal. The mineralisation of organic wastes enables the use of conventional decontamination procedures with greater success.

Wet oxidation is a mineralisation process employing powerful oxidants such as hydrogen peroxide and ozone. The reaction occurs in aqueous medium at a maximum temperature of 100 deg.C under atmospheric pressure. Use of hydrogen peroxide for concentrated organic

waste mineralisation leads to large volumes of secondary aqueous radioactive waste.

Photoxidation is generally suited for aqueous streams containing small concentrations (ppb to ppm levels) of dissolved toxic organics.

Wet air oxidation is an attractive option for treating concentrated organic wastes. Oxygen/Air is used as oxidant in this process. These are the salient and most attractive features of this process. The process is usually conducted at 150 – 300 deg.C and 10 to 50 bar. Its industrial application for sewage sludge treatment is well known. In the present work, application of this process for resin mineralisation is investigated.

Wet Air Oxidation for Resin Mineralisation

Direct wet air oxidation on solid resins leads to mass transfer limitations. To overcome this, a two step procdure was devised consisting of :

- Resin dissolution i.e conversion to water soluble products by treatment with small amount of hydrogen peroxide.
- Wet air oxidation on dissolved resin in presence of copper sulphate catalyst

The present work reports the results obtained in the wet air oxidation of dissolved anion exchange resin of Poly (styrene- DVB) functionalised with quarternary ammonium chloride.

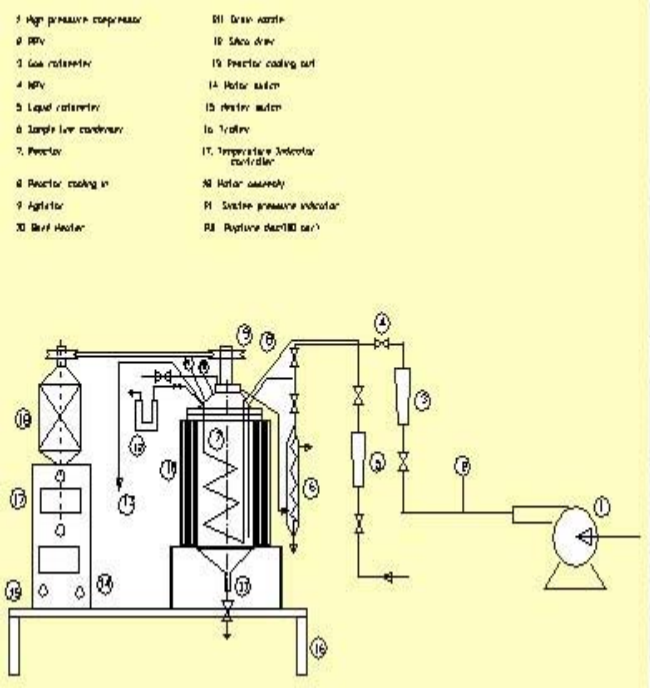

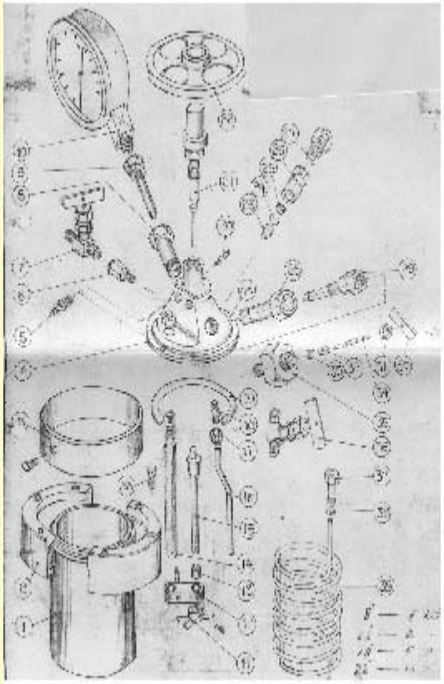

1. WAO reactor
2-3 Split ring
4,19 Reactor Head
5 Nipple
6-7 Vent cock
8-10 Pressure gauge
11,12,13,15 Propellers
16-18 Sparger
20 Leak detectors
21-22 Drive
23-27 Rupture disc
14,28,29 Thermo well
30-36 Sampling cock
37-39 Cooling coil

Fig.1 Details of Wet Air Oxidation Experimental Rig

Experimental procedure

The details of the experimental test rig used for investigation is shown in fig-1. The test rig is batch type SS-316 reactor of capacity of 2 litres. Unit is provided with resistance band heater of 2.5 kw and agitator with variable speeds of 270 to 840 RPM. The instrumentation is provided for on-line measurement of pressure and temperature of reaction media. The oxygen and nitrogen are used from cylinders through a regulator and non return valves. The helical cooling coil is provided to control the temperature of reaction mixture. Provision is also made for on-line sampling. The progress of the oxidation reaction was monitored by determining the COD of an aliquot sample from time to time using E Merck model SQ-118 equipped with thermoreactor TR200.

Resin in bead form of –20+50 mesh was used for dissolution and subsequent oxidation experiments. The dissolution was effected by reacting one kg of resin with one litre of 50% hydrogen peroxide at 50-60 deg.C in the presence of copper sulphate catalyst. Dissolved resin samples having initial COD values in the range of 5000-6000 ppm were used in the experiments. The agitator speed was fixed at 270 RPM in all the experiments.

Results and Discussions

Fig. 2 shows the progress of reaction under different conditions of pressure and temperature. The results clearly show the feasibility of this method. About 80% reduction in COD could be achieved in three to four hours.

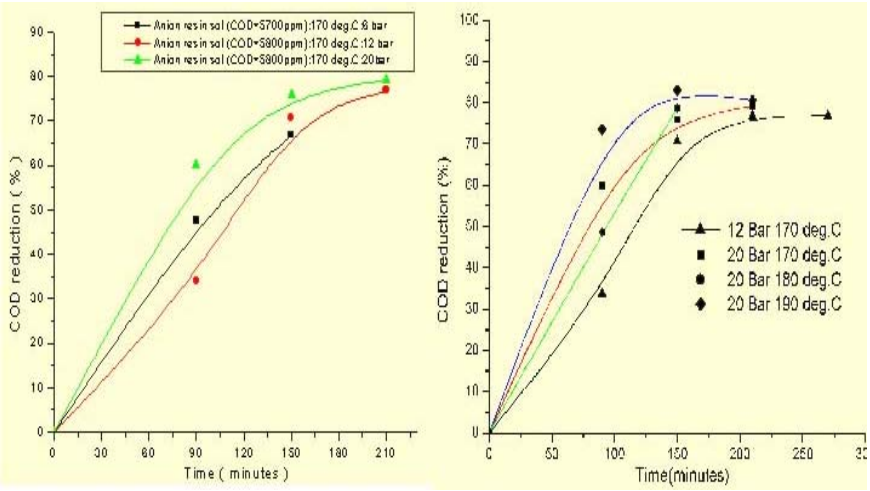

Fig. 2 Wet Air Oxidation results

It is seen from results that reaction is significantly faster at higher pressures, only at initial stages (less than two hours) of oxidation for a given temperature. This may be on account of the accumulation of refractory carboxylic acids over a period of time. It is also observed that increase of temperature from 170 to 180 deg.C was not effective at 20 bar. However further increase to 190 deg.C increased the rate by about 25% again in the early stages only, perhaps due to similar reasons. Preliminary experiments on higher COD (50000 ppm) resin solution indicated that around 90% reduction can be achieved in six hours at 190 deg.C and 20 bar. Further experiments are in progress to optimise the conditions for total mineralisation.

Aknowledgements

The authors wish to thank Dr A. Ramanujam, Head, PDD, BARC, Mr A.K.Misra, AD(P), NRG, Mr C.S. Bilaye and Mr P.K. Wattal for the technical suggestions and discussions.

References

1. Kaiga Atomic Power Station Safety Report, Volume-I
2. Treatment of spent ion exchange resin for storage and disposal, IAEA-TRS-254

This paper received the second Best Paper award in the poster session at the National Symposium of CHEMCON 2001 organised by Indian Institute of Chemical Engineers and held at Central Leather Research Institute, Chennai, during December 19-21, 2001.

About the authors ...

Mr T.L.Prasad *is from 32nd batch of Training School and after completion of one-year post graduate programme in Nuclear Science and Technology joined Nuclear Recycle Group of BARC in 1989 for carrying out the R&D in Back End of Nuclear Fuel Cycle. His major contributions are :*

- *International Atomic Energy Agency – coordinated Research Programme on Decontamination and Decommissioning*
- *Primary Heat Transport System decontamination of Unit-1 of Madras Atomic Power Station for extending plant life of the reactor*
- *Development of Fluid Bed Calciner system for high level liquid wastes*
- *Commercial demonstration of combined processes of Alkaline Hydrolysis and Incineration for spent solvent management, generated from radiochemical plants*
- *Development of Advanced Oxidation Processes for management of organic wastes generated in nuclear industry*
- *Project management for NRG projects*

Presently, he is working for RUSWapp project. He has presented 12 papers in various National symposiums/seminars. He is a member of professional bodies such as Indian Nuclear Society; Institute of Engineers(I) and Indian Institute of Chemical Engineers.

Dr C. Srinivas *presently works in Back-End Technology Development Division of BARC. He did his M.Sc. in Chemistry from Andhra University, Visakhapatnam, and joined 21st batch of Training School, BARC. He obtained his Ph.D. in Chemistry from University of Mumbai in 2000. His current research interests are development of chemical and photochemical methods for the treatment of organic radioactive and other hazardous wastes.*

Reactions of Radiolytically Generated Oxidizing Species with Vinylbenzyltrimethylammonium Chloride (VBT) in Aqueous Solution

Virendra Kumar, Y. K. Bhardwaj and S. Sabharwal
Radiation Technology Development Section
Bhabha Atomic Research Centre

and

Hari Mohan
Radiation Chemistry and Chemical Dynamics Division
Bhabha Atomic Research Centre

Abstract

Transient species generated by reaction of •OH radical with vinylbenzyltrimethyl ammonium chloride (VBT) in aqueous solution, has been investigated by pulse radiolysis technique. The transient spectrum exhibits broad band in 300-330 nm region and two sharp bands with λ_{max} at 275 nm and 350nm. The rate constant for the reaction of OH radicals with VBT, was found to be 1.7 x 10^{10} $dm^3mol^{-1}s^{-1}$ and 4.7 x 10^9 $dm^3mol^{-1}s^{-1}$ by competition kinetics and by transient formation kinetics (of 350 nm band), respectively. Higher rate constant value obtained by competition kinetics indicated that more than one species is formed due to reaction of VBT with •OH. The rate of reaction of radical-cation formed by reaction of VBT with OH radical with VBT was found to be 5.7x10^6 $dm^3mol^{-1}s^{-1}$, this value is about half the rate of reaction of radical-anion with the VBT (1.2x 10^7 $dm^3mol^{-1}s^{-1}$) indicating higher contribution to initiation of polymerization of VBT by radical-anionic species.

Introduction

WATER-SOLUBLE POLYELECTROLYTES, based on quaternary ammonium salts, have been proposed as emulsifiers, flocculants, antistatic agents. PVBT of this family, in pure state, has been reported to show bactericidal properties [1,2], molecular recognition, mimics protein[3] and is also an ion exchange resin of high chemical stability[4]. We have studied radiation synthesized VBT-co-SSS polyampholytic gels and radiation induced grafting polymerization of VBT onto cotton fabric for incorporating anti-bacterial activity. The aim of this study was to investigate the reaction of radiolytically generated oxidizing species with VBT and role of transient species formed in radiation polymerization of VBT in aqueous solution. Pulse Radiolysis technique was used to carry out the investigation.

Experimental

(ar-Vinylbenzyl)trimethylammonium chloride (VBT) Mol wt. 211.74 in powder form from Aldrich was used as received. All other chemicals were of AnalaR grade. Nanopure water (conductivity 0.6μS cm^{-1}) was used for preparing all solutions. The pH of solutions was adjusted using $HClO_4$, KH_2PO_4, $Na_2HPO_4.2H_2O$ and NaOH in appropriate quantities. Details of pulse radiolysis set-up used are described

elsewhere [5,6]. 50ns single pulse of 7 MeV electrons from electron beam accelerator (LINAC) was used for irradiating the solution in 1x1cm square suprasil quartz cuvettes.

Results and Discussion

Reaction of OH radical with VBT: Figure 1(a) shows the transient optical absorption spectrum of the transient formed 2μS after the electron pulse. It exhibits broad absorption band in 300-330 nm region with λ_{max} at 275 nm and 350 nm. The absorption at λ_{max} 350 nm decayed initially by second order kinetics with $2k/\varepsilon l = 1.1x10^5$ s^1 and the band at 275 nm initially decayed by first order kinetics with $k= 5.6 \times 10^3$ s^{-1} (Fig. 1 Inset). Both the absorption bands were not observed in presence of t-butanol (0.3 mol dm^{-3}), an efficient OH radical scavenger indicating that the bands are due to reaction of OH radicals with the solute (Fig. 1(c)).

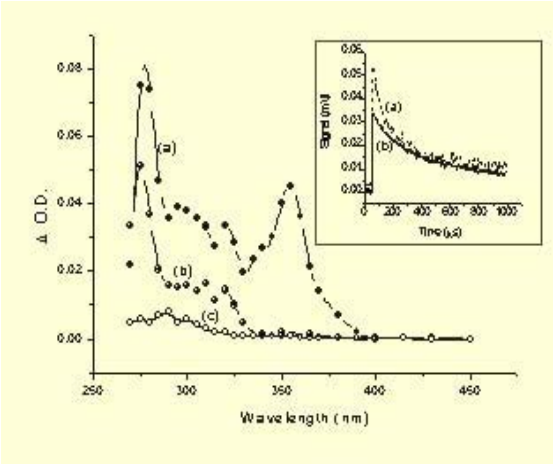

Fig 1 Transient absorption spectra of VBT radicals recorded after pulsing N_2O saturated solution: (a) [VBT]=1 x 10^{-3} mol dm^{-3} (b) [VBT]=5 x 10^{-4} mol dm^{-3} and [NaN_3] = 4x10^{-2}mol dm^{-3} (c) [VBT]=1 x 10^{-3} mol dm^{-3} and [t-butanol]=0.3 mol dm^{-3}. All spectrum normalized to a dose of 15.62 Gy. Inset decay of transient at (a) 275nm and (b) 350nm

For competition kinetics studies KSCN was used as a reference solute under suitable conditions. The bi-molecular rate constant, $k_{VBT + OH}$ was evaluated to be 1.7 x 10^{10} $dm^3mol^{-1}s^{-1}$ using $k_{SCN^- + OH}$ of 1.1 x 10^{10} $dm^3mol^{-1}s^{-1}$[7].

For determining rate constant by formation kinetics the transient absorption at 350 nm was investigated in N_2O saturated aqueous solutions of VBT in the concentration range (0.1-1) x 10^{-3} mol dm^{-3}. Over this range, the pseudo-first order rate (k_{obs}) was found to increase with solute concentration. The bimolecular rate constant was found to be 4.7 x 10^9 $dm^3mol^{-1}s^{-1}$.

The rate constant value obtained by competition kinetics was about three times more than that determined by transient formation. Higher rate constant value obtained by competition kinetics indicates than more than one transient species is formed as a result of this reaction.

OH radicals can react with VBT in either of the following ways, by electron transfer, by addition or by H abstraction. However the high rate constant value may exclude the possibility of H atom abstraction. In order to distinguish between addition and electron transfer reaction reactions of VBT with various one-electron oxidants were investigated.

Reactions of $N_3^\bullet$, $SO_4^{\bullet-}$, $Br_2^{\bullet-}$ and $Cl_2^{\bullet-}$ with VBT: Reaction of VBT with $N_3^\bullet$ to yield a radical cation (equation 1) was investigated by pulse radiolysing N_2O saturated aqueous solution of NaN_3 (4 x 10^{-2} mol dm^{-3}) containing 5 x 10^{-4} mol dm^{-3} of solute. As $N_3^\bullet$ radicals are much more specific in their reaction as compared to OH radicals and predominantly undergo electron transfer reaction, the observed spectrum {Figure 1(b)} was attributed to solute radical cation formed on reaction of $N_3^\bullet$ with the solute.

$$N_3^\bullet + VBT \rightarrow VBT^{\bullet+} + N_3^- \qquad (1)$$

The transient optical absorption spectrum Fig 1(b) exhibits an absorption band with λ_{max} =275 nm with broad absorption shoulder in 300 - 320 nm region. The transient decayed by first order kinetics with k=5.3 x 10^3 s^{-1}. The biomolecular rate constant for the electron transfer reaction was determined by formation kinetics (at 275 nm) to be 3.6 x 10^8 dm^3 mol^{-1} s^{-1}. Formation of radical cation was confirmed by observing formation of $ABTS^{\bullet+}$ at 645 nm[8] in accordance with reaction (2) by pulsing a N_2O

saturated solution containing $5x10^{-4}$ mol dm^{-3} VBT, $2x10^{-2}$moldm^{-3} NaN_3 and $6x10^{-6}$ mol dm^{-3} ABTS{2,2'–Azinobis (3-ethyl benzothiazoline)- 6-sulfonate}.

$VBT^{\bullet+}$ + ABTS $\rightarrow$ VBT + $ABTS^{\bullet+}$ (2)

The bimolecular rate constant of radical cation with the solute (equation 3) was found to be 5.7 x 10^6 dm^3 $mol^{-1}s^{--1}$.

$VBT^{\bullet+}$ + VBT $\rightarrow$ Dimer radical cation (3)

The transient spectra obtained by reaction of $SO_4^{\bullet-}$, $Br_2^{\bullet-}$ and $Cl_2^{\bullet-}$ with solute were also similar to that obtained by reaction of $N_3^{\bullet}$. Their bimolecular rate constant values with VBT are given in Table 1.

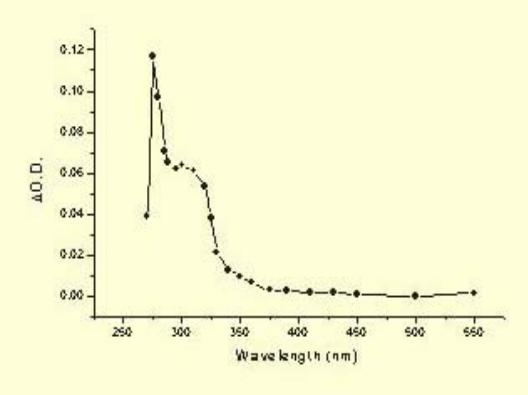

Fig. 2 Transient absorption spectra of the reaction product of $O^{\bullet-}$ with VBT at pH 12.8, 2.5 μs after the pulse, [VBT]=1 x 10^{-3} mol dm^{-3} in N_2O saturated solution.

Table 1 : Spectral and kinetic parameters of the reaction of VBT with various species

Species	pH	λ_{max} (nm)	Rate constant ($dm^3mol^{-1}s^{-1}$)	Transient decay constant (s^{-1})
$^{\bullet}OH$	6.3	275 350	------ $4.0x10^9$	$5.6x10^3$ $1.1x10^{5*}$
$^{\bullet}OH^{\#}$	6.3	-------	$1.3x10^{10}$	----------
$N_3^{\bullet}$	6.3	275	$3.6x10^8$	$5.3x10^3$
$Br_2^{\bullet-}$	6.3	275	$4.1x10^7$	$4.4x10^3$
$Cl_2^{\bullet-}$	1.2	280	$2.3x10^8$	$1.9x10^3$
$SO_4^{\bullet-}$	10.2	275	$3.7x10^9$	$1.5x10^3$
$O^{\bullet-}$	12.8	275	$1.5x10^9$	$3.8x10^{4*}$

Reaction with $O^{\bullet-}$: Further, in order to distinguish between addition and abstraction reaction of OH radical, reaction of $O^{\bullet-}$ with VBT was carried out by pulse radiolysing 1 x 10^{-3} mol dm^{-3} solution of VBT saturated with N_2O at pH 12.8. As OH radical typically behaves as an electrophile, where as its conjugate form $O^{\bullet-}$ is a nucleophile. Therefore, while OH readily adds to the double bonds, $O^{\bullet-}$ does not and hence its rate constants for addition reactions are generally much slower than $^{\bullet}OH$. But both the forms of radical can abstract H atom from C—H bond almost equally efficiently.

The rate constant for the reaction of $O^{\bullet-}$ with VBT was found to be 1.5 x 10^9 $dm^3mol^{-1}s^{-1}$, which is about 3 times lower than that of $^{\bullet}OH$ at near neutral pH indicating that addition reaction is preferred over H abstraction by $^{\bullet}OH$.

Conclusion

More than one transient species are formed due to reaction of OH radical with VBT. OH radical undergoes mainly addition and electron transfer reaction with VBT. Higher rate of reaction of radical-anion with the VBT, compared to that of radical-cation, indicates higher contribution to initiation of polymerization of VBT by radical-anionic species.

References

1. Zarras, P. , Vogl, O.,; (2000). J. M. S. Pure. Appl. Chem. A 37(8) , 817-840.
2. Kanazawa, A., Ikeda, T., Endo, T.,;(1993), J. Polym. Sci. Part A: Polym. Chem., 31,1441-1447
3. M.Senuma, M. Iwakura, S. Ebihara, Y. Shimura, and K. Kaeriyama,; (1993), Angew. Makromol. Chem. Vol. 204. p. 119,

4. Takeoka, Y., Berker, A.N., Du, R., Enoki, T., Grosberg, A., Kardar, M., Oya, T., Tanaka, K., Wang, G., Yu, X. Tanaka, T.,; (1999); The American Chemical Society 82(24), 4683-4685
5. Guha S. N., Moorthy P. N., Kishore K., Naik D. B. and Rao, K.N., (1987). Proc. Indian Acad. Sci. (Chem. Sci.) 99, 261.
6. Priyadarshini, K. I., Naik, D. B., Moorthy P. N. and Mittal, J.P. (1991). Proc. 7th Tihany Symposium on Radiation Chem , Budapest pp.105.
7. Ellison, D.H., Salmon, G. A., Wilkinson, F.,; (1972) Proc. R. Soc. London Ser. A, 328. 23-34.
8. Scott, L.S., Wen-Jang, C., Bakas, A. and Espenson, J.H.,;(1993). J. Phys. Chem. 97, 6710-6714

This paper was adjudged as one of the Best Papers presented at Asian Photochemistry Conference (APC-2002) held at Mumbai during January 6-11, 2002

About the Authors ...

Mr Virendra Kumar *received his M. Sc. Degree in chemistry from IIT Roorkee, Roorkee, in 1998. He graduated from 42nd batch of training school, BARC, in 1998-99 and started his research career in Radiation Technology Development Section, BARC. His research interests include radiation induced grafting polymerization, radiation curing and radiation polymerization / cross-linking behaviour of water-soluble polymers.*

Dr Y. K.Bhardwaj *graduated from 32nd batch of training school, BARC, in 1988-89 and started his research career in Radiation Technology Development Section. His research interests include development of radiation synthesized hydrogels for medical and pharmaceutical applications, synthesis of fast stimuli-responsive hydrogels. EB crosslinking and curing of polymers.*

Dr Sunil Sabharwal *obtained his M.Sc. degree in chemistry from Delhi University in 1978 and graduated from 22nd batch of training School, BARC, in 1978-79. Presently, he is the Head of Radiation Technology Development Section, BARC. His main area of research are industrial application of radiation technology using electron beam irradiation, radiation effects on polymeric materials and pulse radiaolysis studies on crosslinking of water soluble polymers.*

Dr Hari Mohan, *after graduating from the BARC training school in 1967 started his research career in the Chemistry Division. He has worked on various aspects of chemical effects induced by nuclear reactions of halogens, radiation induced polymerization of vinyl monomers and photophysical properties of laser dyes. He obtained his Ph. D degree in 1981 from Bombay University. He worked with Prof. K. D. Asmus, Hahn-Meitner Institute, Berlin, in 1986 and with Prof. O. Brede, Leipzig University, Germany, in 1997. His current interests include fast reaction kinetic studies using electron accelerator and lasers on halogenated and organic sulfur compounds, fullerene derivatives and other biologically important molecules.*

Influence of Radiation and Photolysis on Intracellular Proteases

V.K. Jamadar, S.N. Jamdar and P. Harikumar
Food Technology Division
Bhabha Atomic Research Centre

Hari Mohan
Radiation Chemistry & Chemical Dynamics Division
Bhabha Atomic Research Centre

and

S.P. Dandekar
Seth G. S. Medical College,
KEM Hospital, Parel, Mumbai

Abstract

Two important proteases an endopeptidase; cathepsin D (E.C 3.4.23.5) and an exopeptidase; aminopeptidase (E.C 3.4.11.__) were purified to homogeneity from chicken intestine and their response to ionizing radiation and photolysis was studied. Radiation as well as photolysis was found to inactivate cathepsin D and aminopeptidase with discernible qualitative as well as quantitative differences between the response of the two enzymes. The D_{37} values for cathepsin D and aminopeptidase in aerated condition were 281 Gy and 250 Gy respectively. The inactivation was in the order N_2O> N_2> Air, indicating predominantly an ˙OH mediated mechanism. The response of the enzymes to radiation was found to be dependent on the protein content of the medium and was closely associated with alterations in it's fluorescence characteristics. Investigations carried out using different atmospheric conditions and free radical scavengers along with fluorescence studies provide substantial evidence for the involvement of aromatic amino acids, especially tryptophan in the active site of the enzymes.

Introduction

STUDIES ON PROTEASES ARE OF immense importance in food processing especially in radiation hygeinised flesh foods as they bring about protein degradation and modification, which influence the quality attributes of food products.[1] In the present study, an attempt has been made to understand radiation induced changes in two important proteases from chicken intestine, cathepsin D and aminopeptidase in the purified form. Cathepsin D is the major endopeptidase that mediates tissue autolysis in chicken intestine[2] while aminopeptidases are known to determine the levels of bitter peptides and free amino acids in protein hydrolysates.[3,4] Earlier studies from our laboratory[5] have shown that the radiosensitivity of these proteases is higher in the aqueous tissue extract than in the whole tissue implicating radiolytic products of water in the inactivation of proteases. Radiation studies employing purified enzymes have been used to understand the mechanisms underlying the migration of free radicals through macromolecules and to derive structural information on their active sites.[6] The present studies were undertaken to delineate the interaction of free radicals with aminopeptidase and cathepsin D as a means to obtain insight into their active site residues. Though such studies have been carried out for a number of

enzymes including oxido reductases, lysozyme, and alkaline phosphatase,[7,8,9,10] this is the first report on the radiosensitivity of intracellular proteases.

Materials and Methods

Chicken intestine was obtained from the local abattoir, cleaned individually by flushing tap water and stored at - 20°C until use. L-arginine–β–naphthylamide, cysteine, fast garnet GBC, mersalyl acid and hemoglobin were procured from Sigma Co., USA. Trichloroacetic acid (TCA) was purchased from Thomas Baker, India. All chromatography materials for enzyme purification were products of Pharmacia, Sweden.

Purification of the proteases from chicken intestine was carried out using ion exchange, gel filtration and hydrophobic interaction chromatography. Aminopeptidase activity was determined by the modified method of Skrtic and Vitale.[11] The enzyme was assayed at 50°C using 20mM L- arginine-β-naphthylamide in 0.1M phosphate buffer pH 6 containing 1mM cysteine. The reaction was terminated by addition of 1ml mersalyl reagent. The pink colored complex was read at 520nm. Cathepsin D was assayed at 50°C using 1%hemoglobin in 0.1M glycine-HCl buffer pH 2.5. The reaction was terminated by addition of 10% TCA and the TCA soluble products were estimated.[12]
The purified enzymes were exposed to gamma radiation at ambient temperature in air, N_2 and N_2O using Co^{60} source (Dose rate = 8.5 Gy/min). The enzymes were exposed to light of wavelength 254nm for different time intervals (30 secs – 10 mins) using Rayonnet photochemical reactor. The fluorescence spectra of the enzymes were analyzed on Hitachi Spectrofluorimeter F – 4010.

Results and Discussion

Aminopeptidase and cathepsin D were purified to homogeneity 839 and 900 fold respectively using a series of steps involving ion exchange, gel filtration and hydrophobic interaction chromatographies. Aminopeptidase resolved as two bands of molecular weight 94 kDa and 66 kDa on SDS- PAGE (Fig.1A), while cathepsin D appeared as a single band of molecular weight 33kDa (Fig. 1B).

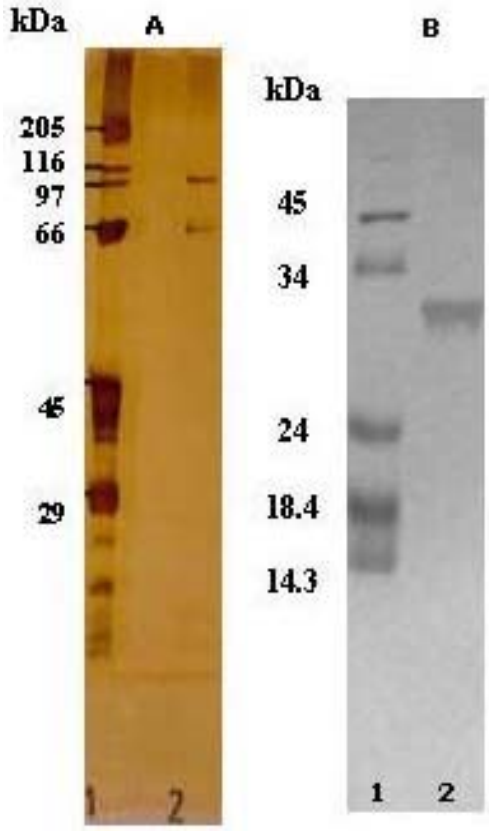

Fig. 1 SDS-PAGE pattern of purified Aminopeptidase and Cathepsin D

A = Lane 1= High molecular weight markers, Lane 2 = Aminopeptidase (30 µg)
B = Lane 1= Low molecular weight markers, Lane 2 = Cathepsin D (15 µg)

Influence of Gamma Radiation on Aminopeptidase and Cathepsin D

Ionizing radiation caused inactivation of aminopeptidase and cathepsin D exhibiting an exponential relationship with radiation dose (Fig. 2A and 2B). These results are in agreement with the earlier studies on interaction of ionizing radiation with enzymes in aqueous solutions.[13]

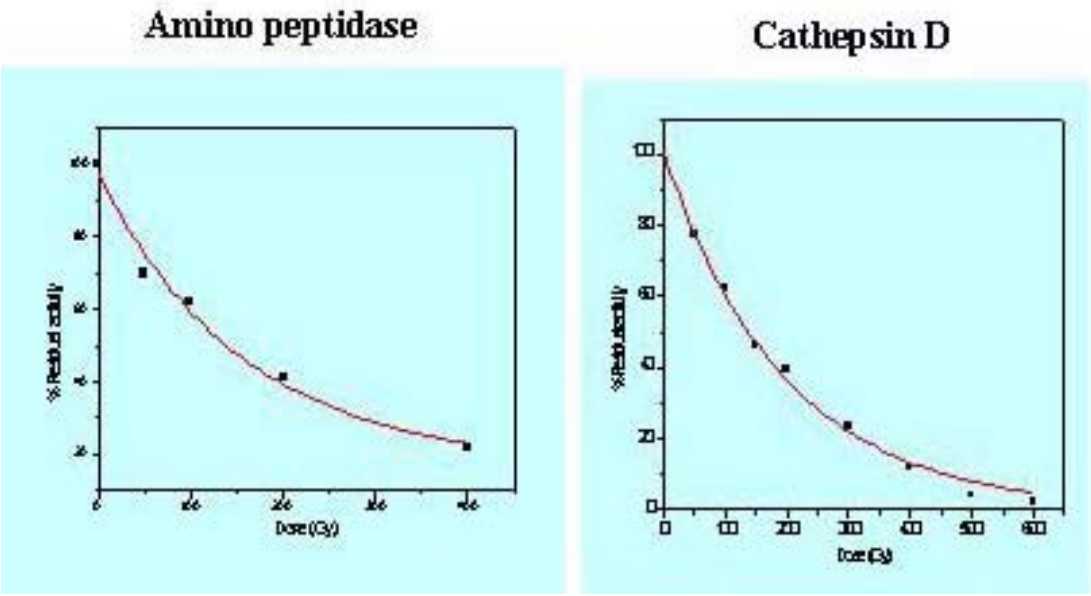

Fig.2 Effect of graded dose of radiation on aminopeptidase and cathepsin D. (Aminopeptidase (17µg/ml) and cathepsin D (31 µg/ml) were subjected to gamma radiation at ambient temperature and the residual activity was determined.)

The exponential function of dose is attributed to the same rate of interaction of water molecules with the active and inactivated enzyme molecules.

cathepsin D, in the range of 20 - 40 µg/ml cathepsin D was found to be more sensitive to radiation (70 – 80% inactivation) than aminopeptidase (55 – 60% inactivation).

Influence of Protein Concentration

The radiation induced damage to enzymatic and non enzymatic proteins is known to depend on factors such as the protein concentration, pH and presence of oxygen in the medium.[14] The results represented in Fig. 3 show that the radiation inactivation of aminopeptidase and cathepsin D decreases with an increase in the protein concentration. Although the protein concentrations used in the study are different for aminopeptidase and

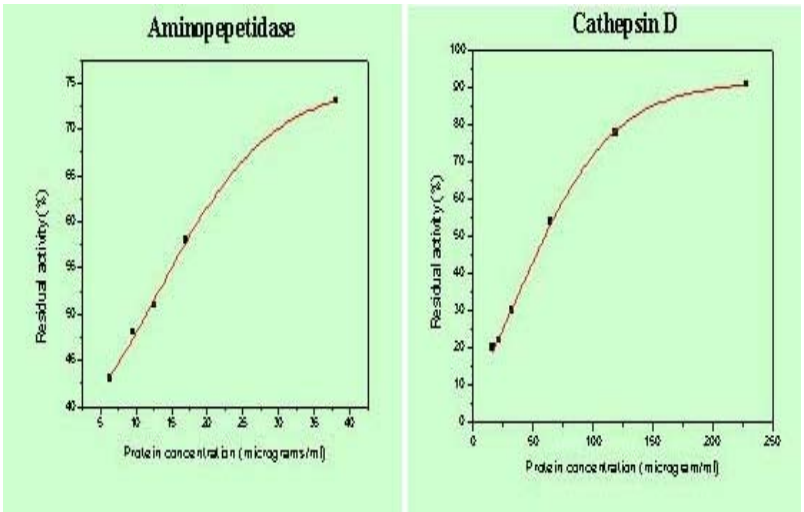

Fig. 3 Effect of protein concentration on the radiosensitivity of aminopeptidase and cathepsin D. (Purified aminopeptidase and cathepsin D were subjected to gamma radiation (200 Gy). The residual activity was determined.)

Effect of Radiation Atmosphere on the Radiation Sensitivity of Proteases

Formation of different radiolytic species could be regulated using different atmospheric conditions during irradiation.[15] Solutions saturated with N_2O have a predominance of $^{\cdot}OH$ radicals. $^{\cdot}OH$ and $O_2^{\cdot -}$ are formed in aerated condition while $^{\cdot}OH$, e_{aq}^- and $O_2^{\cdot -}$ are known to predominate in N_2 saturated solutions.

Data presented in Table 1 shows that inactivation of the proteases was in the order N_2O > N_2 > Air indicating an $^{\cdot}OH$ mediated inactivation.

Table 1: Influence of atmospheric conditions on the radiosensitivity of Aminopeptidase and Cathepsin D

% Inactivation			
	Air	**N_2**	**N_2O**
Aminopeptidase	35	55	70
Cathepsin D	66	81	91

Aminopeptidase (20 µg/ml) and cathepsin D (31 µg/ml) were subjected to a radiation dose of 200 Gy and 300 Gy respectively.
N_2 and N_2O gases were bubbled through the enzymesolutions before irradiation.

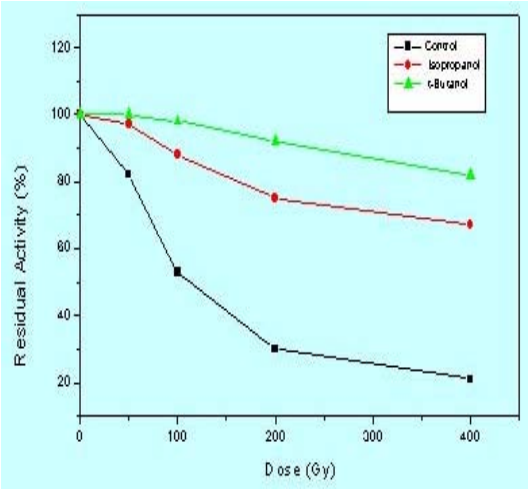

Fig. 4 Influence of $^{\cdot}OH$ scavengers on the radiosensitivity of aminopeptidase. Aminopeptidase (20 µg/ml) was irradiated in presence of 1mM t- butanol and isopropanol in N_2O saturated condition. The residual activity was determined.

As suggested by Spinks and Woods[15], the reduced effect of radiation in aerated system could be attributed to the scavenging effect of H and e^-_{aq} by oxygen. The role of $^{\cdot}OH$ in enzyme inactivation has been confirmed by incorporating known $^{\cdot}OH$ scavengers such as t- butanol and isopropanol during irradiation.[16] Isopropanol and t-butanol in a 1mM concentration offered 80% and 95% protection respectively to aminopeptidase (Fig. 4).

Relationship between Changes in Fluorescence Characteristics and Radiation Sensitivity of Proteases

Presence of chromophoric moieties especially aromatic amino acids imparts characteristic fluorescence properties to proteins.[17] Changes in fluorescence spectra are used by various investigators,[18,19] to ascertain radiation induced structural changes in the active site of enzymes.

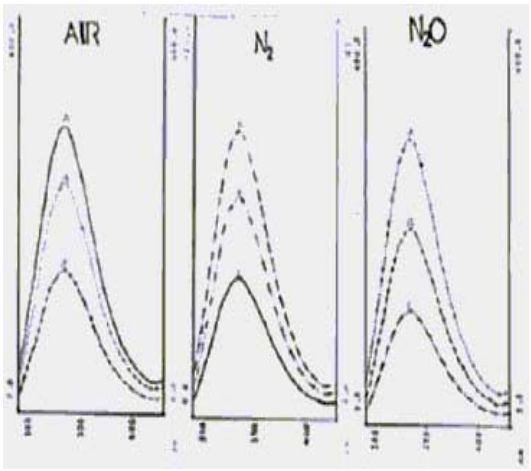

Fig.5a Influence of radiation on the fluorescence spectrum of aminopeptidase. Aminopeptidase was subjected to gamma radiation at ambient temperature under air N_2 and N_2O conditions. The change in fluorescence spectrum was studied. (λ_{ex}= 280 nm and λ_{emm}= 340nm). A = Unirradiated, B = 50 Gy, C = 400 Gy

As shown in Fig 5A aminopeptidase exhibits an emission peak at 340nm, which is characteristic of tryptophan[17]. This peak decreased on irradiation indicating damage to tryptophan residues (Fig. 5A). Cathepsin D showed a fluorescence peak at 340nm and a second peak

at 310 nm indicating presence of tryptophan and tyrosine in the enzyme structure. The peak at 340nm was quenched on irradiation whereas the second peak at 310nm remained unchanged (Fig 5b).

The radiation induced change in fluorescence of aminopeptidase (Fig 5A) in air, N_2 and N_2O followed a pattern in consonance with the decrease in activity (Table 1). These data point to the inter relationship of $^{\cdot}OH$ mediated alteration in tryptophan and loss of enzyme activity, thereby indicating the possible presence of tryptophan residues in the active site of the enzyme. Tyrosine is known to be present in the active site of cathepsin D. Whether radiation brings about a change in the tyrosine residues and whether they are involved in the enzyme catalysis needs to be further investigated.

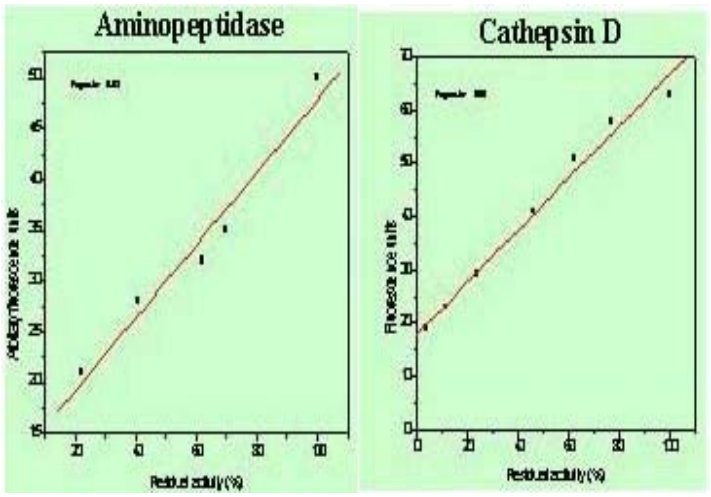

Fig. 6 Relationship between loss of activity and fluorescence quenching.
Aminopeptidase (20µg/ml) and cathepsin D (31 µg/ml) were subjected to gamma radiation at ambient temperature. The residual activity and change in fluorescence was monitored.

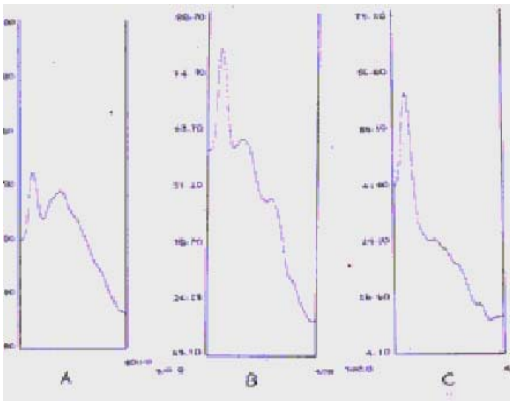

Fig. 5b Influence of radiation on the fluorescence spectrum of cathepsin D.
Cathepsin D was subjected to gamma radiation at ambient temperature. The change in fluorescence spectrum was studied. (λ_{ex}= 280 nm and λ_{emm}= 340nm). A = Unirradiated, B = 150 Gy, C = 600 Gy

In the case of both the enzymes, loss of activity was linear with the quenching of tryptophan fluorescence (Fig 6 A and 6B). This confirms that tryptophan is an essential moiety of the active site of these enzymes.

From the foregoing data it is clear that ionizing radiation brings about on $^{\cdot}OH$ mediated alteration and that tryptophan is the crucial active site residue in aminopeptidase and cathepsin D.

Photolysis

Efforts were made to use photolysis as a means to supplement the information obtained using radiation studies, as it is known to cause changes in specific chromophoric residues of proteins.[20] Data presented in Fig. 7 showed that both aminopeptidase and cathepsin D were inactivated by photolysis. However, the extent of their inactivation could not be compared due to different protein concentrations used.

Tryptophan is known to be the most photosensitive chromophore in proteins[21]. Our results on the photoinactivation of proteases strongly suggest that tryptophan is a crucial residue in the catalytic site of both aminopeptidase and cathepsin D.

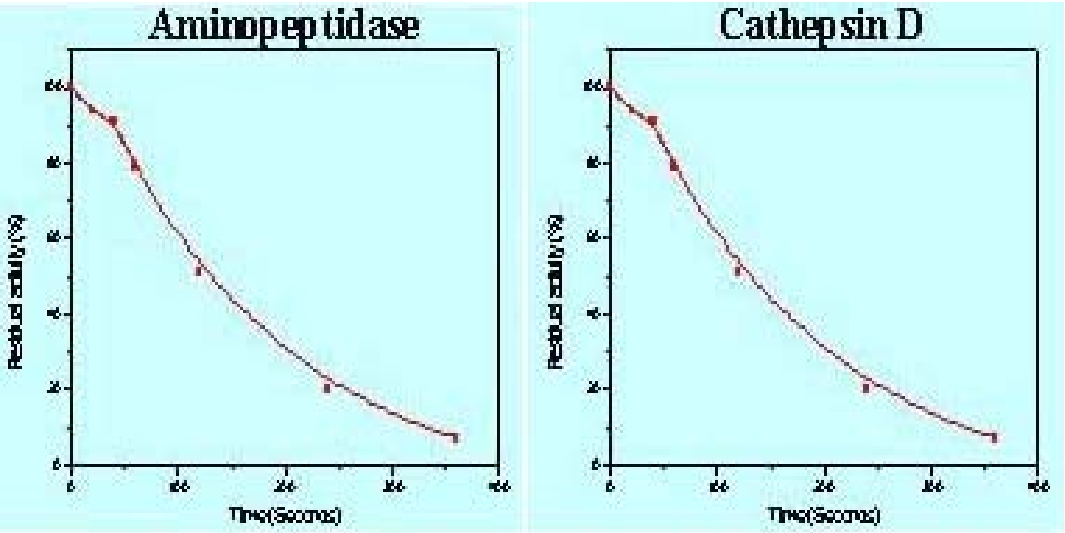

Fig. 7 Photo induced inactivation of aminopeptidase and cathepsin D. Aminopeptidase (20 µg/ml) and cathepsin D (31µg/ml) were irradiated at 254nm and the residual activity was determined.

Conclusion

This report shows for the first time that two major proteases of importance in flesh food processing namely aminopeptidase (an exopeptidase) and cathepsin D (an endopeptidase) are inactivated by gamma irradiation and photolysis. Our studies on the influence of different environmental conditions and free radical scavengers show that radiation induced inactivation of the enzymes is predominantly $^{\cdot}OH$ mediated. Our results strongly suggest the presence of tryptophan in the active site of both the enzymes. Further structural and kinetic studies involving specific amino acid blockers, sensitizers and protectants are in progress to confirm these observations.

References

1. Godfrey T (1996). In: Industrial Enzymology, 2nd Edition, Eds. Godfrey T and West S, Macmillan Press, pp: 87 – 100, 177 – 185.
2. Jamdar S.N, Nair P, Harikumar P (2000). Autolytic degradation of proteins in irradiated chicken intestine. Proceedings of NAARRI Annual conference 2000,Ed. Gangadharan S, Nandakumar A.N, Iyer S. R.K, Chandy P. J, pp: 74 – 76.
3. Tan P.S.T, van Kessel T A.J.M, Van De Veerdonk F.L.M, Zuurendonk P.F, Bruins A.P, Konings W.N (1993). Degradation ad debittering of a tryptic digest from β casein by aminopeptidase N from *Lactococcus lactis subsp. Cremoris* WG2 Appl. Env. Microbio., 1430 – 1436.
4. Bouchier P.J, Cuinn G, Harrington D, Fitzgerald R.J (2001). Debittering and hydrolysis of a tryptic hydrolysate of β casein with purified general and proline specific aminopeptidases from *Lactococcus lactis subsp. Cremoris* AM2. J. Food. Sci., 66, 816 – 820.
5. Jamdar S.N and Harikumar P (2002). Sensitivity of catheptic enzymes in radurized chicken meat. J. Food Sci. Technol., 39, 72 – 73.
6. Von Sontagg C (1987). Enzymes. In: The Chemical Basis of Radiation Biology, Tatlor and Francis, London, pp: 429 – 455.

7. Saha A, Mandal P.C, Bhattacharyya S.N (1991). Radiation induced changes in flavin fluorescence of dihydroorotate dehydrogenase. Int. J. Radiat. Biol., 60, 769 – 778.
8. Cudina I and Jovanovic S.V (1988). Free radical inactivation of trypsin. Radiat. Phy. Chem., 32, 497 – 501.
9. Hasan N.M, Mc Call P.R, Moore J.S, Power D.M (1994). Radiation inactivation of bovine intestinal alkaline phophatase. Radiat. Phys. Chem., 43, 233 – 237.
10. Roberts P.B (1973). A radiation chemical study of the inactivation and active site composition of carboxypeptidase A. Int. J. Radiat. Biol., 24, 143 – 152.
11. Sktric I and Vitale L (1994). Methionine preferring broad specificity aminopeptidase from chicken egg white. Comp. Biochem. Physiol., 107 B, 471 – 478.
12. Takashi T and Tang J (1981). Cathepsin D from porcine and bovine spleen. In:Methods in Enzymology, vol. 80, Proteolytic enzymes Part C, Ed. Lorand L, Academic Press, NY, pp: 565 – 581.
13. Sanner T and Pihl A (1969). Fundamental aspects of enzyme inactivation by ionizing radiation. In: Enzymological Aspects of Food Irradiation, Proceedings of a Panel on Enzymological Aspects of the Application of Ionizing Radiation to Food Preservation, IAEA, Vienna, pp: 23 – 36.
14. Sui R.G.H (1972). Action of ionizing radiation on enzymes. In: Radiation preservation of food. U.S Army Quartermaster corps, Ed., Bailey S.D, Davies J.M, Morgan B.H, Pomerantz R, Sui R.G.H, Teisher R.G, Washington DC, USGPO, pp: 169 – 176.
15. Spinks J.W.T and Woods R.J (1976). Water and aqueous solutions. In: An introduction to radiation chemistry, 2nd Ed., John Wiley Publiation, NY, pp: 247 – 359.
16. Redpath J.L (1981). Free radical reactions with simple biochemical systems. J. Chem. Ed., 58, 131 – 135.
17. Konev S.V (1957). Electronic excited states of proteins. In: Fluorescence and Phosphorescecne of proteins and nucleic acids. Translation Ed., Sidney Udenfriend, Plenum Press, NY, pp: 61 - 106.
18. Cowgill R.W (1966). Fluorescence and protein structure. Biochim. Biophys. Acta, 120, 196 – 211.
19. Maity H, Maiti N.C, Jarori G.M (2000). Time resolved fluorescence of tryptophans in yeast hexokinase P I: Effect of subunit dimerization and ligand binding. J. Photochem. Photobiol. B: Biology, 55, 20 – 26.
20. Bhattacharya D, Basu S, Mandal P.C (2000). UV radiation effects on flavocytochrome b_2 in dilute aqueous solution. J. Photochem. Photobiol. B: Biology, 59, 54 – 63.
21. Creed D (1984). The photophysics and photochemistry of the near UV absorbing amino acids - I.Tryptophan and its simple derivatives. Photochem. Photobiol., 39, 537 - 562

Acknowledgements

The authors express their sincere thanks to Dr (Ms) A.M.Samuel, Director Biomedical Group, Dr D.R. Bongirwar, Ex Head, Food Technology Division and Dr A. K. Sharma Head, Food Technology Division, BARC, for their encouragement and support.

This paper received the Best Poster Award in the field of Radiation Biology at the " Asian Photochemistry Conference 2002" held during January 6 – 11, 2002 at Juhu, Mumbai.

About the authors ...

***Ms Vahbiz Jamadar**, MSc gold medallist (Biochemistry) from University of Mumbai, is a PhD student in the Food Technology Division, BARC. She has been working in this Division since January 2000, on the project entitled, "Influence of ionizing radiations on lysosomal enzymes."*

***Mr Sahayog Jamdar,** MSc (Microbiology) from University of Mumbai, joined BARC in 1996 through BARC Training School (39th batch) and is working in the Flesh Food Biochemistry Section, Food Technology Division. He is currently pursuing Ph.D on the project entitled, "Structure function relationships of proteases and protein degradation."*

***Dr P. Harikumar** is presently the Head, Flesh Food Biochemistry section, Food Technology Division, BARC. He joined BARC in 1967 after graduating from the University of Kerala, obtained MSc and PhD degrees from the University of Mumbai. He has carried out Post doctoral research at Roche Institute of Molecular Biology, Nutley, New Jersey, USA (1982 – 1984) and at University of Medicine and Dentistry, New Jersey, USA (1998 – 1999) on "The role of lysosomal proton ATPase and Ca^{2+} in the regulation of intracellular protein catabolism." His major contribution is in understanding the structure-function relationships of lysosomal proteases and their role in regulating the quality attributes of irradiated flesh foods and in the preparation of value added products from poultry and fish processing wastes.*

***Dr Hari Mohan** joined RC & CD Division, BARC, after graduating from 10th batch of BARC Training School. His main area of research is the study of fast reactions using electron accelerator and lasers. He is a fellow of the National Academic of Science, India, and winner of BARCOA award in science. He has co-authored more than 150 journal publications. He is presently Head, Radiation Chemistry Section of RC & CD Division.*

***Dr (Ms) S.P. Dandekar** is the Head of Biochemistry Department at Seth G.S. Medical College and KEM Hospital. She is also in charge of the Central Clinical Laboratory and National Plasma Fractionation Centre. Her field of research has been the involvement of cellular factors including lysosomal enzymes in male reproductive disorders.*

Thermal Decomposition and Phase Evolution Behaviour of Precursors for YAG Prepared by Solution Combustion Technique

M.B. Kakade and S. Ramanathan
Materials Science Division
Bhabha Atomic Research Centre

and

B.B. Kalekar
Analytical Chemistry Division
Bhabha Atomic Research Centre

Abstract

Precursor powders for yttrium aluminum garnet (YAG) were synthesized by solution combustion reactions (nitrate – urea and nitrate – glycine reactions) and simple decomposition of nitrate solution. The TG – DTA studies of the precursors along with XRD analysis of typical heat-treated samples were carried out to understand the processes occurring at various stages during heating and optimize the calcination conditions to obtain phase pure YAG.

Precursors from all the reactions exhibited about 3 to 5 percent weight loss accompanied by an endotherm in the range of 30 to 300^{0}C, corresponding to dehydration of absorbed moisture and traces of hydroxide. There were no further weight loss and heat effects noticed for the precursor from nitrate – urea reaction (precursor –A), indicating its chemical composition as YAG. This precursor was found to be pure crystalline YAG by XRD. The formation of crystalline YAG was attributed to the higher temperature due to flame formation during combustion. The precursor from nitrate – glycine reaction (precursor –B) exhibited a loss of weight of 5 percent accompanied by an exotherm in the range of 400 to 600^{0}C and a loss of 12 percent accompanied by two shallow endotherms in the range of 900 to 1100^{0}C. The processes occurring at these stages were characterized as burning away of the black carbonaceous contaminant and decomposition of a glycine complex of aluminum and yttrium respectively. The XRD studies showed that the precursor was amorphous up to 890^{0}C and formed into a mixture of hexagonal YAP and cubic YAG phases at 930^{0}C. The YAP phase appeared to be an intermediate that finally transformed into YAG. The precursor from simple decomposition of nitrates (precursor –C) exhibited a loss of weight of about 10 percent in the range of 300 to 500^{0}C and the process was characterized as de-nitridation. Crystalline YAG formed directly from an amorphous oxide compound with no loss of weight but formation of two exotherms (one sharp and one shallow) in the temperature range of 850 to 1100^{0}C. No noticeable intermediate phase was detected.

Introduction

YTTRIUM ALUMINUM GARNET (YAG) powders possessing controlled characteristics find a wide variety of applications in making transparent laser components, advanced engineering material and composites, phosphors, refractory coating etc[1]. Formation of YAG by solid-state reaction requires temperature of the order of 1600^{0}C and long duration. There are various solution based methods reported (such as simple decomposition of nitrates, sol – gel process, homogeneous and heterogeneous precipitation and solution combustion) in which YAG phase forms at a much lower temperature due to mixing of the reactants in molecular scale in solutions.[2-11] The powders formed by

combustion technique can be phase pure crystalline YAG or nano-crystalline compound containing volatiles which need to be calcined to form into phase pure YAG.

In solution combustion technique, from a very concentrated solution of the metal nitrates (oxidizer) and urea or glycine (fuel) a very porous mass of the oxide compound is formed due to the evolution of a large amount of gases. The heat evolved during combustion makes the reaction self-sustaining to form the compound. The stoichiometric amount of urea or glycine required for combustion can be calculated using the reported combustion reactions[9, 12]

$$2\ M(NO_3)_3 + 5\ CO(NH_2)_2 \rightarrow M_2O_3 + 5\ CO_2 + 10\ H_2O + 8\ N_2 \quad (1)$$

$$3\ M(NO_3)_3 + 5\ NH_2CH_2COOH \rightarrow 3/2\ M_2O_3 + 7\ N_2 + 10\ CO_2 + 25/2\ H_2O \quad (2)$$

where 'M' is the aluminum and yttrium ions in 5:3 ratio. M_2O_3 can be represented as $(Y_{3/8}Al_{5/8})_2\ O_3$. For every mole of M_2O_3 formed 23 and 20 moles of gases are evolved for reaction 1 and 2 respectively.

The simple decomposition of the aqueous solution of nitrates of aluminum and yttrium can be represented as

$$2M\ (NO_3)_3 \rightarrow M_2O_3 + 6\ NO_2 + 3/2\ O_2 \quad (3)$$

This reaction is endothermic and the number of moles of gases evolved per mole of M_2O_3 formed is 7.5. Acidic nitrogen dioxide gas polluting the atmosphere is evolved in this reaction which is not present in combustion reactions.

However the exothermicity, fast reaction kinetics and evolution of large amount of gases make the combustion reaction violent and pose problems in scaling up of the process. One way of exercising control over the reaction kinetics is by way of using the fuel for which the heat of combustion is sufficient but not excessively too high (eg., reaction 2 is less exothermic than reaction 1).

A study of the thermal decomposition by thermal analysis (TG – DTA) and phase evolution by XRD of the precursors formed by these reactions is essential in optimizing calcination conditions for formation of phase pure YAG and brings out the advantages and limitations of each reaction. A comparative study of the above aspect has been carried out for the precursors formed by solution combustion reactions (nitrate – urea, nitrate – glycine reactions) and simple decomposition of nitrates.

Experimental

Aqueous stock solutions of aluminum nitrate (1.9 M) and yttrium nitrate (1.1 M) required for YAG composition (batch size ~40 grams) were mixed and concentrated to a viscous liquid (metal ion concentration ~ 10 M) by evaporation at 70^0C in an air oven for three batches. Urea (urea/nitrate ion molar ratio ~5/6) and glycine (glycine/nitrate ion molar ratio ~5/9) were dissolved in two batches of the concentrated liquid of nitrates in two pyrex beakers. The precursors were formed by heating the viscous solutions in the beakers gently on a laboratory assembled nicrome wire heater till the combustion reaction set in accompanied by the evolution of a large amount of gaseous product with heat (called precursor – A and B respectively). The third batch of the nitrate solution in the beaker was decomposed on the same heater till evolution of reddish fumes of nitrogen dioxide subsided (precursor–C). The as formed precursors –A, B and C were dry ground separately in the planetary mill (M/s. Fritsch) for half an hour to form into a homogeneous powder mass. The powders thus obtained were subjected to TG – DTA studies in Netzsch Thermal Analyser (Model STA 409) in air for volatile loss and heat effects (heating rate – 10^0C/min.). XRD studies were carried out for typical heat-treated precursors in a Philips X- ray diffractometer for phase formation. The average crystallite size was determined by the line broadening method (peak corresponding to 420 reflection) using the Scherrer formula.

Results and Discussion

Formation of precursors

The precursors were formed by conducting the combustion and decomposition reactions on a

heater in open, as the heat output of the heater could be easily controlled so that the reaction did not become excessively vigorous and the gases evolved could easily escape. In case of formation of precursor by solution combustion reaction using urea as fuel (precursor- A), as the temperature reached gradually about 200^{0}C, the viscous liquid foamed vigorously with the evolution of a larger amount of bubbles of gaseous product of fuel – oxidizer reaction (CO_2, N_2, H_2O). This was accompanied by the formation of a bright flame (maximum flame temperature recorded by using two color pyrometer was 1600^{0}C) and a porous sponge-like solid. Also in case of formation of precursor using glycine as fuel (precursor –B), as combustion set in above 200^{0}C, a large amount of gas was evolved but no flame formed. The reaction was smooth without any spilling. The combustion was slower and controlling the process for larger batch size was easier. In case of formation of precursor by simple decomposition of nitrates (precursor–C), the solution decomposed smoothly with the evolution of bubbles of reddish brown nitrogen dioxide gas (major acidic pollutant to the atmosphere) forming compact granules of aggregated powder. The precursors – A and C were white while precursor –B was black and contaminated with carbonaceous material. The black color was attributed to segregation of some amount of glycine and its charring due to the lower reaction temperature (~600^{0}C). This was confirmed by the formation of a black product in the initial stage of decomposition of the aqueous solution of pure glycine, which burned off above 600^{0}C. Concentrating the solution of aluminum nitrate and yttrium nitrate before adding urea was necessary to avoid loss of urea by the side reaction - hydrolysis of urea in water above 80^{0}C.

$CO(NH_2)_2 + H_2O \rightarrow CO_2 + 2\ NH_3$ (3)

Combustion set in only when the liquid reactant became viscous.

Characterization of precursors

TG-DTA and XRD studies : The TG – DTA pattern for the precursor -A is given in Fig.1.

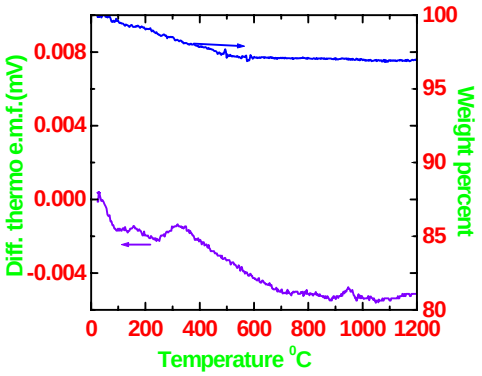

Fig.1 TG – DTA pattern for precursor -A

It exhibited a shallow broad endotherm accompanied by 3 percent loss in weight in the range of 25 to 300^{0}C. This could be attributed to the process of dehydration of absorbed moisture and traces of structural hydroxide in the powder. There were no heat or weight loss effects above 300^{0}C indicating the completion of YAG formation in this combustion reaction due to the higher temperature of the flame. The XRD studies showed that the as formed precursor was well-crystallized YAG phase with an average crystallite size of about 280Å (Fig.2).

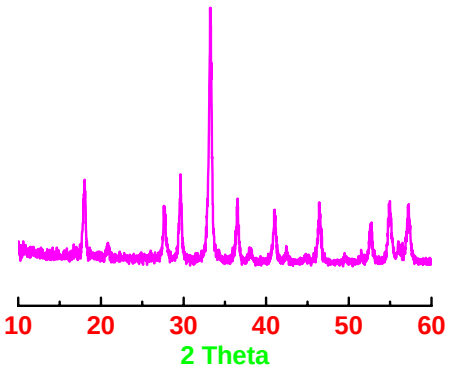

Fig.2 XRD pattern for the as formed precursor -A

The TG-DTA pattern of the precursor –B is shown in Fig.3. It exhibited a broad endotherm accompanied by a loss of weight of 5 percent in the temperature range of 25 to 300^{0}C, attributed

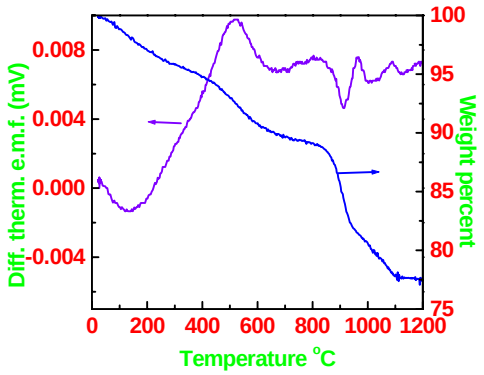

Fig.3 TG – DTA pattern for precursor –B

to the dehydration of absorbed moisture and traces of structural hydroxide in the powder. It showed a broad exotherm accompanied by a loss of weight of 5 percent in the temperature range of 400 to 600^0 C which could be attributed to the burning of the carbonaceous material (free carbon). This was confirmed by the burning off of the black product formed in the initial stages of decomposition of pure glycine in this temperature range. There were two shallow endotherms in the temperature range of 900 to 950 and 1000 to 1050^{0}C accompanied by a total weight losses about 12 percent. The EGA analysis data showed that the gas evolved corresponding to these endotherms to be carbon dioxide. The flat TG curve above 1100^{0}C indicated completion of all volatile losses at this temperature.

The XRD patterns of the as formed precursor and that heated to different temperatures decided from TG – DTA studies are shown in Fig.4. The as formed precursor and that heated to 890^{0}C were amorphous, that heated to 930^{0}C was a mixture of hexagonal YAP and cubic YAG and that heated to 1050^{0}C was pure cubic YAG. Based on XRD studies on isothermal heat treated samples prepared by nitrate – glycine reaction, Hess etal. reported that an intermediate YAP phase formed which subsequently transformed into the stable YAG phase.[8] This is in agreement with the present observation. The total-carbon analysis data by vacuum fusion technique of the precursor was 8 weight percent which was attributed to both the carbonaceous material existing below 600^{0}C and the carbon dioxide evolved in the range of 900 to 1100^{0}C. The important finding of this study is that the amorphous precursor formed by combustion is not chemically pure YAG compound and it releases substantial amount of volatiles not only in the initial stages but also during crystallization, an aspect which has not yet been reported. The loss in weight (carbon dioxide) at the crystallization stage shows that the precursor heated to 890^{0}C is a glycine complex of aluminum and yttrium.

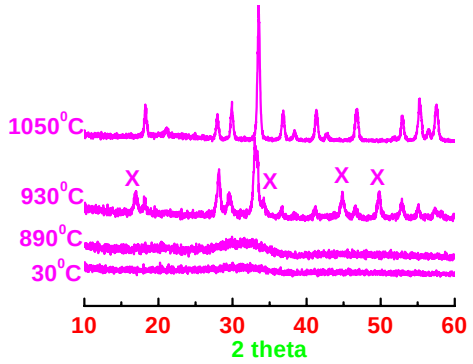

Fig.4 XRD patterns for the precursor –B heated to various temperatures

The formation of hexagonal YAP as an intermediate showed the closeness of its structure to that of the amorphous glycine complex. The kinetically favored YAP phase formed that finally transformed into the thermodynamically stable cubic YAG. The ease of formation of YAG phase from the YAP phase showed that the chemical composition of the YAP phase was $Y_3Al_5O_{12}$ (i.e., it is a solid solution of Al_2O_3 in $AlYO_3$) and not a mixture of Al_2O_3 and $AlYO_3$.

The TG-DTA pattern of the precursor –C formed by the simple decomposition of nitrates is shown in Fig.5. It exhibited an endotherm in the range of 25 to 300^{0}C accompanied by a weight loss of

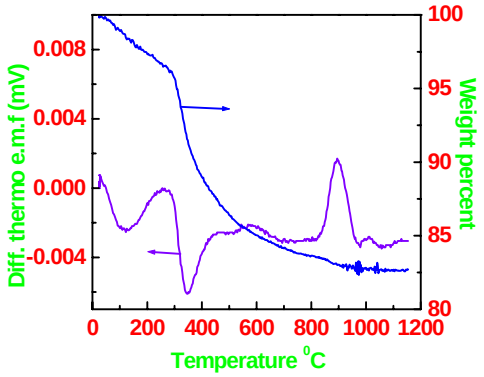

Fig.5 TG – DTA pattern for the precursor -C

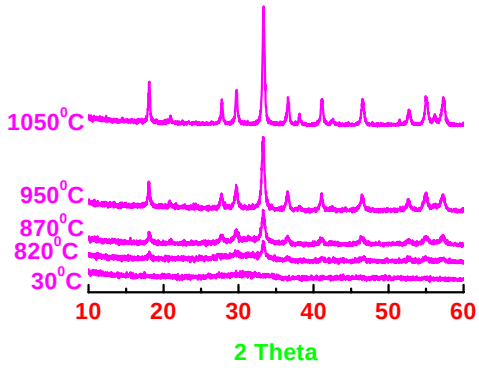

Fig.6 XRD pattern of the precursor –C heated to various temperatures

3 percent, attributed to the loss of absorbed moisture and traces of structural hydroxide in the powder. Another endotherm occurred in the range of 300 to 500^{0}C accompanied by a weight loss of about 10 percent, which could be attributed to the decomposition of left over nitrate in the precursor. There was a gradual loss of weight of about 3 percent in the temperature range of 500 to 800^{0}C with no detectable heat effect. There were two exotherms in the temperature range of 870 to 950^{0}C (sharp) and 950 to 1050^{0}C (very shallow) accompanied by very little loss in weight at these stages. This indicated the chemical composition of the precursor before and after the exotherms was the same i.e., YAG.

The XRD patterns for the precursor and that heated to different temperatures are shown in Fig 6. The as formed precursor and that heated to 820^{0}C were amorphous. Crystallization to pure YAG set in around 870^{0}C and progressed upon further heating. The average crystallite size values for the precursor heated to 870 and 950^{0}C were exactly the same (~280Å) while that for the precursor heated to 1050^{0}C is 350Å. This observation showed that in the temperature range of 870 to 950^{0}C only the progress of crystallization from amorphous precursor took place while further growth of crystallites occurred in the range of 950 to 1050^{0}C. As the crystallite size increased in the range of 950 to 1050^{0}C, the shallow exotherm around 1000^{0}C could be attributed to further growth of crystallites. Thus well-crystallized YAG formed from precursor – C above 1050^{0}C. The point to be noted was crystalline YAG formed directly from amorphous oxide compound of the same chemical composition without any detectable intermediate phase.

The crystallization of pure YAG phase in all these precursors at a temperature around 1100^{0}C established the presence of compositional homogeneity of metal atoms in all the precursor intermediates.

Conclusions

Chemically pure crystalline YAG formed in nitrate – urea reaction. However the reaction is too vigorous with flame formation. The preparation of precursor of YAG powder by nitrate – glycine reaction is a versatile one for scaling up. The reaction yields amorphous precursor that upon subsequent heat treatment exhibits volatile loss in stages due to dehydration, carbon burning, and crystallization. Loss of volatiles during crystallization is an interesting observation in this study which has not been reported so far. The formation of YAG phase from the amorphous precursor takes place via the formation of an intermediate YAP-like structure. These powders are the softest agglomerates

that could be easily ground. Simple decomposition of nitrates yields amorphous precursor. Upon further heat treatment, it evolves volatiles in stages due to dehydration and de-nitridation. Crystalline YAG phase forms directly from the amorphous oxide compound without any loss of volatile.

It can be said that the combustion synthesized powder from nitrate – glycine reaction needs to be calcined just like the one formed by simple decomposition of nitrates. But the powder agglomerates formed by this reaction (nitrate – glycine reaction) is expected to be the softest due to the evolution of large amount of gases and just required amount of heat. The nitrate – urea combustion reaction results directly in the formation of YAG but difficult for scaling up due to flame formation. The study of thermal decomposition and phase evolution for all these precursors established the calcination condition to form chemically pure and crystalline YAG phase.

Acknowledgements

The authors thank Mr. B. R. Ambekar of Applied Chemistry Division and Mr. E. K. Unnikrishnan of Analytical Chemistry Division for their help in carrying out the XRD and carbon analysis studies respectively. The authors acknowledge the help of Dr. P.V. Ravindran in the interpretation of the TG-DTA data. Also they thank Dr. P.K. De, Head Materials Science Division and Dr. S. Banerjee, Director Materials Group for their keen interest in this work.

References

1. M. Nyman, J. Carusa, and M.J.H.Smith, J. Am. Ceram. Soc., 80, 5 (1997) 1231.
2. D. R. Messier and G.E. Gazza, Amer. Ceram. Soc. Bull., 51,9 (1970) 697.
3. Yin Liu. Zhi-Fan Zhang, Bruce King, John Halloran, and Richard M. Laine, J. Am. Ceram. Soc.,79, 2 (1996) 385.
4. K.R. Han, H.J. Koo and C.S. Lim, J. Am. Ceram. Soc. , 82, 6 (1999) 1598
5. Quingmei Lu, Wensheng Dong, Haojing Wang and Xinkui Wang, J. Am. Ceram. Soc., 85,2 (2002) 490
6. S. Ramanathan, S.K. Roy and P.V. Ravindran, Trans. Ind. Ceram. Soc., 59, 1(2000) 12.
7. Naoya Matsushita, Noriyoshi Tsuchiya, and Katsuto Nakatsuka, Takakimi Yanagitani, J. Am. Ceram. Soc., 82,8 (1999) 81.
8. Hes, G.D. Maupin, L.A.Chick, D.S. Sunberg, D.E. Mc Creedy and Armstrong, J. Mater. Sci.. 29 (1994) 1873.
9. Lauren.E. Shea, Joanna Mc Kittrick, Olivia A. Lopez, J. Am. Ceram. Soc. 79 (1996) 3257.
10. M.B. Kakade, S.Ramanathan and S.K.Roy, J. Mater. Sci. Letts. ,21,12 (2002) 927.
11. M.B. Kakade, S.Ramanathan and P.V. Ravindran, Accepted in J. Alloys and Compounds, 350 (2003) 123.
12. L.R. Pederson, G.D. Maupin, W.J. Weber, D.J. McReady and R.W. Stephens Materials Letters, 10, 9-10 (1991) 437.

This paper was awarded the Second Prize at the 13th National Symposium on Thermal Analysis, held at BARC, Mumbai, during January 21-23, 2002

About the authors ...

Mr M.B. Kakade *joined BARC in 1984 after doing M. Sc. from Karnataka University, Dharwar. He has worked on ceramic material processing which includes sintering of magnesia, alumina, spinel, sillimanite grog and zircon wares. At present, he is working on synthesis and characterisation of zinc chromate, yttrium aluminum garnet and lanthanum strontium manganite powders by solution combustion technique for various applications.*

Dr S. Ramanathan *joined BARC in 1976 through 19th batch of Training School and works on processing of advanced ceramic materials. He worked on the development of thoria –yttria solid oxide electrolyte for oxygen sensor applications and obtained Ph D in Materials Science from IIT Mumbai. He worked on synthesis of controlled morphology sub-micron sized oxide powders by homogeneous precipitation technique and impervious oxidation resistant and porous catalytic coatings by sol – gel technique. Presently, he is working on the formation of ceramic shapes by liquid based fabrication techniques (slip and tape casting). He has about forty-five publications in Indian and International journals.*

Mr Bhupesh B Kalekar *graduated from University of Pune and joined Analytical Chemistry Division of BARC in 1998 after completion of one year training course in Analytical Chemistry. He works on thermal analysis to study the decomposition mechanism and kinetics of solid-state reactions.*

Biosorption of Americium using Various Biomasses of *Rhizopus* Species

P. S. Dhami, R. Kannan, P.W. Naik, S. K. Das, V.Gopalakrishnan and A. Ramanujam
Process Development Division
Bhabha Atomic Research Centre

and

N. A. Salvi and S. Chattopadhyay
Bio-Organic Division,
Bhabha Atomic Research Centre

BIOSORPTION OF HEAVY METALS USING microbial cells has been recognized as a potential alternative for the removal of heavy metals from industrial waste streams including radioactive wastes[1,2a,b]. The microbial uptake of metals have been attributed to their accumulation by the cell walls or intracellular components[3]. The metal uptake by microorganisms is a rapid and reversible process and is not mediated by metabolic processes. Hence, there is no difference in the metal uptakes by nonviable biomass and the living microorganisms. Various microbial biomasses are proven to be good biological sorbents for heavy metals[4]. Amongst these, the biomass from *Rhizopus arrhizus* has been extensively used for sorption of salts and complexes of different metals such as iron, nickel, copper *etc.*, present individually or in multi-component systems[5-7a,b]. Earlier, the efficacy of the *Rhizopus arrhizus* (wild type) biomass in adsorption of various radionuclides from aqueous nitrate medium[8a,b] was shown from this laboratory. It was also found that the biomass can selectively adsorb the actinides with high efficiency from low acid effluents. Consequently, with the objective of developing a bioremediation process for nuclear waste management, the present investigation was carried out. To this end, different biomasses obtained from various *Rhizopus* species were evaluated for their americium sorptive capacities as biosorption of metals is known to depend on the culture conditions and the nature of biomass. Subsequently the study was extended to column experiments with low level waste stream of PUREX process using the best biomass preparation and the results of the investigation are presented in the following.

Reprocessing of spent nuclear fuel bundles is very important for regenerating and reusing the unused nuclear fuels in nuclear plants. This is generally carried out by the plutonium uranium reduction extraction (PUREX) process which involves several steps such as decladding of the fuel rod, dissolution of the fuel materials in ~12 M HNO_3 and selective removal of most of the unused nuclear materials like Pu and U from the acidic phase by solvent extraction using tributyl phosphate as the extractant[9]. The last step results in the generation of a huge volume of aqueous raffinate which is concentrated using a number of inter cycle evaporators before further processing/ treatment. The evaporation steps result in the accumulation of condensed vapours from the evaporators as condensed liquid (condensate) which has low acidity (~0.15 M HNO_3) and often contains low levels of radioactivity. However, the low level of waste (LLW) effluent may contain trace amount of long-lived α-emitting actinides which are highly toxic. This warrants

decontamination of the LLW effluents for their safe discharge[10]. Given that *R. arrhizus* biomass can efficiently adsorp various radionuclides from low acidic solution[8a,b], the material appeared promising for remediation of the LLW condensates. For this purpose, the study was conducted employing both batch and column experiments.

Batch Studies

Our earlier uptake studies[8a,b] with *R. arrhizus* (wild type) biomass showed the highest sorption for ^{241}Am at pH 2.0 with an equilibration period of 3 h. Hence, for the present study, the same pH and equilibration period were chosen. The sorption studies for americium were carried out using seven biomasses obtained from different *Rhizopus* species along with that of *R. arrhizus* (wild type). The experiments were carried out in quadruplet and the results of the batch studies presented in Figure 1. The weight distribution ratios (D) were calculated using the following formula[8b].

$$D = [(A_i - A_f)/A_f] \times V/M$$

where, A_i and A_f are the activities of the tracers in initial and final solutions respectively, V is the volume of the solution in ml and M is the weight of the sorbent in g.

It was observed that at pH 2.0, the biomass from the strain *R. arrhizus* NCIM 997 had an impressive and appreciable distribution ratio for ^{241}Am (D_{Am} ~14900) compared to those obtained from the other *Rhizopus* strains. Therefore, all subsequent studies were carried out with *R. arrhizus* NCIM 997 biomass only.

Earlier, the lyophilized cells of *S. longwoodensis* were reported[11] to possess an exceptionally high capacity for uranyl ions. Hence, the sorption experiments were also carried out with the biomasses of *R. arrhizus* NCIM 997, obtained separately by lyophilization and oven drying and the studies were conducted at three different pHs *viz*. 2.0, 4.0 and 6.0. The results (Figure 2) revealed that irrespective of the mode of biomass preparation, the D_{Am}-value decreased gradually with the increase in pH.

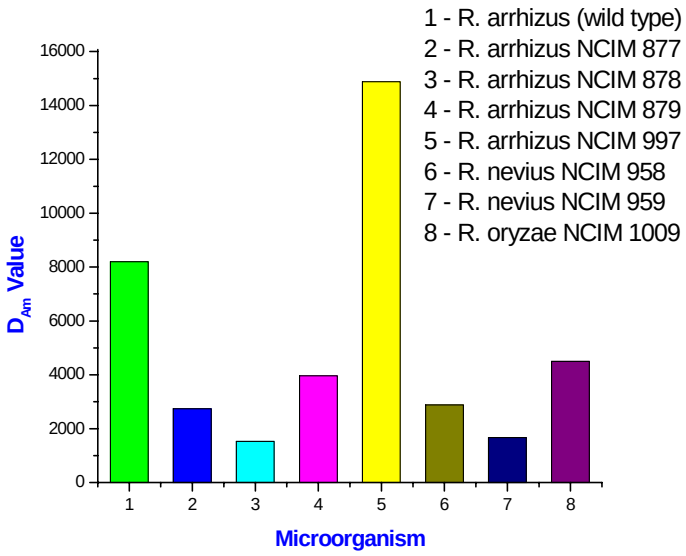

Fig. 1 : feed = 5560 Bq ^{241}Am α/ml in HNO_3 medium, pH = 2.0, volume = 2 ml, contact time = 3 h, wt. of biomass (mesh size 30-50) = 30 mg. The D_{Am}-values are mean ± s. e. (n = 4).

Although the sorptive capacities of the two biomass preparations were not significantly different at pH 2.0, the lyophilized preparation was marginally better than the oven-dried biomass at higher pHs. However, in spite of better performance, the lyophilized biomass was unsuitable for column operation due to its physical nature. The lyophilized material was very soft and the amount of the biomass of the required size (30-50 mesh size) obtained by its grinding was considerably less as compared to that obtained from the oven-dried material. Moreover, the material was found to undergo fast degradation under the acidic condition as is discussed

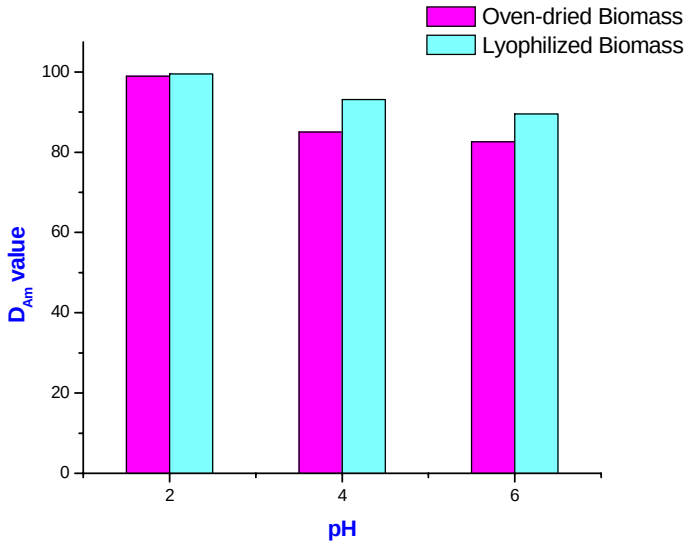

Fig. 2: feed = Aqueous low level waste spiked with 6550 Bq ^{241}Am α/ml, pH = 2.0, weight of biomass (mesh size 30 – 50) = 10 g. The reported eluate activity is the mean of those obtained in duplicate experiments.

in the next section. Therefore, further sorption studies were carried out using the oven dried biomass of *R. arrhizus* NCIM 997 only.

Column Studies

The feasibility of using the dry biomass of *R. arrhizus* NCIM 997 in packed column for decontamination of americium in LLW waste stream depends on its sorptive capacity for the metal under dynamic conditions. Hence, the americium uptake capacity of the biomass was initially studied by small column experiments using 10 g of the dry biomass. It was found that after passing 1 L of the feed waste solution, the column flow rate became 55 ml/ h from the initial value of 100 ml/ h. The column experiment was continued after readjusting the flow rate to the initial value (100 ml/ h). The flow rate reduced again by 45% after passing an additional litre of the waste solution. However, the column operation was continued in the same manner till a total of 4 L of the waste solution has been passed through the column.

The %BTs were calculated from the α-activities of the effluent fractions and are presented in Table 1. All experiments were carried out in duplicate and the precision was found to be within $\pm$5%. As reflected from the data, 1.8 L of the waste solution could be passed through the column without any breakthrough of alpha activity (mainly ^{241}Am). Based on the data, the loading capacity of the biomass was calculated to be 1.18 MBq Am α/ g of the dry biomass. Considering the specific activity of ^{241}Am (7.6 x 10^6 dpm/ μg), the loading capacity amounted to 9.926 μg or 0.039 μmole of ^{241}Am per g of the dry biomass which was the working capacity of biomass under the experimental conditions.

Table 1 : Effect of biomass drying on the Am sorption

PH	% Sorption of different *R. arrhizus* NCIM 997	
	Oven-dried	Lyophilized
2.0	98.9	99.5
4.0	85.0	93.1
6.0	82.6	89.5

Feed = 5676 Bq ^{241}Am α/ml in HNO_3,
pH = 2.0, volume = 2 ml, contact time 3 h
wt. of biomass (mesh size 30-50) 30 mg

Passage of another 0.1 L of the waste solution led to 2.4% BT, while 80% BT was reached after passing a total feed volume of 4.0 L. The column was subsequently washed with nitric acid (pH 2.0) till the activity of the effluent reached the background level. The sorbed actinide was recovered by eluting with 100 ml of 1M nitric acid when ~95 % of the activity

was eluted. The results are in tune with an earlier report where acidic leaching of thorium adsorped on *R. arrhizus* biomass has been reported[12].

Earlier, we have observed[8a] that the americium sorptive capacity of the *R. arrhizus* (wild type) biomass at pH 2.0 was adversely affected in the presence of other lanthanides and actinides as well as the nitrate ion (beyond 0.15 M). The sorptive capacity was nearly halved in presence of 10 ppm of Nd, used as a substitute for the trivalent actinides/ lanthanides. Given that the concentration of ^{241}Am in LLW condensate is at best 1-2 ppm and that of the nitrate ion is also within the designated limit, their presence would not affect the performance of the chosen biomass significantly.

As indicated earlier, the lyophilized preparation of the biomass was too soft for column study. However, in view of its marginally better sorptive capacity for americium, we attempted a column experiment using 1.0 g of the biomass and loading the column with an initial flow rate of 20 ml/ h. However, the feed was not eluted within 2-3 h by which the biomass turned pasty.

Laboratory Scale Experiment

In view of the above excellent result, the column experiment was scaled up using 100 g of the biomass. For this, the Purex condensate was spiked with ^{241}Am to give 1334 Bq/ ml of α-activity and pumped through a packed column of the dry biomass powder at a flow rate of 900 ml/ h (4 bed volume/ h). In this case also, the flow rate reduced drastically. However, the experiment was continued till 10 L of the waste solution was passed and no americium activity was detected in the eluted effluent. Beyond this, it was impractical to continue the elution as the flow rate reduced to ~ 60 ml/ h during the course of loading.

Subsequently, the loaded americium was eluted from the column using 1M nitric acid. The sorptive capacity of the biomass was so strong that no μ-activity was detected in the first 1.4 L of the eluent. At the same time, it was gratifying to note that >90% of the Am activity could be stripped within the subsequent 2.2 L of eluate. Thus, the stripping of the radioactivity from the biomass was also very easy and could be carried out within a small volume of the eluate. This would ensure generation of minimum secondary waste in the actual bioremediation process. However, during the experiment, long exposure of the biomass to acidic solution changed its texture to a homogeneous pasty mass which affected the elution rate significantly. Such a damage to the cellular structure of the biomass is undesirable for its continuous and multiple use.

For studying the reusability of the biomass for decontamination of LLW, the biomass obtained from the laboratory scale experiment was used and its D_{Am} at pH 2.0 was determined in triplicate. The D_{Am} value dropped drastically to 40.11 ± 0.80 from an initial value of 14900. Thus, the biomass can be used in once through basis only.

In conclusion, the whole cells of *R. arrhizus* NCIM 997 provided an excellent and inexpensive bio-material for sorption of americium from the low nitric acid medium as well as from low level waste streams generated in PUREX process. The recovery of the loaded americium activity from the biomass was also excellent (~95%) and could be carried out without generating a large volume of secondary waste using 1M nitric acid solution as the eluent. However, the acid-mediated damage to its cellular structure is undesirable for continuous and multiple use of the biomass. The work on further refinement and improvement of bio-material for technical application is in progress and will be reported latter.

Acknowledgement

The authors thank Mr. M. A. Gawde for his technical assistance.

References

1. Norris, P. R.; Kelly, D. P. (1979) Accumulation of metals by bacteria and yeasts. *Dev. Ind. Microbiol*. **20**: 299-308.
2. a) Shumate II, S. E.; Hancher, C. W.; Strandberg, G. W.; Scott, C. D. (1978) Biological processes for environmental control of effluent streams in the nuclear fuel cycle. In Post, R. G.; Wacks, M. E. eds. *Proc. Od Waste Management Fuel Cycles '78*, Tucson: Univ. of Arizona Press, pp. 347-355. b) Shumate II, S. E.; Strandberg, G, W.; Parrott Jr., J. R. (1978) Biological removal of metal ions from aqueous process streams. *Biotechnol. Bioeng. Symp*. **8**,13-20.
3. Galun, M.; Keller, P.; Maiki, D.; Feldsteinm H.; Galun, E.; Siegel, S. M.; Siegel, B. Z. (1979) Removal of uranium (VI) from solution by fungal biomass and fungal wall-related biopolymers. *Science* **219**, 285-286.
4. Gadd, G. M. (2000) Bioremedial potential of microbial mechanisms of metal mobilization and immobilization. *Current Opinion in Biotechnology* **11**, 271-279.
5. Aksu, Z.; Çalik, A,; Dursun, A.Y.; Demircan, Z. (1999) Biosorption of iron(III)-cyanide complex anions to *Rhizopus arrhizus*: Application of adsorption isotherms. *Process Biochem*. **34**, 483-491.
6. Sag, Y.; Atacoglu, I.; Kutsal, T. (1999) Simultaneous biosorption; chromium(VI); copper(II); on *Rhizopus arrhizus* in packed column; the competitive Freundlich model. *Separation Science & Technol*. **34**, 3155-3171.
7. a) Yesim, S.; Arda, Y.; Tülin, K. (2000) Mono and multicomponent biosorption of heavy metal ions by *Rhizopus arrhizus*. *Process Biochem*. **35**, 787-799. b) Yesim, S.; Arzu, K.; Tülin, K. (2000) Biosorption of lead(II), nickel(II) and copper(II) on *Rhizopus arrhizus* from binary and ternary metal mixtures. *Separation Science & Technol*. **35**, 2601-2617.
8. a) Dhami, P. S.; Gopalakrishnan, V.; Kannan, R.; Ramanujam, A.; Salvi, N. A.; Udupa, S. R. (1998) Biosorption of radionuclides by *Rhizopus arrhizus*. *Biotechnol. Letters* **20**, 225-228. b) Dhami, P. S.; Kannan, R.; Gopalakrishnan, V.; Ramanujam, A.; Salvi, N. A.; Udupa, S. R. (1998) Sorption of plutonium, americium and fission products from reprocessing effluents using *Rhizopus arrhizus*. *Biotechnology Letters* **20**, 869-872.
9. Schulz, W. W.; Burger, L. L.; Navratil, J. D.; Bender, K. P. eds. (1990) Application of tributyl phosphate in nuclear fuel processing. *Science and Technology of Tributyl Phosphate*, Vol. III. Boca Raton, Florida: CRC Press Inc., pp. 55-79.
10. Yong, P.; Macaskie, L. E. (1997) Removal of lanthanum, uranium and thorium from the citrate complexes by immobilized cells of *Citrobacter* sp. in a flow through reactor: implications for the decontamination of solutions containing plutonium. *Biotechnol. Letters* **19**, 251-255.
11. Frils, N.; Myers-Keith, P. (1986) Biosorption of uranium and lead by *Streptomyces longwoodensis*. *Biotechnol. Bioeng.* **28**, 21-28.
12. White, C.; Gadd, G. M. (1990) Biosorption of radionuclides by fungal biomass. *J Chem Technol Biotechnol*. **49**, 331-343.

This paper was adjudged as the Best Paper and was awarded the M.J. Thirumalachar prize from the Mycological Society of India at the 28th Annual Meeting and National Conference on Fungal Biotechnology and Biodiversity, held at Mumbai in February 2002.

About the authors...

Dr P. S. Dhami *(Ph.D, Chemistry, University of Mumbai, 1990) joined BARC in 1982. His areas of interest are process and analytical development studies of relevance to the Purex process, development of radiochemical separation processes based on solvent extraction, ion exchange, extraction chromatography and biosorption. He is currently working in the area of partitioning of actinides and recovery of fission products of importance from Purex HLW.*

Dr R. Kannan *joined the Fuel Reprocessing Division of BARC in 1983, after graduation in Chemistry from Madurai-Kamraj University. He obtained Ph.D. degree in Chemistry in 2000 from the University of Mumbai. Major fields of his research are solvent extraction, extraction chromatography, membrane separation and biosorption technique for the recovery and removal of radionuclides from radioactive waste streams. Presently, he is associated with the process control analytical operations at the Trombay Plutonium Plant.*

Mr P. W. Naik *(M.Sc, Chemistry, University of Mumbai,2001) joined BARC in 1991. His areas of interest are process and analytical development studies related to the Purex process, solvent extraction and extraction chromatography. He is currently working in the area of Biosorption of radionuclides from low level effluents.*

Dr S. K. Das *joined Fuel Reprocessing Division , BARC, in 1982. He obtained his Ph.D degree in Chemistry from the University of Mumbai in 1994. He specialises in the development of ultratrace determination of heavy metals and radionuclides using electro-analytical, radio-analytical and laser-induced fluorimetric methods. Besides, he is also associated with Bio-remediation of low level radioactive waste solutions.*

Dr V. Gopalakrishnan *(Ph.D., Chemistry, University of Mumbai, 2002) joined BARC in 1964. His field of specilization include Purex process chemistry studies, Purex and Thorex flow sheet development and automation in analytical applications. Presently, he has been involved in studies dealing with the partitioning of actinides from HLW by solvent extraction and extraction chromatography and biosorption .*

Dr A. Ramanujam *joined BARC in 1963 after his post graduation in Chemistry from the University of Mumbai and has been associated with the Trombay plutonium plant since its inception. In 1970, he specialised in reprocessing of high burn up fuels at CEA, France. He obtained Ph.D (1980) in the field of solvent extraction and process chemistry of actinides. He was responsible for management of ^{233}U fuel in Purnima-II reactor. His R & D interests include Purex and Thorex process development, partitioning and recovery of minor actinides and important fission products under P&T programme. He was the chief investigator for an IAEA-BARC CRP on P&T. Currently, he is Head, Fuel Reprocessing Division, BARC.*

Dr Neeta A. Salvi *joined the Bio-Organic Division , BARC, in 1982. She obtained her Ph. D degree in Chemistry from the University of Mumbai in 1991 for her work on microbial transformation. She specialises in microrganism-based asymmetric transformations of organic compounds of pharmaceutical and agricultural importances. Besides, she is also associated with the development of bio-remediation of low level radioactive waste solutions.*

Dr S. Chattopadhyay *joined the Bio-Organic Division, BARC, in 1981 after graduating from the BARC Training School in 1980. Currently, he is designated as the Head of the Division. He obtained Ph. D (1989) in the field of synthesis of chiral and achiral insect pheromones. He has been responsible for the development of pheromone technology as an eco-friendly pest management protocol. He has also contributed greatly in the development of new solvents for radioactive metal extraction. He has also formulated a novel bioremediation method for the management of low-level radioactive waste. His other research interests include biocatalysis, asymmetric synthesis, chemical biology of antioxidants and natural radioprotectants.*

Expression of Hepatitis B Surface Antigen in Transgenic Banana Plants and NT- I Cell Line of Tobacco

G.B. Sunil Kumar, T.R. Ganapathi and V.A. Bapat
Nuclear Agriculture and Biotechnology Division
Bhabha Atomic Research Centre

and

C.J. Revathi and K.S.N. Prasad
Shantha Biotechnics Pvt. Ltd., Medchal, Hyderabad 501 401.

Abstract

Hepatitis B is one of the alarming diseases globally. There are about 350 million chronic carriers in the world and it is estimated that 75-100 million of them will die of liver cirrhosis and/or hepatocellular carcinoma. Treatment is expensive and cure rates are not impressive. The advent of recombinant DNA technology resulted in the development of rDNA vaccine using yeast as an expression system. The expense of this vaccine prevented its inclusion in mass immunization programmes, especially in the developing countries. Plant based production of vaccines, preferably in edible parts like fruits, may enable the development of cost effective and more acceptable delicious vaccines. In order to develop edible vaccine for Hepatitis B, researchers world wide, have endeavored to express the surface antigen (HBsAg) of this virus in plants and they could successfully demonstrate the proper folding and immunogenicty of plant derived HBsAg. In our laboratory, Hepatitis B virus 's' gene coding for surface antigen was cloned into plant expression vectors, with and without endoplasmic reticulum retention signal. Transformed NT-I cell lines of tobacco and banana plants were obtained and analyzed for the integration of the transgene by PCR and expression levels were assayed by ELISA. Western blot analysis confirmed the presence of 24 kDa band specific to HBsAg in the transformed tobacco cells. HBsAg was expressed both as intracellular and secreted forms in transformed NT-I cells. This is the first report on the secretion of HBsAg particles by plant cells into the cell culture medium and expression in banana plants.

Introduction

CURRENTLY MOST OF THE VACCINES ARE being administered using needle or syringe subcutaneously or intramuscularly. Only a few like, polio, typhoid and cholera vaccines are given orally. Future generation of vaccines should focus more heavily on mucosal immunization. Vaccines expressed in edible plant parts are known as edible vaccines. Edible vaccines offer many advantages: they can activate the mucosal immune system against many pathogens by oral delivery. The use of injections can be avoided, therefore improving patient compliance, reduces the risk of transmission of infection through contaminated needles and administration costs. They contain antigens rather than whole pathogens, thus

eliminating the risk of causing the disease, the vaccine is intended. They may not require cold storage, therefore increasing the shelf life. Can be produced cost effectively and in large quantities in agriculture based farming. Since plants do not contain human pathogens and plant viruses are not shown to infect humans, plant system serves as an ideal alternative to the existing microbial/animal cell cultures in terms of safety. Beyond these pragmatic advantages is the desirability to exploit the mucosal immune system. Mimicry of the natural route of infection (oral, respiratory and genital) assures the exposure of large surface areas to vaccines, the development of a first line defence mediated by secretory immunoglobulin A, recruitment of a humoral antibody response via lymphocyte trafficking from mucosal lymphoid tissues and involvement of glandular epithelium linked to the mucosal system.

Viral hepatitis is the most lethal and wide spread infectious disease and Hepatitis B virus (HBV) is the single most cause of persistent viraemia in humans. It is estimated that there are about 350 million chronic carriers of HBV, constituting 5% of the total World population and 20 million new infections occur annually (Ginsberg et al., 1993; Joshi and Kumar, 2001). HBV infection result in hepatocellular carcinoma (Tiollais et al., 1981) and about one million new cases of hepatoma results in 3,50,000 deaths annually (Ginsberg et al., 1993). The treatment is expensive and cure rates are not impressive. Currently available recombinant vaccine is produced in yeast, but the expense of yeast derived vaccine prohibits its use in mass immunization programs of developing countries. Plant based production of vaccines, especially in the edible plant parts like banana fruits may offer as an alternative in developing cost effective vaccines for the developing countries. Expression of vaccines in plants gives a heat stable environment and eliminates injection related hazards (Walmsley and Arntzen, 2000). Oral vaccine is one of the economically feasible approaches for mass immunization on a global scale as their production and administration costs are low (Streatfield et al., 2001). It is estimated that approximately 20,000 tonnes of bananas are needed to vaccinate all the world's children which is only a fraction of the total world production and one banana can potentially contain ten doses of vaccine (Arntzen, 1997).

HBsAg has already been expressed in tobacco (Mason et al., 1992), lettuce and lupin (Kapusta et al., 1999) and potato (Richter et al., 2000). The HBsAg derived from transgenic tobacco plants is physically, biochemically and immunologically similar to yeast derived rHBsAg (Mason et al., 1992, Thanavala et al., 1995). Recently Kong et al., (2001) reported successful oral immunization of mice with HBsAg expressed in transgenic potato. Kapusta et al., (1999) demonstrated specific serum-IgG response in human volunteers fed with transgenic lettuce plants expressing HBsAg. These results indicate successful steps towards developing cost effective plant based edible vaccines. There have been no reports on the expression and secretion of large particles (22nm) of HBsAg in plant cell cultures/ expression in banana plants. Plant cells provide a cheaper alternative to other cell types because their only media requirements are nutrients, salts, vitamins and growth regulators (Bodeutsch et al., 2001). In this report, expression of HBsAg in NT-I cells of tobacco and transgenic banana plants has been discussed.

Materials and Methods

Establishment of NT-I cell cultures

NT-I cell lines were obtained from Boyce Thompson Institute for Plant Research Inc., Ithaca, New York, USA (kind gift from Dr. J.M. Van Eck). The callus was maintained on NT-I semi-solid medium composed of MS salts (Murashige and Skoog 1962), 230 mM of 2-(N-Morpholino) Ethanesulphonic acid , 132 mM of KH_2PO4, 55 mM Myo-Inositol , 3 μM Thiamine HCl, 10 μM 2,4-D, 87.7 mM sucrose. Medium pH was adjusted to 5.7 and gelled with 0.2 % Phytagel (Sigma). Cell cultures were initiated by

culturing ~200 mg of callus in 50 ml liquid medium of the same composition. The cell cultures were grown on a gyratory shaker at 80-100 rpm under dark and subcultured once in 10 days. For transformation, 4-6 days post sub cultured cells were used.

Establishment of banana embryogenic cell cultures

Embryogenic cell cultures of banana cv. Rasthali (AAB) were established from six month old shoot tip derived callus obtained by culturing shoot tip sections on MS medium supplemented with 2,4-D (10μM) and Zeatin (1μM) essentially as described previously (Ganapathi et al., 2001). About 100mg of callus was cultured in liquid M2 medium (Cote et al., 1996). Suspension cultures containing embryogenic cells were recovered after 3-4 months. The cells were sub-cultured every 10 days and actively growing ones were used for transformation.

Cloning of HBsAg 's' gene and sub-cloning into plant expression vector

The plant expression vectors used for the studies were based on pBI 121 with *ubq*3 promoter from *Arabidopsis* and pEFE GUS with ethylene forming enzyme promoter from banana (kindly provided by Dr. G.D. May, Boyce Thompson Institute) .

Four plasmid constructs, namely pEFE HER, pHER 100 by cloning HBsAg '*s*' gene with the ER retention signal coding sequences at the 3` end and pEFE HBs and pHBs 100 without ER retention signal were constructed.

The primers used were:

1. 5' TACTGGATCCACCATGGAGAACATCACA 3'.
2. 5' AATGTATACCCAGAGACAAAAGAA 3'.
   5' CGTCCTTCTCGGACATAATGTATACCCAGA 3'.
3. 5' TCTAGAGCTCTTACAGCTCGTCCTTCTC GGACAT 3'.
4. 5' TCTAGAGCTCTTAAATGTATACCCAGA GACAAAAGAA 3'.

Primer 1 was the forward primer with a *BamH*1 site and a Kozak sequence (Kozak, 1981) upstream of HBsAg ATG codon. Primers 2, 3 and 4 were overlapping primers used as reverse primers to incorporate ER retention signal and *Sac*I site at 3' of HBsAg. Primer 5 was the same as primer 2 except for a stop codon and *Sac*I site.

To construct pHER 100, HBsAg gene was amplified from HBV genomic DNA cloned into pBR 322 (obtained from ATCC), using primer 1 as the forward primer and primer 2, 3 and 4 as reverse primers respectively in three successive rounds of PCR with the product of one round as template for the successive round. This resulted in the generation of 5` *BamH*I – Kozak sequence - HBsAg – ER retention signal – *Sac*I 3' fragment. The fragment generated after the third round of PCR was ligated with *Sma*I digested pBluescript SK+ to get pBS HER and DNA sequencing was done to confirm the incorporation of ER retention signal at the 3` end of HBsAg '*s*' gene. pBS HER was restricted with *BamH*I and *Sac*I to release the 699 bp fragment of HER and this was cloned into pBI 121 based plant expression vector to produce pHER 100 and *BamH*I and *Sac*I restricted pEFE GUS to obtain pEFE HER To construct pHBs 100, HBsAg gene was amplified from HBV genomic DNA by PCR using primers 1 and 5. The resulting product, 5` *BamH*I – Kozak sequence - HBsAg – *Sac*I 3' was ligated with *Sma*I digested pBluescript SK+ to get pBS HBs. The 681 bp fragment obtained by *BamH*I and *Sac*I digestion of pBS HBs was cloned into pBI 121 based plant expression vector to produce pHBs 100 and *BamH*I and *Sac*I restricted pEFE GUS to obtain pEFE HBs .

All the PCR reactions were carried out in a 50 μl reaction mixture containing the primers (100 ng each), Pfu DNA Polymerase (MBI fermentas, USA) (1.0 unit), 200 μM of each dNTP, 1 X PCR reaction buffer and 100 ng of template. PCR conditions were: Initial denaturation for 3 minutes at 94°C followed by 30 cycles of amplification, each cycle consisting of the following steps: 94°C for 1 min., 55°C for 1 min.

and 72°C for 1 min, with final extension at 72°C for 10 minutes.

Agrobacterium mediated transformation

Agrobacterium tumefaciens strain EHA 105 (Hood et al., 1993) harboring pHBS 100 and pHER 100 were used for tobacco NT-I cells transformation. Actively growing cells (4-6 days post subculture, 0.5ml packed cell volume) were co-cultured for 30 minutes with Agrobacterium grown overnight in YENB medium (Yeast extract- 7.5 g l^{-1} and Nutrient broth - 8.0 g l^{-1}. Himedia, India) supplemented with 50μg ml^{-1} Kanamycin. After co-cultivation, cells were aspirated onto glass fiber filters and transferred to NT-I semisolid medium and maintained for three days under dark. After three days the filters along with the cells were transferred to medium containing Cefotaxime (400 mg l^{-1}) and Kanamycin (50 mg l^{-1}). The transformed cells were selected with Kanamycin 100 mg l^{-1} and the developed calli were transferred to liquid NT-I medium supplemented with Kanamycin (300 mg l^{-1}) for initiating cell suspension cultures.

4- 6 days post sub cultured banana embryogenic cells were co-cultivated with *Agrobacterium tumefaciens* strain EHA105 harboring pEFE HER/pHER 100/pEFE HBs or pHBs 100 . After co-cultivation the cells were transferred to M2 medium supplemented with Cefotaxime (400 mg l^{-1}) and after a period of three days the cells were transferred to regeneration medium (Ganapathi et al., 2001) with Cefotaxime (400 mg l^{-1}) and Geneticin (G418, Sigma) (5 mg l^{-1}) for embryo development. The germinating embryos were transferred to MS medium supplemented with NAA (5 μM) Cefotaxime (400 mg l^{-1}) and Geneticin (5 mg l^{-1}) for continued development of plantlets. The fully developed plantlets were hardened in the green house.

PCR analysis of transgenic NT-I cells/banana plants

Integration of the transgene was confirmed by PCR using genomic DNA isolated from transformed and control cells. DNA was isolated by CTAB method essentially as described (Stewart and Via, 1993). The following two primers were used to amplify 681 bp fragment of HBsAg *'s'* gene.

1. 5' TACTGGATCCACCATGGAGAACATCACA 3' and
2. 5' TCTAGAGCTCTTAAATGTATACCCAGAGACA AAAGAA 3'.

A 50 µl PCR reaction mix contained the primers (100 ng each), Taq DNA polymerase (1.0 unit), 200 µM of each dNTP, 1X PCR reaction buffer and 100 ng of genomic DNA as template. PCR conditions were 94°C initial melting for three minutes followed by 35 cycles of amplification, each cycle consisting of the following steps: 94 °C for 1 min., 55 °C for 1 min. and 72 °C for 1 min., with a final extension at 72 °C for 10 minutes.

SDS-PAGE and Western blot

Protein was extracted from callus tissue as described earlier (Mason et al., 1992). The total soluble protein from transformed and non-transformed cells was separated on a 12% SDS - PAGE (Laemmli, 1970) and silver stained. Total soluble proteins were extracted from 1 g of callus tissue with 1 ml of 1X sample buffer (50mM Tris-HCl pH 6.8, 10% glycerol, 2% SDS, 5% 2-Mercaptoethanol, 0.0025mM bromophenol blue and 100mM dithiothreitol) by boiling at 100°C for ten min. The resulting extract was concentrated to 100 µl by freeze drying in low mode in a speed vac. The soluble protein was re-extracted into 20mM phosphate buffer pH 7.4 using 100 kDa cut off centricon columns (Amicon) and 25 µl of 5x Sample buffer was added and incubated at 100°C for 5 min. 20 µl of the above sample was used for Western analysis. Yeast derived rHBsAg was used as a standard. Rabbit Anti HBsAg serum (1:1000 dilution) was used as a primary antibody and Anti Rabbit IgG HRP Conjugate (Sigma) as a secondary antibody (1:20,000 dilution). ECL kit of Amersham was used to visualize the specific bands. Western blot was carried out as described (Sambrook et al., 1989).

ELISA analysis

Total protein was extracted from non-transformed control and transgenic cell lines of tobacco/banana leaves as described (Mason et al., 1992). The pellet fractions obtained after Ultra centifugation step were assayed in triplicates for the levels of expression of HBsAg using Auszyme kit (Abbot), the positive control (human serum derived HBsAg) as a standard and negative control (Protein extracted from non-transformed cells). Spent medium from the HER 100, HBs 100 and control cultures were also assayed for secreted HBsAg with the same kit as mentioned above.

Results

Cloning of HBsAg 's' gene into plant expression vectors

In this study, HBsAg '*s*' gene was cloned into plant expression vector with a 'C' terminal microsomal retention signal (SKDEL) to generate pHER 100 and pEFE HER using three reverse primers with overlapping sequences at 3' end and three rounds of PCR (Fig.1). Sequence data confirmed the incorporation of 3' ER retention signal in pHER 100 (data not shown). pHBs 100 and pEFE HBs were constructed without a 'C' terminal microsomal retention signal (Fig. 1).

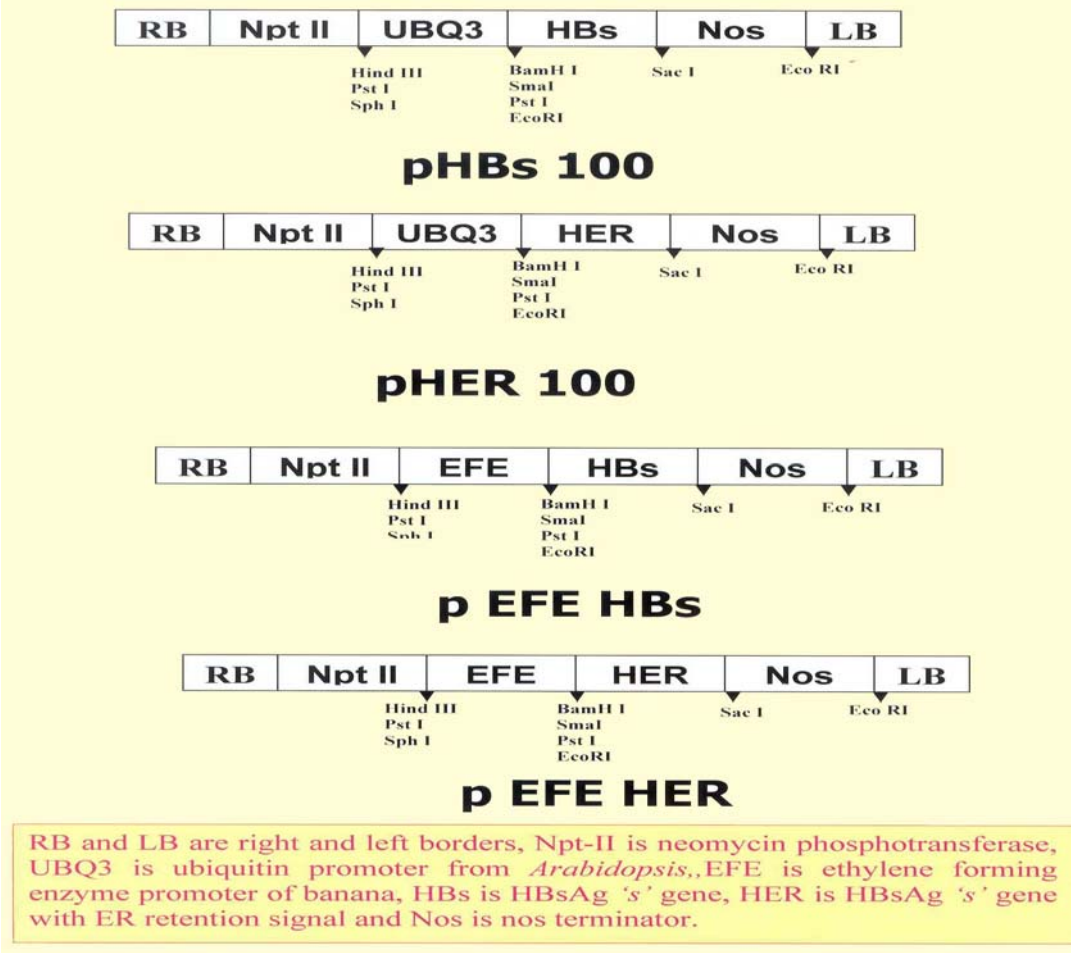

Fig. 1 T-DNA region of plant expression vectors

Development of transgenic tobacco cell lines

NT-I cells co-cultivated with *Agrobacterium* harboring pHBs100 or pHER100 constructs, developed into distinct colonies within three weeks of plating on the selection medium supplemented with 50 mg l^{-1} of kanamycin. Ten randomly selected colonies sub cultured on NT-I semisolid medium, grew luxuriantly and formed a callus mass in three weeks (Fig. 2A,B). Cell cultures were initiated from subcultured callus in liquid NT-I medium (Fig. 2C).

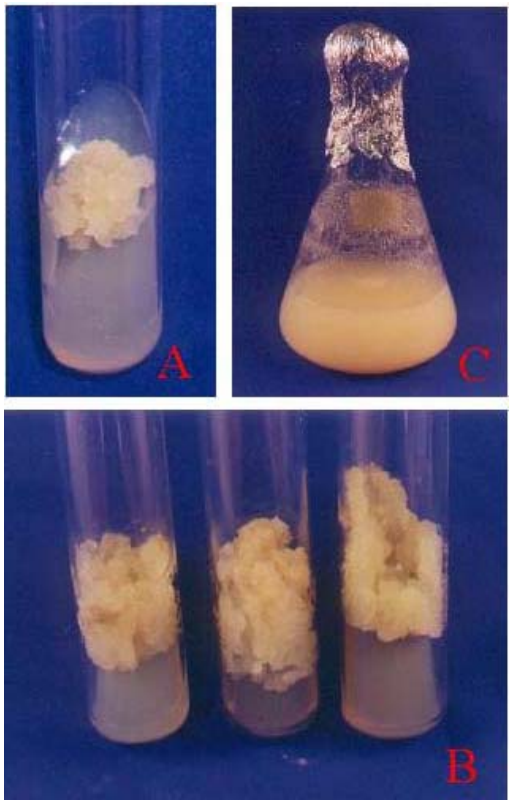

Fig.2 Transformed NT-1 cells of tobacco A: HBs100, B: HER 100, C: HER 100 cell suspension

Development of transgenic banana plants

The embryogenic cells were transformed with the above mentioned four constructs. The co-cultivated embryogenic cells multiplied and developed into globular embryos with in three weeks. Embryos were transferred to regeneration medium for the development of plantlets. Tiny plantlets were obtained in two to three months. These developed further in another 4-6 weeks and formed transplantable plantlets. For each construct around 50 transgenic plants were regenerated from initial 0.5 ml packed cell volume. The transgenic plants were hardened in the green house and used for molecular analysis (Fig.3). Two plants for each construct are being grown up to maturity in our green house to test the expression of HBsAg in fruits.

Fig.3 Transgenic banana plants

Molecular analysis of transgenic cell lines/banana plants

DNA from kanamycin resistant cell lines/banana plants was isolated and confirmed for transgenic nature by PCR. A diagnostic 681 bp fragment amplified with primers specific to HBsAg 's' gene was detected transformed tobacco cell lines/banana plants as well as from the original plasmid, while it was absent in control non-transformed cells (Fig.4A, B). In order to visualize the HbsAg expressed in the transformed cells, Silver staining of total soluble protein extracted from transformed and control cells of tobacco was carried out. The pHBS100 and pHER100 transformed cell lines showed a 24 kDa band corresponding to rHBsAg of yeast, but not in the non-transformed cells (Fig.5). Subsequently, expression levels in transformed tobacco cells/banana leaves were

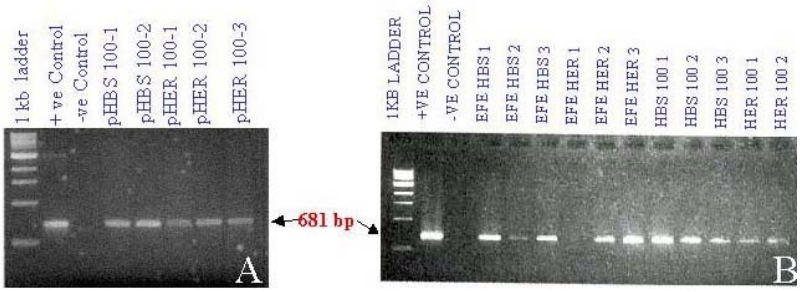

Fig.4 PCR analysis of transformed tobacco cell lines (A) and banana plants (B)

(F.W. of leaf) of HBsAg. No notable expression was observed in leaves of pEFE HBS/HER transformed plants confirming the tissue specificity of EFE promoter.

Western analysis confirmed the presence of HBsAg specific band corresponding to yeast derived rHBsAg in pHBs100 and pHER100 transformed tobacco cells whereas in the control non-transformed cells the same was absent (Fig.7). The results revealed that the denatured HBsAg expressed in plant cells showed 4 kDa peptides similar to yeast derived rHBsAg.

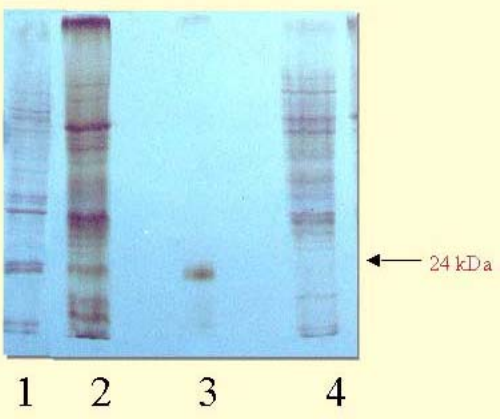

Fig.5 Silver stained SDS PAGE gel photograh of the total soluble protein extracted from tobacco cells. Lanes 1 : pHBs 100 transformed cells, 2: pHER 100 transformed cells, 3 : Yeast derived rHBsAg and 4 : NT-1 control non-transformed cells

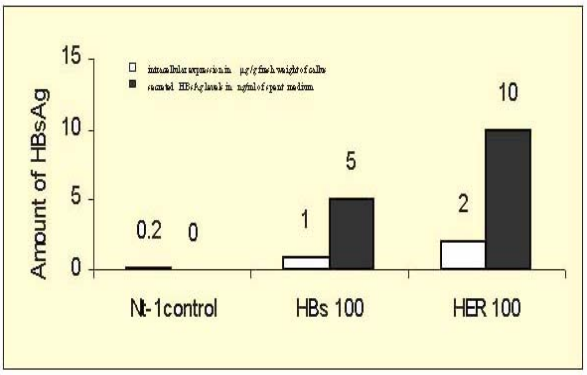

Fig.6a Amount of HBsAg expressed as intracellular and secreted forms in NT-1 cells of tobacco as estimated by ELISA

assayed by ELISA analysis. Expression levels of 1μg HBsAg g^{-1} F.W. of cells in pHBs 100 and maximum expression of 2μg g^{-1} F.W. of cells in pHER100 transformed cell lines were observed (Fig.6A). It was also observed that transformed tobacco cell lines secreted HBsAg into the spent medium. pHER100 transformed cell lines secreted 10ng ml^{-1} whereas pHBS100 transformed cell lines secreted 5ng ml^{-1} (Fig.6A). In transgenic banana plants, maximum expression level of 0.7 μg g^{-1} (F.W of leaf) of HBsAg was noted in pEFE HBs transformed plants grown *in vitro* (Fig.6B). The pHBs 100 transformed plants hardened in the green house showed highest expression level of 0.6μg g^{-1}

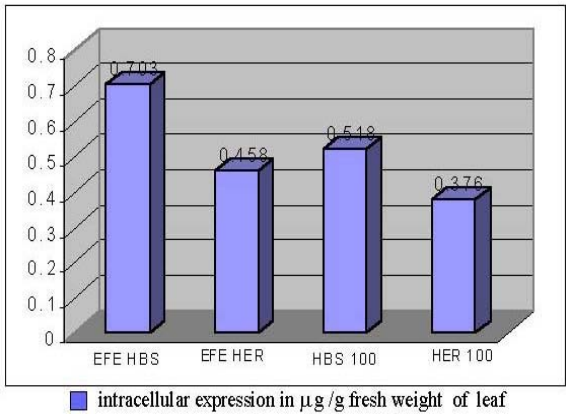

Fig. 6b ELISA analysis of transgenic banana plants

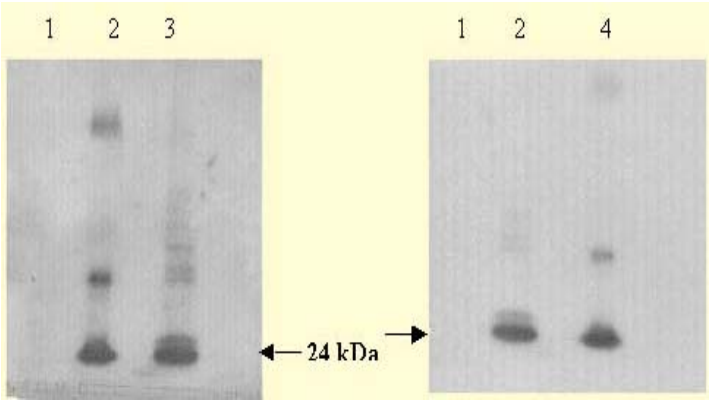

Fig 7 Western blot analysis of transformed NT-1 cell lines of tobacco. Lanes 1: non-transformed control, 2: 38ng yeast derived rHBsAg, 3 : pHBs 100 transformed cell line, and 4 : pHER 100 transformed cell line of tobacco

Discussion

We have chosen tobacco cell line as an expression system to explore possible levels of expression that can be obtained using various plant expression cassettes. It also serves as a model system for the rapid assessment of expressivity using different promoters and to determine the recombinant protein targeting with different signal sequences.

The recombinant proteins when targeted either to endoplasmic reticulum or secretory pathway showed proper folding of proteins, thereby increasing functional protein level expressed in plants (Pen et al., 1993; Schouten et al., 1996). ER retention signal can give 10-100 fold increase in Single chain variable fragments (ScFvs) yield compared to secretory pathway in transgenic tobacco and potato (Conrad and Fiedler, 1998). ER targetting is essential for glycosylation and disulfide bridge formation (Ituriga et al., 1989; Bruyns et al., 1996). Transgenic plants expressing ER retained ScFvs have high antigen binding activity and can be stored for more than 3 weeks without loss of antigen binding activity or specificity in a dried form (Fiedler et al., 1997). Mason and Arntzen (1995) reported that recombinant LT-B produced in tobacco and potato showed enhanced accumulation when a 'C' terminal microsomal retention signal was added. Incorporation of ER retention signal at 'C' terminus led to secretion of recombinant proteins through the intercellular spaces into the guttation fluid in transgenic tobacco plants (Komarnystky et al., 2000). Similarly Borisjuk et al., (1999) reported secretion into the medium of three heterologous proteins of diverse origin through the roots of transgenic tobacco plants using an endoplasmic reticulum signal peptide fused to the recombinant protein gene sequence.

Since the formation of 22nm particle is critical for the immunogenicity of HBsAg, we have incorporated 'C' terminal ER retention signal to facilitate proper folding, disulfide bond and particle formation. The expression levels of HBsAg expressed with and without ER retention signal were compared and higher expression levels were obtained when HBsAg was expressed with microsomal retentional signal. We found higher expression levels of HBsAg ($2\mu g\ g^{-1}$ F.W. of callus or 512 ng mg^{-1} of soluble protein) in comparison with earlier reports of 66 ng mg^{-1} of soluble protein in transgenic tobacco plants (Mason et al., 1992) and 150 ng g^{-1} F.W. of lupin callus (Kapusta et al., 1999). The higher expression levels obtained in our study may be attributed to the use of strong promoter from *ubq3* gene of *Arabidopsis* and the 'C' terminal microsomal retention signal. However, Richter et al., (2000) reported the highest level of HBsAg expression 16 $\mu g\ g^{-1}$ of potato tubers by incorporating 3' region from potato proteinase inhibitor II gene, but plants grew poorly in the green house or had poor tuber yield.

In this study, using the plant expression vector (pHER 100), HBsAg could also be secreted into medium by tobacco cells in the required particulate form as evidenced by ELISA results (Fig.6A). However, the level of secretion was low compared to intracellular accumulation as no secretory signal was fused to the HBsAg gene.

Optimization of expression using stronger promoters, 5'UTRs and secretory signal at the 5' and 3' microsomal retention signal sequences may enable the secretion of higher levels of HBsAg into medium and easier downstream processing. Mason et al., (1992) were unable to analyze the size of the SDS denatured HBsAg peptides on SDS PAGE blots as the tested monoclonal antibodies failed to recognize HBsAg peptides. In this study, rabbit Anti HBsAg serum was used and it was successfully demonstrated that polyclonal antibodies recognized the denatured HBsAg peptides and showed 24 kDa band corresponding to yeast derived rHBsAg in the Western blot.

Cell suspension cultures offer as an ideal system for the production of recombinant proteins under certified good manufacturing practice (cGMP) and certified good laboratory practice (cGLP). These practices assume greater significance especially when the recombinant proteins are intended for clinical use as their production under defined, controllable and sterile conditions are possible with cell suspension cultures (Fischer et al., 1999). The production of recombinant proteins in cell suspension cultures is still at an early stage. We could successfully scale up pHER 100 transformed tobacco cells to two liters in a five litre conical flask with a ten fold increase in F.W. in ten days. The results suggest that this can be scaled up further to produce HBsAg in large quantities under controlled conditions. This is the first report on the secretion of a large molecule of HBsAg into cell culture medium. Studies in this direction are desired to increase the level of expression and scaling up for continuous production.

Alternatively, to obviate the use of sophisticated bioreactors and to make the production of recombinant proteins more economical, these can be produced in an edible part of a plant for the oral delivery of vaccine as reported in potato and lettuce (Richter et al., 2000; Kapusta et al., 1999; Webster et al., 2002). Expression of HBsAg in bananas may be advantageous as they are grown in most of the tropical and subtropical countries, where cost effective vaccines are required and their digestibility and palatability by infants makes it an attractive choice. The concept of producing edible vaccines in banana has been schematically depicted in Fig. 8.

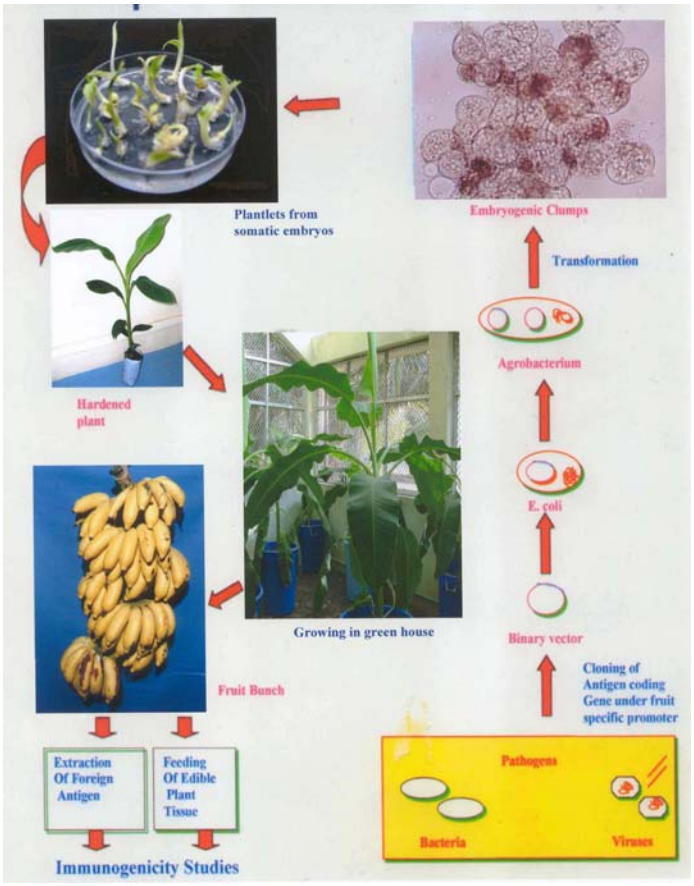

Fig. 8 Concept of edible vaccine in banana

However, a multitude of considerations have to be taken into account in the development of any recombinant vaccine in plants. These include fidelity of the antigen in terms of antigenicity and immunogenicity which in turn, depends on folding, structure and glycosylation; antigen stability; ease of purification, the potential for

scale up of production to produce sufficient quantities, cost and safety issues. Further maximising the expression of the antigenic proteins and stabilization of the foreign protein during post harvest storage in plant tissues need to be monitored. Enhancing the oral immunogenicity of some antigens also is of prime concern since during the oral administration, it has to withstand harsh conditions, high dilution and needs to be transported in an intact form across the epithelial barrier in sufficient amounts. Concerns about allergy and oral tolerance also need to be considered.

Some possible solutions to the above problems can include the use of saponins and special conditions of malnutrition that can facilitate passage of large molecules across epithelial barrier. Oral tolerance may be abrogated by co-administration of cholera toxin or labile toxin of enterotoxigenic *E.coli*. Use of more stronger promoters and 5' and 3' UTRs, optimization of codon usage, targetting of antigens to various organelles like ER etc. may enable proper folding and increase functional protein levels. Expression in seeds can confer stability and allow long term storage of the antigen. Transfer of animal glycosylation enzymes may result in similar glycosylation in plants. Difficulties in the purification of antigens from plants may be circumvented by expression in edible plant parts (for edible vaccines). Alternatively histidines at the 'C' or 'N' terminal of the protein can be tagged to ease the purification of the protein using nickel columns or as an oleosin fusion form for purification in oil fraction.

Acknowledgement

Authors thank Dr.S.F. D'Souza, Head , Nuclear Agriculture and Biotechnology Division and Dr. A.M. Samuel, Former Director, Biomedical Group, BARC, for their keen interest in this work and constant encouragement.

References

1. Arntzen, C.J. (1997). In : infectious diseases in children speciality forum, SLACK incorporated.
2. Bodeutsch, T., James, E.A. and Lee, J.M. (2001) The effect of immobilization on recombinant protein production in plant cell culture. Plant Cell Rep. 20, 562-566.
3. Borisjuk, N.V., Borisjuk, L.G., Logendra, S., Petersen, F., Gleba, Y. and Raskin, I. (1999) Production of recombinant proteins in plant root exudates. Nature Biotechnol. 17, 466-469.
4. Bruyns, A.M., de Jaeger, G., de Neve, M., de Wilde, C., van Montagu, M. and Depicker, A. (1996) Bacterial and plant-produced scFv proteins have similar antigen-binding properties. FEBS Lett. 386, 5-10.
5. Conrad, U. and Fiedler, U. (1998) Compartmen t-specific accumulation of recombinant immunoglobulins in plant cells: an essential tool for antibody production and immunomodulation of physiological functions and pathogen activity. Plant Mol. Biol. 38, 101-109.
6. Cote, F.X., Domergue, R., Monmarson, S., chwendiman, J., Teisson, C. and Escalant, J.V. (1996) Embryogenic cell suspensions from the male flower of *Musa* (AAA) cultivar Grand Nain. Physiol. Plant., 97, 285-290.
7. Fiedler, U., Phillips, J., Artsaenko, O. and Conrad, U. (1997) Optimization of ScFv antibody production in transgenic plants. Immunotechnology., 3, 205-216.
8. Fischer, R., Emans, N., Schuster, F., Hellwig, S. and Drossard, J. (1999) Towards molecular farming in the future : using plant-cell suspension cultures as bioreactors. Biotechnol. Appl. Biochem. 30, 109-112.
9. Ganapathi, T.R., Higgs, N.S., Balint-Kurti, P.J., Arntzen, C.J., May, G.D. and Van Eck, J.M. (2001) *Agrobacterium* -mediated transformation of embryogenic cell suspensions of the banana cultivar Rasthali (AAB). Plant Cell Reports 20, 157-162.
10. Ginsberg, H.S., Brown, F., Chanock, R.M. and Lerner, R.A. (1993) In: Vaccines 93 Modern approaches to new vaccines

including prevention of AIDS., Cold Spring Harbor, USA.
11. Hood, E.E., Gelvin, S.B., Melchers, L.S. and Hoekama, A. (1993) A new *Agrobacterium* helper plasmid for gene transfer to plants. Transgenic Res. 2, 208-218.
12. Ituriaga, G., Jefferson, R.A. and Bevan, M. W. (1989) Endoplasmic reticulum targeting and glycosylation of hybrid proteins in transgenic tobacco. Plant Cell. 1, 381-390
13. Joshi, N. and Kumar, A. (2001) Immunoprophylaxis of hepatitis B virus infection. Indian Jour. Med. Microbiol. 19, 172-183.
14. Laemmli, U.K. (1970) Cleavage of structural proteins during the assembly of the head proteins of bacteriophage T4. Nature 277, 680-685.
15. Kapusta, J., Modelska, A., Figlerowicz, M., Pniewski, T., Letellier, M., Lisowa, O., Yusibov, V., Koprowski, H., Plucienniczak, A. and Legocki, A.B. (1999) A plant derived edible vaccine against hepatitis B virus. The FASEB Jour. 13, 1796-1799.
16. Komarnytsky, S., Borisjuk, N.V., Borisjuk, L.G., Alam., M.Z. and Raskin, I. (2000) Production of recombinant proteins in tobacco guttation fluid. Plant Physiol. 124, 927-933.
17. Kong, Q., Richter, L., Yang, Y.F., Arntzen, C.J., Mason, H.S. and Thanavala, Y. (2001) Oral immunization with hepatitis B surface antigen expressed in transgenic plants. Proc. Natl. Acad. Sci. (USA). 98, 11539-11544.
18. Kozak, M. (1981) Possible role of flanking nucleotides in recognition of the AUG initiator codon by eukaryotic ribosomes. Nucleic Acids Res. 9, 5233-5252.
19. Mason, H.S. and Arntzen, C.J. (1995) Transgenic plants as vaccine production systems. TIBTECH. 13, 388-392.
20. Mason, H.S., Lam, D.M.K. and Arntzen, C.J. (1992) Expression of hepatitis B surface antigen in transgenic plants. Proc. Natl. Acad. Sci. (USA) 89, 11745-11749.
21. Murashige, T. and Skoog, F. (1962) A revised medium for rapid growth and bioassays with tobacco tissue cultures. Physiol. Plant. 15, 473-497.
22. Pen, J., Sijmons, P.C., Van Ooijen, A.J.J. and Hoekema, A. (1993) Protein production in transgenic crops: analysis of plant molecular farming. In: A. Hiatt (Ed) Transgenic plants fundamentals and applications. Marcel Dekker, New York, pp. 239-254.
23. Richter, L.J., Thanavala, Y., Arntzen, C.J. and Mason, H.S. (2000) Production of hepatitis B surface antigen in transgenic plants for oral immunization. Nature Biotechnol. 18, 1167-1171.
24. Sambrook, J., Fritsch, E.F. and Maniatis, T. (1989) Molecular cloning : A laboratory manual. Cold Spring Harbor Laboratory Press, Cold Spring Harbor, NY, USA.
25. Schouten, A., Roosien, J., Van Engelen, F.A., de Jong, G.A.M., Borst, Vrenssen, A.W.M., Zilverentant, J.F., Bosch, D., Stiekema, W.J., Gommers, F.J., Schots, A. and Bakker, J. (1996) The C-terminal KDEL sequence increases the expression level of a single-chain antibody designed to be targeted to both the cytosol and the secretory pathway in transgenic tobacco Plant Mol. Biol. 30, 781-793.
26. Stewart, C.N. Jr. and Via, L.E. (1993) A rapid CTAB isolation technique for RAPD fingerprint and other PCR applications. Biotechniques 14, 748-749.
27. Streatfield, S.J., Jilka, J.M., Hood, E.E., Turnet, D.D., Bailey, M.R., Mayor, J.M., Woodard, S.L., Beifuss, K.K., Horn, M.E., Delaney, D.E., Tizard, I.R. and Howard, J.A. (2001) Plant-based vaccines : unique advantages. Vaccine 19, 2742-2748.
28. Thanavala, Y., Yang, Y.F., Lyons, P., Mason, H.S. and Arntzen, C.J. (1995) Immunogenicity of transgenic plant derived hepatitis B surface antigen. Proc. Natl. Acad. Sci. (USA). 92, 3358-3361.

29. Tiollais, P., Charnay, P. and Vyas, F. (1981) Biology of Hepatitis B virus. Science 213, 406-411.
30. Walmsley, A. M. and. Arntzen, C.J. (2000) Plants for delivery of edible vaccines. Current Opinion in Biotech. 11, 126-129.
31. Webster, D. E.,Cooney, M.L.,Huang, Z., Drew, D.R., Ramshaw, I.A., Dry, I.B., Strugnell, R.A., Martin, J.L. and Wesselingh, S.L. (2002) Successful boosting of a DNA measles immunization with an oral plant-derived measles virus vaccine. Jour. Virol.76, 7910 - 7912.

This paper won the Best Poster presentation award at the Symposium on "Biotechnology at the turn of the millennium", held at Anna University, Chennai during February 4-5, 2002.

About the authors ...

Mr G.B. Sunil Kumar, *M.Sc. (Biotech) is from 42nd batch of BARC Training School. He is working on the Plant based Molecular Farming for Human Health Care in the Plant Cell Culture Technology Section of Nuclear Agriculture and Biotechnology Division, BARC.*

Dr T.R.Ganapathi *did his Ph.D. from Karnatak University, Dharwad, and joined BARC in 1991. He is working in the Plant Cell Culture Technology Section of Nuclear Agriculture and Biotechnology Division. His specialization is in the field of Plant Tissue Culture. He has standardized micropropagation protocols in banana and the technique has been transferred to user agencies. He has also established methods for somatic embryogenesis and Agrobacterium mediated transformation in banana using embryogenic cell cultures. He was awarded "DBT Overseas Associateship" for his post-doctoral work on genetic transformation in banana at the Boyce Thompson Institute for Plant Research Inc., Ithaca, NY, USA. Currently, he is working on Genetic Transformation for the incorporation of useful traits into Crop Plants.*

Dr V.A. Bapat *is working in the area of Plant tissue culture for the last 31 years. The main thrust area of his work is on Micropropagation and Genetic Transformation of Plants. He has effectively contributed for clonal propagation, suspension cultures, protoplasts, synthetic seeds and bioreactor production of somatic embryos in a precious forest tree-Sandalwood. He has also done extensive work on micropropagation of Banana and Mulberry. He has several publications in National and International journals to his credit. Currently he is heading the Plant Cell Culture Technology Section, Nuclear Agriculture and Biotechnology Division, BARC.*

Dr Revathi J. Chaganti*, Sr. Scientist, Shantha Biotechnics Pvt. Ltd., has 20 years of research experience at Centre for Cellular and Molecular Biology from where she obtained her Ph.D. degree. She has vast experience in Molecular Biology, Cell Biology and Biochemistry. She has been associated with Shantha Biotechnics since 1996. At Shantha Biotechnics, she has gained expertise in cloning and optimization of expression of heterologous genes in the yeast Pichia pastoris, to suit commercial production. She had contributed to the development of hepatitis B vaccine and was a key member of the team that developed interferon alpha.*

Dr K S N Prasad, *Head, R&D, Shantha Biotechnics Pvt. Ltd., did his Ph.D. at the Biochemistry department of Regional Research Laboratory, Hyderabad (forerunner of present day Centre for Cellular and Molecular Biology). He did his postdoctoral research at Curie Institute, Orsay, France. He has over 20 years of research experience in Biochemistry, Microbiology and molecular biology. Dr. Prasad had been a scientist at the reputed Centre for Cellular and Molecular Biology for several years. He has been associated with Shantha Biotechnics since 1995 and played an important role in the development of Hepatitis-B vaccine as well as interferon alpha.*

Transmission Electron Microscopy of Semi-thin Sections of Cyanobacterium - *Anacystis nidulans* at 160kV

D. N. Dani and J.K. Sainis
Molecular Biology Division
Bhabha Atomic Research Centre

and

G.K. Dey
Material Science Division
Bhabha Atomic Research Centre

CONVENTIONALLY TRANSMISSION electron microscopy for biological samples is done with TEM operating at 80-100kV using ultra-thin sections of 70 -100 nm. Since higher voltage electron microscopes are not traditionally used for biological samples, semi-thin sections (over 100 nm) are rarely used for electron microscopy. In this report we present our results on use of Transmission Electron microscope at 160 kV to investigate the structural details of *Anacystis nidulans* cells using semi-thin sections.

Anacystis nidulans is a unicellular cyanobacterium having a specialized system of internal membranes, called thylakoid membranes. We are interested in understanding supramolecular organization of photosynthetic enzymes around thylakoid membranes. Cells of *Anacystis nidulans* (strain BD1) were fixed and embedded in araldite by conventional protocols. Thin and semi-thin sections (70 nm, 200nm, 300nm and 500 nm) were cut using Leica Ultracut UCT. The sections were contrasted with uranium acetate. Thin sections were observed under 80 kV TEM (Jeol JEM 1010) and semi-thin sections were observed under 160kV TEM (Jeol JEM 2000 FX).

Figure 1 shows the conventional ultra thin sections (70 nm) of *Anacystis* seen under 80kV Jeol Transmission Electron Microscope. The outer cell wall and inner thylakoid membranes are seen clearly. These images were similar to those observed earlier (Allen, 1988). Figures 2-4 show sections of *Anacystis* cells which are 200, 300 and 500 nm in thickness. The sections show typical cell wall, 3-4 layers of thylakoid membranes running parallel to each other, enclosing nucleoplsam, carboxysomes and polyphosphate granules as described by Stanier (1988). The electron transparent thylakoid membranes appear to be around 50-60 nm thick and the electron-opaque layers around thylakoid membranes are 20-30nm thick. The electron opaque region shows regular globular bodies along the thylakoid membranes. Interconnections between the thylakoid membrane systems and cytoplasmic membranes are clearly visible in 500 nm thick sections.

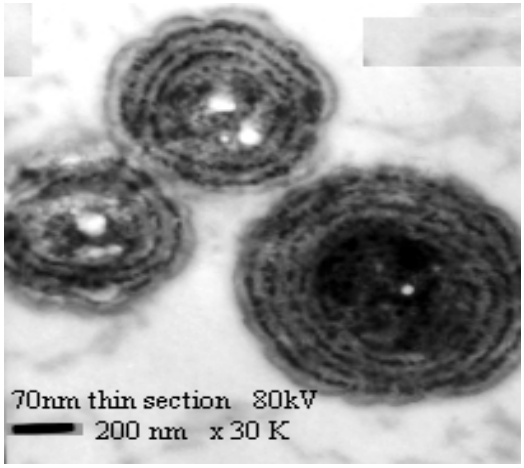

Fig. 1 Ultrathin section - 70 nm

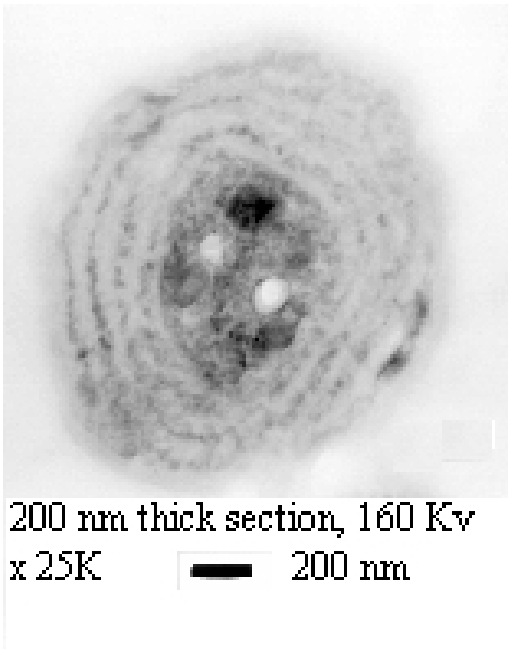

Fig. 2 Semi thin section - 200 nm

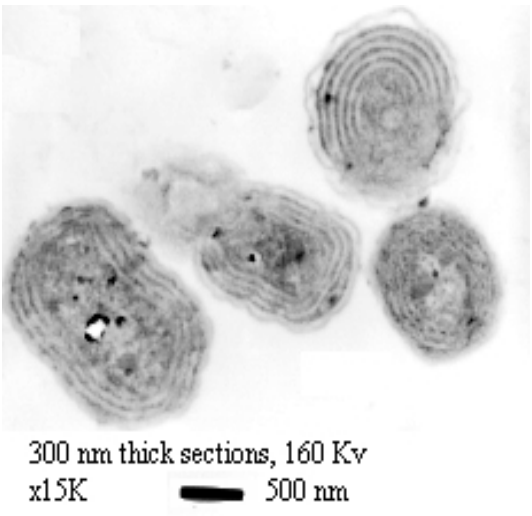

Fig. 3 Semi thin section - 300 nm

These results are similar to those observed in the case of an unicellular halotolerent cyanobacterium *Agemenellum quadruplicatum* with 250 nm thick sections using 1.0 MV High Voltage Electron Microscope (Nierzwicki-Bauer, et al., 1984).

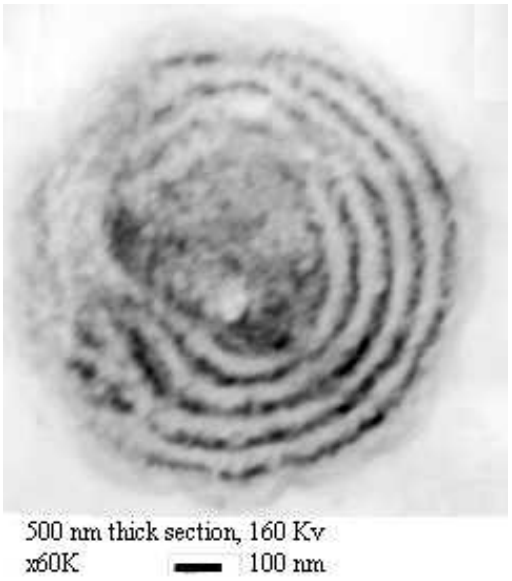

Fig. 4 Semi thin section - 500 nm

The results indicate that, TEM operating at 160kV can be used to investigate structural details of biological samples using section thickness up to 500nm. Since *Anacystis* cells are simple prokaryotic cells without any complex intracellular structural features, thin sections at low voltage and semi-thin sections at higher voltage were comparable. There was no loss of information. However, the thylakoid membranes show interconnections and continuity, which can be easily observed in 500 nm sections (figure 4) which is not seen in thin sections. Thus TEM at 160kV will be useful to observe semi thin sections (up to 500nm) of biological sample which can give 3-7 times more structural information as compared to conventional 80kV TEM. Besides semi thin sections will be useful for 3D reconstruction of images as well as immuno-labeling.

References

1. Allen. M. M., 1968, Photosynthetic membrane system in *Anacystis nidulans, Journal of Bacteriology*, 96, 836-841.
2. Nierzwicki-Bauer et al., 1984, The use of high-voltage electron microscopy and

semi-thick sections for examination of cyanobacterial thylakoid arrangements, *Journal of Microscopy*, 133, 55-60

3. Stanier G,1988, Fine structure of Cyanobacteria, *Methods in Enzymolgy*,167, 157-172.

Acknowledgements

We wish to thank Dr. S. K. Mahajan, Head, Molecular Biology and Agriculture Division, BARC, and Dr S. Banerjee, Director, Material Sciences Group, BARC, for the encouragement. We also want to thank Dr A. R. Chitale, Head, Electron Microscopy Facility, Jaslok Hospital and Mr D. B. Kanaskar and Mr S. S. Bhosale, Electron Microscopy Section, Jaslok Hospital, for the help in taking images with 80 kV TEM.

This paper received the Best Poster Presentation award at the Silver Jubilee Conference of the Electron Microscope Society of India on Electron Microscopy and Allied Fields, held at IIT,Bombay, during February 20-22, 2002

About the authors ...

Ms Diksha N. Dani *has done M. Sc in Botany from Mumbai University and joined Molecular Biology Division in 1999. She holds Senior Research Fellowship for Ph.D from Department of Atomic Energy and is studying the supramolecular organization among photosynthetic enzymes and thylakoid membranes.*

Dr Jayashree Krishna Sainis *is working in Molecular Biology Division. She has done M.Sc in Biochemistry from Nagpur University in 1971. She joined BARC in 1972 after completing one year Training Course in Biology-Radiobiology (15th batch). She did her Ph. D from Gujarat University in Biochemistry. Her research deals with various aspects of Plant Biochemistry and Photosynthesis. She has over 50 papers in journals and symposia proceedings.*

Dr Gautam Kumar Dey *obtained his B.Tech in Metallurgical Engineering in 1979 from the Institute of Technology, Banaras Hindu University. He joined the 23rd batch of Training School and was awarded the Homi Bhabha prize for standing first in his discipline. On completion of training, he joined the Metallurgy Division. He obtained his Ph.D. degree from Banaras Hindu University in 1988. He was a postdoctoral fellow at University of Cincinnati from 1994 to 1996. He has won several awards for his scientific contributions. Of these mention can be made of the Young Scientist award of Indian National Science Academy, Young Metallurgist Award given by Ministry of Steel and Mines and MRSI Medal given by Materials Research Society of India. Areas of his research interest are Phase Transformation in Zirconium and Nickel Base Alloys, Amorphous Alloys, Rapidly Solidified Crystalline and Quasicrystalline Alloys, Electron Microscopy and Defect Characterization and High Resolution Electron Microscopy. He has more than 150 scientific publications to his credit.*

TEM Studies on Microstructural Evolution in Hot Pressed Silicon Carbide Ceramics

Abhijit Ghosh, Abdul Gulnar, R.K. Fotedar, G.K. Dey, D.D. Upadhyaya, RamPrasad and A.K. Suri
Materials Group
Bhabha Atomic Research Centre

SILICON CARBIDE (SIC) CERAMICS belong to an important class of structural materials for high temperature applications. The specific attributes that account for their utility as engineering ceramics are the high value of thermal conductivity and a lower thermal expansion coefficient and hence, better thermal shock resistance. Being a covalent solid, the heat treatment operations need to be carried out at exceedingly high temperatures for achieving full densification. Various approaches are thus followed, such as reaction bonding, pressureless sintering, hot pressing, etc.. Incorporation of certain additives is known to promote the densification process as well as generates a favourable bimodal microstructure. The latter provides an effective in situ toughening mechanism in to the matrix phase[1]. Several workers have studied the influence of aluminium, boron and carbon, in densification and phase transformation reaction of SiC ceramics[2-3].

In the present work for densification studies, fine powder of β-SiC powder (Electro Abrassives, USA) was used along with the additives of Al (1.0 %), B (0.5 %) and C (3.0%). Hot pressing was carried out in graphite dies in the temperature range of 1700-1900^{0}C for 30min., under vacuum at 32 MPa pressure. For microstructural studies the fine polished and etched (Murakamis` reagent) surfaces were examined under optical microscope. Fractured surfaces were observed under SEM . For TEM investigations, the electron transparent thin foils were prepared by argon ion milling (Gatan, 600TMP). A JEOL 200 FX microscope was used to image the general morphological features and a JEOL 3010 microscope with a point to point resolution of 0.21 nm was utilized to examine the intra and inter granular fine-structure features under HREM conditions.

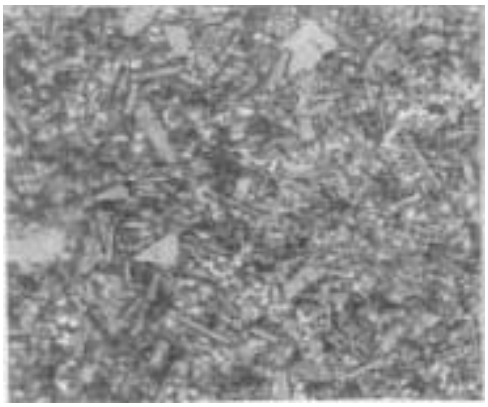

Fig.1 Optical micrograph showing elongated SiC grain morphology

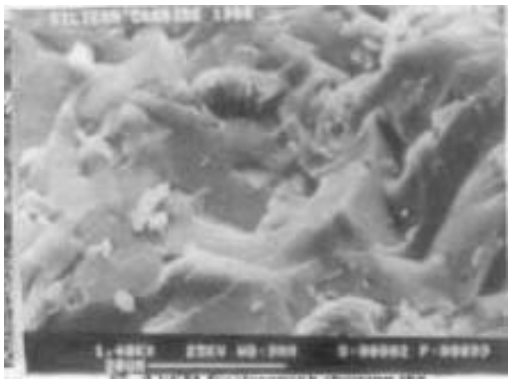

Fig.2 SEM fractrograph showing the dense pore free matrix

Fig.3 (a), (b) TEM images revealing the large SiC grains and associated dislocation network.

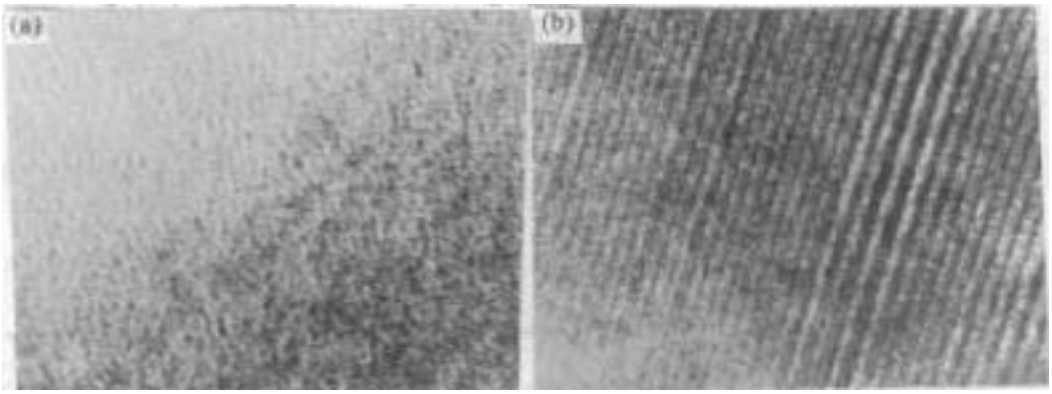

Fig.4 HREM images of (a) grain tri-junction, and (b) intragranular regions

Fully dense (bulk density 3.18 g.cm^{-3}) SiC samples were obtained after hot pressing at 1900^{0}C. Typical optical micrograph presented in Fig.1 shows the characteristic plate like morphology of α–SiC grains having aspect ratio of about five. Conversion to high temperature α-phase is generally very rapid at these temperatures in the presence of additives used here[4]. The bimodal grain size distribution pattern is also revealed in SEM fractrographs (Fig.2). The grain boundaries appear generally free of secondary phase as seen in bright field conventional TEM images (Fig.3 a&b). The prominent features are about the polytypes of SiC, which is a complex mixture of different variants. The presence of other fine scale features like the in-grown dislocation network is also observed. HREM analysis, however, provides evidence for distribution of amorphous phase, (a) at the grain triple-junctions Fig.4a and (b) as very thin (< 2 nm) intergranular film. Fig.4b shows the different stacking sequence in SiC lattice. Results are very significant for the development of strong and creep resistant ceramic components.

References

1. Chen.D., et al., Acta Mater 48 659-74 (2000)
2. Lin.B.W., et al., J.Am.Ceram.Soc., 69 C67-68 (1986).
3. Zhang. X.F., wt al., J.Am.Ceram.soc. 84 813-20 (2001)
4. Hauer.A.H., et al., J.Am.Ceram.Soc., 61 406-12 (1978).

This paper received the Best Poster award at the 25th EMSI Conference held at IIT, Bombay, during February 20-22, 2002.

About the authors ...

Mr Abhijit Ghosh *received his B.Sc (Tech) in ceramics from University of Calcutta in 1995 and M.Tech (Ceramics) degree from IT-BHU in 1997 and joined Materials Processing Division, BARC, after completing 6th OCPGE in nuclear science. Since then, he is associated with R&D activity on advanced ceramics, especially structural and electrical ceramics. He is involved in the development of silicon carbide based ceramic, preparation and characterization of nano zirconia based materials, and development of solid oxide fuel cell devices. He has published more than 15 research papers in different journals and conference proceedings.*

Dr (Ms) Gulnar Abdul Karim *received her M.Sc (Chemistry) degree from Mumbai University in 1985. The Mumbai University awarded her doctorate degree in 1994 for her work in Synthesis and Characterization of new perovskite compounds. Since 1984, she has been actively pursuing R&D work on ceramics, especially superconductivity and structural ceramics. Her current research interests include the development of silicon carbide and materials for solid oxide fluid cells. She has published more than 20 research papers in different journals and conference proceedings.*

Mr R.K. Fotedar *is currently working in Process Equipment Development Group of Materials Processing Division. He is a Mechanical Engineer from 21st batch of BARC Training School. He has been closely associated with divisional development programes. He has made outstanding contribution in setting up a hydrostatic extrusion facility for the cold extrusion of thin walled aluminium, copper tubes and rods. Some of the important contributions of Mr Fotedar are as follows: (i) In-pile creep device for measurement of irradiation creep in nuclear materials. (ii) Development of high vacuum high temperature (2000°C) hot presses, (iii) Evaluation of pressure, temperature parameters for the fabrication of B_4C, borides (TiB_2+CrB_2+$MoSI_2$), and SiC pellets for reactor applications, (iv) Parameters for solid state welding of aluminium and SS 304, TZM to TZM, and (v) Development of superplasticity deformation facility to study the superplasticity behaviour of Zr_2 and Al Li 8090 alloy.*

Dr Gautam Kumar Dey *obtained his B. Tech in Metallurgical Engineering in 1979 from the Institute of Technology, Banaras Hindu University. He joined the 23rd batch of Training School and was awarded the Homi Bhabha prize for standing first in his discipline. On completion of training, he joined the Metallurgy Division. He obtained his Ph. D degree from Banaras Hindu University in 1988. He was a postdoctoral fellow at the University of Cincinnati from 1994 to 1996. He has won several awards for his scientific contributions. Of these, mention can be made of the Young Scientist award of Indian National Science Academy, Young Metallurgist Award given by Ministry of Steel and Mines, and MRSI Medal given by Materials Research Society of India. He has more than 150 scientific publications to his credit.*

Dr D.D.Upadhyaya *joined BARC after completing the orientation course in nuclear science in 1968-69. He earned the Ph.D. degree in physics (1985) and published more than 80 research papers in different journals and conference proceedings. His fields of interest are in structure property correlation in electronic and engineering ceramics, lattice defect-structure characterization, and advanced synthesis and consolidation techniques. He visited Max-Planck Institute, Metals Research, Stuttgart, Germany during 1987-89, under the Indo-German exchange programme.*

Mr Ram Prasad *joined Metallurgy Division in 1963 after completing BARC training school course in 6th batch. He was associated with the ceramic materials development programmes for nearly four decades. His main fields of interest have been electronic and magnetic ceramics, structural ceramics and bioceramics materials in which he has published more than 200 research papers. He retired from BARC on superannuation in Deccember 2002.*

GC-MS in Combination with Solid Phase Micro Extraction for Determination of N-Nitrosamines in Environmental and Food Matrices

S. Mahapatra, R.M. Tripathi, S. Bhalke and S. Sadasivan
Environmental Assessment Division, Bhabha Atomic Research Centre

Abstract

A method for the estimation of nitrosamines in environmental and food matrices using gas chromatography mass spectrometry (GC-MS) in combination with solid phase micro extraction (SPME) has been standardised. Solid phase micro extraction of nitrosamines was done using polydimethylsiloxane / divinylbenzene fibres. Food, air, tobacco and sea water samples were collected from different sites in Mumbai. Samples were extracted in dichloromethane, preconcentrated on polydimethylsiloxane / divinylbenzene fibres and analysed using GC-MS technique. The validity of the extraction procedure was checked by recovery of spiked nitrosamine standards. The detection limits for nitrosamines varied between 0.2-0.5 pg. The recovery of different nitrosamines from different matrices varied between 95-98%.

Introduction

The POTENT CARCINOGENICITY OF MOST N-nitroso compounds in laboratory animals has led to considerable attention from researchers in environmental carcinogenisis. About 90 % of 300 tested compounds have shown carcinogenic effects in bioassay and no animal species is shown to be resistant. Nitrosamines have classically associated with nitrite preserved food stuffs and tobacco, evidence of their presence in other environmental matrices had increased with new highly sensitive monitoring methods.

Nitroso compounds are known to be strong carcinogens in various animals including human beings. Human exposure to carcinogenic N-nitrosamines may result directly from ingestion or inhalation of preformed compounds from the environment. Essentially they are formed by the reaction of amines especially secondary and tertiary amines or amino group containing compounds with nitrite. As both nitrite and amine precursors are present in many commonly consumed foods, exposure could also result from N-nitrosamines formed within the body. N-nitrosodimethyl amine (NDMA) and N-nitrosodiethylamine (NDEA) are the most common nitrosamines found in food materials.

Analytical methods for determination of nitrosamines in environmental samples should provide sufficient sensitivity as their concentrations in these samples are very low. Most of these techniques combine a separation technique such as a gas chromatography (GC), liquid chromatography (LC) or supercritical fluid chromatography (SFC) with a selective detection like mass spectrometry (MS), thermal energy analysis (TEA), flame photometric detection (FPD) or inductively coupled plasma-mass spectrometry (Maria, 2000; Supelco, 1997; Osterdahl and Slorach, 1983). The purpose of the study is to standardise a method for measurement of nitrosamines in environmental and food materials using GC-MS technique in combination with SPME.

Instrumentation

A GC-MS system (Shimadzu QP5050 A) attached with Shimadzu GC-17.0 has been used for the analysis of nitrosamines in environmental samples. Solid phase micro extraction was done using polydimethylsiloxane /divinylbenzene fibres. The quantitative estimation of samples has been done using calibration curves.

Analytical Procedure : The collection and extraction of samples was done using procedures adopted by Maria, 2000; Marano et al, 1982; Osterdahl and Slorach, 1983). Preconcentration of nitrosamines in extracted samples was done using polydimethylsiloxane/ divinylbenzene fibres (65 μm film). The preconcentration of nitrosamines on fibres was done for 15 minutes with rapid stirring in immersed conditions. After preconcentration, the nitrosamines collected on fibres were desorbed in capillary column (DB-1) at 270 deg C (Supelco, 1997). The oven temperature was programmed from 50 deg C to 250 deg C at a rate of 5 deg.min^{-1}.

The analytical parameters for estimation of nitrosamines using GC-MS technique are given in Table-1. The recovery study of nitrosamines from water and food samples was carried out.

Table-1 : Instrumental parameters of gas chromatograph-mass spectrometer

S.N.	Instrument	Parameter	Optimum Value
1	*GC*	Initial temperature	50 deg. C
2		Final temperature	250 deg. C
3		Scan Rate	5 deg. / min
4		Analytical column	Glass capillary, DB-1, 30 m
7		Career gas	Helium
	MS	Instrument Model	Shimadzu QP 5050 A
2		Scan range	10-300
4		Scanning mode	TIC
5		Ionization technique	Electron impact
		Interface temp	230 deg. C

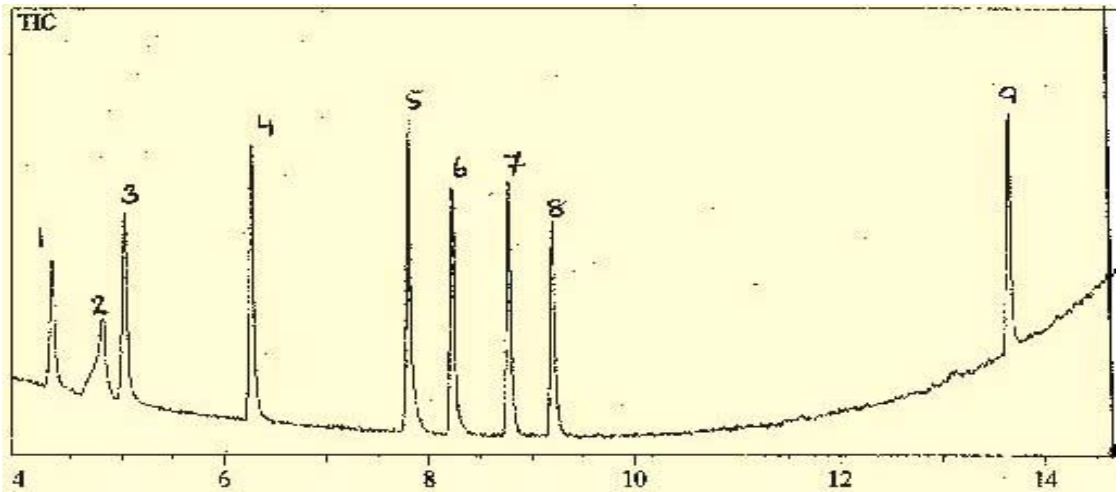

Fig. 1: Total Ion Chromatogram of Nitrosamines (1. N-Nitrosodimethyl amine; 2. N-Nitroso methyl ethyl amine; N-Nitrosodiethyl amine; 4. N-Nitroso dipropyl amine; 5. N-Nitrosodibutyl amine; 6. N-Nitroso piperidine; 7 Nitroso pyrrolidine; 8. N-Nitroso morpholine; 9. N-Nitroso diphenyl amine)

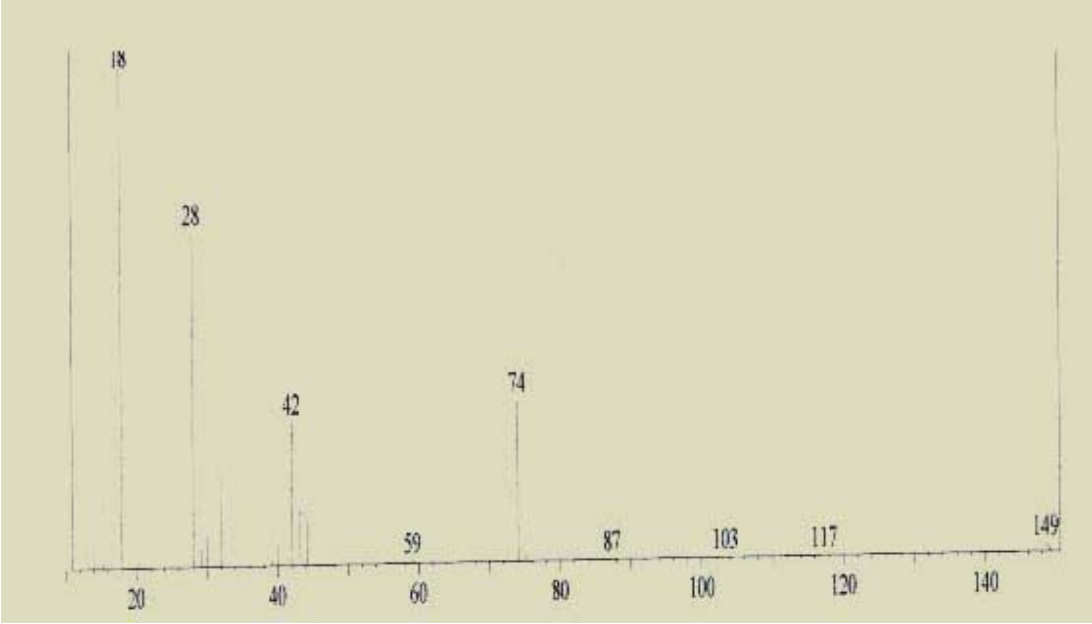

Fig. 2: Typical mass fragmentation pattern of N-Nitroso dimethyl amine in a tobacco extract sample.

Water and food samples were spiked with nitrosamines and measured for nitrosamine contents. The recovery of different nitrosamines varied between 95-98 %. A total ion chromatogram of different nitrosamines is given in fig.-1. Sea water, air, food and tobacco samples were analysed for nitrosamine contents. Concentrations of nitrosamines in commonly available chewing tobacco samples varied from 0.2 –1.4 $\mu g\ g^{-1}$. The concentrations of N-Nitrosodimethyl amine in ambient air at Mumbai was found to vary from 20-45 ng m^{-3}. A typical mass fragmentation pattern of N-Nitroso dimethyl amine in a tobacco extract is given in fig.-2.

References

1. Supelco (1997). Chromatographic Applications. Analysis of Nitrosamines using SPME –GCMS. Supelco, pp A18, 1997.
2. Maria FA. J Chromatography A, 889, 2000, 3-14.
3. Marano S. et al, (1982). Anal Chem. 54, 1947-1951.
4. Osterdahl BG and Slorach SA . Food Chem. Toxicology 21, 1983, 759-762.

This paper was selected for the Dr K.K. Majumdar Memorial Award for the Best Paper presented in the 16th National Symposium of Indian Society of Analytial Scientists, held at Shilong during March 8-9, 2002 and the award was presented to Ms Suchismita Mahapatra

About the authors ...

Ms Suchismita Mahapatra *joined Environmental Assessment Division, BARC, in 1998 after completing one-year advanced training course (OCES-41) in Chemistry discipline conducted by Human Resource Development Division, BARC, Mumbai. Basically, she is engaged in the development of analytical techniques for estimation of toxic metals in environmental and biological matrices. She has standardised analytical techniques for metals at trace and ultra-trace levels using spectroscopic and electroanalytical techniques. She has carried out exposure assessment studies for Mumbai population for toxic metals through inhalation and ingestion pathways. She is also involved in speciation studies of organometallic compounds and carcinogenic organo-pollutants in environment using advanced analytical techniques like solid phase micro extraction – Gas chromatography mass spectrometry (SPME-GC/MS) technique.*

Dr R. M. Tripathi *obtained his M.Sc. (Chemistry) from Lucknow University and Ph. D. from Bombay University. He belongs to 25th batch (1981-1982) of BARC training school. After successful completion of one-year training course in chemistry discipline, he joined Air Monitoring Section of BARC. He has worked on development of analytical techniques for study of toxic heavy metals in environmental and biological materials using spectroscopic and electroanalytical techniques. His main areas of interest are heavy metals in environment, atmospheric removal processes for heavy metals, precipitation chemistry, speciation of organo metallic compounds, intake and biokinetic studies of heavy metals He is also involved in the development of speciation techniques for organometallic compounds in environment using advanced analytical techniques like solid phase micro extraction – Gas chromatography mass spectrometry (SPME-GC/MS). He is a recognized guide of Mumbai University for M.Sc. and Ph.D. in Analytical Chemistry. He has 93 scientific papers in international/national journals and conferences to his credit.*

Mr Sunil Bhalke *joined Environmental Assessment Division, BARC, in 1998 after successful completion of one-year stipendiary training course (CAT-I) in Health Physics conducted by HPD, BARC. His main areas of interest are basically speciation studies of organometallic compounds and carcinogenic organo-pollutants in environment using advanced analytical techniques like Solid Phase Micro Extraction – Gas Chromatography Mass Spectrometry (SPME-GC/MS) technique. He is also involved in the estimation of trace metals in environmental matrices using spectroscopic and electroanalytical techniques. He has worked on radiochemical separation of plutonium, strontium and lead isotopes in environmental samples.*

Dr S. Sadasivan *joined Health Physics Division of BARC in December 1961 after graduating from Madras University. He obtained Ph.D. from Mumbai University for his work on Atmospheric Science. He had specialised in country-wide radioactivity fallout measurements and subsequently was involved in studies on both fallout measurement and natural radioactivity in the environment. He has also worked extensively in analysis of toxic and trace elements in different environmental matrices, such as air particulates, and sediments, by using nuclear and related analytical techniques. He has more than 150 publications in various National and International journals. He is the ex-head of Environmental Assessment Division, BARC.*

Immobilization of Antibody Spots on Glass Surfaces – Potential Use as Antibody Chips for Multianalyte Assays

M.G.R. Rajan and Bharti Gupta
Laboratory Nuclear Medicine Section, Bio-Medical Group
Bhabha Atomic Research Centre

MULTI-ANALYTE IMMUNOASSAYS (MAIA) – a concept put forth by Prof. Ekins over a decade ago – promises to be a cutting edge technology in clinical chemistry. It will offer the advantage of estimating many analytes in one assay as compared to present assays where each assay can estimate only one analyte. MAIA, based on antibody chips (similar to DNA chips) will use miniscule amounts of reagents and patient sample compared to the latter. By enabling simultaneously, a battery of tests related to a given disease or associated diseases, it can save valuable time for patient management. In short, antibody-chip MAIA can revolutionize immunoassay technology just as the DNA chip is revolutionizing gene analysis.

However, putting MAIA into practice needs team-effort from immunoassayists, chemists, physicists, instrumentation and robotic engineers.

Objective

At the core of MAIA is the 'antibody chip' a small inert glass or plastic matrix on which a number of antibodies, each specific to a different analyte, is immobilized at spatially determined sites.

We have plans to develop this technology and have carried out preliminary experiments to standardize and gain expertise in making antibody coated matrix.

Materials and Methods

Standard microscope cover slips, 13 mm dia., were used as the substrate. They were silanized and activated with glutarladehyde as the bifunctional agent.

Polyclonal antibodies to T4 and monoclonal antibodies to TSH were spotted on the activated glass surface, incubated for 1 h, unreacted antibodies washed off and surface blocked with BSA.

Fixed amounts of ^{125}I-T4 mixed with different concentrations of T4 standards in serum (RIA format) were used to test the viability of the coated anti-T4 antibody spots.

Using TSH standards and a second anti-TSH antibody labeled with ^{125}I, the coated anti-TSH monoclonal antibodies were tested in a sandwich (IRMA) assay.

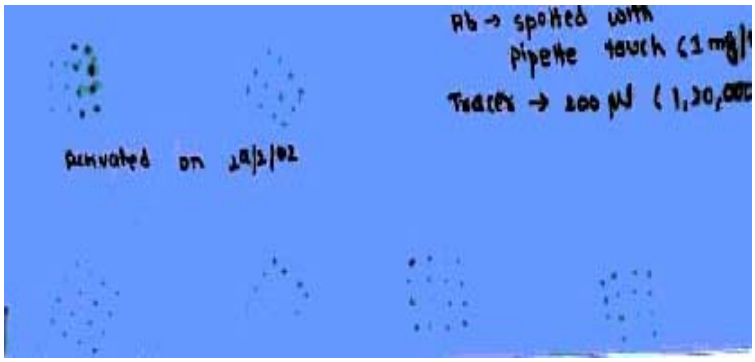

Fig. 1 Anti-T4 antibody spots made by touching activated glass disc with a pipette tip, containing antibody solution (1mg/ml).
Entire disc reacted with 200 µl of I^{125} labeled T4 tracer (1,20,000 cpm)
Autoradiography exposure time –3 days.

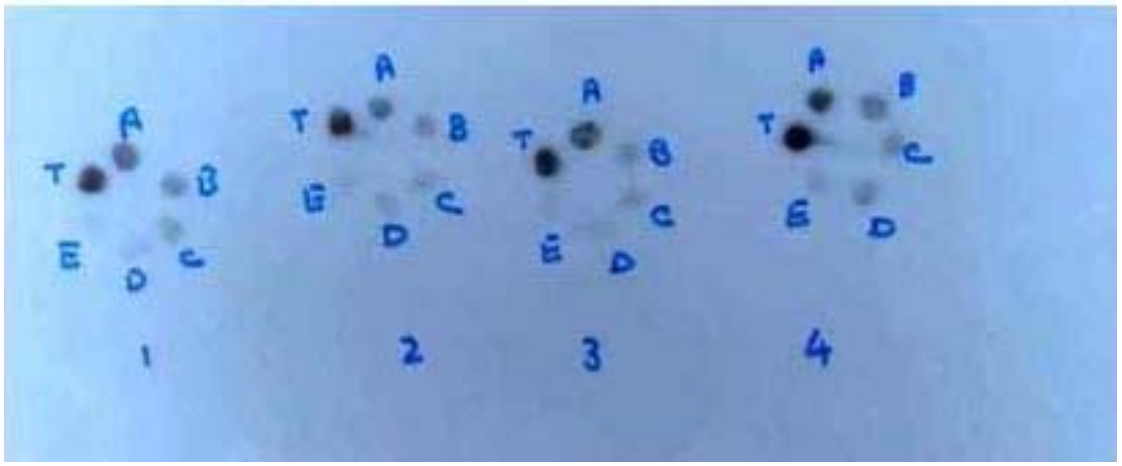

Fig 2 Anti-T4 polyclonal antibody spotted - 2 μl (1mg/ml).
1μl of T4 standard (20,10,5,2.5,0 μg/dl) was mixed with 1μl I^{125}-T4 (30,000-cpm/μl) placed on antibody spots. Incubated for 1 hour and rinsed with PBS-Tween 20.
Autoradiography exposure time - 2 days

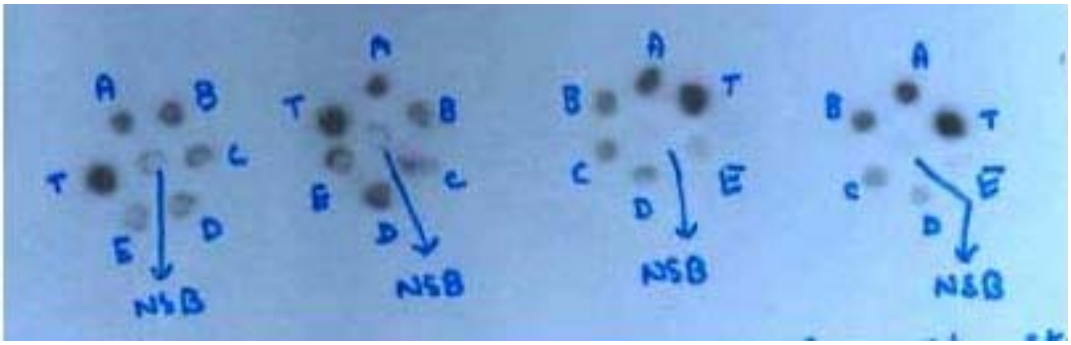

Fig 3 Stability study. 2 μl of anti-T4 antibody (polyclonal) was spotted
Assay done 14 days after antibody spotting. Procedure same as in Fig.2
For testing of non-specific binding 1 μl of 100 μg/dl of T4 standard mixed with 1 μl I^{125} T4 (20,000 cpm/μl) was used.
Autoradiography exposure time - 2 days

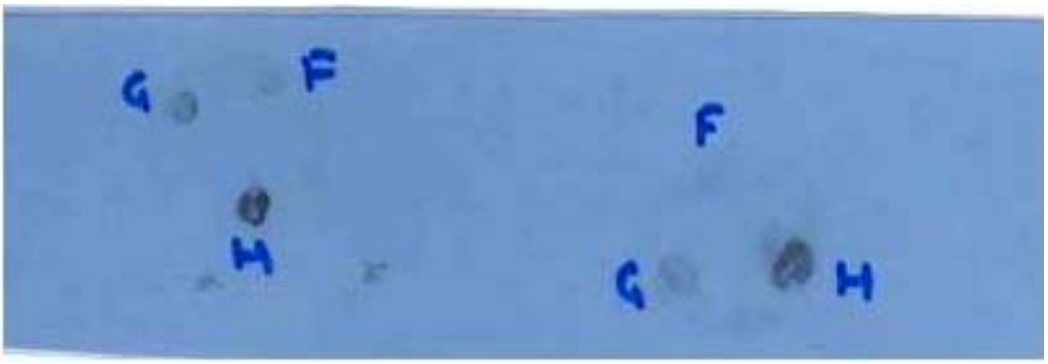

Fig 4 Anti –TSH monoclonal antibody spotted – 2 μl.
Incubated for 1 hour with 3 μl of different TSH standards (100,50,25 μIU /ml) and rinsed with PBS.
Incubated for 2 hrs with 200 μl of TSH tracer (1,40,000cpm/disc) and rinsed with PBS-Tween 20. Autoradiography exposure time - 4 days.

After washing away the unreacted tracer, the amount of tracer that was bound was visualized by autoradiography using AGFA X-ray film.

Results

Using our procedure we could spot antibodies at multiple locations. They were covalently bonded, with negligible background. The antibodies retained their antigen binding property.

The amount of tracer that reacted was visualized by autoradiography. Dark spots were seen with an intensity inversely relative to the concentration of T4 (RIA) and directly relative to the concentration of TSH (IRMA).

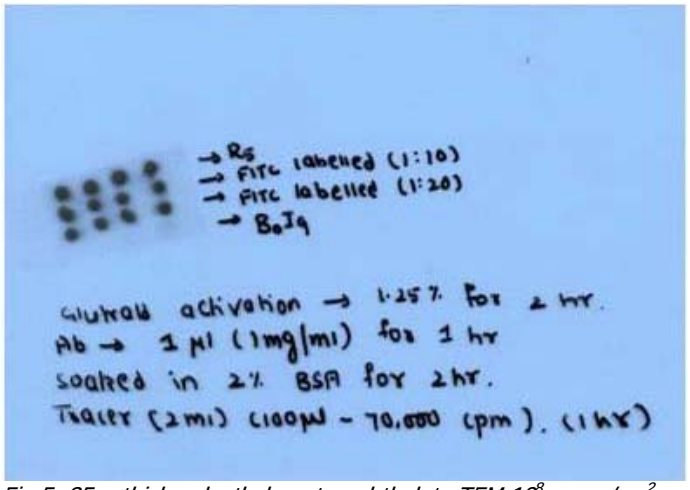

Fig 5. 25 µ thick polyethylene terephthalate TEM 10^8 pores/cm^2 and 1µ dia were activated with glutaraldehyde and antibody was spotted on them as was done for the glass discs. Good coupling of plain and FITC conjugated antibodies are seen. The background and non-specific binding is insignificant

Discussion

Our experiments are preliminary, but show that we have standardized the chemistry required for covalently coupling antibodies to small glass discs, which could be used as the 'antibody-chip' matrix.

Using autoradiography we have demonstrated the validity of our process although radioactivity is not the tracer of choice for multi-analyte immunoassays.

The uniform darkening, within the spot, shows that quantitative information is independent of the size of the spots. Hence, very minute spots could be used and antibody chips, until recently just a concept, can be realized in practice.

A lot more work involving immunoassayists, chemists, physicists, instrumentation and robotic engineers is required before MAIA comes into routine use.

References

1. R.P. Ekins and F.W. Chu: Multianalyte Microspot immunoassay – Microanalytical "Compact Disk" of the future. Clin Chem 37: 1955-1967 (1991)

Addendum

Following the above study, there was a continued search for a better substrate which was flexible, porous and required minimal activation for coating the antibodies. We tested track etched membranes (TEM) prepared by Dr. R.H. Iyer, Emeritus Scientist, Nuclear Recycle Group, B.A.R.C., as potential substrates. These are thin polycarbonate and and bombarded with heavy ions in a Pelletron accelerator to a pore density of 10^5 - 10^8 /cm^2. Further these membranes are etched in nitric acid to give very uniform pore dimensions. Although plastics have been used for coating antibodies with polystyrene being the most popular, it is not suitable for MAIA because of its physical, chemical and background fluorescent properties. Our preliminary experiments show that polyethylene terephthalate films (10 – 25 µ metres) thick with a pore density of 10^8/cm^2 and pore diameter of 1µ was quite suitable as a substrate for coating antibodies as shown in Fig.5. Further work is in progress.

This paper was awarded the Best Poster Award in the 9th Asia Pacific Congress of Clinical Biochemists held at Delhi during March 9-14, 2002

About the authors ...

Dr M.G.R. Rajan, *Head, Laboratory Medicine Section, Bio-Medical Group, BARC, joined BARC in 1978 through the 21st batch of Training School. He underwent training during May-July 1984 in the culturing of malarial parasites and extracting antigens for immunodiagnosis at Guys Hospital, London. He also studied the theory and practice of Radioimmunoassay, particularly the concept of free thyroid hormones and multianalyte immunoassays at Middlesex Hospital Medical School, London. He underwent a IAEA-sponsored course on preparation, storage and distribution of bulk reagents for radioimmunoassay in October 1989 at National Institute of Health, Nonthamburi, Bangkok, Thailand. The course gave practical and theoretical training in all the aspects pertinent to producing and preparing and quality control of reagents required for radiommunoassay.*

Dr Rajan has been involved in the development of new RIAs for thyroid disorders and other diseases. His field of work has been in pursuing the objective of developing a comprehensive set of assays for a thorough in-vitro evaluation of thyroid disorders and, presently, for diabetes.

His current interest is in developing multi-analyte immunoassays (MIA) to assay all analytes relevant to a given disease. He supervises the routine RIAs for thyroid related hormones carried out on patients coming to RMC for diagnosis and treatment.

Dr Rajan also engages himself in teaching of radioimmunoassay and statistics to students doing the DRM and DMRIT course at RMC and BARC Training School.

He received his Ph.D. for his work entitled, "Studies in the estimation of free (non-protein bound) thyroid hormones", from Mumbai University in 1993. He has 21 papers published to his credit and has presented 30 papers at Conferences. He has delivered the Brig S.K. Muzumdar Oration at the 30th Annual Conference of the Society of Nuclear Medicine - India on December 3, 1998. He is a Life Member of the Society of Nuclear Medicine (India), Endocrine Society of India, Association of Clinical Biochemists of India, Indian Association for Nuclear Chemistry and Allied Sciences, Indian Association for Radiation Protection, Indian Immunological Society and Action Council against Tobacco.

Ms Bharti Gupta, *M.Sc. (Biochemistry) from Jamia Hamdard University, is actively involved in develolpment of multianalyte immunoassay, which allows simultaneous measurement of several analytes related to a given disease. This will save time in patient management.*

Patient oriented services involve serum measurement of T4, TSH and Tg by RIA and IRMA.

Post-Weld Heat Treatment – Case Studies

Khaleel Ahmed and J. Krishnan
Centre for Design and Manufacture
Bhabha Atomic Research Centre

Introduction

HEAT TREATMENT IS AN IMPORTANT operation in the final fabrication process of many engineering components. Only by heat treatment it is possible to impart high mechanical properties to steel parts and tools for sophisticated applications.

Heat treatment is considered to be very important tool of the metallurgist by which he can alter the properties of steel easily. The same steel can have a very wide range of mechanical properties if subjected to different heat treatment. Today when science and technology are advancing very rapidly in pursuit of higher and higher properties in materials, heat treatment plays a very important role.

Principles of Heat Treatment

Heat treatment may be defined as a sequence of heating and cooling designed to get the desired combination of properties in the steel. The changes in the properties of steel after heat treatment are due to the phase transformations and structural changes that occur during the heat treatment. The factors, which determine and control these structural changes, are called the principles of heat treatment. The important principles of heat treatment are as follows:

1. Phase transformations during heating.
2. Effect of cooling rate on structural changes during cooling.
3. Effect of carbon content and alloying elements.

Post Weld Heat Treatment

High level residual stresses can occur in weldment due to restraint by the parent metal during weld solidification. The stresses may be as high as the yield strength of material itself. When combined with normal load stresses these may exceed the design stresses. The removal of residual stresses takes place due to the fact that the thermal energy received by the metal allows for grain boundary sliding and removal of metallurgical defects like dislocations, vacancies and slip planes. A most important aspect of Post Weld Heat treatment is the prevention of Brittle Fracture. Post weld heat treatment softens the hardened zones and makes the machining easy. Removal of residual stresses becomes necessary where dimensional stability is required. The heat treatment consists of the stress-relief, annealing or solution annealing depending upon the requirements.

Thermal Stress Relief

Residual stresses resulting from welding are reduced by a post weld thermal stress relief heat treatment. The residual stress remaining in a material after stress relief treatment will depend on rate of cooling.

The percentage relief of internal stress is independent of steel type, composition or yield strength. The effect of varying time and temper are shown in the graph below:

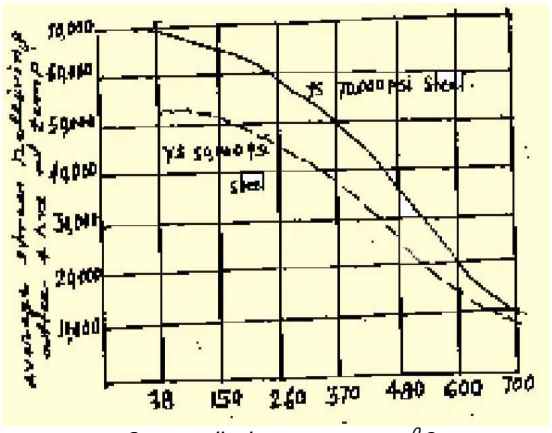

Stress relieving temperature ^0C

The temperature reached during the stress relief treatment has a far greater effect in relieving stresses than the length of time the specimen is held at that temp. The closer the temperature is to the critical or re-crystallization temperature, the more effective it is in the removal of residual stresses.

When a thermal stress relief treatment is employed to reduce residual stresses, other important properties must be taken into account. The micro-structure, tensile and impact strength are among the properties affected by the Stress relief treatment.

A post weld heat treatment at 1040° C – 1090° C, spheroidizes the ferrite present in type 347 SS weldments, which effectively reduces sigma formation. This treatment also takes some of the ferrite into solution. An intermediate hold at 595° C is recommended for those weldments to relieve residual stresses and to reduce the susecptibity to cracking during post weld heat treatment.

The heat affected zone (HAZ) in the vicinity of welded joints are aided considerably by post weld heat treatments. The properties of those zones are improved by the reduction of residual stresses together with the metallurgical changes brought about by the H.T. If any dissolved hydrogen is present it is given an aided opportunity to escape.

The necessity for post heating increases with higher carbon content, increased alloy content and cross-sectional thickness of the part.

The temperatures recommended for stress relieving low carbon steels are 595° C to 675° C. One hour per inch of thickness is the basis used to determine the length of time at the desired temperature. Larger periods of time are required at 595° C to achieve the same degree of stress relief as of 675° C.

Thermal stress relief can be conducted in any furnace suitable for heating of the entire weldment. Same time only a portion of the weldment is heated if the structure is uniform in cross-section and the unheated ends are free to move and do not restrict the expansion of the heated part.

The heating and cooling must be gradual and at a rate that will ensure approx. uniform temperature across wall thickness. In general, the greater the difference between max. and min. thickness, the slower should be the rate of temperature change. Because of variable factors such as strength characteristics of the metal and geometry of the parts, it is not possible to recommend formula for max. heating or cooling rates. The following rules can be used as an approx. guide for simple cases:

Case 1

Where the ratio of max. to min. thickness does not exceed 4 to 1 heating or cooling rate should not exceed 200° C/hr divided by the max. thickness in inches at the weld.

Case 2

Where the ratio of maximum to minimum thickness exceeds 4 to 1, heating or cooling rates should not exceed

1 inch thick – 95° C/hr
2 inch thick – 65° C/hr
3 inch thick – 38° C/hr
4 inch thick – 27° C/hr
5 inch thick – 16° C/hr
6 inch thick – 10° C/hr

For complicated structures with members of widely varying thickness the safest procedure is to attach thermo-couples to all critical sections and not permit more than 42°C difference between any two sections

In this paper six case studies of post weld heat treatment for nuclear components have been discussed.

Case Studies

12" NB Carbon Steel Pipe: 12" NB Carbon Steel pipe have been welded by GTAW required for Kaiga Atomic Power Project. After joining/welding, thermal stress is developed, to reduce their thermal stresses post weld heat treatment done.

The welded pipe, after cleaning the joint has been loaded in a localised set up furnace and pre-heated to 300° C and then Temp. raised to 625°C to 650° C at the rate of 150° C/hr (max.)
Soaking time: 45 minutes

Rate of cooling 150° /hr cool up to 300° C and then still air cool. The treatment has been done to achieve full strength.

12" NB C.S. Elbow: 12" NB C.S. Elbows welded by GTAW required for Kaiga Atomic Power Project. After welding post weld heat treatment have been done.

The job loaded in BHF and pre-heated to 300° C Temp. raised to 625° C to 650° C at the rate of 150°/hr
Soaking time: 45 minutes

Rate of cooling 150° C/hr cooled up to 300° C then still air cool.

The purpose of the treatment was to achieve full strength.

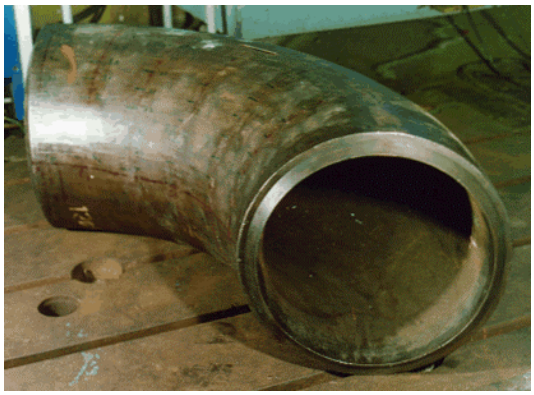

12" NB C.S. elbow

Detector Frames for Station II – PHENIX

CDM was assigned to develop and manufacture North and South hanging structures (for N & S arm magnets) out of Aluminium Alloy 6061 T6. Each of these structures consists of 4 Front and 4 Rear chambers and each of these chambers is made up of a pair of Al. Alloy Frames. To develop the manufacturing procedure, one North side Front chamber was built on prototype basis, adopting weldment route for Aluminimum structures, welded structure calls for post-weld heat treatment (Stress relief) for which a special furnace, of triangular shape with 2.5 m long slides was built. The prototype chamber was inspected and approved by Los Alamos National Labs, USA at CDM.

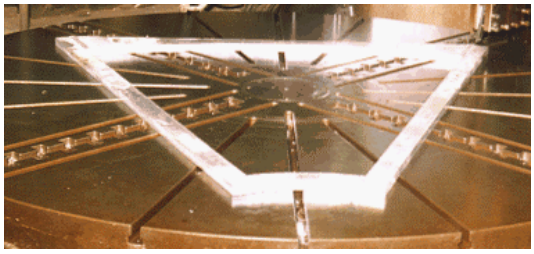

Phenix aluminium frame

Solution annealing of the frame carried out (Fr. Stress relieving to effect solid solution of alloying constituents (e.g. Mg, Cr, and Si) and to improve mechanical properties of Aluminium alloy.

Material: Al 6061 (Al, 1.0 Mg, 0.25% Cu, 0.6% Si, 0.20% Cr)
Soaked for 2 hrs at 55° C ± 5° C and then water quenched.
Aging (precipitation hardening) (to be done within 18 Hrs of solution treatment) at temp. 170° C ± 5° C
Soaked for 12 hrs and still air-cooled.
(Hardness obtained 100 – 120 BHN).

During this process precipitation of soluble constituents (e.g. Mg, Cr, Si) from Super saturated solid solution takes place. As this precipitation progress the strength of material increases.

Stress Relieving of SS 316 Pipe after Stellite Deposition

Pipe loaded in furnace at 300°C pre heat temp. of and heated to 900°C (rate 150°C/hr) soaked

for 30 minutes at 900°C and allowed to cool at rate of 150°C/hr up to 400°C and then furnace cool. This operation was carried out to obtain full hardness and uniform stresses.

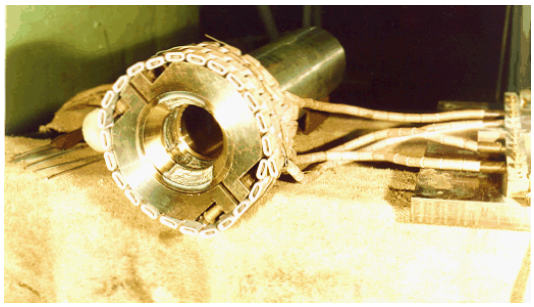

PFBR sleeve

Post Weld Heat treatment of Aluminium Servo-Drive Housing

Material: Al LM-14
Composition: Al, Cu: 3.5% to 4.5%
Si: 0.7 %
Mg – 1.2 to 1.8%
Cr < 0.21%
Solution Heat treatment –
Temp. 515° C ± 5° C for 6 hrs and then Air blast quenching
Aging (Precipitation Hardening)
Temp: 232° C ± 5° C for 1 to 3 hrs
And cool in still air
T.S: 215 to 280 Mpa
Hardness: 100 BHN (approx.)
This has been done for stress relieving of the housing.

Post Weld Heat Treatment of SS 430 (Martensitic) + SS 304 (Austenitic) Weld

Job heated at the rate of 100° C/hr up to 700° C 20° C and soaked at this temp. for 5 hrs. Furnace cool at rate of 30° C/hr up to 595° C and then cool in still air. This operation carried out to achieve impact properties.

Seal Disc

Seal disc is used to prevent escape of heavy water from the coolant channel. The seal disc consists of a disc made of 17-4 PH heat treated to H 1100 condition to which is bonded an annular disc of nickel, about 1.5 mm thick by electro deposition from an aqueous bath. Sealing is accomplished by deflecting the sealing disc on the face of the end fitting of the coolant channel and then locking the deflection. Nickel serves as a sealing gasket. For efficient sealing the nickel should be soft (hardness not more than 170 HV) and the bond between nickel and SS should be adequately strong.

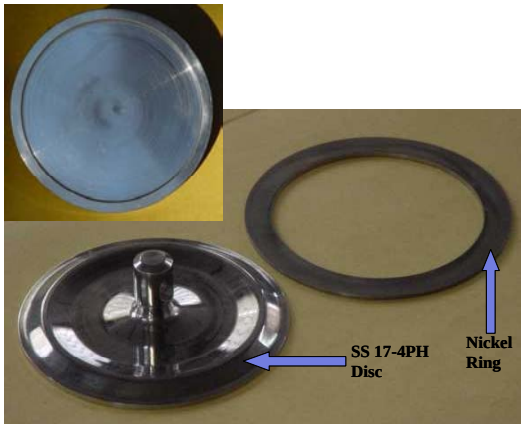

Seal disc

The seal disc is heat treated after Nickel diffusion bonding as per procedure stipulated below.

Seal disc are given solution treatment and precipitation hardening. Seal disc are heated in furnace to 1050°C at the rate of 25-50° C/hr and held for 30 minutes. Thermo-couples are fitted at the ends and the middle zone. The job then quenched in oil at room temp. 30° C. Subsequently quenched in cold water at 5-10° C. Then precipitation hardening at H1075 (570 to 585° C) carried out.

This has been done to achieve appropriate conditions prior to diffusion bonding.

Conclusion

Post weld heat treatment is necessary to satisfy one or more end requirements. Every case has to be independently treated.

This paper was adjudged as the Best Paper presented at the International Symposium on Thermal Spray held at Mumbai during May 2-4, 2002

About the author ...

Mr Khaleel Ahmed, *F.I.E, is working as Engineer-in-charge of Surface Treatment and FHT group of Manufacturing Section of Centre for Design and Manufacture, BARC. He is a B.E (Mechanical) from College of Engineering, Guindy (University of Madras).*

Dr J. Krishnan is *heading the Manufacturing Section of Centre for Design and Manufacture, BARC. He is a Ph.D in Welding from I.I.T Mumbai and a Fellow of Indian Institution of Welding. Apart from welding and fabrication, surface engineering is also a part of Manufacturing Section. He has 50 technical papers presented / published. He is actively involved in various programmes of IIW, ISNDT, ASM and various educational institutions.*

Molecular Motions in Condensed Matter Neutron Scattering Studies

S. Mitra and R. Mukhopadhyay
Solid State Physics Division
Bhabha Atomic Research Centre

Introduction

THERMAL NEUTRON IS A POWERFUL probe to study the dynamics in condensed matter due its energy matches closely with the excitations of the molecules in condensed matter. Periodic motions give rise to characteristic frequencies in the spectrum whereas stochastic motions lead to Doppler broadening of the scattered neutrons which result in the broadening of the elastic line known as quasielastic broadening. Quasielastic neutron scattering (QENS) is a unique technique [1,2] which provides information on the time scale, geometry of the stochastic motions as well as the shape of the potential. Further, systems containing protons are especially suitable for neutron scattering studies due to its large scattering cross-section. In this paper, the study of molecular motions in variety of solids and liquids in different environments, namely, the molecular motions in confined media, e.g., molecular motions in different zeolitic systems, porous alumina; reorientational motion of molecules in plastic crystals and in nanophase materials in different phases will be presented. Most of the experimental work is performed using the QENS spectrometer at Dhruva reactor at Trombay. The quasielastic spectrometer at Dhruva designed by modifying the conventional triple axis spectrometer facilitates higher throughput. The scattered neutrons are energy selected by a large analyser crystal and detected by a position sensitive detector. Thus, an energy scale is set up along the detector and the spectrometer provides energy spectrum for one instrumental configuration. This type of spectrometer is known as MARX (Multi Angle Reflecting X-tal) spectrometer, first built in Risö, Denmark [3]. This MARX spectrometer is designed, built, fabricated and commissioned, indigenously, at Dhruva, Trombay. It has been working for several years and a number of experiments have been carried out, collaborating with many Institutes/Universities in India, resulted in many interesting scientific revelations. Details on this spectrometer are given in Ref. 4. Some basic principles of QENS technique will be discussed below.

In an inelastic neutron scattering experiment, the quantity measured is the double differential scattering cross section which represents the probability that a neutron is scattered with energy change ħω into the solid angle dΩ [1]. For hydrogenous systems, incoherent scattering dominates and the measured intensity is proportional to $\frac{k}{k_0}\left[\sigma_{inc} S_{inc}(\mathbf{Q},\omega)\right]$. $S_{inc}(Q,\omega)$ is known as the scattering law, where *inc* denotes the incoherent scattering components. k and k_0 are the final and initial wave-vectors. Q = k- k_0 is the wave-vector transfer and ħω= E-E_0 is the energy transfer. For quasielastic events, the incoherent scattering law for rotational motion of a molecule can be approximated as addition of an elastic and a quasielastic component. Quasielastic part is a Lorentzian function whose half width at half-maximum (HWHM) is inversely proportional to the time scale of the rotational motion. It is convenient to analyse the data in terms of elastic incoherent structure factor (EISF) which can be defined [1] as the fraction of elastic intensity out of the total intensity in $S(Q,\omega)$ and provides information about the geometry of the molecular motions.

In the case of translational motion, incoherent scattering law, $S^{T}_{inc}(Q, \omega)$, consists only a Lorentzian [1]. For a system, where both translation and rotational motion exist simultaneously, the scattering law can be written as $S^{Tot}_{inc}(Q,\omega) = S^{T}_{inc}(Q,\omega) \otimes S^{R}_{inc}(Q,\omega)$. Here $\otimes$ represents the convolution product.

Few examples of rotational and translational motion studied by us are discussed below.

Dynamics of Water Molecules in Confined Media of Porous Alumina

Water in porous materials such as vycor glass, silica gel, Nafion, lignite coal [5] etc. have been actively under investigation because of their relevance in catalytic and separation processes. Alumina exemplifies the physiochemical properties of this class of porous materials in that firstly, it has high surface area and in aqueous suspensions has variable pH values and secondly, that it undergoes reversible chemical changes when exposed to water. These properties make alumina very useful in adsorptive and separation processes.

QENS experiments were performed on alumina gel heat treated at 700 ^{o}C with hydration level of 30 wt% using the high resolution LAM-80ET spectrometer (resolution 17 μeV and 6.5 μeV) at KENS, KEK, Japan [6] and the medium resolution QENS spectrometer (resolution 200 μeV) at Dhruva [4]. The translational motion is studied using higher resolution instruments where the faster dynamics (rotational) contribute only as a background. After incorporating the information about translational motion, the data from the medium resolution instrument were analysed to obtain the information about the rotational dynamics [7].

Translation motion of water confined in the pores is observed in the high resolution data only. It may be noted that due to the confinement effect there exists an elastic line in the scattering law for translational motion also, as the water molecules are not allowed to leave the spherical pores [8] and is attached to the

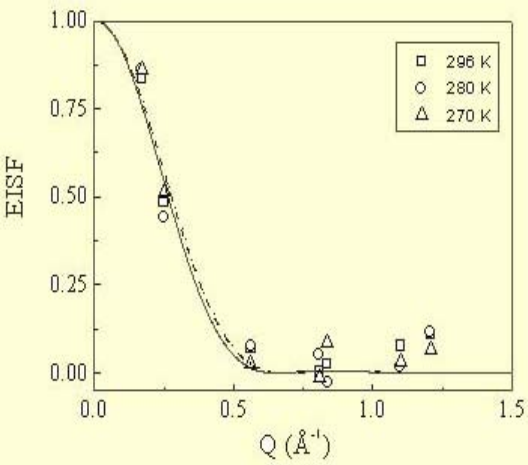

Fig. 1 Experimentally obtained EISF in case of water in hydrated alumina gel at different temperatures. Solid line is the fit with the theoretical EISF for water confined in spherical pores with radius of spherical pores as a parameter.

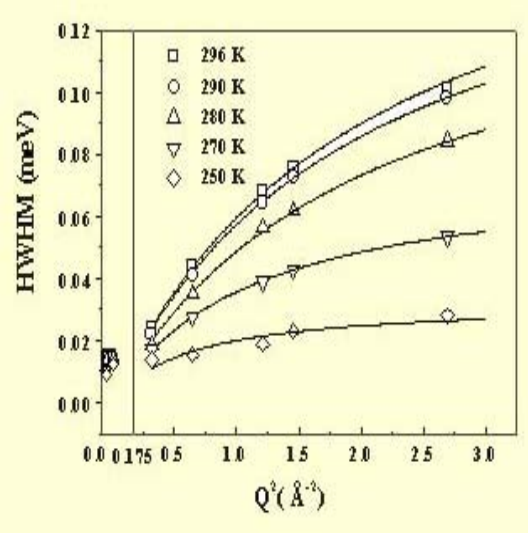

Fig. 2 Variation of HWHM with Q^2 in hydrated al-gel. Solid lines are the fits with jump diffusion model.

surface of the pores. Fig. 1 shows the extracted EISF at different Q values. The radius of spherical pores *a* is known as the localisation radius. The variations of HWHM of quasielastic lines at different temperatures with Q^2 are shown in Fig. 2. $\Gamma(Q)$ Vs. Q^2 shows a flat and constant value Γ_0 at small Q and increases asymptotically approaching another constant

value Γ_∞ at large Q. The first feature is due to the confinement effect. Volino and Dianoux [8] predicted $\Gamma(Q)$ to remain constant ($\Gamma_0 = 4.33[D_{loc}/a^2]$) from Q=0 to $Q=Q_0=\pi/a$. The D_{loc} represents the local diffusion constant within the volume of confinement. At larger Q values, the linewidths follow the jump diffusion behaviour [9] with diffusion constant (D_l) and residence time *in between* jumps (τ). From the constant value of $\Gamma(Q)$ at low Q, local diffusion constant, D_{loc} is estimated.

The data from the QENS spectrometer at Dhruva have a contribution from both the translational and rotational motion of the water molecules. A full scattering law comprising the translational and rotational motions was used to analyse the data from the QENS spectrometer. For the rotational part of the scattering law, isotropic rotational diffusion as derived by Sears [10] was assumed. The parameters corresponding to translational motion of water as obtained from high-resolution experiment are used as known parameters. Rotational diffusion constant of 0.1 meV was obtained at room temperature. This is very similar to the bulk water diffusion constant at room temperature [11] suggesting that the rotational dynamics remain unaffected.

Dynamics of Alkyl Chains in Monolayer Protected Clusters (MPCs)

The study of structure and properties of ultra thin films at interfaces has advanced at a rapid pace with their potential applications in the fields of optoelectronics and molecular engineering. These ordered films have been classified into Langmuir-Blodgett films and self assembled monolayers (SAMs). The 3D SAMs are monolayers of surfactants formed on a nano-sized metal-core, the whole system together is called the monolayer protected metal clusters (MPCs). The core of this system consists of dense-sphere packing of metal atoms resulting in nanocrystals with specific lattice planes on the surface and the alkylthiolates are adsorbed on these lattice planes. Fig. 3 represents the a) schematic of a MPC and b) superlattice assembly of MPCs. Dynamics of alkyl chains in such a system have been investigated for the first time by quasielastic neutron scattering (QENS) technique [9]. In the cluster superlattice, QENS broadening was observed even at room temperature which is lower than the chain melting temperature (T_{cm}=333K) whereas for the isolated cluster it was seen only above T_{cm}. Similarly in the layered silver thiolate, it was observed above the melting point.

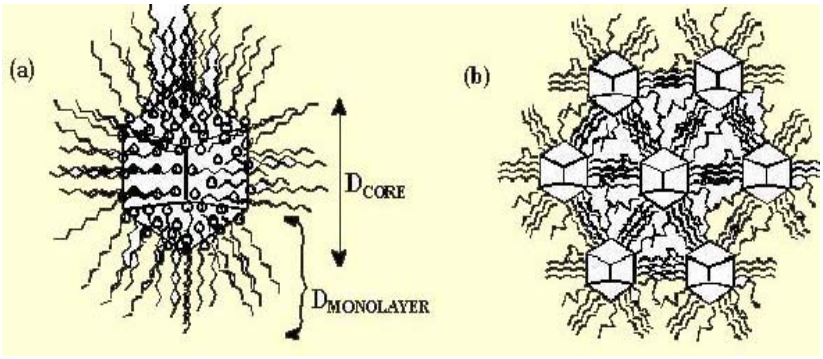

Fig. 3 (a) Schematic of a Monolayer Protected Cluster (MPC) system, (b) Schematic of the superlattice assembly of MPCs.

The experimentally extracted EISF at different temperatures are shown in Fig. 4 for AgC_8. Solid lines in Fig. 4 are the fitted ones assuming uniaxial rotational diffusion [13] about the chain axis, with proportion of alkyl chains participating in the dynamics taken as a parameter. AgC_8 forms a superlattice structure and this is by virtue of the chain interdigitation among the neighboring clusters. The fact that 50 % of the protons participating in the dynamics in the temperature range 300–360 K is in accordance with the structural conformation. However, at 380 K, data show that almost all the chains are contributing to the dynamics. This being closer

to the melting point, the chains, which were earlier held fixed due to interdigitation, now have enough energy to be dynamic.

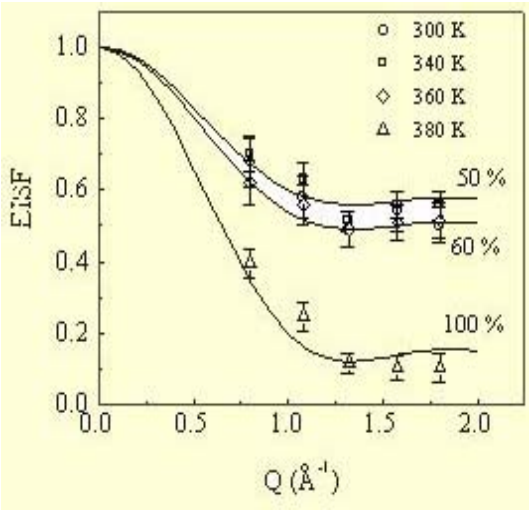

Fig. 4 EISF for AgC_8, as extracted from the measured QENS spectra at different temperatures. The lines correspond to the model in which particle performs uniaxial rotational diffusion.

In case of AuC_{18}, it is seen that above chain melting temperature, all the chains are participating in the dynamics, in contrast to the findings on superlattice AgC_8. In case of layered thiolate AgC_{12}, data could also be described with a uniaxial rotationa diffusion model with 100% of the chains being dynamic.

Reorientational Motion in Plastic Crystal Pyridinium Iodide

Pyridine salts belong to a big family of molecular-ionic crystals. Extensive study has been reported by others on various pyridinium salts to understand the nature of pyridinium ion in its different solid phases since many pyridinium salts reveal solid-solid phase transitions related to the changes in the ion dynamics. Reorientational motion of pyridinium cation in pyridinium iodide is investigated by high-resolution QENS technique both above and below the transition (T_c=247 K) temperature [15]. Fig. 5 shows the variation of extracted EISF at different temperatures. Lines (*a*), (*b*), (*c*) and (*d*) correspond to the theoretical EISF for 2-fold, 3-fold, 6-fold jump and isotropic rotational diffusion respectively. A clear evidence of order-disorder transition with respect to the pyridinium ion reorientation is established. In the high temperature phase, pyridinium ion is found to undergo reorientational motion around the axis perpendicular to its plane and is best described by a 6-fold jump rotation model. Weak quasilelastic broadening is observed below the phase transition temperature, at T=240 K, indicating presence of some residual disorder. Reorientational time and activation energy of rotation are also obtained in the high temperature phase.

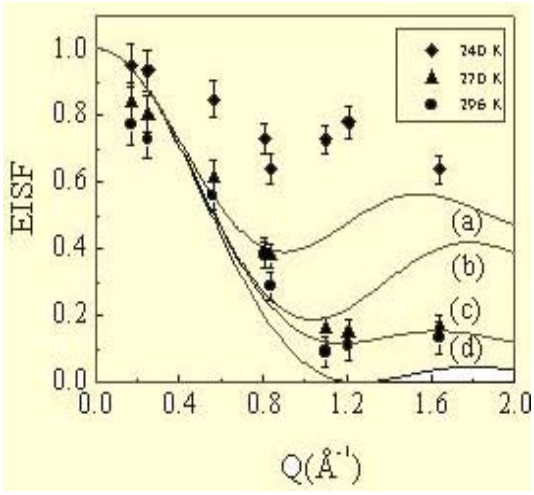

Fig. 5 EISF for pyridinium iodide, as extracted from the measured QENS spectra at different temperatures. Lines (a), (b), (c) correspond to the theoretical EISF for 2-fold, 3-fold and 6-fold jump respectively. Line (d) corresponds to the theoretical EISF for isotropic rotational diffusion.

Conclusions

To conclude, quasielastic spectrometer in Dhruva, Trombay has been operating successfully for last several years and is successfully used to elucidate dynamics of molecules in different systems, viz. liquid crystals [16], dynamics of different hydrocarbons in cages like zeolite, molecular

sieves [17,18], molecular reorientations of alkyl chains in monolayer protected clusters (MPC) [12], molecular reorientations in various organic and inorganic salts in different solid state environments, etc.

References

1. M. Bée, *Quasielastic Neutron Scattering*, (Adam-Hilger, Bristol, 1988).
2. W. Press, *Single Particle Rotations in Molecular Crystals*, (Springer, Berlin, 1981).
3. J.K. Kjems and P.A. Reynolds, *Inel. Scatt. Neut.* (IAEA, Vienna, 1972) p. 733.
4. R. Mukhopadhyay, S. Mitra, S.K. Paranjpe and B.A. Dasannacharya, *Nucl. Inst. Meth. A* **474**, 45 (2001).
5. S. Mitra, R. Mukhopadhyay and K.S. Chandrasekaran, Physica B, **292**, 29 (2000).
6. K. Inoue, T. Kanaya, Y. Kiyanagi, S. Ikeda, K. Shibata, H. Iwasa, T. Kamiyama, N. Watanabe and Y. Izumi, *Nucl. Instrum. Methods A* **309**, 294 (1991).
7. S. Mitra, R. Mukhopadhyay, I. Tsukushi and S. Ikeda, *J. Phys.: Cond. Mat.*, **13**, 8455 (2001); S. Mitra, R. Mukhopadhyay, K.T. Pillai and V.N. Vaidya, *J. Non-Cryst. Solids*, **235-237**, 229 (1998).
8. F. Volino and A.J. Dianoux, *Mol. Phys.*, **41**, 271 (1980).
9. P.A. Egelstaff, *An Introduction to the Liquid State*, (London, Academic, 1967).
10. V.F. Sears, *Can J. Phys.* **44**, 1999 (1966).
11. J. Teixeira, M-C Bellissent-Funel, S.H. Chen and A.J. Dianoux, *Phys. Rev. A*, **31**, 1913 (1985).
12. S. Mitra, Binoj Nair, T. Pradeep, P.S. Goyal and R. Mukhopadhyay, *J. Phys. Chem. B*, **106**, 3960 (2002).
13. J.D. Barnes, *J. Chem. Phys.* **58**, 5193 (1973).
14. A.J. Dianoux, F. Volino and H. Hervet , *Mol. Phys. B*, **30**, 1181 (1975**).**
15. R. Mukhopadhyay, S. Mitra, I. Tsukushi and S. Ikeda, *Chem. Phys. Lett.*, **341**, 45 (2001).
16. S. Mitra, R. Mukhopadhyay and K. Venu, *Chem. Phys.*, **261**, 149 (2000).
17. A.K. Tripathi, A. Sahasrabudhe, S. Mitra, R. Mukhopadhyay and N.M. Gupta, *Phys. Chem. Chem. Phys.*, **3**, 4449 (2001); S. Mitra, R. Mukhopadhyay, A.K. Tripathy and N.M. Gupta, *Appl. Phys. A*, (in press).
18. S. Mitra, R. Mukhopadhyay, A. Sayeed, A.V. Anil Kumar, S. Yashonath and S.L. Chaplot, *Appl. Phys. A*, (in press).

This paper received the 3rd Best Presentation award at the XX Colloquium for Young Physicsts, organised by the Indian Physical Society, held at Saha Institute of Nuclear Physics, Kolkata, during August 22-23, 2002.

About the authors ...

Mr Subhankur Mitra *joined Solid State Physics Division, BARC, in 1994 after completing his MSc. (Physics) from University of North Bengal. Since joining, he is working in neutron scattering group and is involved in neutron scattering instrumentation at Dhruva. His field of research includes the study of molecular motions in condensed matter using quasielastic neutron scattering technique. He has 22 research papers to his credit in international journals and about 35 papers in international and national conferences.*

Dr Ramaprasad Mukhopadhayay *joined 23rd batch of BARC Training School in 1979 after completing his MSc. (Physics) from Kalyani University. Since joining, he is associated with neutron scattering group of Solid State Physics Division. Topic of his Ph.D. thesis was "Phase Transitions and Rotational Dynamics of Molecular Solids". He has worked as visiting scientist at ISIS facility, Rutherford Appleton Laboratory, UK during 1990-91, visiting professor at Depto de Fisica de Materiales, Universidad del Pais Vasco, Spain during 1996-97 and at KENS, KEK, Japan in 2000. He has about 55 papers to his credit in international journals and about 70 papers in International and national conferences.*

Surface Evaporation of Metal Substrates by a High Power Strip Electron Beam Source: Laser Spectroscopy Based Characterisation and Monitoring

S.J. Gaur, R.C. Das, A.K. Tak, G.K. Sahu, R.A. Patankar, G.K. Bhowmick, K.G. Manohar, K.B. Thakur and B.N. Jagatap
Laser & Plasma Technology Division
Bhabha Atomic Research Centre

Abstract

Zirconium atomic vapor is generated using an in-house developed strip-focused electron gun capable of delivering up to 100 KW of power. Tunable diode laser based absorption spectroscopic technique is implemented to characterize the zirconium vapour above the source. Atom density is measured at various vertical heights from the two-dimensional source (117 mm x 7 mm) for electron beam powers ranging from 40 kW upto 91 kW. These results are interpreted in terms of the vapour flow models reported in the literature.

Introduction

THERE HAS BEEN A CONSIDERABLE interest in the studies related to the surface evaporation of metal substrates by electron beam and properties of the ensuing atomic vapour. It is known that the atomic vapour, generated in such an evaporation process, undergoes adiabatic free expansion in vacuum and encounters all the regions of hydrodynamics. The resultant vapour then acquires various characteristics such as forwardly peaked atom density, high Mach numbers, non-equilibrium population distribution in the low lying atomic metastable levels and temperature splitting. Understanding of these vapour characteristics, in terms of the gas dynamics and collision physics, is therefore important in designing atomic beam sources for specialized metallurgical applications.

In this paper, we report our work on spectroscopic characterization of an atomic vapour generated by surface evaporation of zirconium using strip electron beam. Absorption spectroscopy using narrow band tunable diode lasers is implemented to this end. The laser beam is coupled to the evaporation chamber using optical fibres, which offers the advantage of a remote and online diagnostics. These features are essential since the evaporation is carried out in a hostile environment consisting of high temperature, high vacuum, high voltage and corrosive metal vapour. Our interest here is in the variation of the atom density of evaporated zirconium as a function of the electron beam power and the distance along the vapour flow direction. This information is valuable for benchmarking the models of electron beam evaporation of zirconium in particular, and refractory metals in general.

Experimental

The schematic representation of the complete experimental set-up used in this study is shown in Fig.1. It consists of two distinct parts: a zirconium vapour generation system and an online diagnostic system involving diode laser and absorption spectroscopic equipment.

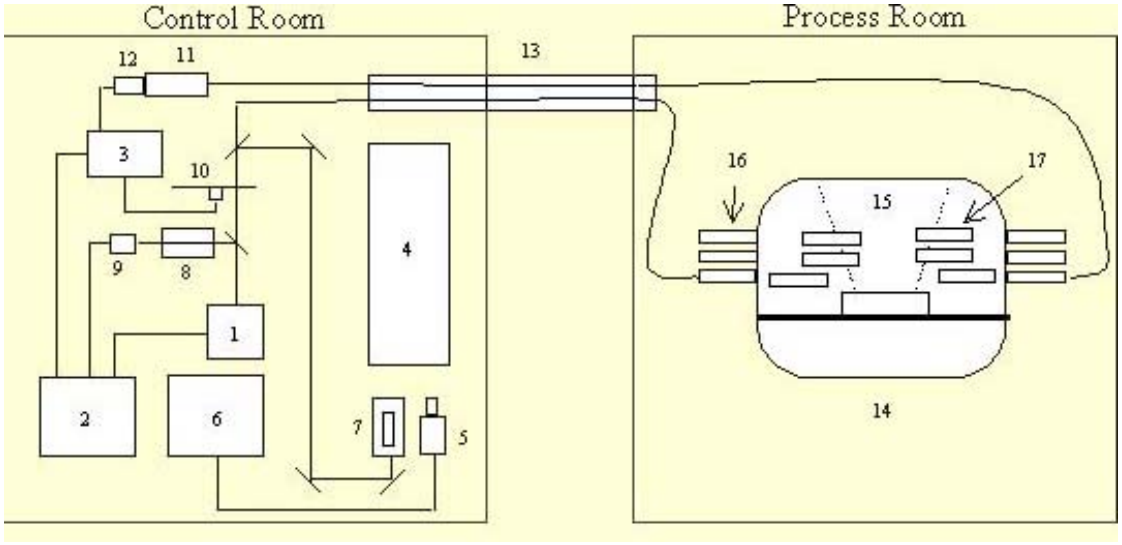

Fig. 1 Schematic diagram of the experimental setup: (1) Diode laser, (2) Computer, (3) Lock in amplifier,(4) High resolution monochromator, (5) CCD Camera, (6) Monitor, (7) Zirconium HCL, (8) Fabry-Perot interferometer, (9) photo diode, (10) chopper, (11) Monochromator, (12) PMT, (13) optical fiber, (14) process chamber, (15) atomic vapor, (16) optical ports, and (17) interaction zone definer.

Zirconium vapor is generated in a strip electron beam heated evaporation chamber, which is essentially a high vacuum compatible double walled water-cooled stainless steel enclosure. A separating flange divides it into two compartments: the lower and upper ones are used respectively for housing an electron gun and a water-cooled copper crucible containing zirconium ingot. The in-house developed [1] electron gun has strip type filament (130 mm long and 3.75 mm wide). Thermionic electrons from the hot filament are electrostatically focused and accelerated to a high energy (40-50 kV), to form a thin sheet by properly shaped grid-anode geometry. The electron beam is rotated by 270^0 using an external magnetic field (50-60 Gauss) generated by two electro-magnetic coils kept in Helmholtz configuration before impinging on the zirconium target.

The temperature of the hot zone on the molten metal pool is measured using a single color disappearing filament type pyrometer through a periscopic arrangement on top of the chamber. The dimension of the hot strip is measured by photographing hot surface along with internal graphite standard using a high-resolution digital camera. The rise of temperature of the hot strip is nonlinear with power due to Marangoni flow and convective conductivity of the liquid metal pool at higher powers [3]. These initial conditions, in turn, govern the propagation of the zirconium vapour above the effective two-dimensional source.

In order to monitor the atom density of the zirconium vapour by laser spectroscopic technique, the process chamber is provided with optical ports on both ends for the entry and exit of a tunable diode laser. These optical ports are designed to avoid deposition of vapor, which can deteriorate the transmission of the diagnostic laser beam. To confine the laser-atomic beam interaction zone length and height, three pairs of cylindrical ss channels are kept at heights 40, 110 and 180 mm above vapor source. These three pairs of channels are kept parallel to the vapor source symmetrically on both sides along length of the source exposing 300, 150 and 150 mm of atomic beam respectively. The channels are kept firmly on their position by graphite plate, which can withstand high thermal radiation from the hot source.

Absorption spectroscopy of zirconium vapour is carried out using external cavity tunable single mode continuous wave diode laser of center wavelength of 675 nm with a typical power of ~ 50 mW and situated in a control room. The laser is scanned electronically across the 676.24 nm spectral line of zirconium, involving ground (0 cm^{-1}) and excited (14784 cm^{-1}) electronic level [2], to generate the absorption spectrum. The atomic line has weighted oscillator strength gf = 0.0022 which ensures that the absorption studies can be done in a vapour of path length in excess of 10 cm and number density in excess of 10^{11} cm^{-3}.

The basic features of the laser and optical setup for the atomic beam diagnostics are as follows: A part (90%) of the narrow band (~ 1 MHz) output of the diode laser is coupled into an optical fiber, which carries the light to the evaporation chamber. The laser light emerging from the fiber is collimated and sent through the zirconium vapour. The transmitted light is again coupled into another fiber to bring it back to the control room where it is filtered by a monochromator for background suppression and detected by a photomultiplier tube (PMT) as shown in Fig.1. A combination of light chopper and lock-in-amplifier (LIA) is used for phase sensitive detection of the PMT signal for filtering of the DC background, which is due to the intense glow from the hot target. The output of the LIA is digitized by an A/D converter. The remaining 10% of the diode laser light is split into two parts: one part is sent through a confocal interferometer (FSR = 150 MHz) and detected by a photodiode to generate frequency marker fringes; while the other part is sent through a high resolution monochromator (1.5 m) along with the emission light from a zirconium hollow cathode lamp (HCL) for tuning the laser accurately to the desired zirconium atomic transition. The laser scan control, data acquisition and storage are performed fully under program control by a computer [4] in the control room. This experimental set up has enabled us to obtain absorption spectra with an excellent S/N ratio. Typical time scale to generate an absorption spectra is ~ half a minute. The control program simultaneously records the digitized LIA output, laser power output and the photo diode output from the interferometer.

Results And Discussion

The experimental procedure, outlined as above, was used to obtain transmission spectrum, $I(\nu)$ vs ν, of zirconium vapour for various electron beam powers dumped on the zirconium ingot. Here I is the transmitted intensity and ν is the frequency of the diode laser; later was tuned in ~10 GHz range across the atomic line center. The atom density of the zirconium atoms in the vapour is related to the optical density (OD), which can be evaluated in a straightforward manner using the transmission data. In Figure-2, we show the OD obtained at 4, 11 and 18 cm above the vapour source when electron beam power is 84 KW. These curves may be used to obtain the number density in the vapour using the relationship, $A(OD)=n_g\sigma L$, where A(OD) is the integrated optical density, n_g is the number density of ground level zirconium atoms integrated over the absorption length L and σ is the integrated absorption cross-section. For the atomic line chosen for this work, σ = 7.35 x 10^{-5} cm^2s^{-1}, which is derived from the reported oscillator strength [2]. The total atom density n is then obtained by the relation $n = n_g/f_g$, where f_g is the fractional population of the ground level. The later value is obtained by evaluating the electronic partition function of zirconium atom by specifying the temperature of the hot zone.

In order to compare the experimental results with theoretical models, the following procedure is used. The source atom number density is calculated using reported vapor pressure formula

$$\log_{10} P(torr) = 9.38 - \frac{30300}{T(^{o}K)}$$

and universal gas law *PV= nRT.* The z'-mean atom number density above the two-dimensional source is then calculated for distance of all the

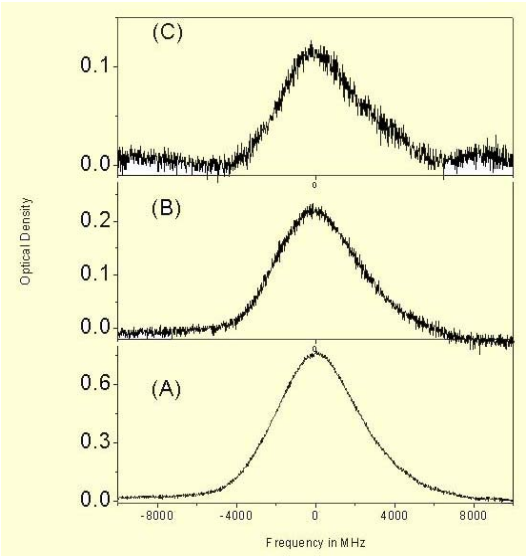

Fig. 2 Absorption spectrum of zirconium vapor as a function of distance from the source. (A) 40 mm, (B) 110 mm and (C) 180 mm. Electron beam power is 84 KW. Frequency is measured with respect to the atomic line center.

three ports after modifying L-mean number density formula reported by Rosengard [5].

$$n(z'\text{–}mean, r) = \frac{n_0 D}{L}\frac{\cos\theta}{2\pi r}\left\{\left[\left(\frac{L+z'}{2}\right)^2 + r^2\right]^{\frac{1}{2}} - \left[\left(\frac{L-z'}{2}\right)^2 + r^2\right]^{\frac{1}{2}}\right\}$$

Here, L is source length (111mm), and D (7mm) is source width, z' (=150mm for interaction at height of 110 and 180 mm) is interaction zone length, r is interaction zone height with respect to target (40,110,180 mm) and θ (=0^0) is angle of inclination of interaction zone with respect to the vertical plane. The experimental and theoretical results are summarized in Table-1.

A combined plot for the source number density, mean-number density found experimentally from absorption experiments and the number density calculated using above formula for all the three ports is given in Figure-3. It can be seen that experimental values and observed values for mean number density matches within 20% for interaction zone at 110 and 180 mm, which are well defined using SS-pipes. The mismatch between observed and calculated values of mean number density for interaction zone at the height of 40 mm is due following reasons: Firstly, vapour in this region is in the transition flow regime of rarefied gas dynamics. Secondly, interaction zone is not well defined as it increases with increasing incident power and source temperature whereas in calculation it is assumed to be same as source length in absence of exact value.

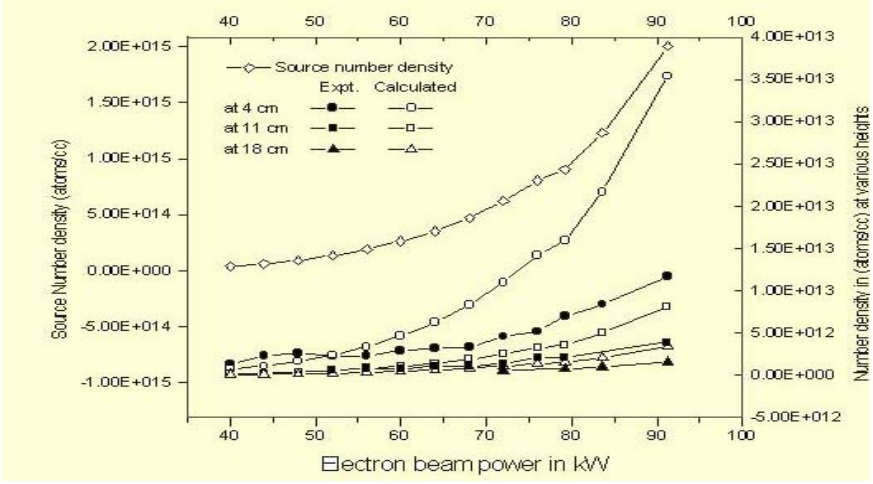

Fig. 3 Comparison of experimentally found number density and calculated values using Rosengard formula (Source temperature measured using single color pyrometer is used for calculation of number density)

Table 1 : Experimental and calculated results of average number density of zirconium as a function of incident e-beam power and vertical height from source using diode laser absorption spectroscopy

Power kW	Temp (K)	V.P. (Torr)	N_0 (Cal)	At 4 cm			At 11 cm			At 18 cm		
				N_1 (Expt) x 10^{12}	N_1 (Cal) x 10^{12}	**FWHM** GHz	N_2 (Expt) x 10^{12}	N_2 (Cal) x 10^{12}	FWHM GHz	N_3 (Expt) x 10^{12}	N_3 (Cal) x 10^{12}	FWHM GHz
40	2673	0.011	3.98E13	1.3	0.7	2.47		0.11			0.05	
44	2722	0.018	6.25E13	2.3	1.1	3.16		0.18			0.08	
48	2768	0.027	9.4E13	2.6	1.7	2.74		0.27			0.12	
52	2811	0.04	1.36E14	2.3	2.4	2.68	0.56	0.39	2.52		0.18	
56	2852	0.057	1.92E14	2.3	3.4	2.48	0.85	0.54	--		0.25	
60	2891	0.079	2.63E14	2.9	4.6	2.62	0.75	0.75	2.95		0.35	
64	2929	0.108	3.55E14	3.2	6.3	2.52	1.1	1.0	2.53		0.47	
68	2966	0.146	4.72E14	3.3	8.3	2.8	1.1	1.3	2.32		0.63	
72	3003	0.195	6.23E14	4.6	11	2.64	1.3	1.8	2.34	0.58	0.8	1.75
76	3038	0.255	8.05E14	5.2	14	2.52	2.1	2.3	2.39		1.1	--
79.2	3054	0.287	9.03E14	7.0	16	2.44	2.1	2.6	2.36	0.78	1.2	1.86
83.6	3098	0.398	1.23E15	8.4	22.7	2.48		3.5	2.32	0.96	1.7	1.87
91.2	3170	0.663	2.01E15	12	35	2.4	3.9	5.8	2.1	1.6	2.7	1.82

- Experimental number Density was obtained by using ground state population fraction corresponding to source temperature

In conclusion, we have measured atom density as a function of electron beam power and vertical distance from a two-dimensional source, generated by heating of zirconium using a strip electron beam source. These results are then used to show the validity of the theoretical model on beam formation.

Apart from the measurement of atom density, the laser absorption spectroscopy can be gainfully utilized to study the energetics of the atomic beam; the studies related to this aspect will be published elsewhere.

References

1. K.B.Thakur, G.K.Sahu, R.V.Tamhankar and Kartik Patel, Rev. Sci. Inst., 72(1), 207-15(2001).
2. W.F.Meggers, C.H.Corliss and B.F.Seribner. NBS Monograph 145 (1975).
3. G.K.Sahu, R.A.Patankar and K.B.Thakur, Symposium on Applications of Plasma, Laser & Electron Beams in Material Processing, 25-28 September2002, BARC, Mumbai, India.

4. S.Pradhan, S.J.Gaur, V.S.Rawat, K.G.Manohar and B.N.Jagatap. in "Recent Advances in Atomic and Molecular Physics", ed. Rajesh Srivastava (Phoenix Publishing House 2001) p.296.

5. Rosengard A 1989 *16th Rarefied Gas Dynamics Conf.* (AIAA) 313-26.

This paper was awarded the Best Paper prize in the Diagnostics and Modeling session of the DAE-BRNS Symposium on "Applications of Plasmas, Lasers & Electron Beams in Advanced Materials Processing (PBAMP-2002)," held at BARC, Mumbai, during September 25-28, 2002.

About the authors ...

Ms Savita J. Gaur *is a Senior Research Fellow in the BARC-Mumbai University Collaboration Programme. She did her M.Sc. (Physics) from Mumbai University (1999). Her field of work is laser spectroscopy and laser cooling of atoms.*

Mr R.C. Das *is from 41st batch of BARC Training School. He did his M.Sc. (Physics) from Utkal University (1997). His field of work is laser spectroscopy and quadrupole mass spectrometry.*

Mr A.K. Tak *is from 37th Batch of BARC Training School. He obtained his M.Sc. (Physics) from IIT Kanpur (1993). His field of work is laser spectroscopy and cluster formation in plasmas.*

Mr G.K. Sahu *is from 38th batch of BARC Training school. He obtained his M. Sc. (Physics) from Berhampur University (1993). His present field of work is electron beam technology, evaporation and rarified gas dynamics.*

Ms A. Patankar *did her M.Sc.(Physics) from University of Mumbai (1995). She is working in electron gun development programme.*

Dr G.K. Bhowmick *is from 24th batch of BARC Training School. He obtained his Ph.D. from University of Mumbai (1992) and carried out his Post-Doctoral work at University of Mainz, Germany (1994-95). His research interests are high- resolution laser spectroscopy and its applications.*

Dr K.G. Manohar *is from 24th batch of BARC Training School. He obtained his Ph.D. from University of Mumbai (1992) and carried out his Post-Doctoral work at University of Kaiserslautern, Germany (1993-94). His research interests are laser spectroscopy, laser cooling & trapping and laser & optics technology.*

Dr K.B.Thakur *is from 21st batch of BARC Training School. He did his Ph.D. from University of Mumbai (1986). He represented the Ohio State University in NASA, USA, as a postdoctoral research associate (1986). His research interests are laser spectroscopy, electron beam technology and rarified gas dynamics studies of atomic beams.*

Dr B.N. Jagatap, *Homi Bhabha Awardee for Science & Technology (1999), is from 20th batch of BARC Training School. He obtained his Ph.D. from University of Mumbai (1988), Post-doctoral fellow (1993-94) and was Visiting Scientist (1999) at University of Western Ontario, Canada, and Senior Visiting Fellow (2000-01) at Centre for Chemical Physics, Canada. His research interests are laser-atom/molecule interactions, laser spectroscopy, laser cooling & trapping and physics of laser selective processes.*

Software for Computation of Laser Beam Photon Distribution in Curved Reflecting Cavity

Sachin P. Gujar, Sachin R. Ghodke and Mandar P. Gokhale
Project trainees from Rajiv Gandhi Institute of Technology
Navi Mumbai 400 708.

and

S. S. Thattey and S. K. Sarkar
Laser & Plasma Technology Division
Bhabha Atomic Research Centre

Abstract

Knowledge of photon density distribution in a given experimental region is very important for computation of yield in a photochemical experiment. Here we report development of interactive user-friendly software for computation of photon density in a curved reflecting cavity.

The curved reflecting cavity consists of two curved reflecting mirrors placed at a variable distance. A laser beam is introduced from a small hole in one of the mirrors, at a suitably chosen angle of incidence.

The software developed comprises a graphical user interface. It facilitates user to input various parameters related to the reflecting cavity (like, radius of curvature of the mirrors, the distance between them, and aperture size) and also parameters related to the laser beam (like beam diameter, angle of incidence of the beam, beam divergence and beam profile). A database stores all the input parameters for future use.

Various modules deal with three-dimensional geometrical computations, modeling the interaction of the rays with mirrors, generation of different views, computing various densities and displaying the density distribution. The software also assists the user to decide the best parameters for given experimental arrangement. The software will be useful for computation and visualization of the photon density distributions in various multiphoton experiments.

Introduction

THE PHENOMENON OF THE multiphoton excitation and dissociation of various molecular species is being studied extensively after availability of tunable lasers. A typical photochemical reactor, in which such an experiment is conducted, comprises a sample enclosed in a curved reflecting cavity irradiated by a laser beam. In order to improve the yield of the photochemical reaction, the cavity is designed so as to facilitate multiple passes through the sample. The yield of photoexcitation and photodissociation depends on the laser fluence as seen by the sample inside the cavity. Hence it is imperative to have an 'a priori' idea of the photon density distribution inside the photochemical reactor, for process optimization.

Here we report development of software to compute and visualize the photon density distribution inside a photochemical reactor. The

software is interactive and user friendly and various parameters can be given either as numerical inputs or can be set from the graphic display of the system using a mouse. The photon density distribution patterns as computed by the software were compared with the actual patterns obtained in the cavity of a photochemical reactor.

The Experimental Setup

The experimental setup consists of a reflective cavity formed by two curved mirrors with respective radii of curvature R_1 and R_2, having an aperture size A and separated by a distance D. One of the mirrors has a hole with radius R_H through which the laser beam is introduced in the cavity. The laser beam undergoes a number of reflections before it is reflected out of the cavity through the hole.

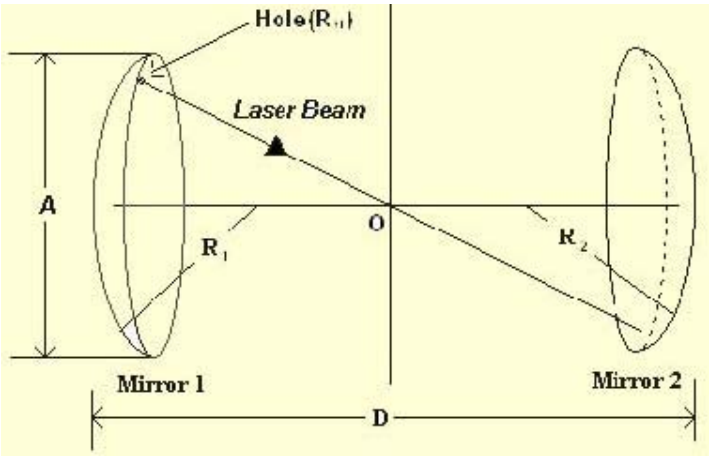

Fig. 1 The experimental set up

Software Emulation

The software emulation of the laser beam propagation inside the photochemical reactor cavity is attained basically by ray tracing with the help of laws of reflection. The emulation requires various initial parameters that are obtained from the user through a Graphical User Interface. In order to do this, the user follows through various input screens.

The screen '*Mirror Details'* accepts the parameters related with mirror dimensions, like the radii of curvature, radius of aperture, distance between mirrors, hole radius and hole position. '*Beam Details'* screen accepts the beam radius, beam divergence. '*Beam Position Details*' screen accepts the position of beam entrance and projection either in the Cartesian coordinate system or in the Polar coordinate system. Along with this it also presents the position on the opposite mirrors so that user can get the idea about his selection. Alternately, the user can directly go for selecting the position by pointing the location on the screen itself using a mouse. '*Plane Position Details'* screen accepts the plane position along which the Photon density is to be calculated and also the initial density value.

Similarly, the results are also displayed using various screens. The screens '*Left view', 'Right view', 'Top view', 'Front view'* represent the four views of the experimental setup after the completion of the tracing of the beam.

Dataflow Diagram and Software modules

The Figure 2 represents the Data flow diagram. It also shows major modules of the software.

The modules are *'Ray Tracing'*, *'Density Distribution'*, and *'Best Setup Generation'*. Along with these modules the figure also shows the input and output parameters.

'Ray Tracing' module accepts mirror and beam parameters as represented in the figure. It finds the points of intersection between the rays and the mirror surfaces, and stores these intersection points in an intermediate file.

'Density distribution' module accepts the geometrical parameters of the plane in which the density distribution is to be computed, and the initial density of the laser beam. The input parameters are processed and the plane-beam intersection points are calculated along with

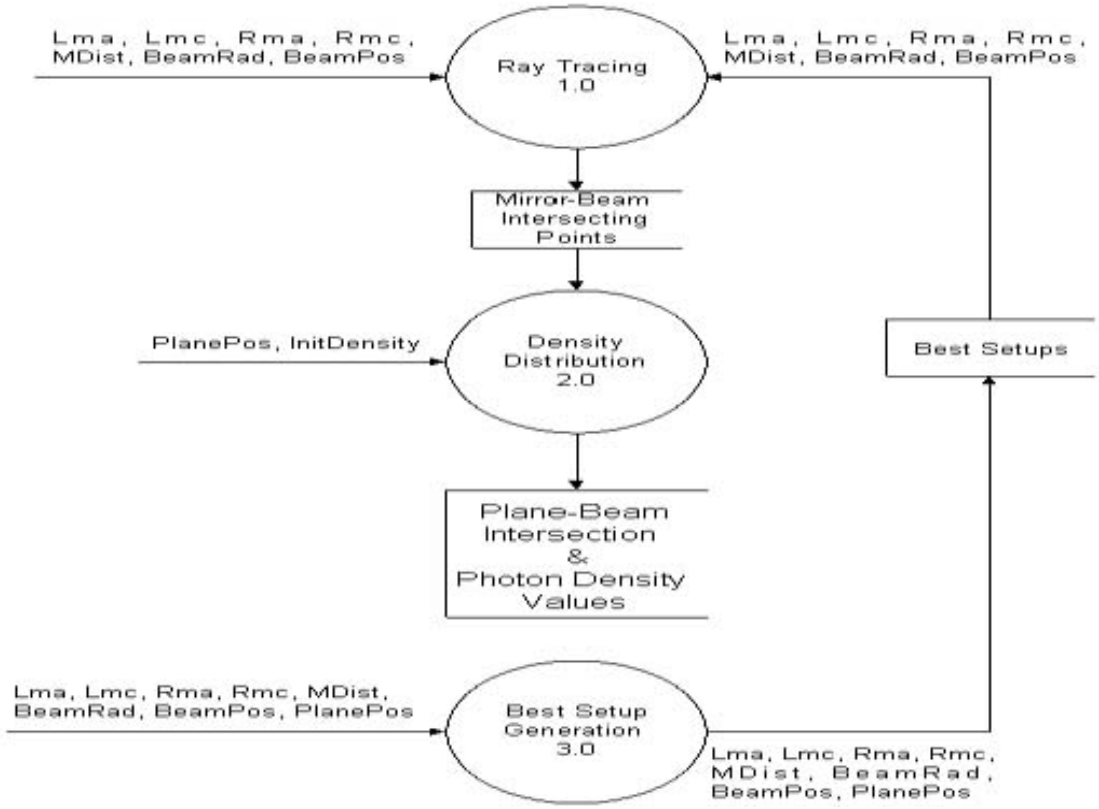

Fig. 2 The Dataflow diagram

density value for the current pass. These parameters are also stored in an intermediate file.

'Best Setup Generation' module uses these two modules internally. With the help of the *'Ray Tracing'* module it initially finds out the path of the laser beam and then with the help of *'Density Distribution'* module it finds the density distribution and at the end it compares and ranks the setups which are being generated. In this way the module tries various parametric configurations and then stores the result in an intermediate database file.

The symbols contained in Figure 2 are:

Lma : Aperture of Left Mirror.
Lmc : Radius of Curvature of Left Mirror.
Rma : Aperture of Right Mirror.
Rmc : Radius of Curvature of Right Mirror.
Mdist : Distance between the Mirrors.
BeamRad : Radius of the Beam.
BeamPos : X, Y, Z coordinate values that represents the position of the beam entrance.
PlanePos : X intersection value of the plane and the X-axis.
InitDensity: Initial Density of the Laser Beam.

Comparison with Actual Patterns

An experimental set up consisting of two mirrors with radius of curvature 1000 mm, and an aperture of 150 mm each were positioned at a distance of 1170 mm. A low divergence He-Ne laser beam with radius 1 mm was introduced in to the cavity through a 35 mm diameter hole having its centre located at (Y = 40.2 mm, Z = -33.7 mm) on the left mirror. The beam intersected the left mirror at (r = 40 mm, theta = 130 degrees) and the right mirror at (r = 40 mm, theta = 60 degrees) in their respective

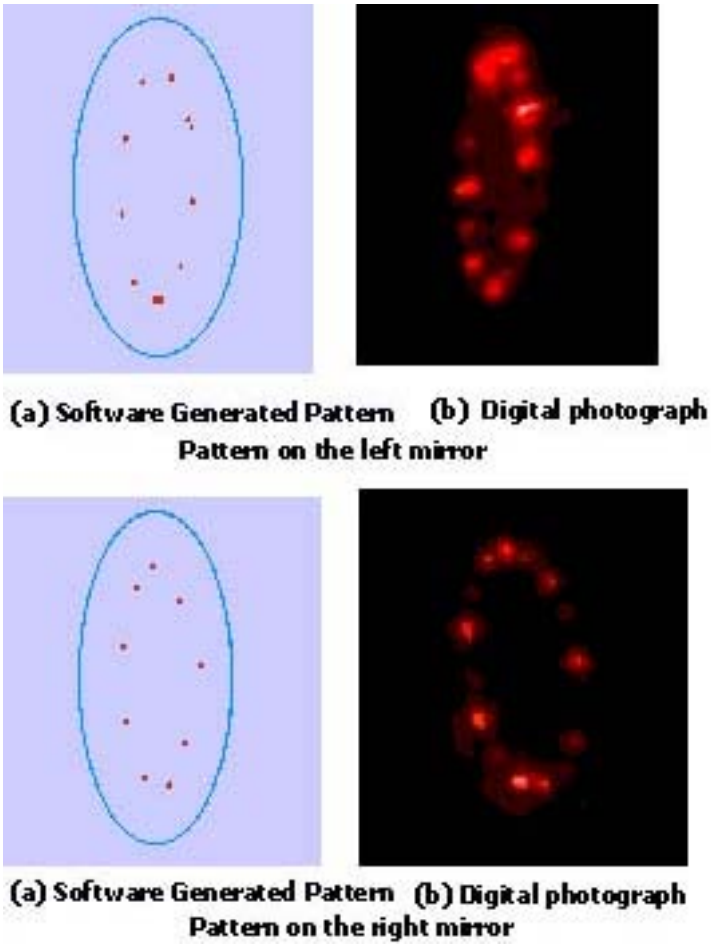

Fig. 3 The patterns on the two mirrors

polar co-ordinate system, with origin at the centre of the respective mirrors. The resulting patterns generated on the left and right mirrors of the cavity were photographed using a digital camera. Then the same parameters were used in the software and the patterns generated by it were compared with the digital photographs. The patterns and the actual laser spots on the left and right mirrors are shown in Fig. 3.

The interaction length provided by the multipass arrangement was calculated to be 21 meters. The mirror patterns and the interaction length when compared with those for experimental set up are found to match satisfactorily.

Conclusion

The software is found to be useful to compute and visualize the photon distribution patterns in a cavity. It also helps to choose the cavity and laser parameters for optimum distribution of photons in photochemical experiments.

This paper presented at the DAE-BRNS Symposium on "Applications of Plasmas, Lasers and Electron Beams in Advanced Materials Processing (PBAMP-2002)", held at Mumbai in September 2002 was selected for the Best Presentation award.

About the authors ...


S.P. Gujar


S.R. Ghodke


M.P. Gokhale

Mr Sachin P. Gujar, Mr Sachin R. Ghodke and Mr Mandar P. Gokhale *participated in this work at BARC, as Engineering Degree Project Trainees from Rajiv Gandhi Institute of Technology, Navi Mumbai 400 708. Subsequently, they completed their project and received their B.E. degrees from the University of Mumbai.*

Dr S. S. Thattey *obtained his M.Sc. in Theoretical Nuclear Physics from University of Mumbai in 1975. He joined BARC in 1976, and is currently working in Laser & Plasma Technology Division on problems related to application of digital image processing in laser related processes. He got his Ph.D. from University of Mumbai in 1997 for his work on application of digital image processing. He published his ideas on application of some of fundamental laws from the realm of science to the behaviour of human society, in a Marathi book "Eka Shevatachi Suruvat" which was honoured with 'Damani Literary Award' in 1996. He is a popular science writer, and has received a number of awards, which include, a special prize for a science fiction in an international competition by Deutsche Welle, the German TV and Radio Corporation, and two State Literary Awards by the Government of Maharashtra for his science books for children.*

Dr Sisir K. Sarkar *joined BARC in 1974 and is currently heading Molecular Isotopic Photochemistry Section of Laser & Plasma Technology Division, BARC. He did his post-doctoral work at Columbia University, New York, in the area of chemical dynamics using high-resolution semiconductor diode laser. He has worked extensively as visiting scientist at the P.N. Lebedev Physical Institute & Institute of Spectroscopy, Russia, Kyoto Institute of Technology, Japan, and Institute of Chemical Process Fundamentals, Czech Republic, with various laser systems which include Free Electron Laser. His research interest includes laser selective photophysics and photochemistry, chemical dynamics, spectroscopy and laser development.*

Preparation and Characterization of MgB_2 Superconductor

Shashwati Sen, D.K. Aswal, Ajay Singh, T.V.C. Rao, K.P. Muthe, J.C. Vyas, S.K. Gupta and V.C. Sahni
Technical Physics & Prototype Engineering Division
Bhabha Atomic Research Centre

and

L.C. Gupta
Tata Institute of Fundamental Research, Mumbai

Abstract

Superconducting MgB_2 crystallites having a size up to 3 X 2 X 1 mm^3 have been grown using a liquid-assisted-sintering process under atmospheric pressure of argon. The magnetization measurements have been carried out on MgB_2 samples to determine upper critical field, critical current density and irreversibility line. The obtained values of critical current density and upper critical field were ~10^6 A/cm^2 (at 1 T and 5 K) and 12 T, respectively. The Andreev reflection studies carried on metallic MgB_2/Ag planar junctions revealed a novel two-energy gap like structure for MgB_2. Surface analysis using X-ray photoelectron spectroscopy revealed that MgB_2 is sensitive to environmental degradation.

Introduction

THE DISCOVERY OF SUPER-conductivity at 39 K in MgB_2 has attracted great interest because it introduces a new, simple (3 atoms per unit cell) binary intermetallic superconductor with record high superconducting transition temperature (T_c) for a non-oxide and non-C_{60}-based compounds [1]. The reported value of Tc seems to be either above or at the limit suggested by BCS theory. This raises the question whether this remarkable high T_c is due to some exotic form of electron pairing. Therefore, any experimental data that can shed light on the mechanism of superconductivity in this material is of great interest, and for this, availability of high quality samples is necessary. Reported bulk sintered MgB_2 samples prepared by reacting Mg and B have been found to be porous and mechanically weak [2]. The sample density, however, can be improved by synthesizing the samples using hot isostatic pressing (HIP) at 950°C under high pressure of several GPa [3]. However, synthesis of denser MgB_2 material at ambient pressure is important for large-scale technological applications of the material. Here we present an alternate route of synthesis of MgB_2 superconductor starting from Mg in two forms, namely, powder and flakes, and B as powder using solid-state sintering method under atmospheric pressure of Argon.

Material stability is another issue of great concern for device applications of superconductors. Clearly material should preferably be stable against prolonged atmospheric exposures as well as during fabrication processes, such as photolithography (where superconductor could be exposed to water/various solvents). With this in view, we have investigated the degradation behavior of MgB_2 against exposures to moist air and water.

Synthesis of MgB_2

We have synthesized MgB_2 samples by conventional solid-state reaction method. The

starting boron (B) was in the form of powder with average particle size <10 μm; while magnesium (Mg) was selected in two different forms: (a) powder with grain size < 100 μm and (b) flakes with an average size 3 mm x 2 mm x 0.1 mm. Mg and B powders were mixed in stoichiometric ratio and pressed into pellet (15 mm diameter and 2 mm thickness). These pellets with extra Mg flakes were enclosed in a Tantalum foil. The extra Mg flakes were put to compensate the loss of Mg from the pellets. The Tantalum foil was then sealed in presence of high purity argon gas. The enclosed pellets were kept in a tubular furnace and sintered under flowing argon ambient, for 2 hours at 650°C, and 4 hours at 750°C followed by 2 hours at 950°C. After sintering the samples were quenched in liquid nitrogen. MgB_2 pellets prepared using Mg and B powder is termed as sample I, while those prepared using Mg flakes and B powder is termed as sample II. These samples were characterized for their physical as well as superconducting properties, as described below.

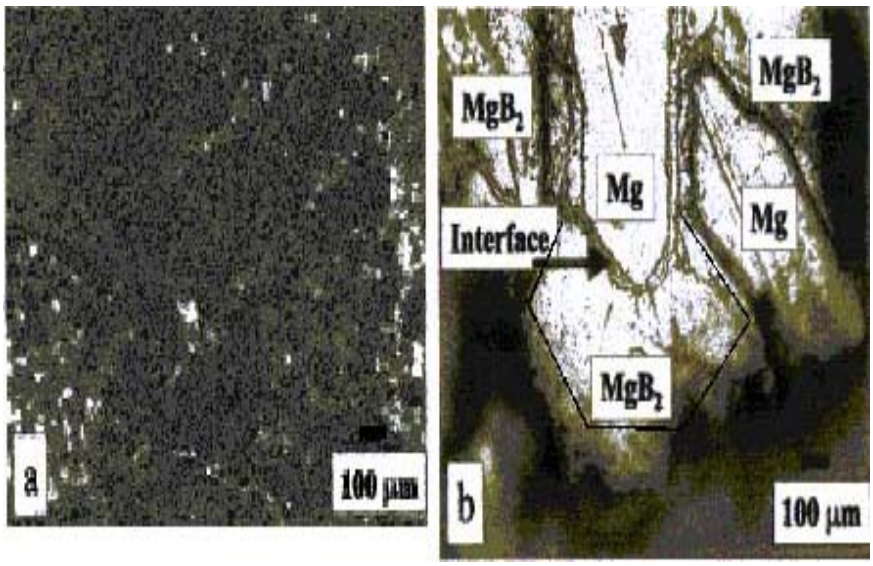

Fig. 1 (a) Optical micrograph of sample I (synthesized using Mg and B powder), (b) Optical micrograph sample II. (Synthesized using Mg flakes and B powder)

Optical Microscopy

The sample morphology of these pellets was investigated using optical microscopy (Olympus BX60M optical microscope). The images of the samples at various magnifications were captured using a CCD camera mounted on top of the optical microscope and were directly stored in the computer. Sample I was found to be black in colour and very fragile whereas sample II was very hard to break. The micrographs of sample I and sample II are given in Figure 1 (a) and (b), respectively. As observed in figure 1(a), sample I was found porous with unreacted boron. Few Mg particles were also found on the surface. The size of MgB_2 grain was very small (of the order of 10 μm).

Figure 1(b) shows the optical micrograph of a mechanically broken part of the pellet of sample II. Under higher magnification, the presence of magnesium and MgB_2 in the pellet could be distinguished based on their colors; Mg has a silvery white and MgB_2 a golden tint. A large amount of unreacted Mg was found and the size of MgB_2 grains was very large. As seen in Figure 1(b) the MgB_2 grains were found to grow with hexagonal habit. The hexagonal boundary is drawn to mark the growth boundaries of MgB_2 grain. It is observed that unreacted Mg around the MgB_2 grain restricts the growth of MgB_2 grains. We have successfully retrieved several MgB_2 grains from the charge by mechanical methods. These MgB_2 grains had metallic luster with golden tint, which is in contrast to the black color of polycrystalline sample I. The largest size of cleaved MgB_2 grain was 3 mm x 2 mm x 1 mm. A photograph of such a cleaved MgB_2 grain is shown in Figure 2.

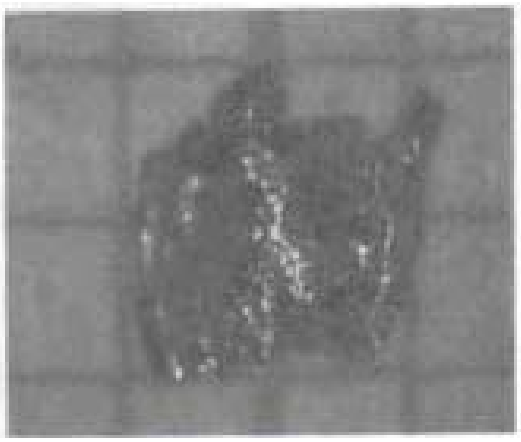

Fig. 2 Optical micrograph of a single grain of sample II retrieved from the pellet. (The grid in the background is 1 x 1 mm^2)

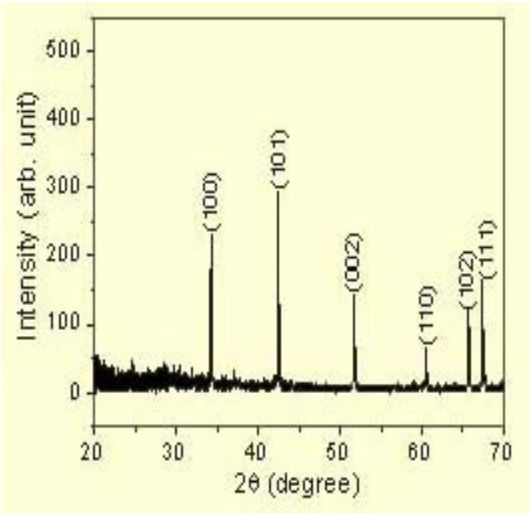

Fig. 4(a) XRD plot recorded for sample II (powdered MgB_2 grains).

X-Ray Diffraction studies

Figure 3 shows a typical XRD pattern of sample I. Reflections corresponding to both MgB_2 and B are clearly observed. Since the samples are sintered at 950°C most of the Mg evaporates (melting temperature of Mg 650°C), therefore only a small amount of Mg is left in the charge to react with B to form MgB_2. The samples thus consists of MgB_2 and unreacted boron.

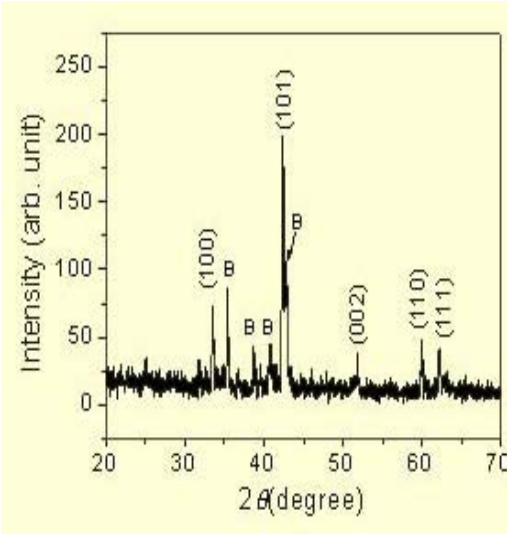

Fig. 3 XRD plot recorded for sample I. The peaks marked as 'B' correspond to unreacted boron

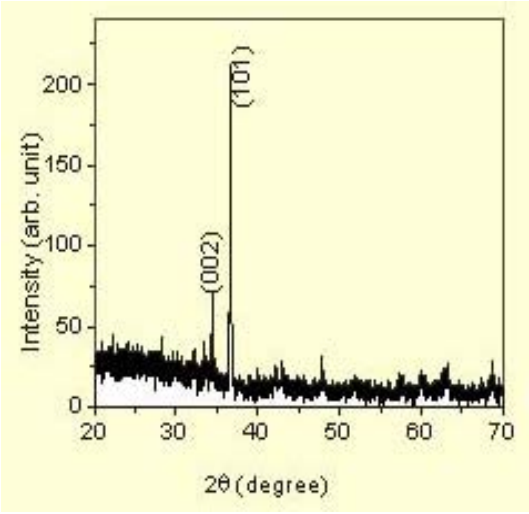

Fig.4(b) XRD pattern of the residual material obtained after separating out the MgB_2 (sample II) grains from the charge which correspond to those of magnesium

MgB_2 grains retrieved from sample II were crushed in to fine powder to record XRD pattern and a typical plot is shown in Figure 4 (a). All the reflections corresponding to that of MgB_2 phase are present in the pattern, indicating the formation of the single phase MgB_2. The XRD pattern of the residual material obtained after

separating out the MgB_2 grains from the charge (sample II) is shown in Figure 4(b). All the peaks correspond to those of magnesium. Thus it is confirmed that grains of MgB_2 are formed and some Mg is left unreacted in sample II, as inferred from the optical microscopic observations.

A plausible explanation for the dependence of MgB_2 grain size, on the size of the starting material i.e. Mg powder or Mg flakes is as follows. Mg melts at ~650°C and starts evaporating as the temperature is increased, while B with a melting point of ~2079°C remains stable. At 950°C, the synthesis temperature, Mg in powder form has more surface-to-volume ratio than Mg flakes, melts and evaporates easily. Therefore only a small amount of Mg will react with B to form MgB_2, resulting in small grains of MgB_2 and some unreacted boron as observed using optical microscopy and XRD measurements. On the other hand, the slow melting of Mg flakes gives rise to lot of liquid Mg, which have more time to react with the available boron powder thus yielding larger grains of MgB_2. This also indicates that the formation of MgB_2 is due to the diffusion of magnesium into boron.

Four-probe resitivity

The temperature dependence of resisitivity for samples I and II is given in Figure 5. Sample I exhibits superconductivity with transition temperature of 36 K, while sample II shows a two step transition with onset occurring at ~39.5 K and ~36 K. The width of transition for sample II was found to be wider. The two-step transition observed in sample II indicates the possibility of presence of two or more superconducting phases. This may be due to the fact that sample II is formed by the diffusion of Mg into B grains which may result in lower concentration of Mg at the centre of the boron grain as compared to its outer surface. The presence of this second phase was however not revealed by XRD indicating that it is present in very small quantity.

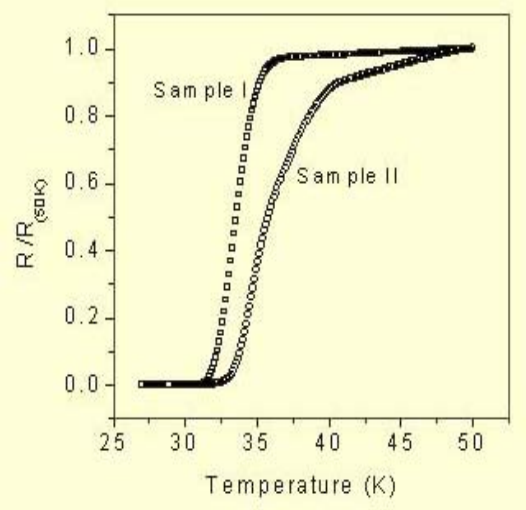

Fig. 5 Resistance vs Temperature plot of sample I and II.

Figure 6 shows the superconducting transition of sample II at three different magnetic fields. The onset is found to decrease with increasing magnetic field, without significantly changing the transition width.

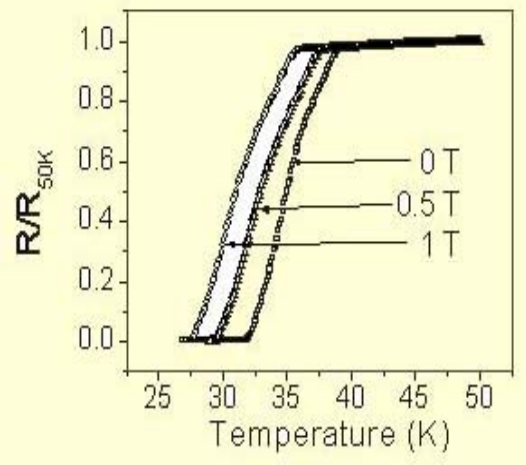

Fig. 6 The magnetic field dependence of the resistive transition. The resistance is normalized to 50 K value.

Data of Figure 6 was used to determine H_{c2} as function of temperature and Figure 7 shows the plot of H_{c2} versus temperature. The slope dH_{c2}/dT was found to be –0.44 T/K. The value of $H_{c2}(0)$ is determined using the WHH relation [4]

$H_{c2}(0) = -0.69\ T_c\ dH_{c2}/dt$ (1)

$H_{c2}(0)$ is found to be ~12 T. This value is comparable to that reported in literature [5].

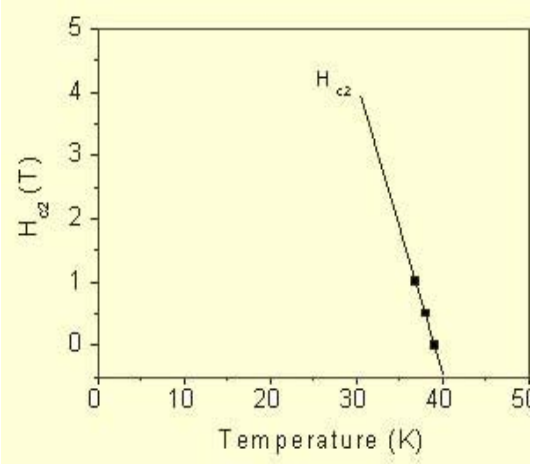

Fig. 7 Plot of Hc_2 versus temperature as calculated from T_c offset at different applied magnetic field.

DC magnetization

The diamagnetic transition recorded for both samples in field-cooled (FC) and zero-field cooled (ZFC) conditions is shown in Figure 8. For these measurements, sample I of size 0.25 x 0.15 x 0.054 cm^3 and sample II of size 0.25 x 0.15 x 0.06 cm^3 were employed.

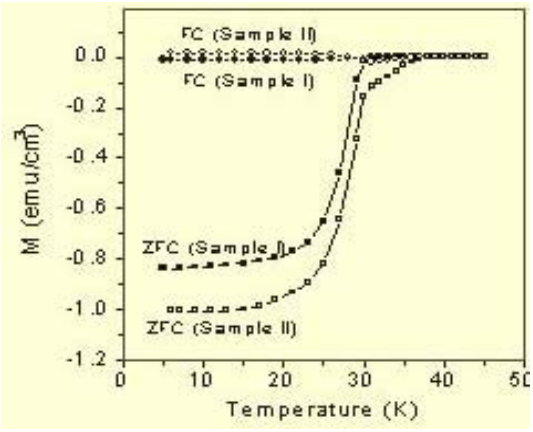

Fig. 8 Field cooled (FC) and Zero field cooled (ZFC) magnetization data of MgB_2 polycrystalline powder (Sample I) and MgB_2 grain (Sample II). The applied field was 10 Gauss.

The data obtained is almost similar to that obtained for resistive transition. Sample I has a single superconducting transition, while sample II shows two step transition to superconductivity. Further, sample II has higher difference between ZFC and FC data than that in sample I and the magnitude of diamagnetic signal in ZFC data is also larger in this case. The difference between ZFC and FC signals arises due to the trapped flux [6], indicating that the weaker superconducting phase present in sample II acts as flux trapping centers.

To further study the nature of the mixed state for these samples, *M-H* hysteresis loops were recorded at different temperatures and the results are given in Figures 9 (a) and (b). The magnetic critical current density (J_c) was calculated from the hysteresis loop using the relation for a flat plate in perpendicular field using Beans model.

$J_c = 20\Delta M / (a\text{-}a^2/3b)$ (2)

Here J_c is in A/cm^2, ΔM is the difference in magnetization for increasing and decreasing fields in emu/cm^3 and a and b are the lateral dimensions of the sample in cm. The calculated value of J_c at 5 K and 1 T from the *M-H* curve was found to be 1.2 x 10^4 A/cm^2 for sample I and 4 x10^5 A/cm^2 for sample II.

As shown in Figure 9 at lower applied fields (i.e. H < 1 T), rapid fluctuations in magnetization are observed for *M-H* loops recorded at lower temperatures. The fluctuations are more pronounced for sample II than in sample I and are found to gradually reduce as the temperature increases. Since magnetization (ΔM) is proportional to the critical current density J_c, the data of Figure 9 (b) indicate that low field magnetization-fluctuations are pronounced when the sample has large J_c. Magnetization-fluctuations at low fields and higher J_c suggest that they could arise due to the "flux-jumps" [7].

In Figure 10 we have plotted J_c as a function of H for samples I and II calculated using data of Figure 9 (a) and (b). Due to the flux-jump

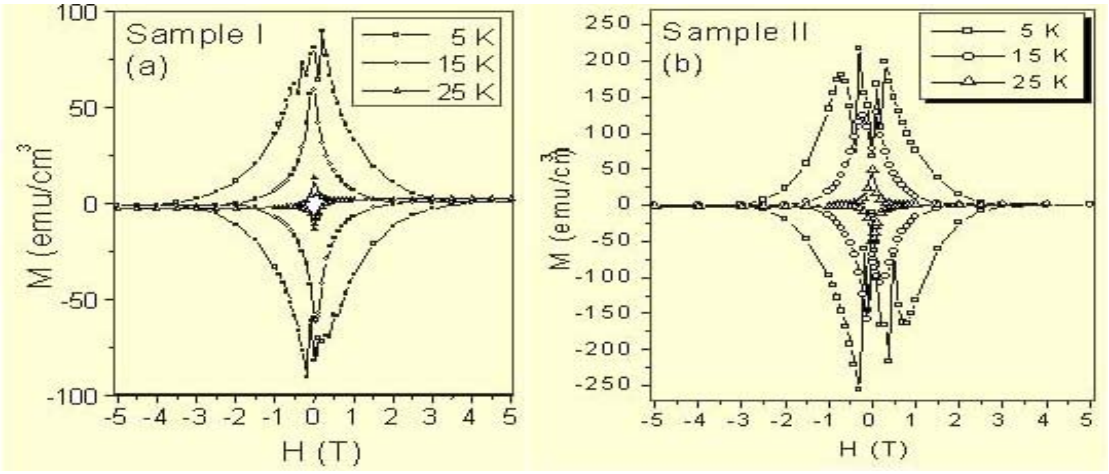

Fig. 9 Magnetic hysteresis loops measured at different temperatures for (a) sample I (b) sample II .

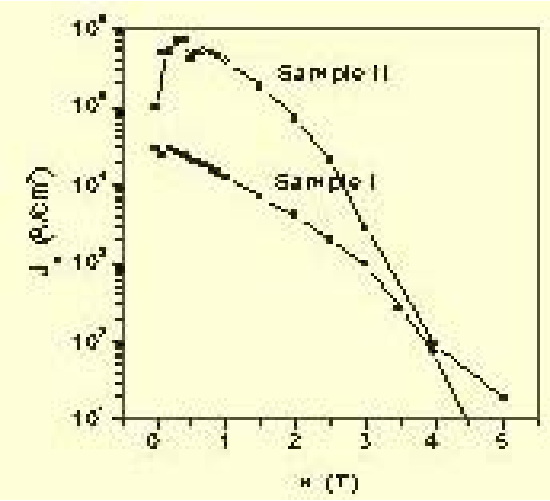

Fig. 10 Field dependence of critical current density at 5 K

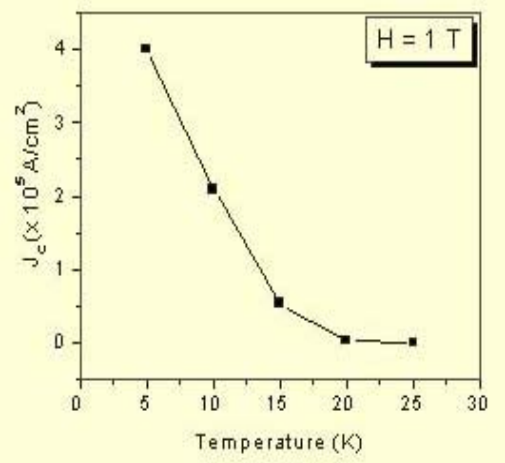

Fig. 11 Temperature dependence of the critical current density at H = 1 T for sample II

behavior observed in *M-H* hysteresis loops the J_c values calculated for magnetic field <1 T are not reliable and are expected to be much higher than shown in Figure 10. As the magnetic field is increased the J_c is seen to drop sharply and tends to zero at fields much lower than H_{c2} indicating the existence of an irreversibility line. Temperature dependence of J_c for sample II at fixed magnetic field (H = 1 T) is plotted in Figure 11. In this case also J_c drops sharply as the temperature is increased.

Figure 12 shows the field dependence of critical current density for sample II at different temperatures. The J_c-H plots, have been used to determine the irreversibility line, by taking a J_c criterion of 10 A/cm^2. The H-T phase diagram is plotted in Figure 13 showing the irreversibility and upper critical field lines.

It is seen that there is a large separation between the two lines i.e. $H_{c2}(T)$ and $H_{irr}(T)$. At temperatures and fields below irreversibility line, vortices are strongly pinned in the form of lattice or glass; while above this line vortices are weakly pinned or are in the liquid state. At irreversibility line ($H_{irr}(T)$) magnetization becomes reversible i.e. vortices start flowing or

melting (liquid) and therefore, both ΔM and J_c vanish. The vortex state of MgB_2 has been further investigated using current-voltage characteristic measurements and the results showed that the vortecies form a glassy state.

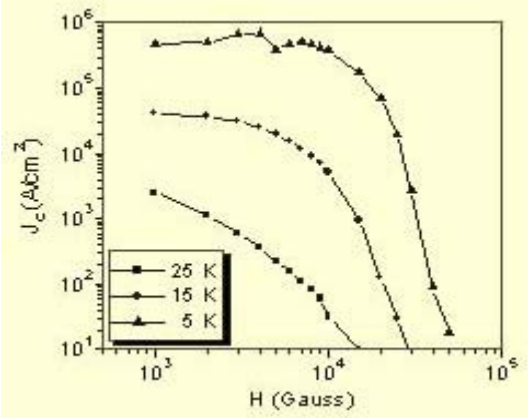

Fig. 12 Critical current density as a function of field measured at different temperatures for MgB_2 grains

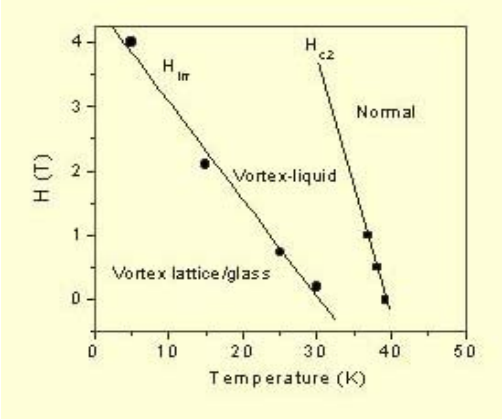

Fig. 13 H-T phase diagram for the liquid assisted grown MgB_2 superconductor

Energy Gap in MgB_2

In BCS theory of superconductivity, electrons with opposite momentum and spin condense to form Cooper pairs through an attractive phonon-mediated electron-electron interaction that is larger than the repulsive Coulomb interaction. In the newly discovered MgB_2 superconductor (T_c = 39 K) small atomic mass of boron suggests the likelihood of high phonon frequencies. High phonon frequencies are expected to yield high values of T_c. Experimentally observed boron isotope effect [5] suggests that pairing mechanism is in accordance with BCS theory. T_c of strong-coupled superconductor within the framework of BCS theory is given by [8]

$$T_c = \frac{\Theta}{1.45}\exp\left[-\frac{1.04(1+\lambda)}{\lambda-\mu^*(1+0.62\lambda)}\right] \quad (3)$$

where, Θ is the Debye temperature, μ^* Coulomb coupling constant and λ electron-phonon coupling constant. With experimentally determined values of Θ =1050 K, λ = 0.51 [9] and μ^* often taken as 0.1 [8], the value of T_c works out to be 11.5 K, which is much less than the 39 K.

In order to investigate the paring mechanism in MgB_2 superconductor, several groups have measured energy gap (Δ), using various techniques, such as, tunneling spectroscopy [10], point contact spectroscopy [11], specific heat studies [12], Raman spectroscopy [13] and high-resolution photoemission spectroscopy [14]. The reported values of Δ are found to vary in a large range between 1.2 and 8 meV. In addition, whilst some groups have reported a single gap, others found two or multiple gaps. BCS theory relates Δ and T_c through relation: $2\Delta = 3.5\ k\ T_c$ (k is the Boltzman constant). If MgB_2 is simple BCS superconductor then a T_c of 39 K would yield Δ of ~6 meV. The Δ values higher than 6 meV can be explained by using high λ values, but lower Δ values (i.e.<< 6 meV) are not explainable within the framework of BCS theory. To explain lower Δ or double gap, three different explanations have appeared in the literature [10-14]. The first explanation attributes low gap to degraded surface layers having lower T_c. X-ray photoelectron spectroscopic analysis, as we will show in the next section, has indeed confirmed the surface degradation of MgB_2 on atmospheric exposures [20]. In the second scenario, two energy gaps, as theoretically predicted by Liu et al [15], are intrinsic to MgB_2, which arise due to segmented Fermi surface. The Fermi surface of MgB_2 is reported to consist of nearly cylindrical hole-

sheets arising from quasi-2D boron bands and a 3D tubular network. A ratio of 1:3 has been predicted between small and large gaps. If this scenario is true then one should be able to measure both the gaps upto the T_c. The reported literature showing existence of both the gaps upto T_c are not very reliable because, close to T_c, the thermal smearing parameter becomes much larger than the gap values. The gap parameters, therefore, are determined through fitting process. The third explanation is based on the anisotropic energy gap, which essentially may arise due to anisotropic crystal structure of MgB_2. Reported anisotropy in other physical properties of MgB_2, such as, lower and upper critical fields [16], suggest the possibility of the anisotropy in energy gap as well. In fact, depending upon the sample orientation, Δ has been found to have different values, which indicated anisotropic s-wave pairing symmetry. Thus, there is substantial controversy over the value of Δ as well as about its symmetry. Clearly, more direct information on the energy gap are needed. To measure the energy gap in MgB_2, we have carried out Andreev reflection studies on MgB_2/Ag planar junctions.

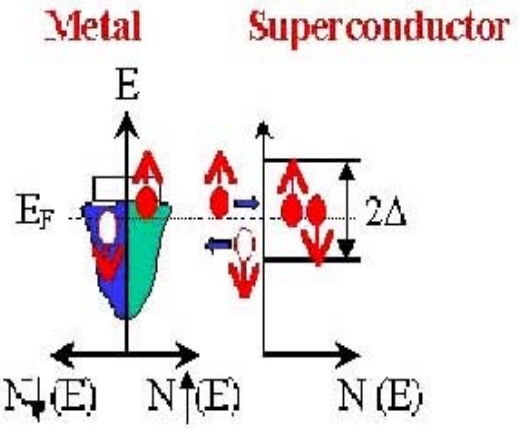

Fig. 14 Schematic of Andreev reflection process at a metal-superconductor junction

Andreev reflection and BTK theory

Figure 14 shows a schematic of Andreev-reflection process at a metal (N)-superconductor (S) interface [17]. When a voltage V is applied across a N-S junction such that excess energy of electrons in N becomes greater or equal to Δ, electrons can cross the junction and enter into quasiparticle states in the superconductor. For $E<\Delta$, the traversing electron condenses into superconducting state by forming a Cooper pair with another electron which leaves behind it a hole with opposite velocity in N. This so-called Andreev-reflection process leads to excess current and, to a lower resistance for $eV<\Delta$. The voltage dependence of differential resistance (dV/dI) therefore contains direct information about Δ.

The electronic transport in *N-S* junctions is described by Blonder-Tinkham-Klapwijk (BTK) formalism [18]. For an isotropic superconductor, BTK theory predicts the differential resistance at T = 0 K by the expression

$$\left(\frac{dV}{dI}\right)^{-1} = \frac{dI}{dV} \sim 1 + A(E) - B(E) \qquad (4)$$

where *A(E)* and *B(E)* are the coefficient giving the probabilities of Andreev and ordinary reflections, respectively. For $E<\Delta$:

$$A = \frac{\Delta^2}{E^2 + (\Delta^2 - E^2)(1+2Z^2)^2}, \text{ and } 1\text{-}A. \qquad (5)$$

For $E>\Delta$:

$$A = \frac{u_0^2 v_0^2}{[u_0^2 + Z^2(u_0^2 - v_0^2)]^2}, \quad \text{and}$$

$$B = \frac{(u_0^2 - v_0^2)Z^2(1+Z^2)}{[u_0^2 + Z^2(u_0^2 - v_0^2)]^2} \qquad (6)$$

Here Z is dimensionless barrier parameter. Z=0 implies no barrier at the *N-S* interface. u_0 and v_0 are the Bogoliubov factors given as $u_0^2 = 1 - v_0^2 = \frac{1}{2}[1 + \{(E^2 - \Delta^2)/E^2\}^{1/2}]$.

For $T \neq 0$, in above expressions, E is replaced by $E + i\Gamma$, where Γ is the thermal smearing parameter.

Junction preparation and dV/dI vs V measurements

For the present investigations, two different types of junctions namely MgB_2/Ag and

MgB_2/insulator/Ag junctions were prepared. The metallic MgB_2/Ag junctions were prepared by thermally evaporating Ag spots (0.5 mm diameter and 300 nm thick) onto freshly cleaved and polished MgB_2 surface. To make MgB_2/insulator/Ag junctions, the MgB_2 sample were first exposed to atmospheric conditions (temperature ~30°C and relative humidity >75%) for different periods. As will be shown in the next section, the surface MgB_2 reacts with atmospheric moisture and CO_2, which results in the formation of an insulating layer at the surface. Depending upon the ambient exposure time, the thickness of the insulator layer is expected to change. Finally, Ag electrodes were thermally evaporated on to this insulating layer.

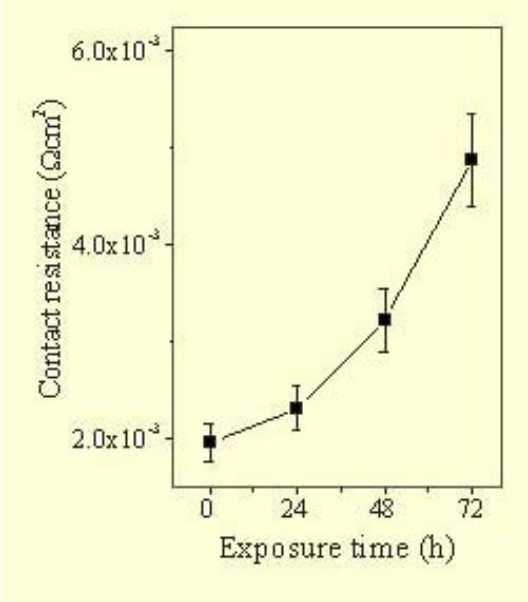

Fig. 15 Variation of the contact resistance of MgB_2/Ag junction with atmospheric exposure time of MgB_2 surface. The bar denotes the range of the contact resistance measured in different samples.

All the clean MgB_2/Ag junctions exhibited a metallic character. For instance, typical contact resistance for MgB_2/Ag junction was found to linearly fall from its 300 K value of $1.9x10^{-3}$ Ωcm^2 to $1.1x10^{-3}$ Ωcm^2 at 40 K. Due to high surface roughness of MgB_2 samples, the interface with Ag spots is expected to consist of large number of contacts formed at high points. Each contact can be considered to be Sharvin contact and the resistance of the interface is assumed to be average of all such contacts. On the other hand, as shown in Figure 15, the resistance of MgB_2/insulator/Ag junction at room temperature is found to increase with increasing ambient-exposure time of MgB_2 surface. The temperature dependence of the resistance of these junctions exhibited semiconducting or insulating character i.e. an increase in junction resistance with decreasing temperature.

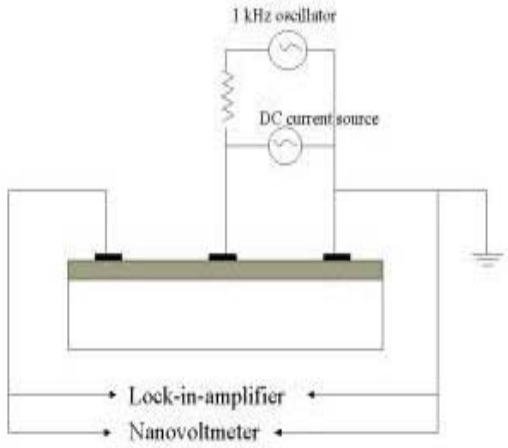

Fig. 16 Experimental setup for recording of tunneling spectra.

The schematic of the circuitry used for the measurement of *dV/dI* versus applied bias voltage (*V*) is shown in Figure 16. A slowly varying bias current, which was additionally modulated by a small sinusoidal current (~10μA) oscillating at a frequency of 1kHz, was applied to the current electrode on the sample. The ac voltage developed between first and the third electrodes was fed to a lock in amplifier. The output of the Lock-in amplifier is actually the *dV/dI*. The dc voltage that developed between these two terminals was also given to a nanovoltmeter (Keithley), which essentially measures the bias voltage developed across the junction due to the flow of slowly varying bias current.

Temperature dependence of dV/dI vs V characteristics

Figure 17 shows normalized dV/dI vs. V spectrum for MgB_2-Ag planar junction in the superconducting state (T = 4 K, B = 0 T). The first point to note is that the spectrum is symmetric with respective to bias voltage. The salient features to be read off directly from the spectrum are; (i) a V-shaped structure centered at V = 0, we refer it as zero-bias-anomaly (ZBA), (ii) a contribution from Andreev-reflection process indicating that a (k, -k) type of Cooper pairing is realized, (iii) a double-minimum structure near 7.3 meV (marked by arrows) and (iv) a pronounced peak structure at threshold voltage (V_{th}).

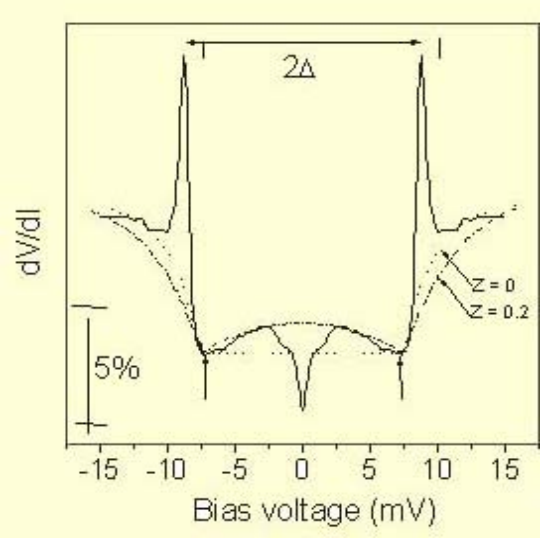

Fig. 17 dV/dI vs V plot recorded at 4 K for MgB_2/Ag planar junctions. Dotted and dash-dotted lines are simulated curves using BTK theory with Z parameter equal to 0 and 0.2, respectively. The bar represents the signal intensity.

The simulated curves using BTK model for isotropic superconductor i.e. equation 3.8 with Z parameter equal to 0 (dotted line) and 0.2 (dash-dotted line) are also shown in Figure 17. In both the cases, the fitting parameters Δ and Γ were 7.3 meV and 0.33 meV (equivalent to 4 K), respectively. It is seen from Figure 17 that for Z = 0, a poor fit is observed for entire V values. For Z = 0.2, although for $V<\Delta$ a reasonable fitting of data is observed, for $V>\Delta$ the fitting became much poorer. In addition, ZBA and sharp peaks could not be accounted by BTK fittings. This implies that the energy gap in MgB_2 might not be isotropic.

The exact origin of the observed double-minimum feature is not known yet. However, it can be explained using following three different possibilities. (i) The double-minimum feature is expected for a superconductor with an anisotropic order parameter i.e. s-wave symmetry but different magnitude in different crystallographic directions [19]. This is because the differential resistance is dependent on the k value of the electrons incident on N-S interface. The deviation from the isotropic BTK fit at higher bias, as observed in Figure 17, could be attributed to averaging over an anisotropic gap. However, a clear confirmation can only be achieved by conducting directional dependence Andreev reflection measurements on the single crystals. (ii) The double-minimum feature can also be explained using the theoretically predicted two-gap scenario in MgB_2 [15]. The superposition of the two gaps – one of small value and hence broadened, and one of larger value, and less affected by thermal fluctuations – could lead to a double-minimum feature. (iii) The observed double-minimum feature in MgB_2 is analogous to that experimentally observed for the heavy fermionic superconductors, such as UPt_3, URu_2Si_2 and $CeCu_2Si_2$ etc. [20,21]. These heavy fermionic superconductors are known to have unconventional order parameters (e.g. analogous to d-wave order parameter in high temperature superconductors), suggesting that MgB_2 might also have an unconventional order parameter.

So far there is no theory, which explains the sharp peaks observed at V_{th}. The origin of these peaks has been attributed to a resonance in a layer of suppressed order parameter and, is predicted to appear slightly above the bulk energy gap. Lacking the exact knowledge of the gap function and corresponding BTK expression, we take distance between the two maximum as

2Δ value, which would be the upper limit of the bulk superconducting gap. The value of Δ for MgB_2 at 4 K obtained in this way comes out to be 8.6 meV, which is higher than the value (7.3 meV) determined using isotropic BTK fitting (although poor).

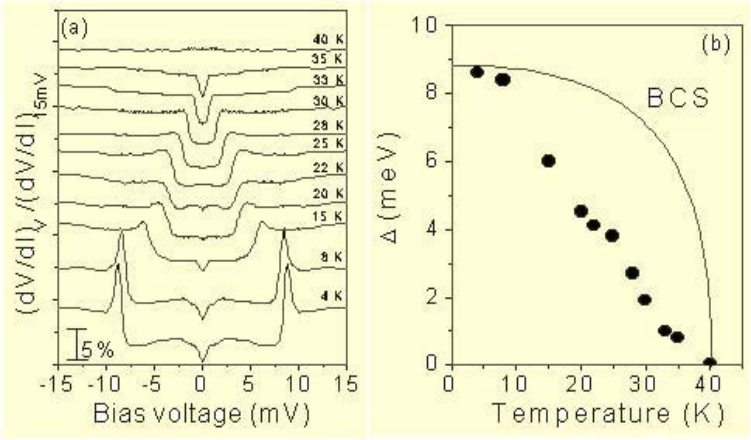

Fig. 18 Temperature dependence of (a) dV/dI vs V and (b) energy gap (Δ)

In order to further elucidate the features observed in the tunneling spectrum, presented in Figure 17, we have investigated the temperature dependence of *dV/dI* vs. *V* characteristics. The obtained spectra are presented in Figure 18(a). It is seen that with increasing temperature the double-minimum feature vanishes. The temperature dependence of the energy gap, measured from distance between the two peaks, is presented in Figure 18(b). The energy gap decreases more rapidly with temperature than expected for Δ of an isotropic BCS superconductor. This temperature dependence of Δ could be due to an averaging over the anisotropic energy gap.

Field dependence of dV/dI vs V characteristics

The dV/dI vs V spectra recorded at 4 K but under different magnetic fields are shown in Figure 19(a). On application of magnetic field, the resonance peaks exhibit multiplicity. Since MgB_2 is a type-II superconductor, application of magnetic field produces vortices in the sample and, therefore the order parameter at the contact region becomes inhomogeneous. Thus multiplicity in resonance peak could be attributed to the multiple-resonance at the contacts arising due to inhomogeneous order parameter. Alternatively, the multiplicity in the resonance peak could also be explained using two-gap scenario. The magnetic field suppression of the gaps would yield the multiplicity in the resonance peak as the gap features overlap. As shown in Figure 19(b), the energy gap rapidly reduces with increasing field, which is also inconsistent with BCS theory.

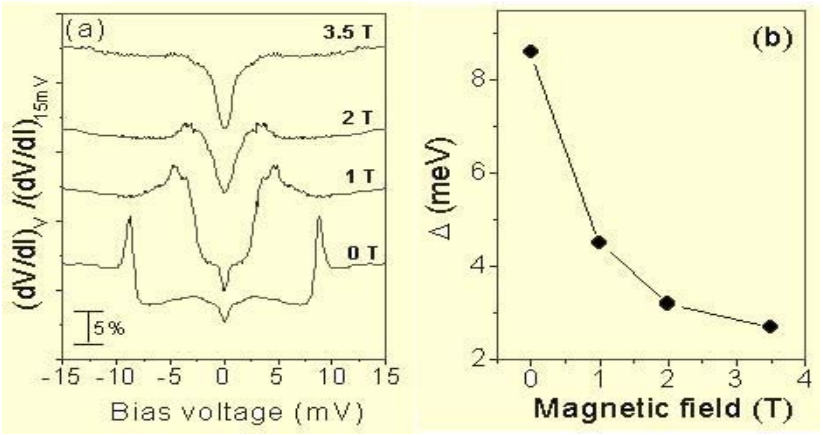

Fig. 19 Field dependence of (a) dV/dI vs V and (b) energy gap (Δ).

Now, we focus attention to the zero-bias-anomaly (ZBA). In high T_c superconductors, such ZBA are used as an evidence for *d*-wave gap symmetry. The ZBA arising due to *d*-wave gap symmetry is known to symmetrically split across the 0 *V* in the presence of magnetic field. The data, presented in Figure 19(a), show that ZBA does not split under magnetic field, suggesting that MgB_2 does not have *d*-wave gap symmetry. ZBA in present case could arise due to microshorts (metal-metal junctions) at the MgB_2/Ag interface, which is supported by increase in ZBA intensity with magnetic field. Since the number of vortices produced in the sample is proportional to the magnetic field and, the vortex core is a normal region, therefore, numbers of microshorts (or ZBA intensity) is expected to be proportional to the magnetic field.

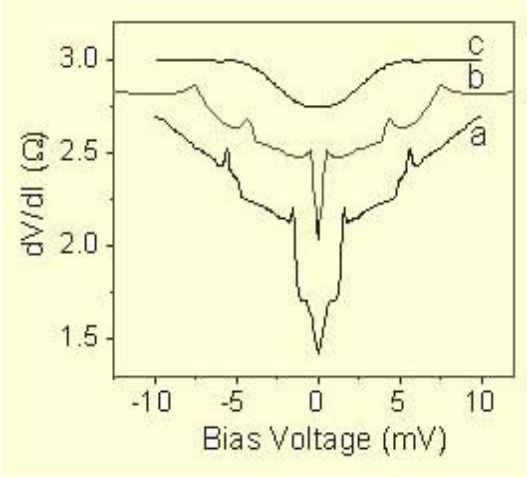

Fig. 20 dV/dI vs V plots recorded as a function of ambient exposure time of MgB_2 surface; (a) 24 h, (b) 48 h and (c) 76 h.

Junction dependence of dV/dI vs V characteristics

The dV/dI vs V characteristics for MgB_2/insulator/Ag junctions, prepared by exposing the MgB_2 surface to atmosphere for different periods, are shown in Figure 20. For a junction prepared by ambient-exposure for 24h, in addition to ZBA, the spectrum exhibits two sets of resonance peaks at ±1.6 and ±5.6 meV, respectively. Increasing ambient-exposure time to 48h resulted in a significant reduction of ZBA and increase in sets of resonance peaks to three occurring at ±0.8, ±4.2 and ±7.4 meV, respectively. In fact, the resonance peak positions were found to vary with the samples and the exposure time. This indicates that the degradation of MgB_2 at the surface is inhomogeneous, which results in degraded phases of different transition temperatures. As shown in Figure 20, all the features nearly vanished when the exposure time exceeded more than 72 h, indicating that the thickness of the insulator layer becomes much larger than the coherence length of the MgB_2 superconductor.

In conclusion we have carried out Andreev reflection studies on metallic MgB_2/Ag and MgB_2/insulator/Ag planar junctions. The analyses of differential resistance (*dV/dI*) versus bias voltage (*V*) spectra obtained for metallic MgB_2/Ag junction could not be modeled using an isotropic BTK theory. The temperature dependence of measured energy gap did not follow the BCS relation, suggesting that MgB_2 does not have an isotropic energy gap. Presence of double minimum feature indicate the possibility of two-energy gaps, which in fact has been confirmed by other groups. The *dV/dI* vs *V* characteristics of MgB_2/insulator/Ag planar junctions exhibited peaks corresponding to degraded phases with reduced transition temperatures.

Degradation Behavior of MgB_2

We encountered strong tendency of MgB_2 to degrade for the first time when superconducting (T_c ~ 39 K) thin bridges (2 mm long, 0.5 mm wide and 0.2 mm thick) - mechanically fabricated for the measurement of current-voltage characteristics - were found to become insulating after 8-10 h of atmospheric exposure (ambient temperature ~28°C and relative humidity >70%). These bridges, however, showed improved stability when stored in dry atmosphere, which indicated that MgB_2 reacts with moist air. Therefore, it is important to investigate the degradation behavior of MgB_2

against exposures to moist air and water, and here we deal with this issue.

To investigate the effects of water-exposure on physical and chemical properties of MgB_2, commercially available MgB_2 powder was pressed into pellets and sintered at 950°C for 2 hours. These pellets were cut into bar-shape and were immersed in deionized water for different periods (upto 72 h) and dried in ambient atmosphere (ambient temperature ~28°C and relative humidity >70%). All the samples were characterized for superconducting properties and morphological, structural and chemical changes.

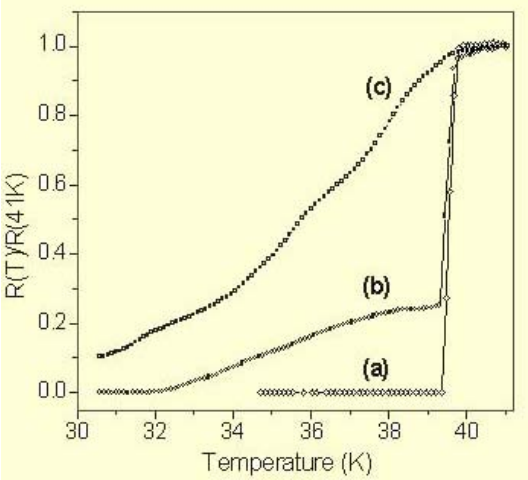

Fig. 21 Temperature dependence of resistivity recorded on polycrystalline MgB_2 samples. (a) Before exposure to water, (b) after 12 h exposure to water and (c) after 24 h exposure to water.

The resistance versus temperature plots after exposing MgB_2 sample to water for various periods are shown in Figure 21. The room temperature resistvity was found to increase with increasing water exposure time. For the sample exposed for 12 h in water, although the T_c^{on} remained at 39.7 K, the transition to superconducting state developed a tail and zero resistance is observed only at ~32 K. The transition width was seen to increase with water exposure time, while the T_c^{on} remained constant at ~39.7 K. For the sample exposed to water for 24 h, the zero resistance state could not be observed till 30 K. The sample became insulating for water exposure time greater than 72 h.

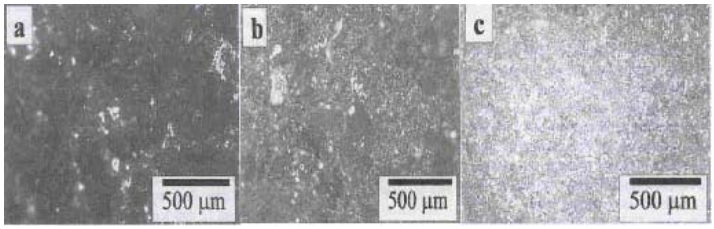

Fig. 22 Optical micrograph of a MgB_2 pellet after exposed to water for different periods : (a) fresh (b) 12 hrs (c) 72 hrs.

The dense and hard MgB_2 samples were found to decompose into a powder on prolonged exposure to water. Optical micrographs, shown in Figure 22, depict the changes in surface morphology as a function of water exposure time. The grains become more and more isolated as the exposure time increases, indicating a definite reactivity of MgB_2 with water, which preferentially occurs at the grain boundaries.

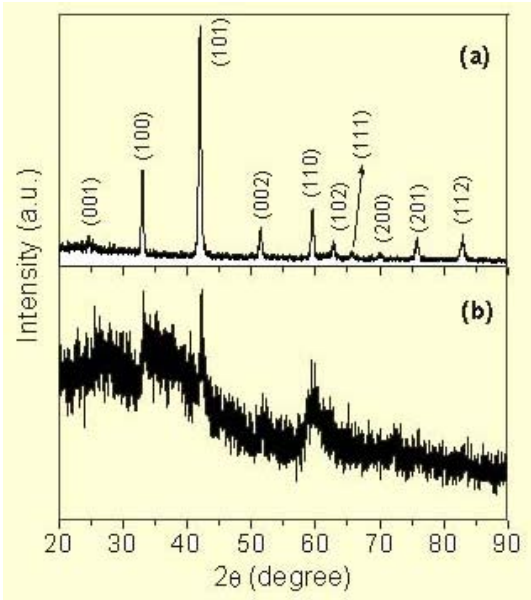

Fig. 23 Powder X-ray diffraction pattern recorded for MgB_2 samples: (a) before and (b) after 72 h water exposure.

The XRD patterns recorded for fresh and 72 h water exposed samples are shown in Figure 23. The XRD pattern for the fresh sample corresponds to that of single-phase MgB_2 superconductor**.** For the water-exposed sample, only few faint reflections corresponding to MgB_2 are observed. The XRD pattern indicates that the decomposed material(s) mostly contains amorphous phase(s).

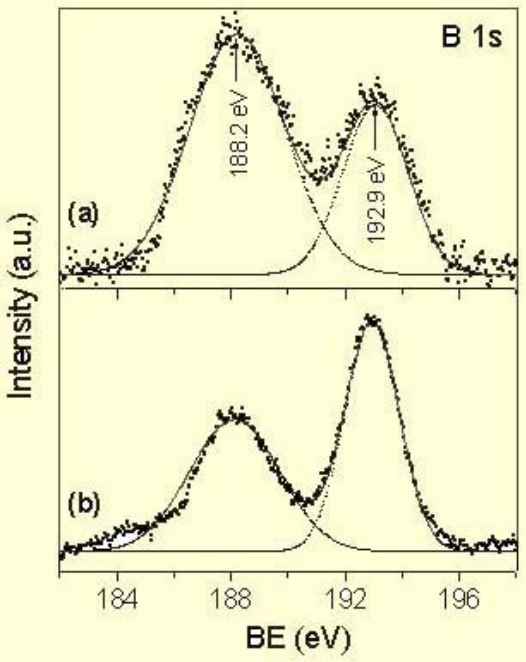

Fig. 24 Core level B 1s spectra recorded for MgB_2 samples: (a) before and (b) after 72 h water exposure. The curves are fit to Gaussian line shape.

In order to investigate the degradation behavior of MgB_2, both fresh (only exposed to atmosphere) and degraded (exposed to water for 72 h followed by atmospheric exposure) samples were characterized by x-ray photo electron spectroscopy (XPS). The B 1s core level spectra recorded for the fresh and degraded samples are shown in Figure 24. It is observed that the B 1s signal in both the cases consists of two peaks occurring at binding energy values of 188.2 eV and 192.9 eV, respectively. The lower binding energy value is assigned to MgB_2 [22]**,** and is consistent with BE values (187.2 – 188.5 eV) reported for transition metal diborides [23,24]. The existence of peak at 192.9 eV indicates formation of B_2O_3 at the surfaces of both fresh and degraded samples. This indicates that surface oxidation is unavoidable even for fresh sample. The intensity of B_2O_3 peak increased considerably in the water exposed sample indicating that B_2O_3 is one of the products when MgB_2 reacts with water and air.

The Mg 2p core level and Mg $KL_{23}L_{23}$ Auger spectra recorded for the fresh and degraded samples are shown in Figures 25 and 26. For the fresh sample, Mg 2p line is broad and could be fitted in terms of two peaks corresponding to binding energies of 49.5 and 50.7 eV, respectively indicating that Mg is in two different states. This is confirmed by presence of two clear Auger $KL_{23}L_{23}$ signals at kinetic energies of 1186 eV and 1180 eV. The lower Mg 2p binding and higher Auger kinetic energies are assigned to MgB_2 [22]. The binding energy peak at 50.7 eV and corresponding Auger peak at 1180 eV indicate presence of Mg in hydroxide and/or carbonate form [25-27]. For the degraded sample, both Mg 2p core level and Auger $KL_{23}L_{23}$ spectra contain single peak, at 50.7 eV and 1180 eV respectively, which suggest that Mg is in hydroxide and/or carbonate form.

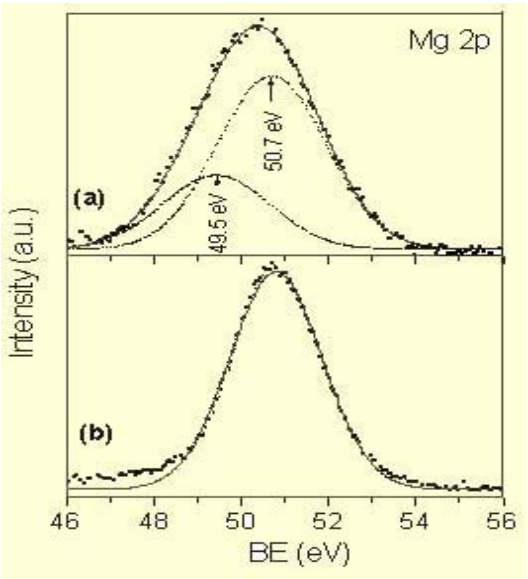

Fig. 25 Core level Mg 2p spectra recorded for MgB_2 samples: (a) before and (b) after 72 h water exposure. The curves are fit to Gaussian line shape.

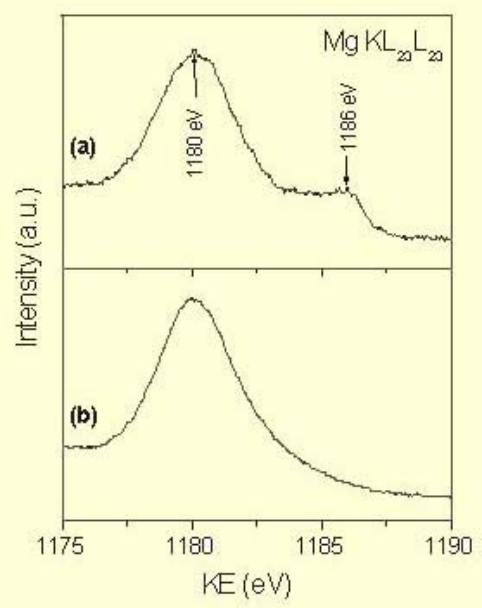

Fig. 26 Mg $KL_{23}L_{23}$ Auger line recorded for MgB_2 samples: (a) before and (b) after exposure to water for 72 h.

The formation of oxides, hydroxides and carbonates could also be inferred from O 1s and C 1s spectra, as shown in Figures 27 and 28, respectively. For the fresh sample, O 1s spectrum has two peaks at BE values of 531.5 and 532.8 eV, while for the degraded sample, an additional peak at 534 eV is needed for best fit. The peak at 531.5 eV is attributed to B_2O_3 and, peaks at 532.8 eV and 534 eV to $Mg(OH)_2$ and $MgCO_3$, respectively. The formation of carbonates in the degraded sample is confirmed from the C 1s spectra, as shown in Figure 26. For the fresh sample, only one peak at 284.9 eV corresponding to adventitious carbon is observed, while for the degraded sample evolution of peak at 289.5 eV suggests formation of the $MgCO_3$ [25-27].

Based on XPS results presented above, the reaction of MgB_2 with water could be written as:

$$MgB_2 + 2H_2O \rightarrow Mg(OH)_2 + 2B + H_2$$

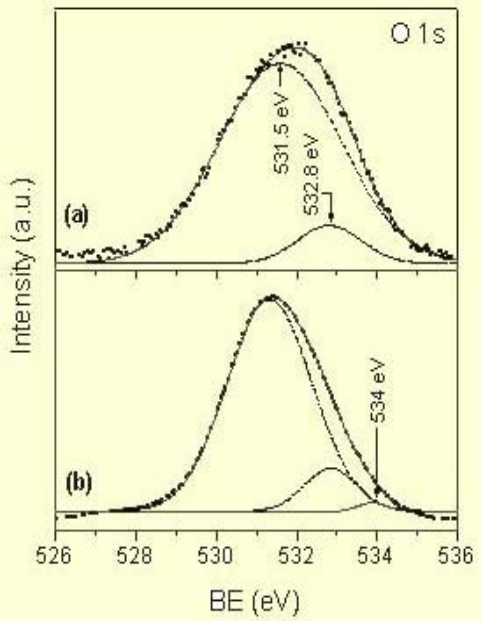

Fig. 27 Core level O 1s spectra recorded for MgB_2 samples: (a) before and (b) after 72 h water exposure.

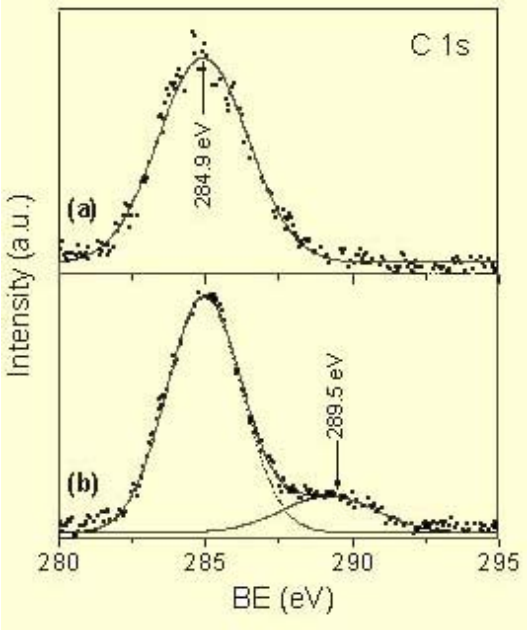

Fig. 28 Core level C 1s spectra recorded for MgB_2 samples: (a) before and (b) after 72 h water exposure.

On further exposure to ambient atmosphere, B reacts with oxygen to form boron oxide and, $Mg(OH)_2$ reacts with CO_2 to form magnesium carbonate:

$4B + 3O_2 \rightarrow 2B_2O_3$

$Mg(OH)_2 + CO_2 \rightarrow MgCO_3 + H_2O$

The XPS spectra of B 1s and Mg 2p were also used to estimate the surface composition of the fresh and the degraded samples. The relative atomic concentration (C_i) is calculated using the relation [26, 27]:

$$C_i = \frac{(I_i / S_i)}{\sum (I_j / S_j)} \quad : \ i, j = \text{B or Mg} \qquad (7)$$

Where I_i represents the intensity of the Mg or B and S_i is the atomic sensitivity factor. The intensities (I_i) were calculated by finding the total area under the core level peak using the least-square fitting of Gaussian line shape and for S_i, values reported in ref. [26] were used. The results are presented in Table 1. It is seen that the surface composition of the fresh sample is fairly close to theoretical atomic concentration (i.e. B = 66.67% and Mg = 33.33%), considering the accuracy (10-20%) [27] of the XPS technique. The surface of the degraded sample showed depletion of B or enrichment of Mg. The enrichment of Mg at the surface of water-exposed sample is presumably due significantly high solubility of B_2O_3 in water as compared to those of $Mg(OH)_2$ and $MgCO_3$ (see solubility data in Table 2).

Table 1 : Surface chemical composition of the fresh and the degraded MgB_2 samples
The atomic sensitivity factors are taken from ref. [27]

Sample	XPS line	Intensity (I_i) (cps-eV)	Atomic sensitivity factor (S_I)	Relative atomic concentration (C_i) (%)
Fresh	B Is	7.72	0.13	61.93
	Mg 2p	4.38	0.12	38.06
Degraded	B Is	8.69	0.13	53.72
	Mg 2p	6.91	0.12	46.27

Table 2 : Solubility of various salts in water [28]

Salt	Solubility (g/100 ml H_2O)
B	Insoluble
B_2O_3 (amorphous)	1.1
$Mg(OH)_2$	0.0009
$MgCO_3$	0.0106

Conclusions

Depending upon the form of starting Mg (powder or flakes) employed for synthesis, the grain growth and superconducting properties of MgB_2 have been found to change. Large size MgB_2 grains (upto 3 X 2 X 1 mm^3) could be grown using Mg flakes. However, these samples exhibit two phase like character with weaker superconducting phase acting as flux-trapping centers. The MgB_2 samples exhibited critical current density of ~10^6 A/cm^2 (at 1 T and 5 K) and upper critical field of 12 T. Andreev reflection studies carried on MgB_2/Ag planar junction indicated a possibility of two energy gaps. XRD and XPS studies showed that MgB_2 is unstable against atmospheric moisture and CO_2. MgB_2 on reaction with moisture and CO_2 leads to B_2O_3, $Mg(OH)_2$, $MgCO_3$. Thus, in order to maintain long term stability of this material in applications, coating of suitable protective layer would be necessary.

References

1. J. Nagamatsu, N. Nakagawa, T. Muranaka, Y. Zenitani, J. Akimatsu, *Nature* **410** (2001) 63.
2. D. K. Finnemore , J. E. Ostenson, S. L. Bud'ko, G. Lapertot, P. C. Canfeild, *Phys. Rev. Lett.* **86** (2001) 2420.
3. C. U. Jung, M. S. Park, W. N. Kang, M. S. Kim, S. Y. Lee, S. I. Lee, 2001 *cond-mat/0102215*
4. N. R. Werthamer, E. Helfand, P. C. Hohemberg , *Phys. Rev.* **147 (**1966**)** 362.
5. S.L. Bud'ko, G. Lapertot, C. Petrovic, C.E. Cunningham, N. Anderson and P.C. Canfield, *Phys. Rev. Lett***. 86** (2001) 1877.
6. C.P. Poole Jr, H.A. Farach, R.J. Creswick, *Superconductivity,* Academic Press, London, 1995, p- 317.
7. Y. B. Kim, M. J. Stephen, *Superconductivity, Vol. 2,* editor Parks R D, Marcel Dekker Inc, New York, 1969.
8. W.L. McMillan, Phys. Rev. **167** (1968) 331.
9. .M. An W.E. Pickett, Phys. Rev. Lett. **86** (2001) 4366.
10. G. Karapetrov, M. Iavarone, W.K. Kwok, G.W. Crabtree, D.G. Hinks, *Phys. Rev. Lett.* **86** (2001) 4375.
11. H. Schmidt, J.F. Zasadzinski, K.E. Gray and D.G. Hinks, *Phys. Rev. B* **63** (2001) 220504.
12. Y. Wang, T. Plackowski, A. Junod, *Physica C* **355** (2001) 179.
13. X.K. Chen, M.J. Konstantinovic, J.C. Irwin, D.D. Lawrie and J.P. Franck, *cond-mat/0105215* (2001).
14. T. Takahashi, T. Sato, S. Souma, T. Muranaka and J. Akimitsu, *Phys. Rev. Lett.* **86** (2001) 4915.
15. Y. Liu, I.I. Mazin and J. Kortus, *Phys. Rev. Lett.* **87** (2001) 08700.
16. A. Buzea and T. Yamashita, *Supercond. Sci. Technol.* **14** (2001) R115.
17. A.F.Andreev, *Sov. Phys, JETP* **19** (1964) 1228.
18. G. E. Blonder, M. Tinkham, T. M. Kalpwijk, *Phys. Rev B* **25** (1982) 4515.
19. C. Bruder, *Phys. Rev. B* **41** (1990) 4017.
20. H. Lohneysen, *Physica B* **218 (**1996) 148.
21. G. Goll, H. Lohneysen, I. K. Yanson, L. Taillefer, *Phys. Rev. Lett.* **70** (1993) 2008.
22. R.P. Vasquez, C.U. Jung, M.S. Park, H.J. Kim, J.Y. Kim, and S.I. Lee, 2001, *cond-mat/0103215*
23. G. Marvel, J. Escard, P. Costa and J. Castaing, *Surf. Sci.* **35** (1973) 109
24. C.L. Perkins, R. Singh, M. Trenary, T. Tanaka, Y. Pederno, *Surf. Sci.* **470** (2001) 215.
25. H.B. Yao, Y. Li and A.T.S. Wee, *Appl. Surf. Sci.* **158** (2000) 112.
26. C.D. Wagner, W.M. Riggs, L.E. Davis, J.F. Moulder, J.E. Millenberg, *Handbook of the X-ray Photoelectron Spectroscopy,* Perkin-Elmer, Eden Draivie, MN, 1979
27. D. Briggs, M.P. Seah, Practical Surface Analysis by Auger and X-ray Photoelectron Spectroscopy, Wiley, 1983
28. D.R. Lide, CRC Handbook of Chemistry and Physics, 74th edition, CRC Press, Boca Raton. 1993-1994.

This paper received the Best Poster Paper award in the International Symposium on "Advances in Superconductivity & Magnetism : Materials, Mechanisms and Devices" held at Mangalore during September 25-28, 2002

About the authors ...

Ms Shashwati Sen *has completed her M.Sc. in Physics from Devi Ahilya Vishwa Vidyalaya , Indore, in 1996. After completing the 40nd batch of Training School of BARC, she joined TPPED. Her research areas are related to high temperature superconductors and gas sensors.*

Dr D.K. Aswal *joined TPPED (BARC) through 30th batch of Training School. He has made several contributions in the field of thin/thick films and single crystals of various high temperature superconductors and colossal magnetoresistive materials. He has also worked on recently discovered magnesium-di-boride superconductor. Presently, he is working on HTS/CMR multilayers, metallic-multilayers using molecular-beam-epitaxy and thermoelectric materials. Dr. D. K. Aswal is a recipient of prestigious JSPS fellowship during 1997-99 and was awarded Paraj-2000 prize for excellence in science. He has authored more than 120 scientific publications.*

Mr Ajay Singh *joined TPPED through 42nd batch of Training School. His area of research are development of thermoelectric devices and thin films & multilayer structures of high temperature superconductors and colossal magnetoresistive materials.*

Over the years, ***Dr T.V. Chandrasekhar Rao*** *had carried out detailed magnetization studies on a number of superconducting and other magnetic systems, down to ultra low temperatures and under high pressures. He was also involved in setting up a number of low temperature experimental facilities in the center. He has authored about 35 papers in international journals till date. He obtained his Ph.D. in Physics in 1996 and subsequently worked as a postdoctoral researcher in prestigious laboratories in Japan and USA. He had also been a user of muon facilities at Rutherford Appleton Lab, UK and x-ray facilities at the Advanced Photon Source, Argonne National Lab, USA.*

Mr K. P. Muthe *has been working in the field of thin film growth and characterization. He has studied the growth behavior of HTSC films using MBE. The reference value of this work has fetched him a place in Marquis Who's Who of the world (1997) and Dictionary of International Biography (1999). He has extensively used X-Ray photoelectron spectroscopy to solve several material related problems like mechanism of H_2S gas detection and corrosion and contributed to around 50 publications. His interests also include development of Toxic gas sensors and synthesis of Alumina based radiation sensors for Personal Dosimetry. He belongs to the 30th batch of Training School.*

Dr J. C. Vyas *joined R.Cn.D. (BARC) through 23rd batch of Training School, and was involved in the fabrication of space quality Si-solar cells. This technology was then transferred to BHEL, Bangalore. Later he joined TPPED and worked on growth and characterization of optical quality single domain lithium niobate crystals. Subsequently, he worked on growth of high-temperature superconducting thin films using molecular beam epitaxy and laser ablation, and made Josephson junctions. Presently Dr. Vyas is also involved in fabrication of MOS based gas sensors.*

Dr S.K. Gupta *joined BARC in 1975 and is presently Head of Thin Films Devices Section in TPPED. Over the years, he has worked on space quality silicon solar cells, high temperature superconductor thin films and single crystals, gas sensors and thermoelectric materials. He is a member of the National Academy of Sciences, India.*

Dr V.C. Sahni, *Director, Physics Group, BARC, joined BARC in 1965. He has made important contributions in lattice dynamics of complex crystals, group theoretical methods as applied to solid state physics, Raman spectroscopy, measurement of electron momentum densities, quasi crystals, magnetization studies of many superconducting and several magnetic materials using SQUID magnetometer, etc. Besides condensed matter physics, Dr. Sahni has specialized in the indigenous development of physics related instrumentation, particularly UHV based instruments and synchrotron radiation utilisation equipment for the storage ring INDUS-1 & upcoming ring INDUS-2 at Centre for Advanced Technology (CAT), Indore. Dr. Sahni is a Fellow of the National Academy of Sciences, India and an INSA Young Scientist Awardee. He has also been a Visiting Fellow at the Centre for Chemical Physics UWO, Ontario, Canada during 1981 -1982, INSA-USSR Academy Exchange Fellow in 1987 and INSA-Royal Society (UK) Exchange Fellow in 1993. Dr. Sahni has published over 250 scientific papers, coauthored the book "Dynamics of Perfect Crystals" and co-edited another book "Developments in Theoretical Physics".*

Prof. L.C. Gupta *has special interest on the studies of phenomena such as ferroelectricity, magnetism, valence fluctuations and superconductivity applying microscopic techniques of NMR, NQR, Mossbauer and Mu-SR as well as bulk techniques. Subsequent to the discovery of supercondcuting quaternary borocarbide system Y-Ni-B-C (reported in Solid State Commun. 87, 413 (1993) and Phys. Rev. Letters 72, 274 (1994)), he has been particularly concerned with the identification of new intermetallic ternary and quaternary superconducting materials.*

Study of Operating Characteristics of the 50 kV Electron Gun Modulator for 10 MeV, 10 kW RF Electron Linac

Kavita P. Dixit, V. Yadav, R.B. Chavan, A.R. Chindarkar, K.C. Mittal and R.C .Sethi
Accelerator & Pulse Power Division
Bhabha Atomic Research Centre

Abstract

A line-type pulsed modulator for 50 kV, 1 Amp, to generate 10μs pulses at 400 Hz, has been designed and developed at APPD, BARC. This modulator is used to bias the cathode of the electron gun, which is the injector to a 10 MeV, 10 kW RF industrial electron linac. Variable dose rate is needed depending upon the application of the linac. This is achieved by varying the pulse repetition rate, so that average power output from the linac is varied. This paper describes some of the characteristics of the modulator operating in the variable rep.rate mode.

Introduction

A 10 MeV, 10 kW RF INDUSTRIAL electron linac [1] has been designed and is under development at BARC. This linac is an on-axis coupled cavity linac, operating in the pulsed mode, at an RF frequency of 2856 MHz. Plastic modification, diamond coloration, food processing, medical sterilization, etc., are the main applications of this linac. For each of these applications, different dose rates [2] are required. Hence, it is necessary to design the linac system, so that variable dose rates are available for the users. One of the methods of obtaining variable dose rates is by varying the average power output from the linac. This can be accomplished by varying the pulse repetition rate keeping the pulse width fixed. Both the electron gun as well as the RF power source should be synchronized to operate at the variable repetition rates.

Fig.1 shows the photograph of a prototype electron gun [3] used for this study. This gun is operated in the triode configuration, with an indirectly heated LaB6 cathode. This electron gun is required to produce a maximum pulsed current of 1 A, at a voltage of -50 kV ± 10% and pulse width of 10 μs. A line type pulsed modulator [4] generates this voltage, which is applied to the cathode of the electron gun. This paper gives a study of the behaviour of the modulator in the variable rep.rate mode.

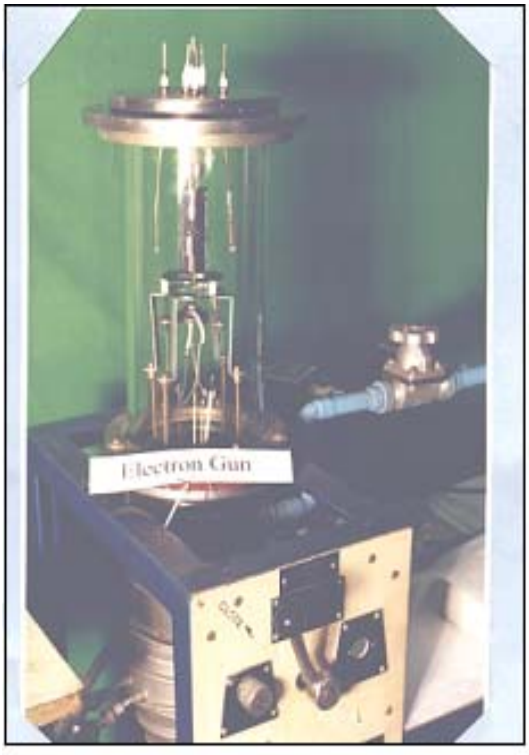

Fig. 1 Photograph of electron gun

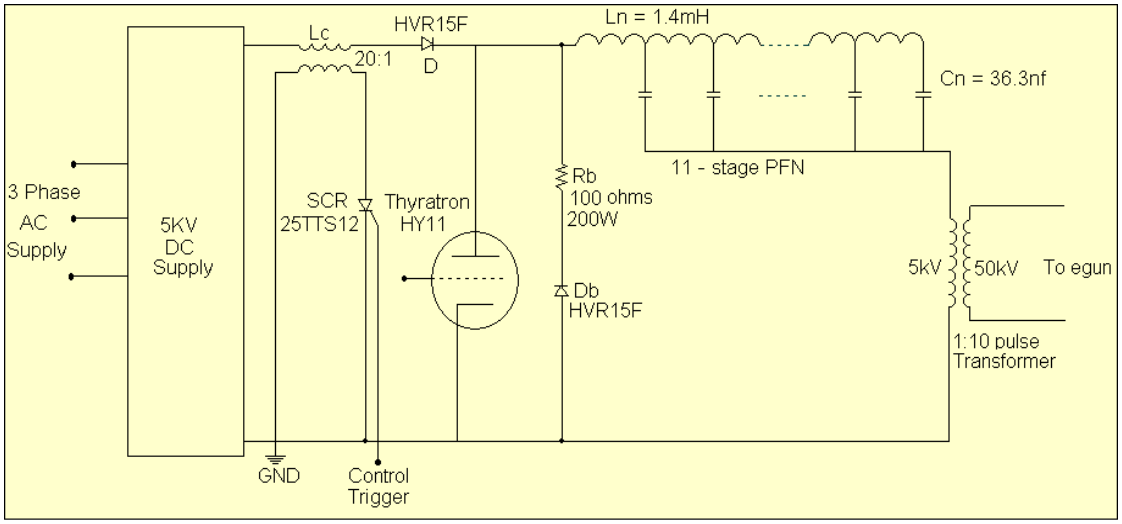

Fig.2 Schematic of the line-type pulsed modulator

Circuit description

The schematic of the line-type modulator is shown in Fig. 2. This consists of a 10 kV HVDC power supply, the charging choke, charging diode, 12-stage pulse forming network (PFN), hydrogen thyratron switch, pulse transformer and associated circuitry. The operation of the line-type modulator consists of the charging and discharging cycles. During the charging cycle, 5 kV (DC) is fed to the PFN by inductive charging, which results in 10 kV voltage build-up on the PFN capacitors, because of resonant charging [5].

In the discharge period, the hydrogen thyratron is triggered, thereby discharging the PFN capacitors through the PFN inductors, the thyratron and the primary winding of the pulse transformer. The voltage resulting across the primary of the pulse transformer is a pulse of required width of 10 μs.

By designing the PFN impedance to match the equivalent load impedance, pulse amplitude is 5 kV, i.e. equal to half the voltage across the PFN capacitors. The role of the pulse transformer is to step-up voltage to the required value of 50 kV, at a peak current of 1 Amp. The prototype modulator is shown in Fig.3.

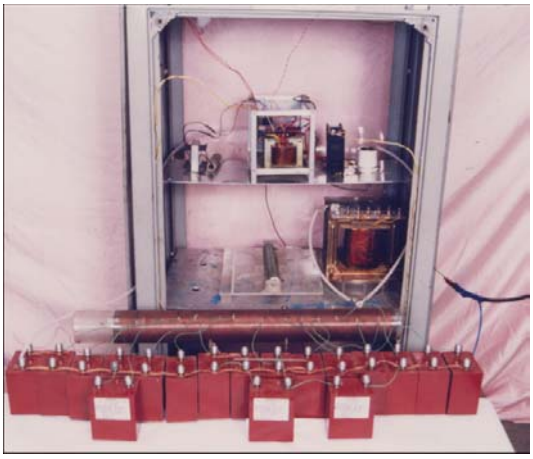

Fig.3 Prototype 50 kV, 1 Amp line-type pulsed modulator

The modulator has been tested up to 50 kV across a matched load. Fig.4 shows the 50 kV output pulse, measured with a calibrated 890:1 capacitive divider. Variation in the flat-top is found to be within ± 4%.

Description of thyratron grid pulser

The above modulator is operated at variable repetition rate by appropriately changing the frequency of the thyratron trigger. The thyratron

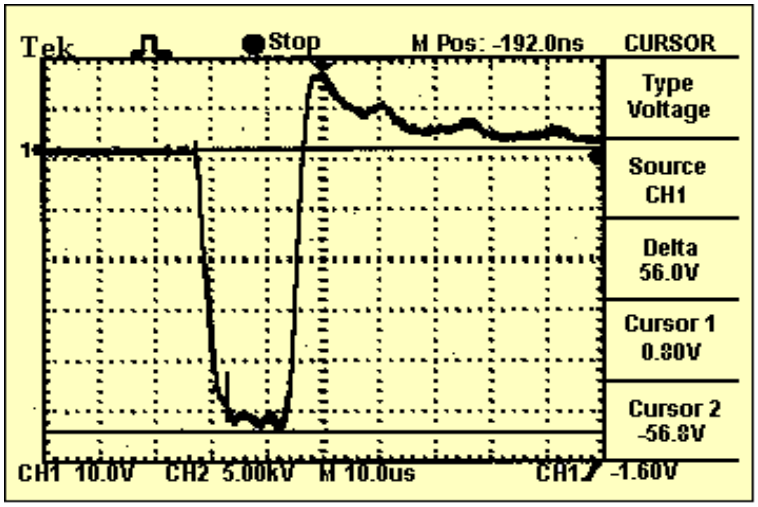

Fig.4 Output pulse of 50 kV as measured with a calibrated 890:1 capacitive probe

a minimum positive voltage of 190 volts. Grid impedance is 500 Ω. For this study, the grid power supply for this thyratron has been designed for variable pulse width and variable pulse amplitude as well.

Fig.5 shows the details of the grid driver circuit. IC 555 is operated in the astable mode, to derive pulses as per the requirement. By properly adjusting potentiometer (P1), the pulse width can be varied from 4μs to 50μs. Amplitude variation has been achieved by varying the output voltage of voltage regulator (LM317), with potentiometer (P2). These 2 parameters are adjusted for minimum grid dissipation. Pulse repetition rate is variable from 50 Hz to 500 Hz.

used in this set-up is a hydrogen thyratron (EG&G make HY-11), the grid of which requires

The output pulse from IC555 is fed to a MOSFET (IR1310), which gives an amplified pulse of 30V peak voltage, which is stepped up to 200 V by means of a ferrite core pulse transformer. This pulse transformer was designed and fabricated in-house. Droop is less than 5% for a pulse width of 10μs. Insulation of 15 kV has been provided between primary and secondary.

Characteristics of the modulator

In order to study the operating characteristics of the modulator in the variable rep.rate mode, the following procedure was adopted. For a set value of repetition rate, the DC charging voltage applied to the PFN capacitors, so that a peak output voltage of 50 kV was obtained across the resistive load. Charging choke value of 25 H was used for this experiment. Peak charging current was measured on the oscilloscope, with the help of Tektronix current probe (AM502S). The sensitivity selected for this experiment was 10mV/100 mA.

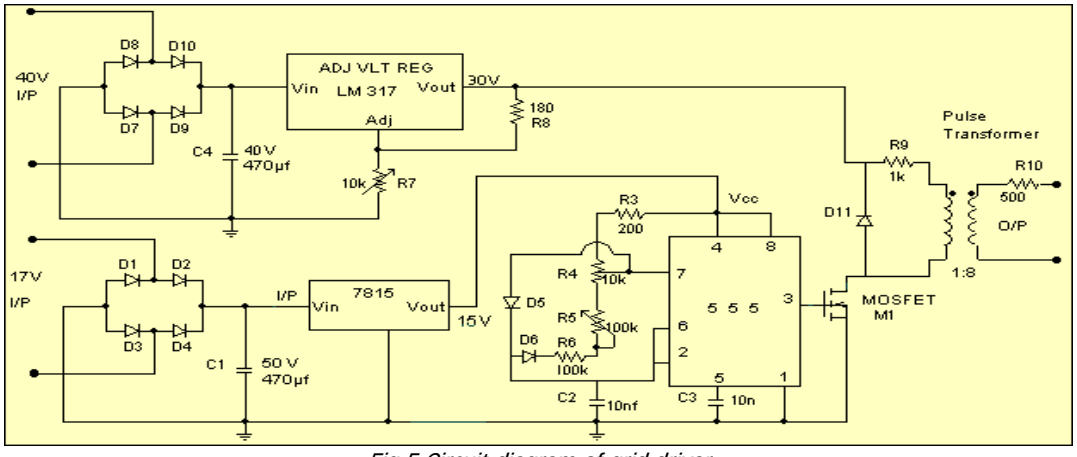

Fig.5 Circuit diagram of grid driver

Effect of variable repetition rate

Fig.6 shows the waveforms of peak charging current (trace 1) and voltage across the PFN capacitors (trace 2). It can be seen that for a dc charging voltage of 6 kV, the PFN voltage is 12 kV and the peak charging current is 340 mA. This current is in agreement with the calculated value of peak current.

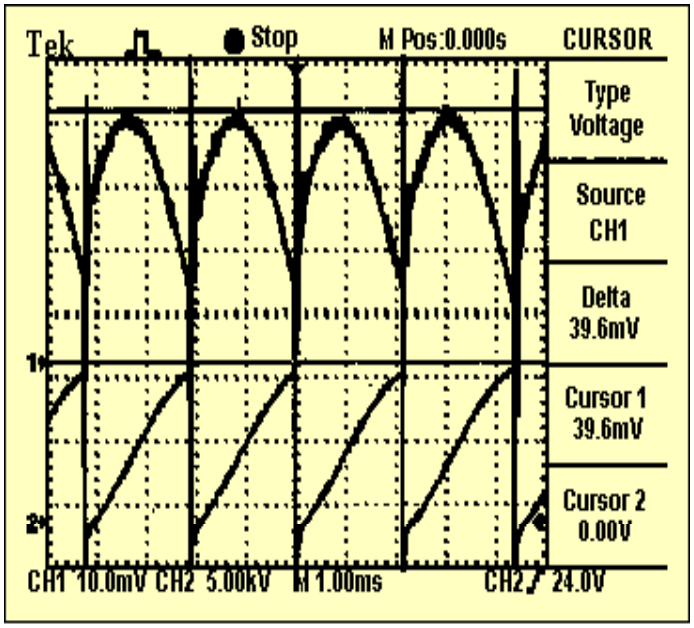

Fig.6 Waveforms of peak charging current (trace 1) and PFN voltage (trace2)

The repetition rates were varied from 100 Hz to 400 Hz and the resulting characteristics are shown in Fig.7. DC current increases proportionally with the rep.rate, while there is a marginal drop in the dc voltage. This is due to the fact that as rep.rate increases, so does the duty cycle, thereby causing an increase in average output power. It can however, be seen that in the entire range from 100 to 400 Hz, the output voltage remains constant at 50 kV.

Effect of charging inductance

Theoretical estimates show that the charging inductance value decides the peak current drawn from the dc power supply. Lower the value of inductance, larger is the peak current, which requires higher power rating of components, such as diodes, PFN capacitors, etc. In practice, the selection of the inductance is a compromise between size, cost and peak current. Optimization of these parameters resulted in 25 Henry inductance to be used.

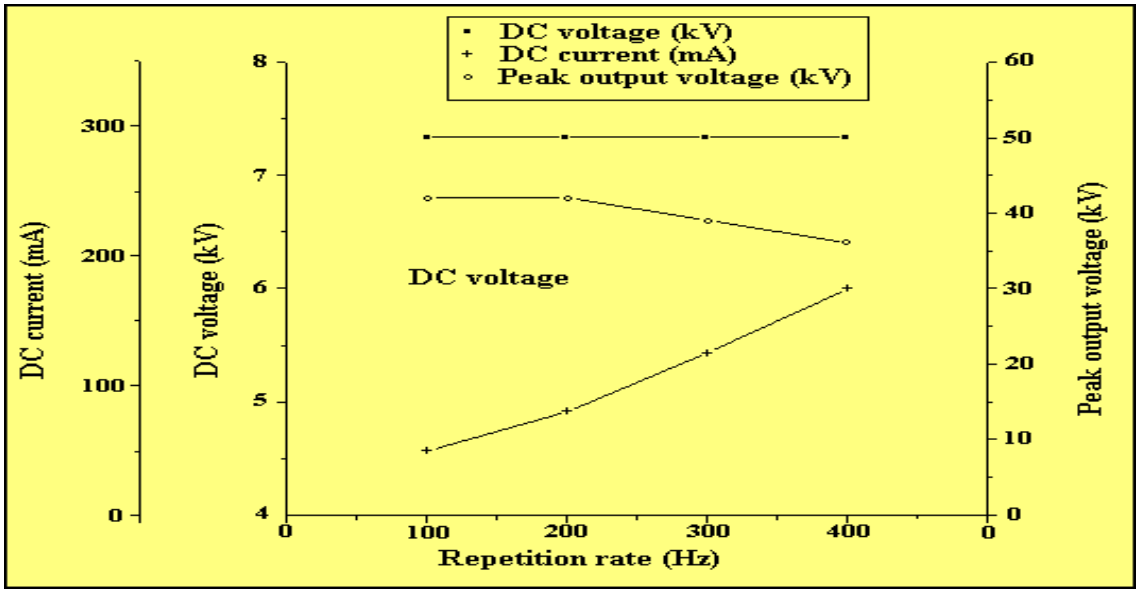

Fig.7 Characteristics of the modulator

Conclusions

The line-type modulator that has been developed is capable of delivering 50 kV, 1 Amp, 10 μs pulses with repetition rates from 100 to 400 Hz to a matched load. By varying the repetition rate, it is possible to vary the dose rates on the target in the operation of the 10 MeV linac.

Acknowledgements

The authors would like to thank the project team of the 10 MeV accelerator.

References

1. R.C. Sethi, V.T. Nimje, M. Sengupta, A.J. Dabeer, K.P. Dixit and P.H. Ron, "Design and Development of 10 MeV RF Electron Linac for Applied research and Industrial Applications", First Asian Particle Accelerator Conference APAC98, March 23 - 27, 1998, KEK, Tsukuba, Japan.
2. E.A. Abramyan, "Industrial electron accelerators and applications", Springer – Verlag, 1998, pp33
3. A.R. Chindarkar, K.C. Mittal, K.P. Dixit, V. Yadav, R.B. Chavan, A. Jain & R.C. Sethi, "Development of a high vacuum 50 keV, 1 Amp pulsed electron gun", Proceedings of the International Symposium on Discharges and Electrical Insulation in Vacuum, Jun.30 – Jul.5, 2002, Tours, France
4. K.P.Dixit, V.Yadav, R.B.Chavan, K.C.Mittal, A.R.Chindarkar, A.S.Paithankar & R.C.Sethi, "Design and Development of a 50 kV pulsed modulator for the electron gun of the 10 MeV, 10 kW RF Electron Linac", International Symposium on High Voltage (ISH-2001), Aug.20-24, 2001, IISc, Bangalore.
5. G.N.Glasoe & J.V.Lebacqz, "Pulse Generators", MIT Rad. Lab. Series, vol.5, McGraw-Hill, New York, 1948

This paper was adjudged as a prize winning paper (consolation) in the poster session I, at the DAE-BRNS Symposium on "Applications of Plasmas, Lasers & Electron Beams in Advanced Materials Processing (PBAMP-2002)", held at BARC, Mumbai, during September 25-28, 2002

About the authors ...

Ms Kavita P. Dixit, *B.E. (Electronics & Communication), graduated from the 30th batch of BARC Training School. She has been working in the field of RF Electronics for particle accelerators. She was awarded the M.Sc. (Engg.) degree in 1998 from IISC, Bangalore, for her thesis on the 'Characterization of the RFQ Accelerator.' Presently, she is actively involved in the design and development of the 10 MeV RF Electron linac.*

Mr Vivek Yadav*, B.Tech (Electronics), is from the 41st batch of BARC Training School. He is actively working for the development of E-gun modulator, microwave source and microwave components. He has successfully developed directional coupler for 10MeV RF Linac.*

Mr Ramchandra Chavan*, B.E (Computer Engineering) from Mumbai University, joined BARC in August 2000. Since then, he is associated with development of Electron Gun Modulator for 10MeV RF Linac.*

Mr A.R. Chindarkar *joined BARC in 1973. He has been working on the development of vacuum systems for pulsed and dc accelerators. He has developed electron guns for 500 keV, 3 MeV and 10 MeV electron industrial accelerators.*

Dr K.C. Mittal *is from the 18th batch of BARC Training School. He has been working on generation of pulsed intense gigawatt electron beams for plasma related applications. He has also worked on electron guns for DC and pulsed electron accelerators for industrial applications. Currently, he has taken up the development of superconducting RF cavities for ADS system.*

Dr R.C. Sethi *joined BARC in 1969 after graduating from the 12th batch of BARC Training School. Since then, he has been working in the areas of physics & technology of Charged Particle Accelerators, specially related to linacs, RFQs, cyclotrons, RF / Microwave Structures, Ion sources, magnets, etc. At present, as the Head of the Accelerator & Pulse Power Division, he is imparting guidance & leadership to the accelerator-based programmes of BARC.*

A Laser Beam Welding Facility for Sealing of Miniature Radiation Sources

S.K. Saxena, C. Mathew, Ramu Ram, R.B Manolkar, M.A. Majali, S.A. Balakrishnan and M.R.A. Pillai
Radiopharmaceuticals Division
Bhabha Atomic research Centre

and

G.L Goswami
Laser Processing & Advanced Welding Section
Bhabha Atomic research Centre

Abstract

A Nd: YAG laser welding facility was installed in the radioactive laboratory of the Radiopharmaceuticals Division, BARC to obtain high quality welds of the titanium encased radiation sources. Radiation sources based on ^{125}I for the treatment of ocular tumors were developed which are encapsulated in ISO specified titanium capsules. The inner core of the tiny sources were prepared and were sealed in titanium capsules of dimensions 0.8mm (ϕ) x 4.5mm (l) by laser welding. The laser beam parameters such as energy, frequency, pulse duration and welding speed were optimized to obtain leak proof welds. Laser welds were also characterized by optical and scanning electron microscopy for assessing their quality. The welded sources showed a total release < 5 nCi of ^{125}I, which is less than the permissible levels. In this paper we describe the laser welding set up and results of initial development work to obtain radioactive leak proof laser welding of the ^{125}I sources in titanium capsules.

Introduction

RADIOISOTOPE SOURCES OF LOW energy such as ^{103}Pd, ^{125}I, and ^{106}Ru are extensively used in the treatment of tumors such as ocular melanoma and retinoblastoma. Retinoblastoma frequently occurs in children in India, while ocular melanoma is rare among the Indian population. These tumors are treated with low energy radiation sources for their complete remission. Fabrication of sealed radiation sources involves sealing of active materials in a capsule made of inactive and inert metal, compatible with human tissues. While designing the capsule, factors such as mechanical strength and suitability for the intended use and environmental conditions under which the source is likely to be used, are to be carefully evaluated. Capsules made from pure titanium metal have been selected for this purpose, which can be subsequently welded for the intended use. Radiopharmaceuticals Division of BARC has developed ocular sources based on ^{125}I for the treatment of these ocular tumors. The tiny sources of dimension of 3.5 mm (l) and 0.5mm (ϕ) made of silver wire pieces coated with ^{125}I are encapsulated in titanium capsules of dimensions stipulated by ISO as illustrated in Fig-1.

We present here our experience to obtain radioactive leak proof laser welding of the ^{125}I sources in titanium capsules as per the stringent conditions set by Atomic Energy Regulatory Board (AERB) for type testing of these sources for the intended use.

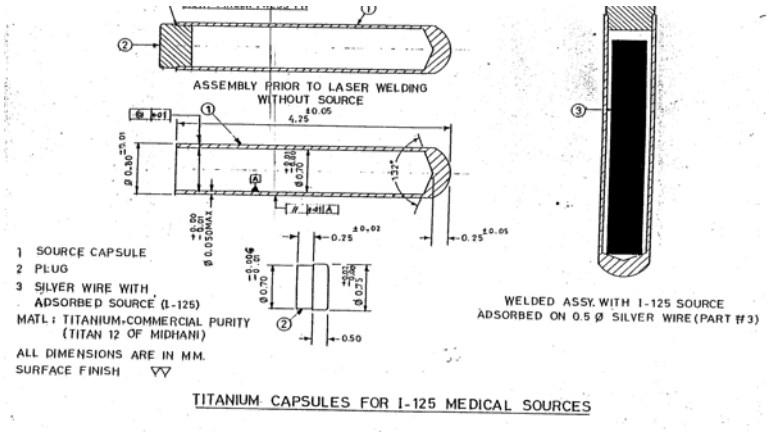

Fig 1 Sketch of titanium capsule

Materials and Methods

Silver wire (99.9% pure) of diameter 0.5 mm was obtained from a reputed commercial supplier. These were cut into pieces of 3.5mm in length. Iodine-125 as sodium iodide, reductant free was obtained from Perkin Elmer Life Sciences Inc. Boston, USA. Approximately 3.5mCi of ^{125}I – radioiodine was coated uniformly on these wire pieces by a special method [1]. Chemicals used in the work were of GR grade and used without purification. Titanium ingots were obtained from M/s Mishra Dhatu Nigam Ltd. Hyderabad, India for the fabrication of capsules.

A Laser welding machine was procured exclusively for this work. The technical specifications of the welding system were as follows:

Laser Type	:	Flash lamp excited Nd: YAG
Wavelength	:	1064 nm (IR)
Max. Av. Power	:	50 W
Peak Power	:	8 KW
Output Beam Dia.	:	8 mm
Pulse width	:	2 to10 mSec
Repetition rate	:	up to10 Hz
Aiming Beam	:	< 5 mW, 635 nm red diode laser
Beam Delivery	:	With an optical fiber
Power Supply	:	230 VAC, Single Phase, 16A, 50 Hz

Fabrication of Titanium Capsules

Initially, there were problems in getting the ISO specified titanium capsules of dimension 0.8mm(ϕ) X 4.5mm (l). The wall thickness of the capsules required to be fabricated was extremely small (50 microns), to encapsulate ^{125}I (with low energy x-rays and gamma photons) miniature inner source core for minimizing the attenuation effect. Thus, difficulties were observed in obtaining such small uniform thickness all along the length (4.5 mm) of the capsule. Also, due to the minute inner diameter of the capsule (0.7mm), the capsules developed cracks during turning operations rendering them useless for the intended purpose. Later the fabrication of titanium capsules was got done by M/s Hindustan Machine Tools Ltd. (HMT Ltd.) - a public sector company at Bangalore to maintain the required quality.

Laser Welding of Dummy Titanium Capsules

On account of extremely small wall thickness and highly oxidizing nature of titanium, the encapsulation of the radiation sources had to be carried out by laser welding. Initially the welding was carried out at Laser Processing & Advanced Welding Section, Nuclear Fuel Group, BARC. Subsequently, a new Nd: YAG laser system was procured exclusively for this work and installed. The laser machine was set up in a well-ventilated fume hood at Radio-pharmaceuticals Division, BARC (Fig-2). Titanium capsule was inserted with a radiation source (core) and cap was placed on the top. This was manually loaded on to the machine and held vertically. A laser beam was focused to the weld joint horizontally, by an optic fiber based delivery system. All laser parameters along with

rotation of the capsule including inert gas supply for shielding was controlled through PC. The system was operated remotely. Manual operation was also possible if required. A camera with a separate fiber based lighting arrangement was provided to view the welding region. This facilitated the operator to focus the beam properly.

Fig. 2 Laser welding set-up inside a fume hood.

Laser welding trials were carried out using inactive silver wire filled in titanium capsules fabricated at HMT. The welding parameters such as energy, frequency, pulse duration etc. were systematically optimized to obtain good uniform leak proof welds. These welds were evaluated by leak test and metallography. The leak test was carried out in different ways. The welded samples were kept in hot water and observed for the presence of any bubbles. Later, the samples were kept in helium chamber at 6 atmospheric pressure for 22 hrs and taken out one by one. These samples were tested by UL-200 (Lebold make) unit and found to be leak free. The observed leak rate for the samples are given in Table -1.

The metallography test of inactive welded capsules was carried out by Optical metallography and Scanning Electron Microscopy; SEM (Fig-4). The penetration depth in the samples were found to be ~ 2-3 times the wall thickness of the capsules (Fig-3).

Table 1: Leak Rate of Titanium Capsules

S.No.	Vacuum (Torr)	Leak Rate (std. cc/sec)
1.	$7.3x10^{-3}$	$0.5x10^{-9}$
2.	$9.2x10^{-3}$	$0.7x10^{-9}$
3.	$1.2x10^{-3}$	$0.8x10^{-9}$
4.	$9.0x10^{-3}$	$0.7x10^{-9}$
5.	$1.2x10^{-3}$	$1.1x10^{-9}$
6.	$9.7x10^{-3}$	$1.1x10^{-9}$

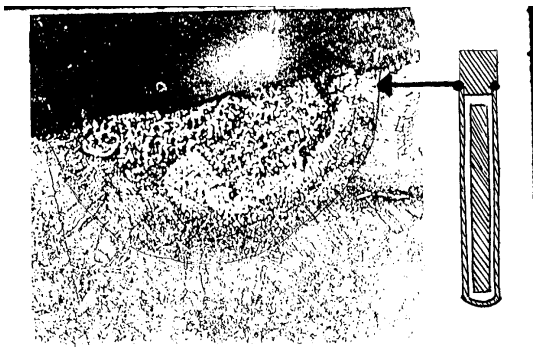

Fig. 3 Metallography of weld showing penetration.

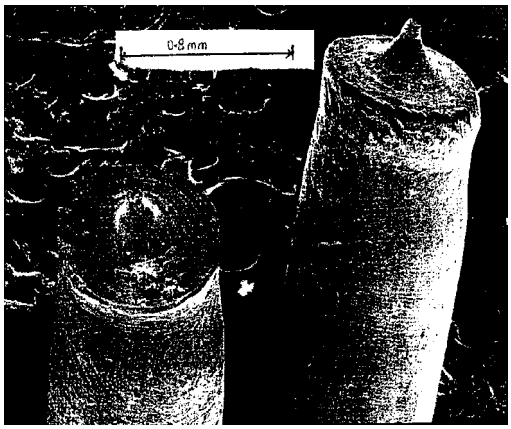

Fig. 4 SEM Photographs of welded capsules

Welding of ^{125}I encapsulated Sources

The welding of titanium capsules containing ^{125}I ocular sources was carried out for qualification and regular production. The welded sources

were cleaned in an ultrasonic bath to remove surface contamination (if any) and tested for leak as prescribed by AERB [2] .The air activity was constantly monitored during the process of welding.

Results

The laser welding process is the most appropriate sealing process for the above type of capsules used in this work and the system set-up is ideal for regular production of ^{125}I sources. The leak test of laser welded inactive titanium capsules and metallography was found to be satisfactory. The average leak rate with inactive samples was found to be ~ $0.8X10^{-9}$ std cc/sec in an average vacuum of $9.8x10^{-3}$ torr. The optimized parameters for leak proof and uniform welding of the radioactive capsules have been established. No air activity was observed during the welding. The total leakage with radioactive sources was found to be less than $5x10^{-9}$Ci (<185Bq) of ^{125}I when tested as per AERB standard. No surface contamination was observed.

Conclusion

Low energy radioactive sources based on ^{125}I are encapsulated in titanium capsules for good dosimetric properties. Laser welding is a better option for these miniature sources used in the treatment of eye tumors. Leak proof quality welds of these sources containing ^{125}I could be obtained by optimizing laser welding parameters without any detectable air activity.

Acknowledgement

Authors wish to thank Dr N. Ramamoorthy, Associate Director, Isotope Group, BARC, for his encouragement and support. Authors also wish to thank to Mr P.C. Bhat of Laser Processing & Advanced Welding Section, BARC, for his help in initial laser encapsulations. The special thanks are due to CDM, BARC, for the initial fabrication and dimensional check-up of titanium capsules. The help sought from RP&AD, BARC, and AERB for the quality assurance of the sources is gratefully acknowledged.

References

1. C. Mathew. M.A. Majali, and S.A. Balakrishnan "A novel approach for the adsorption of ^{125}I on silver wire as matrix for brachytherapy for the treatment of eye and prostate cancer ". Appl. Rad. Isot, 57 (2002) 359-367.
2. "Testing and classification of sealed radioactive Sources". AERB SS-3-1990.

The paper was adjudged as a prize winning paper in the poster session II at the DAE-BRNS symposium on "Applications of Plasmas, Lasers & Electron Beams in Advanced Materials Processing (PBAMP-2002)," held at BARC, Mumbai, during September 25-28, 2002

About the authors ...

Mr S.K.Saxena, *after graduating from Allahabad University, joined BARC in 1987. He has initially worked in the field of separation of fission produced isotopes. He has been involved in the development and routine production of various therapeutic sources based on ^{137}Cs, ^{125}I, ^{166}Ho, $^{186/188}Re$, etc. He has several research papers to his credit.*

Mr C. Mathew, *former scientific officer of RPhD, BARC, has worked initially in the separation programme of uranium fission products. He also contributed in the development and production programme of low dose rate brachytherapy sources based on ^{137}Cs and ^{125}I. He has several research papers to his credit.*

Mr Ramu Ram *joined the Isotope Division of BARC in 1998 after graduation in science from Maharshi Dayanand Saraswati University. He is presently working in Radiopharmaceuticals Division, BARC, and is involved in the preparation of ^{137}Cs-brachytherapy/industrial sources.*

Dr R.B.Manolkar *obtained his PhD degree from Mumbai University in 2000. He has worked on the development of ^{32}P coated stents for the prevention of restenosis. He has also contributed in the field of development of ^{125}I based brachytherapy sources. He has several research papers to his credit.*

Dr (Ms) M.A. Majali *obtained her PhD degree in 1990 from Mumbai University. She has formulated and developed a number of radiopharmaceutical preparations based on various medically useful radioisotopes which are used in clinical studies on a routine basis. She has several papers to her credit in national and international journals. She is a chief investigator of coordinated research programme of IAEA on the development of low energy radiation sources for the treatment of eye and prostate cancer.*

Mr S.A. Balakrishna, *former Head, Therapeutic Sources Section, RPhD, BARC, initiated the programme for the development of ^{125}I ocular sources based on silver-palladium combination. He has several national and international research papers to his credit.*

Dr M.R.A. Pillai, *after graduating from 19th Batch of BARC Training School, joined Isotope Division. Presently, he is heading the Radiopharmaceuticals Division, BARC. He is also concurrently holding the post of Senior General Manager, BRIT, and is looking after the Medical and Biological Products Programme (MBPP) of BRIT.*

A metallurgist from the 14th batch of training school, ***Mr G. L. Goswami*** *has significantly contributed in plutonium metallurgy, plutonium based fuel and its fabrication, welding technology, laser material processing and acoustic emission testing programme undertaken by BARC. He has set up a laser material processing lab at south site at BARC. He has been a member of many professional bodies, DST committees and coordinating international programme on laser material processing and welding technology. He is now active in laser based system development for different applications.*

Synthesis of Thermosensitive Poly(N-isopropylacrylamide) Hydrogel and its Copolymer by Gamma Irradiation

Anjali Acharya and S. Sabharwal
Radiation Technology Development Section
Bhabha Atomic Research Centre

and

Hari Mohan
Radiation Chemistry & Chemical Dynamics Division
Bhabha Atomic Research Centre

Abstract

The linear polymer of N-isopropylacrylamide (NIPA) formed by irradiating dilute aqueous solution is found to be a thermosensitive polymer with lower critical solution temperature (LCST) of ~ 33 ^{o}C. Gamma radiation induced polymerization studies showed that the reaction of $^{\cdot}H$ / $^{\cdot}OH$ / e_{aq}^{-} radicals with NIPA result in nearly equal yield of gel fraction and the hydrogel is observed to have very little swelling below pH 3 and above pH 10. NIPA has also been copolymerized by chemical crosslinking method with ethylene glycol methacrylate acid phosphate (EGMP) for extraction of lanthanide ions from aqueous solution utilizing the difference in binding characteristic of the metal ions with the copolymer below and above LCST.

Introduction

THE GEL SYNTHESIZED FROM NIPA monomer is a well known thermosensitive gel which shows a discontinuous volume phase transition in response to temperature changes (Panda et al., 2000). The crosslinked gel of NIPA undergoes a reversible volume transition at ~ 34 ^{o}C. Below this temperature the polymer dissolves in water and chains exist in an extended state. Above 34 ^{o}C, it acquires a dehydrated coiled state expelling bonded water and polymer precipitates out from solution. When extractant molecules are coploymerized in a polymer network, the mobility of extractant molecules is limited and the complex formation between metal ion and extractant molecules may be affected by the conformation of polymer network (Kenji and Yoshio, 2000).

Experimental

The linear polymer of NIPA was synthesized by irradiating aqueous solution of NIPA (4 wt%) in a gamma chamber to a total gamma dose of 8 kGy. The crosslinked polymer of NIPA was synthesized by irradiating aqueous solution of NIPA (10 wt %) for different times in a gamma chamber (dose = 0.48 kGy/hr) under experimental conditions such that only $^{\cdot}H/^{\cdot}OH/e_{aq}^{-}$ radicals react with the monomer. The % gel formed was estimated from the weight ratio of water insoluble fraction to the feed monomer. The copolymer of NIPA and EGMP

were prepared by free radical polymerization in dimethyl formamide (DMF). N,N'-methylene bis(acrylamide) was used as a cross linker. The polymerization was carried out at 60 ^{o}C for 24 hours.

Results and Discussion

Gamma radiolysis of 4 wt% aqueous solution of NIPA was found to give very good yield of linear polymer after irradiating with 8 kGy dose (dose rate = 8 kGy/hr). The aqueous solution of linear polymer of NIPA (10.25 mg/ml) was observed to be a temperature sensitive material. The LCST of linear polymer was determined by laser light scattering method. The diameter of polymer molecules decreased from 290 nm (25 ^{o}C) to 20 nm (35 ^{o}C) having a transition temperature of ~33 ^{o}C (Fig 1).

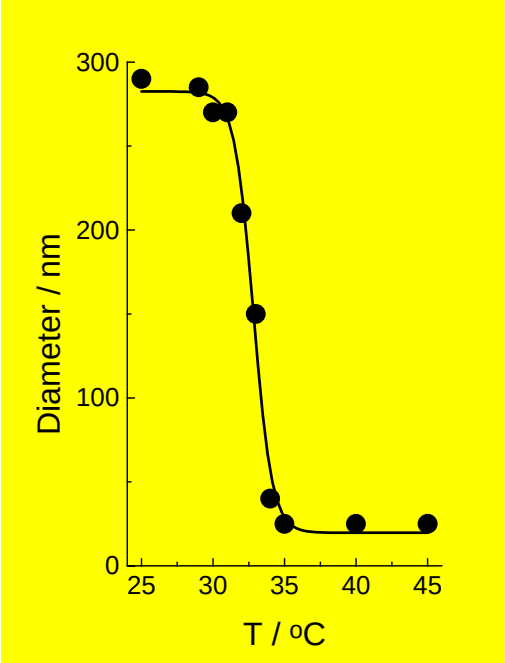

Fig. 1 The variation of diameter of polymer molecules as a function of temperature

At 25 ^{o}C, strong hydrogen bonding hydrophilic groups on the polymer chains with surrounding water molecules makes it water-soluble. However at higher temperature the hydrogen bonding weakens hydrophobic interactions result

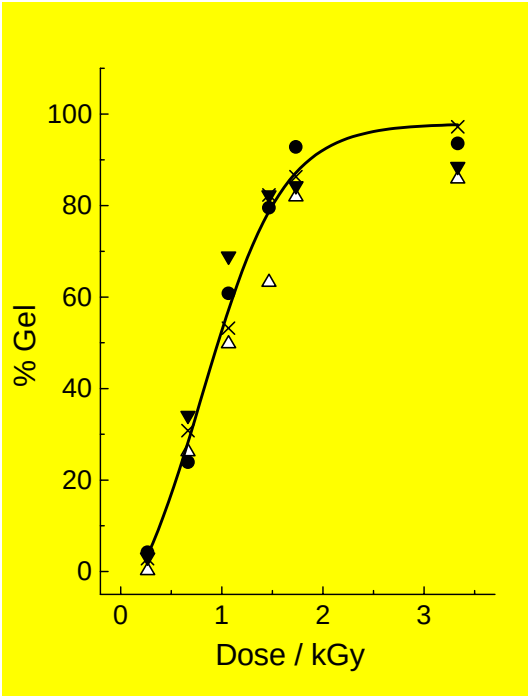

Fig. 2 : % gel formed on γ–radiolysis of aqueous solution of NIPA (10 wt %) under different conditions of γ–radiolysis. N_2O-saturated,pH 7 (•) ; N_2-saturated, pH 1, tertbutyl alcohol=0.3 M (x) ; N_2-saturated, pH 7, tert-butyl alcohol =0.3 M (Δ) ; O_2-saturated, pH 7,tert-butyl alcohol =1.0 M (▼).

in the folding of the polymer chains and the polymer precipitates out from the solution. 10 wt% aqueous solution of NIPA was gamma irradiated (dose rate = 0.48 key/hr) for different periods of time, under conditions such that only one of the radiolytic species ($^{\cdot}H$/ $^{\cdot}OH$/e_{aq}^{-}) react with NIPA. The gel % was observed to increase with gamma dose (Fig 2), although the yield of the gel formed on reaction with e_{aq}^{-} was low, but the yields have not followed the G values of primary radiolytic species of water radiolysis. tert-Butyl alcohol radical contribution may explain the high yield of gel formed on reaction with e_{aq}^{-} and $H^{\cdot}$ atoms. The swelling ratio of NIPA hydrogel was determined in aqueous solution of different pH. It is clear from Fig 3 that swelling ratio remained same in the pH range of 3 – 10. Both at lower and higher pH,

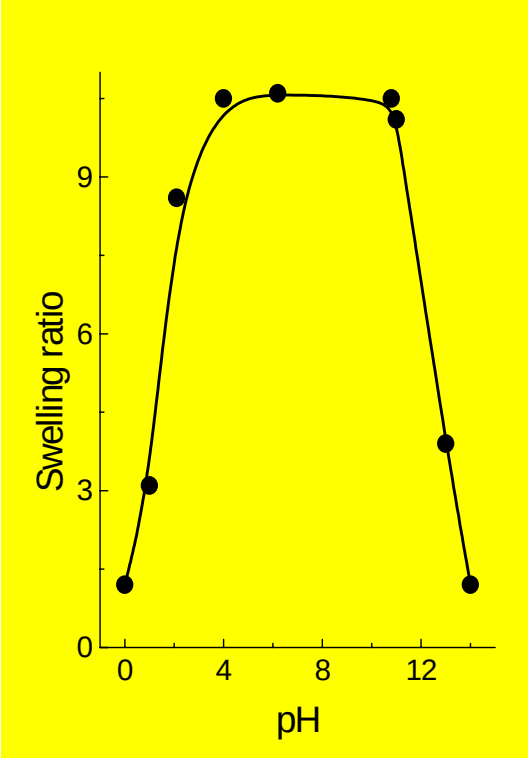

Fig. 3 Swelling ratio of NIPA hydrogel kept in aqueous solution of different pH.

appreciable decrease in swelling ratio was observed. This may be due to hydrolysis of amide group of the polymer in highly alkaline and acidic solutions. Copolymer of monomer such as NIPA and EGMP were prepared by free radical polymerization in DMF by both chemical and radiation means. N,N'-methylene bis (acrylamide) was used as a crosslinker. For chemical polymerization, benzoyl peroxide was used as an initiator. The gel synthesized by gamma irradiation (10 kGy, dose rate = 0.48 kGy/hr) was found to be thermo insensitive and its swelling ratio was independent of temperature. The gel synthezed by chemical polymerization shows thermosensitivity in water and have been used to extract lanthanide elements into the gels from an aqueous solution containing 500 mg of metals/dm^3. the initial pH of aqueous solution were adjusted over the range of 0.5 to 3.5 by adding HNO_3.

In preliminary experiments, extraction of Europium, Eu(III) was 81% and 17% at 50 ^oC and 28 ^oC respectively. 0.05g of dry gel was used for the experiment. Further experiments are in progress to optimize experimental conditions wherein radiation polymerize gel retain their thermosensitivity.

Conclusions

The % of PNIPA gel formed increased with gamma dose and reached a saturation of ~ 90% at a gamma dose of 0.22 kGy. The yield and the nature of the polymer depend on total gamma dose, dose rate and monomer concentration, but independent of initiating radical. The NIPA and EGMP copolymer gel obtained by conventional method can be beneficially used for the extraction of the lanthanide elements from an aqueous solution.

References

1. Panda, A.; Manohar, S.B.; Sabharwal, S.; Bhardwaj, Y.K. and Majali, A.B. 2000, Radiat. Phys. Chem., **58**, 101.
2. Kenji, T. and Yoshio, N. 2000 Solvent Extraction and Ion Exchange, **18**, 375.

This paper was adjudged as one of the Best Poster Papers in the 13th Annual Conference of Indian Nuclear Society (INSAC-2002)on "Nuclear Technology - Catalyst for National Development", held at Mumbai, during October 9 – 11, 2002. The prize was awarded to Dr Anjali Acharya.

About the authors ...

Dr Anjali Acharya *obtained her M.Sc. and Ph.D. in Chemistry from Utkal University. She joined as a Research Associate in Radiochemistry Division, under CSIR-scheme in 1997. She was awarded Dr K.S. Krishnan Research Associateship in 2000 and worked on synthesis, characterization and applications of stimuli sensitive hydrogels in RTDS. She has 25 publications to her credit.*

Dr S. Sabharwal *graduated from BARC Training School (Chemistry) in 1979 and is presently Head, Radiation Technology Development Section. He has been associated with developing industrial application of radiation technology in the area of polymer processing. His current research interest include studying radiation effects on synthetic and natural polymer specially application of responsive hydrogels.*

Dr Hari Mohan *graduated from BARC Training School (Chemistry) in 1967. His main area of research is the study of fast reaction kinetics using electron accelerator and lasers. His current research interest include free radical reactions of biomolecules and natural products.*

Modular Sludge Lancing Equipment for Mushroom Type Steam Generators of Pressurised Heavy Water Reactors (PHWRs)

Shirish Nawathe, K.L. Soni, J. Aparna, J.N. Kayal, B.B. Rupani, L.R. Mohan and H.P. Vyas
Reactor Engineering Division
Bhabha Atomic Research Centre

Abstract

Periodic sludge lancing enhances steam generator life by mitigating corrosion between its tubes and tube sheet. The present modular sludge lancing equipment has been designed to dislodge and remove sludge from secondary side of tube sheet of mushroom type steam generators of PHWRs. This equipment comprises of a closed loop De-mineralised Water Circulation System (DWCS), high-pressure remote lancing Jet Manipulator Assembly (JMA) and Remote Visual Inspection System (RVIS). This entire system including JMA & RVIS is monitored and maneuvered by electronic instrumentation and PLC based supervisory control units.

Introduction

THE EQUIPMENT IS BASICALLY DIVIDED into six process modules, specially designed JMA, I & C panels, electrical power supply panel and RVIS. All dimensions of modules are within 2.8 m. The modules are interconnected with suitable flexible hoses with cam type Quick Release Couplings (QRC). Successful working of sludge lancing equipment is demonstrated on a steam generator mock up assembled in Engg Hall-3 for this purpose. The schematic flow diagram of the sludge lancing equipment is shown below.

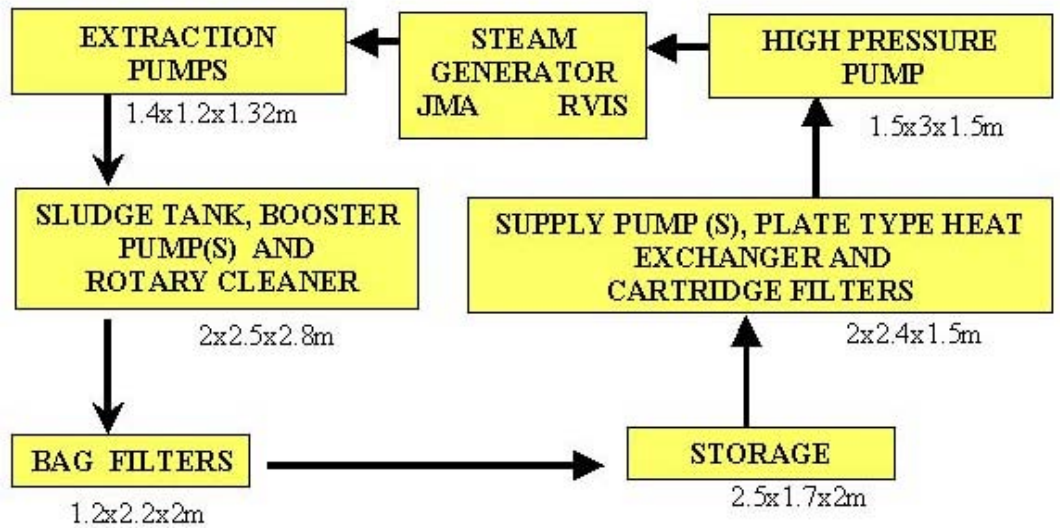

System Description

The high-pressure water jet dislodges the sludge from the secondary side of Steam Generator tubes (of limited heights ~~ 150 mm) and tube sheet face, which gets collected on the bottom tube sheet. This is extracted to Sludge Tank (ST-1) by self-priming air operated double diaphragm pump (EP-1 or EP-2) capable of handling 0 to 18.0 m^3 / hour of sludge water. The Sludge Tank (ST-1) has in-built filtering (wire mesh of size 200 microns) provision to collect the sludge particulate above 200 microns. The flow of sludge water is from out side to inside. The provision has been made to clean the tank using wire brushes from three hand holes. The provision also exists to remove the special filtering part outside for cleaning purpose as and when required. A set of low-pressure hoses of 40 (from SG to diaphragm pump) & 50 mm size (for interconnection of all other modules), pressure gauges, thermowells and safety devices such as relief valves are provided. The sludge water is fed from ST-1 to a Rotary Cleaner (RC) for the separation of particulate above 100 microns with the help of a centrifugal booster pump (BP-1: 18 m^3 / hr at 5 kg/cm^2). The rotary cleaner consists of motorised rotary filter drum and a scraper. It is basically useful when liquid is heavily loaded with sludge. Sludge is collected into the bottom hopper and periodically withdrawn by operating drain valve as and when required. The outlet from the RC is passed through basket filters BF-1 (30 microns) & BF-2 (2 microns) or BF-3 (30 microns) & BF-4 (2 microns) and then to the main storage tank (ST-2).

The storage tank has a total capacity of 4.0 m^3 and is divided into two partial compartments for the sludge settling purpose. Drains are provided for each of these compartments. A central manhole of 600 mm diameter is provided for internal access and cleaning

The sludge water is then passed through a compact Plate type Heat Exchanger (PHE) or a bypass line and a cartridge filter CF-1 or CF-2 or CF-3 (each 0.5 micron) with the help of a Supply pump (SP-1: 18 m^3 / hr at 8 kg/cm^2) for further finer filtration. A high pressure Triplex Pump (TP: 9 m^3/hr at 250 kg/cm^2 from main discharge and 6 m^3/hr from pump bypass with available Jet Manipulator Assembly and nozzles) feeds the filtered sludge water to SG through Nozzle head as high-pressure jets. The Triplex Pump can operate from 0-250 kg/cm^2. The Jet Manipulator Assembly maneuvers the nozzle head. Triplex pump (TP) is connected to valve station by 25mm high-pressure hose and the nozzle head is connected to valve station through a 15mm high-pressure hose. The sludge of the secondary side of SG is cleaned with the help of high-pressure water jet stream emerging from eight nozzles of Jet Manipulator Assembly.

The total system hold up is about 6 m^3 of DM water. The system material of construction is stainless steel and the flexible hoses are PVC with inner ss wire braiding with quick release couplings at the ends. High-pressure hoses are made from metal wire reinforced rubber with high pressure QRC at the ends.

During the cleaning process, pH and conductivity of DM water are continuously monitored and recorded on duel channel recorder. DM water is to be replaced if the conductivity exceeds 100 microns Si/cm (micro siemen per centimeter) at increased foaming and if the pH goes out of the range (5 to 10).

Module Description

For ease of mobility and accommodations the entire lancing system has been divided into 6 main modules. Each module has been provided with collection trays at bottom to collect small spillage from the system. Spillages from different modules will be collected in a central drain or trench by PVC hoses. The modules are designed for ease of mobility with chassis frame mounted on lockable swivel castor wheels. Suitable jacks have been provided to allow the trolley to take a firm location wherever required. Properly designed lifting lugs/ hooks have also been provided for lifting/ pulling the entire module with help of crane for transportation, loading

and unloading. The six modules are described in following paragraphs.

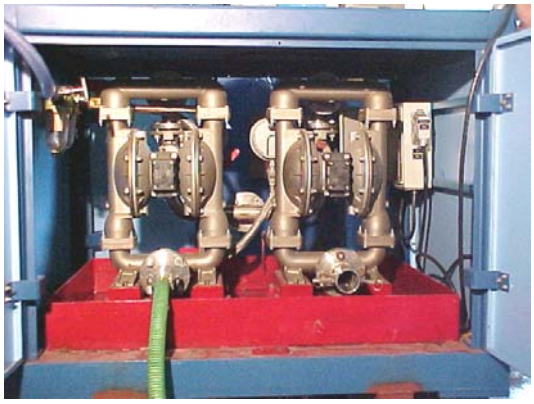

Module No 1: This module (1.4 x 1.2x 1.34 m) houses two air operated diaphragm pumps (EP-1 and EP-2), suction and discharge piping, associated valves and instrumentation. The provision of supporting suction hose on a magnetic stand exists to avoid obstruction in suction flow.

Module No 2 : This module (2 x 2.5 x 2.8m) houses sludge tank (ST-1), Centrifugal Pump (BP-1), Rotary Cleaner (RC) (suitable to remove particulate of 100 microns and above), associated piping, valves and instrumentation. However, a spare Centrifugal Pump (BP-2) is also available.

Module No 3: This module (1.2 x 2.2 x 2m) has a set of Stage-I filter assemblies namely BF-1 & BF-2 and BF-3 & BF-4 in series parallel arrangement. These are bag type filters capable of separation of sludge 30 microns from BF-1 or

BF-3 and 2 microns from BF-2 or BF-4. One set of filter assemblies (BF-1 & BF-2 or BF-3 & BF-4) will be on line during lancing operation. The other set of filter assemblies will be either standby or under cleaning as the case may be. The filter bags are made out of polypropylene material and capable of withstanding a pressure of 6.0 Bar.

Module No 4: Main storage tank (ST-2) occupies the entire space of module No 4 (2.5 x 1.7 x 2m) and is mounted on an open trolley/chassis frame. This has two compartments to facilitate settling of crud

escaped from module No 3. The volume of this tank is about 4.0 m^3.

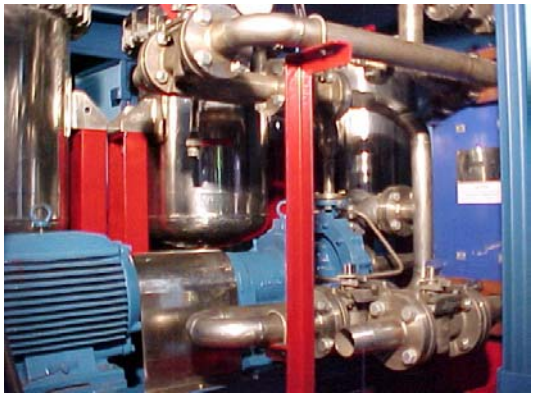

Module No 5: This module (2 x 2.4 x 1.5m) accommodates a supply pump (SP-1), plate type Heat exchanger (PHE) and a set of stage-II filters (CF-1, CF-2 & CF-3) (suitable to remove particulate of size 0.5 micron and above), associated piping, valves and instrumentation. However, a spare Centrifugal Pump (SP-2) is available.

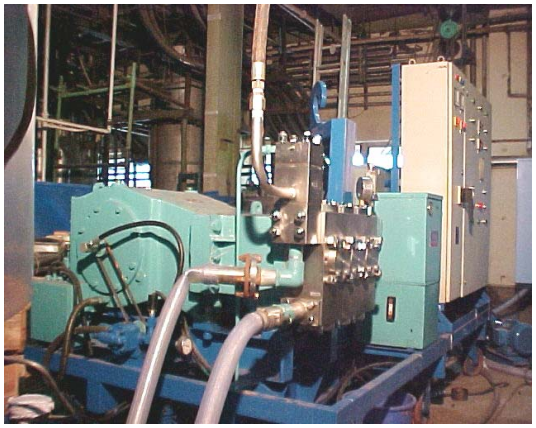

Module No 6 : This module (1.5 x 3 x 1.5m) houses High pressure Triplex plunger pump (TP) that is most critical assembly of lancing process. An accumulator shall be provided at the discharge end of this pump to smoothen the flow pulsation if desired at a later stage. The pump is equipped with a pressure relief valve to obviate any abnormal pump behaviour. A bypass with pre set pressure device for low- pressure discharge with unloader device on discharge has also been provided. The main pump motor control panel and other related accessories are located on this module itself. This pump is mounted on open movable chassis frame.

Jet Manipulator Assembly (JMA)

The jet manipulator assembly consists of mainly three sub assemblies, namely horizontal positioning device, Lifting device and nozzle head (photograph given below). Each sub assembly is designed to pass through hand hole, having 180 mm diameter and 100 mm wide gap between steam generator shell and shroud. All wetted components of the jet manipulators assembly are made from stainless steel and gripping shoes are made offrom aluminium to avoid damage to the tubes. All three components of JMA are assembled after insertion through a hand hole.

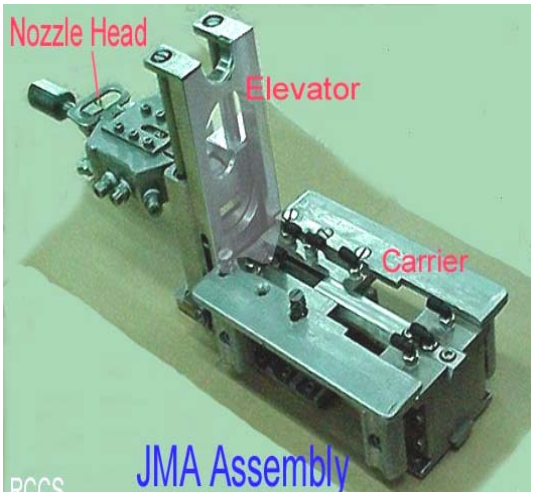

The jet manipulator moves in forward or backward direction along with central no-tube lane to dislodge the sludge and deposits from the tube sheet of the secondary side of steam generator. The nozzle head directs the multiple jets along the narrow inter tube lanes having 3 mm width, on both sides of the central no tube lane. The nozzle can be set to move at different elevations such that the multiple jets will graze along the narrow tube lane to create the sludge lancing action. The provision exists for lancing in both forward & reverse movement of JMA.

Remote Visual Inspection System (RVIS)

The inspection system is based on standard 1/3" CCD B&W/ colour miniature camera module with a suitable lens to carry out the visual inspection of the area after sludge lancing operation.

Mock-Up Facility

A full-scale mock-up of more than half of the lower part of the steam generator secondary side has been fabricated to qualify the handling procedure of JMA and RVIS & qualification and training of manpower. The mock-up includes the two hand holes at extreme ends of no-tube lane and one hand hole perpendicular to the No- tube lane. The tubes are arranged in three rows on each side and along the No-tube lane, five rows perpendicular to the No-tube lane and another five rows at 30º/150º from the No-tube lane. The base plate simulates the tube sheet. The mock-up has been made of stainless steel material to avoid corrosion and the tubes are of Incalloy material to simulate the actual tubes of steam generator. The lancing operation can be demonstrated for its satisfactory performance as regards to its accuracy and speed of positioning with the space restrictions on this mock-up. The sludge removal ability can be demonstrated, while maintaining the system parameters.

Performance Testing And Characterisation

The entire system has been tested successfully in Hall-3, however, the work for preparation of dummy sludge and simulation of its bonding is being planned. The performance tests shall commence very soon.

Conclusion

This equipment has been developed successfully by BARC as an import substitution against a purchase order from NPCIL following a global tender, which meets all the technical requirements of tender specifications.

Acknowledgement

The authors are especially indebted to Mr R.K. Sinha, Associate Director, Reactor Design & Development Group for his kind guidance in development of sludge lancing equipment. The authors would also like to express their gratitude to Mr R. K. Modi of Division of Remote Handling & Robotics and Mr P.B.S. Sengar of Waste Management Division for their valuable contributions to design and development of sludge lancing equipment.

This paper was adjudged as the Best Paper in the poster session presented at the 13th Annual Conference of Indian Nuclear Society (INSAC-2002) on "Nuclear Technology - Catalyst for National Development", held at Mumbai during October 9-11, 2002

About the authors ...

Mr Shirish Nawathe, *B.E. (Mech) from 28th batch of Training School, is actively working for design & development of mechanical systems/ components required for PHWRs, AHWR, Critical Facility for AHWR, Sub Critical Facility etc. Earlier, he has also worked for technology transfer related activities.*

Mr K.L. Soni, *B.E. (Mech) from 18th batch of Training School, is actively working for design & development of mechanical systems/ components required for PHWRs and AHWR. He is also working for development of import substitution components.*

Ms J. Aparna, *B.E. (I & C) from 33rd batch of Training School, is actively working for design, procurement, installation and commissioning of process instrumentation & control for various testing facilities required in support of R & D for PHWRs & AHWR.*

Mr J.N. Kayal, *B.E. (Mech) from 20th batch of Training School, is working on development of technologies for inspection and repair of reactor components and life extension of the same.*

Mr B.B. Rupani, *Head, Reactor Coolant Channel Section, RED, is from 17th batch of Training School and has taken a leading role in design & development of various systems and technologies required for in-service inspection, repair and life extension of coolant channels of PHWRs. He is also responsible for development of many technologies regarding AHWR coolant channels.*

Mr L.R. Mohan, *Head, Instrumentation section, RED, is from 15th batch of Training School and has carried out design, procurement, installation and commissioning of process instrumentation & control for Dhruva reactor, many engg set-ups and IX plan projects.*

Mr H.P. Vyas *graduated in 1970 from L D college of Engineering, Ahmedabad, in electrical engineering and joined 14th batch of Training School. After successful completion of training, he joined RED. He obtained MBA in 1984 from University of Mumbai. He has sound knowledge of French language. He actively worked for design & development of components & systems of Dhruva reactor. He worked for design of Superconducting Super Collider project in Dallas-Texas during 1991-92. Presently, he is heading Technical Services Section, RED, and working for design & development of AHWR systems.*

Use of Image Analysis in Mutation Breeding for Changing Grain Shape in Durum Wheat

S.G. Bhagwat
Nuclear Agriculture and Biotechnology Division
Bhabha Atomic Research Centre

Summary

INDUCING MUTATIONS IS A USEFUL technique where a defect in a variety needs to be corrected. A durum wheat with excessively long grains was mutagenised using gamma rays and successive generations were screened by measuring grain length and width. Shorter grains with minimum loss of width were selected. The seeds in M_6 generation showed small but significant reduction in grain length and width. The ratio of width to length was comparable or better. The study shows that combining mutation breeding with image analysis may help in using induced variation which otherwise was difficult to use in crop improvement.

Introduction

Grain size and shape are important components of quality in wheat. Larger plump grains have more consumer preference. In general larger plump grains are expected to yield more flour per unit grain weight (Blackman and Payne 1987) on account of higher volume to surface area ratio. Mutagenesis has been used to improve grain shape or size characteristics. These are usually major changes which can be picked up by the eye when screening the early generation segregating population. A number of important traits including grain size are influenced by many genes indirectly through floret fertility, vernalisation, photoperiodism and height or directly by genes reported to be located on the chromosomes 1A,1D and 7A (Worland et al 1987). The grain parameters are thus governed by polygenes. The phenotypes in these traits are determined by many small genes each with a small contribution. These traits are also influenced by the environment which may interact with the genetic variation. Mutations in the polygenes induce small phenotypic changes which are difficult to study with naked eye. Computer based image analysis which is considered young science (Sapirstein 1995) is finding a lot of applications in biological and agricultural sciences. The use of image analysis allows measurements of grain dimensions in large numbers with ease and accuracy. At the Bhabha Atomic Research Centre, studies have been carried out demonstrating the use of image analysis in grain morphometric studies of wheat (Shouche et al 2001) and groundnut (Badigannavar et al 2001). In this paper results on selection and stabilization of mutants with small changes in grain length of a local durum variety, with the help of image analysis are presented. The variety PBND-1625 has excessively long grain which is prone to breakage during threshing, the bran proportion of longer grains is higher and the variety also suffers from concavity on the crease side of the grain. This study was carried out to attempt improvement by eliminating the defect(s). The results show that it is possible to select for morphometric mutants for grain quality improvement.

Materials and Methods

The local durum wheat variety PBND-1625 was obtained from Dr. K.A. Nayeem of the Marathwada Agricultural University, Parbhani. The original variety was irradiated with 20kR gamma rays. The M_1 generation and subsequent generations were raised in the field at Trombay. The M_1 plants were allowed to self and individual plant harvests were collected.

Image analysis and measurements

The image analysis system consisted of a black and white CCD camera attached to a PC (Pentium II). The software used was obtained from Expert Computers (I) Ltd. The programme Biovis Image Plus version 1.4 is capable of capturing images and computing several morphometric characters. In this study grain length (major axis) and grain width (minor axis) were measured. The calibration as carried out for vertical as well as horizontal axes to get values in millimeters. Most often, 20 grains were used per sample for collecting measurement data. The grains were arranged in crease down position on a platform. The grains were arranged on rows parallel to each other with their embryos pointing in one direction. Care was taken to avoid any grains touching each other. Lighting was kept comparable between different samples. The programme provided means of all the grains in the view and the standard error.

From the length and the width means, ratio of width to length was calculated. Selection was for lower average grain length compared to the control (parent variety) and also for higher width to length ratio. Better plants were carried forward in plant to row fashion. Although, the plants were well spaced in the field, to avoid mixtures single spikes were collected in most cases. Hundred kernel weights were estimated mostly from the same twenty grains used for image analysis.

When image analysis was not possible, five or ten grains were lined up and actual measurements were taken from which the average length and width were calculated.

Results and Discussion

The parent variety on the basis of actual measurements showed following characteristics as shown in Table-1.

The selfed M_1 plant harvests i.e. the M_2 seeds showed variation for grain length and width. There were no extreme mutations showing reduced length, hence, the small variations were used. There was a positive association between grain length and width (Fig. 1), however some exceptions were observed.

Table-1

Parameter	Mean of ten grains (mm)	Mean
Grain length (ten grains)	101,102, 102	10.17
Grain width (ten grains	30,30,29	2.97
W/L ratio		0.29
HKW		6.14

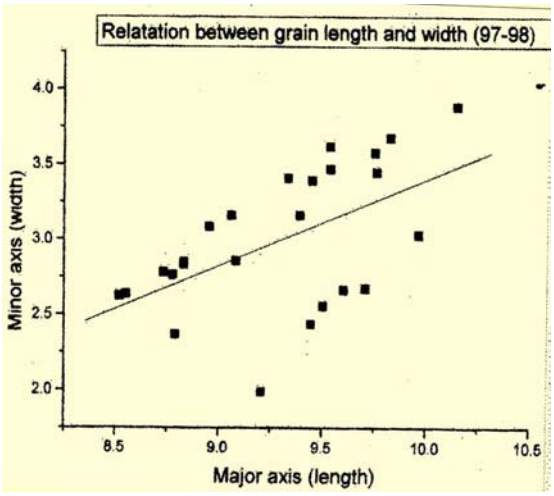

Fig. 1 Relation between grain length and width.

The grains in the M_6 generation measured using image analysis and their parents measured using actual measurements are shown in the Table-2.

The pedigree of one of the mutants traced from M_3 generation onwards is shown in Table-3.

The results showed that reduction in grain length was brought about and was consistently seen over generations. The W/L ratio was also consistently higher.

Statistical analysis using actual measurements (five grains at a time) showed that two lots of the control did not differ from each other in length and width (50.0, 49.6 and 15.3,15.2) significantly, however the mutant 02-4-5 was

significantly lower in both grain length (45.0) and width (14.3) at 5% level of significance. The W/L ratio of the mutant was higher in the mutant (0.32) compared to the parent (0.31).

Table-2

No.	Length	Width	W/L ratio	HKW
Control	9.664	3.260	0.3373	5.985
02-3-37 (M_6)	9.378	3.247	0.3462	6.275
01-1-6 (M_5)	9.2	2.8	0.3043	
02-4-5.2 (M_6)	8.953	2,245	0.3624	6.090
01-3-45 (M_5)	8.6	2.6	0.3023	
02-4-5.3 (M_6)	8.999	3.087	0.3430	5.725
01-3-45 (M_5)	8.6	2.6	0.3023	
02-3-12 (M_6)	9.076	3.138	0.3457	5.815
01-17-24 (M_5)	9.2	2.8	0.3043	

Table-3

Generation	No.	Length	Width	W/L ratio
M_6	02- 4- 5	8.95 (9.66)	3.25 (3.26)	0.362 (0.33)
M_5	01- 3-45	8.60 (9.60)	2.60 (2.86	0.302 (0.30)
M_4	00-11-39-1	8.93 (9.20)	2.56 (3.04)	0.286 (0.33)
M_3	99-4A-3-1	8.82 (9.50)	2.28 (2.28)	0.254 (0.24)

The grain characteristics are often quantitative traits, governed by several genes with small contribution to the phenotype by each gene. Obtaining major phenotypic change is not very likely in such a case. When there is a mutation in one of the polygenes, it is not easy to notice it or follow it through generations because the change is small and also the environment modifies the phenotype. Also, in wheat, its polyploid nature poses problems because the mutation can be partially compensated by the normal gene on homoeologous chromosome(s). Image analysis allows detection of small changes by taking observations accurately on a large number of samples.

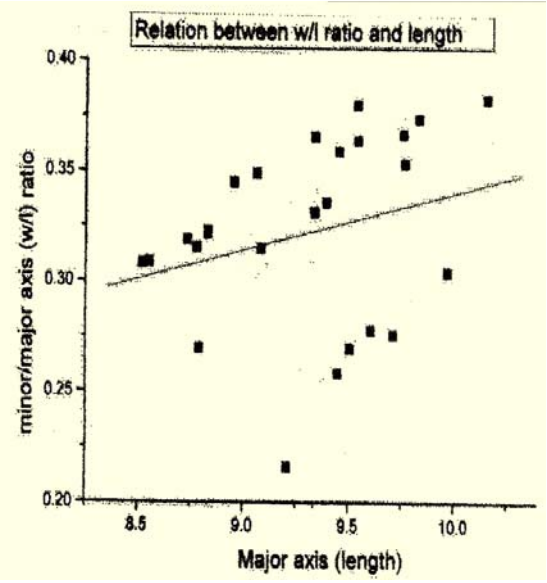

Fig. 2 Relation between grain length and width to length ratio

The mutants observed in this experiment showed small but consistent reduction in grain length. In general the grain length and width were found to be associated. Reducing grain length thus would mean reducing grain width as well, thus, reducing the grain size. An attempt was made to prevent proportionate loss of width by selecting also for higher W/L ratio. The mutants selected thus had significantly lower length and width but the W/L ratio was not reduced or in many cases it was better (Fig. 2, Table-2). Although the grain length reduction appears small it made appreciable difference in the appearance of the grain (Fig. 3, 4) as the concavity was also reduced considerably.

Using this technique many mutants with small induced variation can be obtained and subsequently recombined to enhance the phenotype. This approach will allow handling the polygenic traits with more ease.

Fig.3 Grains of parent and some of the mutants

Fig. 4 Grains of parent and mutant

Thanks are due to Mr B.K. Das for some measurements in the M_2 generation.

References

1. Badigannavar A.M., Kale D.M., Bhagwat S.G. and Murty G.S.S. 2001. Image analysis in groundnut morphometric studies. Image analysis in materials and life sciences. Proc. SCIAMAL-99. Ed. C. Babu Rao, P. Kalyansundaram, K.K. Reddy, Baldev Raj. Oxford and IBH Publishing Co. Pvt. Ltd. 178-183.
2. Blackman J.A. and Payne P.I. 1987. Grain quality In :Wheat breeding, Ed. F.G. H. Lupton. Chapman and Hall Publication. 455-485.
3. Sapirstein H.D. 1995. Varietal identification by digital image analysis. In Wrigley C.W. (Ed). Identification of food grain varieties. American Association of Cereal Chemists Inc. St. Paul, MN, pp91-130.
4. Shouche S.P., Rastogi R., Bhagwat S.G. and Sainis J.K. 2001. Shape analysis of grains of Indian wheat varieties. Computers and Electronics in Agriculture. 33, 55-76.
5. Worland A.J., Gale M.D. and Law C.N. 1987. Wheat genetics, In: Wheat Breeding, Ed. F.G.H. Lupton, Chapman and Hall Publication. 129-171.

This paper was adjudged as the Best Poster in the 13th Annual Conference of Indian Nuclear Society (INSAC-2002) on "Nuclear Technology – Catalyst for National Development" held at Mumbai during October 9-11, 2002

About the author ...

Dr. S.G. Bhagawat did his M.Sc. in Botany with Cytogenetics from Poona University, Pune, in 1975. He joined the 19th batch of Training school in the Biology and Radiobiology discipline. For Ph.D., he has worked on "Grain protein variation in wheat". Currently, he is working in the Nuclear Agriculture and Biotechnology Division of the Bioscience Group, BARC. His research interests are improvement of wheat grain quality and rust resistance.

Development of a Remotely Operated Dispensing Unit for the Production of ^{131}I Therapeutic Capsules

B.G. Avhad and M.V. Swamy
Isotope Applications Division
Bhabha Atomic Research Centre

and

P. N. Ajgaonkar
Medical & Biological Products Programme,
Board of Radiation and Isotope Technology
Vashi Complex, Navi Mumbai

Introduction

RADIOTHERAPY WITH PARTICULATE emitting radioisotopes in the form of radiopharmaceuticals is used in nuclear medicine centres for treating hyperthyroidism and various type of cancers. The radioisotope ^{131}I is one such radionuclide used for the above application. At present sodium iodide solution is given to the patient as oral administration form for the treatment of thyrotoxicosis. A method has been developed by the (MBPP), BRIT to produce 5 mCi of therapeutic capsules required for thyrotoxicosis treatment. In order to produce these capsules on a regular basis, it is essential to design and fabricate a machine having the following qualifications:

I. Machine should be operated in remotely controlled shielded facilities.
II. Accurate pipetting of ^{131}I solution of volume 5 ml in to the syringe from a 20 mm USP type glass vial containing the stock solution.
III. Dispensing of ^{131}I solution of volume 50μl within an accuracy of ±2 % in to a gelatin capsule of 7mm (ϕ) x 15 mm.(l).
IV. Encapsulation of the gelatin capsule by appropriate pneumatic system with specially designed tong.
V. Transferring of the gelatin capsule containing ^{131}I in to a glass vial for the assay of activity.

Remotely Operated Machine

A survey was made for commercially available equipment which can be used with minor modification to meet our specification. No suitable equipment could be found to fulfill the requirements of adopting within the limited space available in the shielded fume hood, high precision pipetting and type of operation in capsule making. It was therefore decided to design and fabricate a remotely controlled machine in the Group facility workshop of Isotope Applications Division. The schematic diagram of the machine designed is shown in Figure 1.

The first operation envisages the filling up of sodium sulphate powder in to the gelatin capsules. The capsule holding mechanism essentially consists of capsule and cap holding ring type device. The empty capsules are fed into the slot (circular pocket) either manually or mechanically. Rotation of the ring generates vacuum in the applicator and pulls the cap of capsules, thereby gets opened. When the capsule gets opened, it is to be filled with sodium sulphate powder.

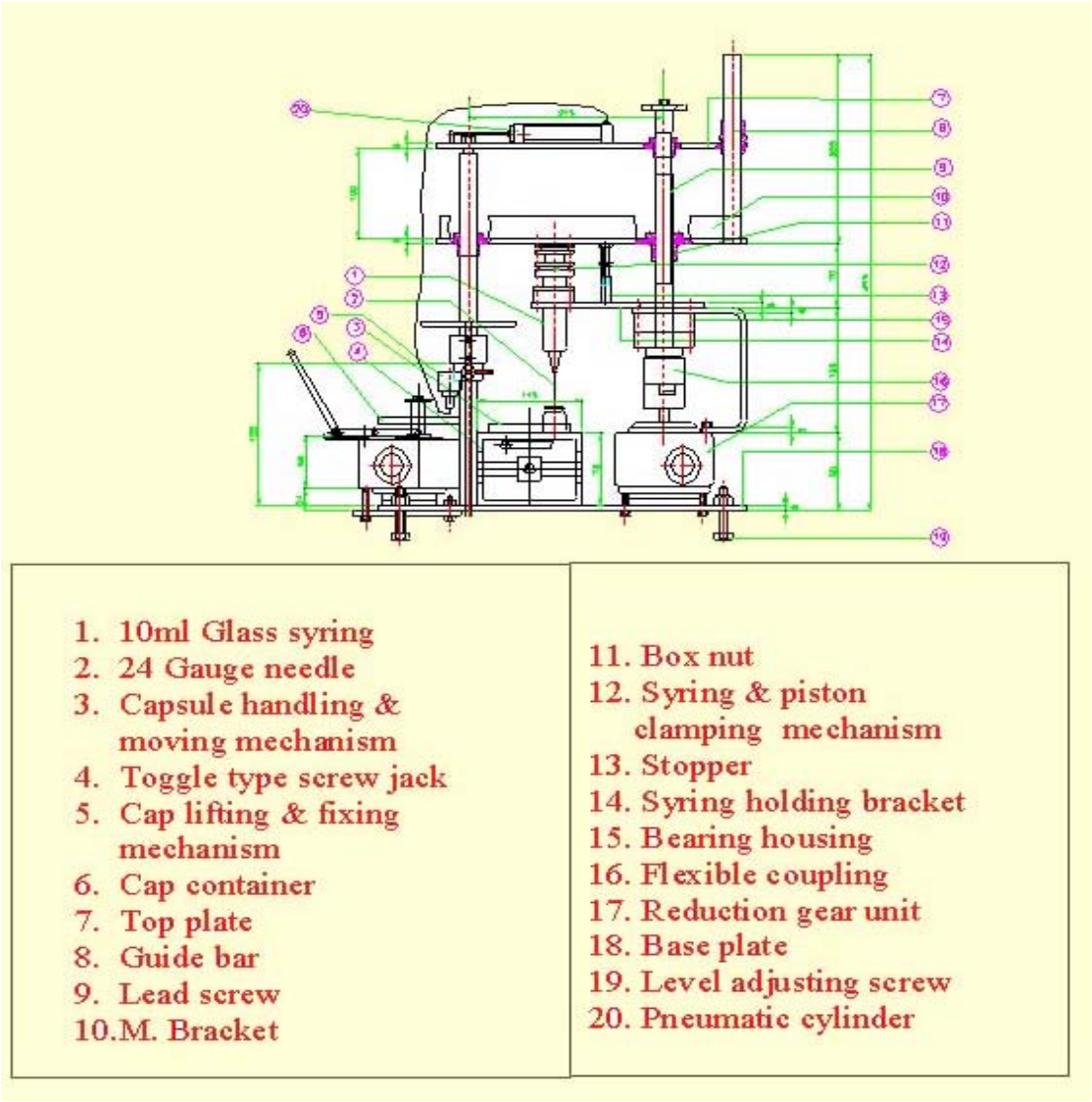

Fig. 1 ^{131}I Capsule production machine

The next operation is to dispense accurate amount of ^{131}I solution in to the capsule containing sodium sulphate powder. The capsule containing sodium sulphate powder is transferred in to the dispensing slot of the pipetting station with the help of a specially designed remote tong which moves in vertical direction but not in the horizontal direction. The operation of the capsule lifting tong is performed by a button pressing system.

The pipetting station consists of an indexing table of circular shape which is an integral part of the unit. This indexing table has an arrangement of 10 equidistant circular pockets to hold gelatin capsules of sizes 7 mm(ϕ) x 15 mm(l). This indexing table rotate in both clockwise and anticlockwise direction by warm and warm gear wheel arrangement made at the bottom of the plate. The circular motion is actuated by a knob which protrudes outside

the shielded wall and can be operated remotely by hand.

Pipetting of ^{131}I solution ($Na^{131}I$ in $Na_2S_2O_3$) from the stock solution contained in a 20mm USP type glass vial is carried out employing suction mechanism with the help of a needle syringe. The needle of the syringe is pushed downward into the glass vial containing radioactive solution. The solution is sucked in to the glass cylinder of the syringe. The upward and downward movement of the syringe is achieved by lead screw and bracket mechanism. In one rotation, a predetermined volume of the solution can be dispensed in to the syringe. Total amount of solution to be pumped out can be ascertained by performing the number of rotations. In order to perform the operation remotely, a knob has been provided which can perform the pipeting operation. When the knob is rotated clockwise, the solution is sucked into the needle from the glass vial. Before the installation of the machine, this operation was checked repeatedly and it was observed that reproducibilities of volume sucked is obtained.

The next task is to dispense the above sucked radioactive solution in to the capsule. A locator arrangement has been made to align the capsule and needle in position after which activity is dispensed into the capsule. Dispensing of 50μl of ^{131}I solution with an accuracy of ±2 % into the capsule was carried out using the above mentioned mechanism but in reverse direction i.e. anticlock wise with the same instrumental set up. Adequate care needs to be taken while performing this operation so that the needle does not touch the powder in the capsule. In such an event, the powder in the capsule gets sucked into the syringe and will lead to an error in the precision of pipetting. Once the dispensing of the last drop is over, it is essential to suck the reminder of the radioactive solution into the cylinder of the syringe. This can be accomplished by rotating the corresponding knob clockwise, which should be limited to 3-4 number of turns only. More number of rotations will lead to bubble formation inside the syringe and will affect precision of pipetting in the subsequent operation.

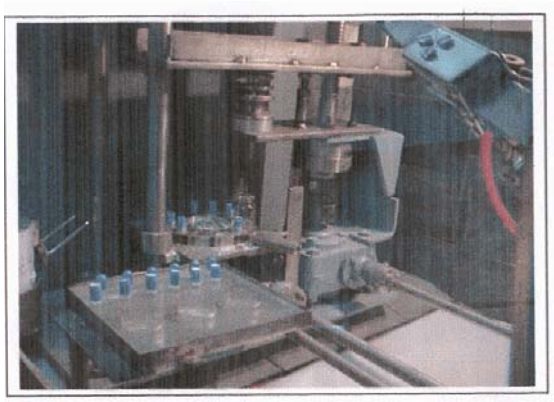

The gelatin capsule is next encapsulated by fixing of cap. A knob has been arranged in such a way that when it is rotated in clockwise direction, the position of the capsule can be raised where as rotation in anticlockwise direction will lower its position. This arrangement helps to adjust the position of the capsule to any predetermined height. A suitable provision has been incorporated in the machine to encapsulate the gelatin capsule by fixing the cap. The ring type device generates vacuum in the applicator and holds the cap of capsules. The vacuum is generated by means of a pneumatic cylinder piston system. When the applicator holding the cap is positioned above the capsule, vacuum is released and after this compressed air is passed through the same cylinder piston, the cap gets fixed on the capsule tightly.

The next operation is the transfer of capped capsule into a glass vial. This operation is performed using the same applicator with vacuum arrangement. The filled capsule is sucked into the applicator and brought in to the mouth of the USP 20 ml vial. Once the vacuum is released, the filled capsule falls into the vial. Two such capsules were placed in a single vial kept inside a lead pot for the assay of activity. Each vial containing capsule was labeled suitably indicating the batch No., radioactivity content and reference data.

Once this operation of dispensing is over for a batch, the remaining radioactive liquid left in the cylinder of the syringe is collected back in the stock solution and can be used. Subsequently, the needle of the syringe is washed with double distilled water to prevent blockage and pipetting error in the subsequent batch.

The machine has been installed at the Radiopharmaceutical Laboratory, MBPP Vashi complex, BRIT. After installation, the unit has been tested. It is now being used for the regular production and supply of ^{131}I therapeutic capsules for treatment of hyperthyroidism.

Acknowledgment

The authors are thankful for the technical support provided by all the staff members of Group facility workshop, Isotope Applications Division, BARC, during the assembly and installation of the equipment. The authors would like to thank Dr A. Dash of Radiopharmaceuticals Division for his help in the preparation of manuscript of this paper. The guidance of Dr. M. R. A. Pillai, Head, Radipoharmaceuticals Division, BARC, and Dr. N. Ramamoorthy, Associate Director, Isotope Group, BARC, throughout the project is gratefully acknowledged. The authors would also like to thank Mr Gursharan Singh, Head, Isotope Applications Division, BARC, and Mr M.L. Dutta, Head Engineering Services Section of IAD for their keen interest and providing necessary administrative support during the course of this work.

This paper was adjudged as a prize winning paper in the poster session II in the 13th Annual Conference of Indian Nuclear Society (INSAC-2002) on "Nuclear Technology – Catalyst for National Development" held at Mumbai during October 9-11, 2002

About the authors ...

Mr B. G. Avhad *joined BARC in 1983. He obtained AMIE (Mech.) in 1995. He is presently working as a group leader in Engineering Services Section of Isotope Applications Division, BARC. He has designed and developed a number of equipment for radioisotope programme.*

Mr M.V. Swamy *joined in 1985 as stipendary trainee in NAPP, Narora. He is currently working in the Isotope Applications Division of BARC since 1999. He is involved in the fabrication of equipment required by the Isotope group for different applications*

Mr P. N. Ajgaonkar *is working in the Medical & Biological Products Programme (MBPP) of Board of Radiation and Isotope Technology (BRIT). He is involved in the medical isotope programme of BRIT.*

Hollow Fiber Membrane Contactor: Novel Extraction Device for Plutonium Extraction

S.K. Gupta, N.S. Rathore, J. V. Sonawane, Anil Kumar Pabby, R.R. Singh, A.K. Venugopalan and P.K. Dey
Nuclear Recycle Group,
Bhabha Atomic Research Centre, Tarapur

and

B. Venkatramani
Radiation Chemistry & Chemical Dynamics Division,
Bhabha Atomic Research Centre

Abstract

This paper presents experimental data on hollow fiber dispersion-free solvent extraction (DFSX) of Pu(IV) from nitric acid medium using micro porous hydrophobic polypropylene hollow fiber contactor using Aliquat-336 /Solvesso-100 as an extractant. The DFSX operation was carried out with various concentrations of Aliquat-336/Solvesso-100 (5%-50% v/v) by pumping acidified (1-5 M HNO_3) aqueous solution of Pu(IV) (conc. 10^{-5} – 10^{-6} mol/L) through the tube side and organic extractant through the shell side. Extraction studies were performed under different chemical parameters (H^+ 1-5 M HNO_3) in counter-current mode. The flow rates of aqueous and organic phases were optimized at 5.83 cm^3sec^{-1} and 1.53 cm^3sec^{-1}, respectively. The validity of hollow fiber contactor data was evaluated with experimental data and was found to be well in agreement with the theoretical values. It was possible to extract Pu(IV) efficiently by employing this technique. The stripping of Pu(IV) from Aliquat-336 was accomplished by using 0.5 M $NH_2OH.HCl$ in 0.3 M HNO_3 or 1 M CH_3COOH in 0.3 M HNO_3 .

Introduction

NORMALLY PACKED TOWERS, MIXER settlers, extraction columns etc. are employed to carry out traditional liquid-liquid extraction processes [1-2], which provide high interfacial area for contacting and therefore, results in higher mass transfer rates. The intimate mixing that often occurs in these devices can lead to the formation of stable emulsions of the two phases, thereby inhibiting phase separation and product recovery. In addition, the flooding and loading limits in continuous counter-current devices, the need for density difference between the phases, and the high operating and maintenance costs of equipments are the major disadvantages encountered. Furthermore, scale up is always difficult.

In view of this, recently developed membrane extraction processes using micro porous hollow fibers are of particular interest because of their versatility and the fact that they overcome problems encountered in conventional liquid-liquid extraction [3,4]. Dispersion Free Solvent extraction (DFSX) is simply a liquid-liquid extraction in hollow fiber contactor which involves the use of a hollow fiber membrane module to contact an aqueous phase with an organic phase without dispersion, which minimizes the possibility of forming emulsion/third phase or crud with extractant. A second module can be used to strip the solute from the loaded organic phase. Also, the hollow fiber modules may be connected in series or in parallel and the length and diameters of the fibers and modules can be varied to provide the required interfacial area [5]. Such membrane

processes not only remove the required components from the streams but can also concentrate the species simultaneously on the product side, facilitating further processing.

In membrane contactors the function of the membrane is to facilitate diffusive mass transfer between two contacting phases, which can be liquid-liquid, gas-liquid or gas-gas. The traditional stripping, scrubbing, absorption, and liquid/liquid extraction processes can be carried out with this new device. Compared to conventional systems, membrane contactors provide various advantages such as non-dispersion of the phases, independent variable flow rates without flooding limitations, freedom from phase density difference limitations, absence of phase separation requirements, higher surface area per unit volume, values of which may be as high as 10^4 m^2 / m^3 and the possibility of direct scale–up due to the modular design. These advantages may be offset, by an increased mass transfer resistance, because of the need for diffusion through the membrane pores. However, recent studies indicate that with careful design, this resistance can be minimized [6].

DFSX techniques have been extensively deployed in separation science applications such as metal recovery from leaching waste waters, extraction of precious and strategic metals from neutral waters, and treatment of large volumes of the effluents including toxic and hazardous waste generated by industries. Kathios et al. [7] have demonstrated the utility of the membrane-based extraction system for the extraction of actinides. The performance of this technique was stated to be promising.

Recently, we have started study on extraction of Pu(IV) employing DFSX technique using hollow fiber contactors. In the previous studies, the hollow fiber supported liquid membrane configuration was studied with TBP-Pu(IV) from nitric acid media. Although the results were consistent with respect to the operating conditions and stability of the system [8], high flow rates (to obtain high mass transfer) could not be used in the impregnation mode, which could force out the organic extractant from the pores. Therefore, to obtain a high mass transfer coefficient, the dispersion free hollow fiber liquid-liquid extraction process was selected. The aim of this paper is to evaluate the effect of various chemical and hydrodynamic parameters to optimize performance of hollow fiber modules for the DFSX of Pu(IV) from nitric acid media. The overall mass transfer coefficient (K^{E}_{Pu}) for extraction of Pu(IV) was evaluated.

Experimental

Reagents

All the chemicals were of A. R. grade. The ^{239}Pu tracer was purified by the usual ion-exchange method [9]. Reagent grade Solvesso-100 was used as received. The organic solution was prepared by dissolving a required volume of Aliquot-336 (A.R. grade) in solvesso-100 to get carrier concentration of varying percentage.

Fabrication and characteristics of hollow fiber contactor

The hollow fiber contactor was fabricated with micro-porous polymeric lumens having specifications as given in Table-1.

Table-1

Material	: Polypropylene membrane equivalent to Accurel-PPS $_{6/2.}$
Number of lumens	: 20
Effective length	: 27 cm
I.D. of lumen	: 1800 µm
I.D. of glass tube	: 1.6 cm
Inner surface area of lumens	: 305.21 cm^2
Volume occupied by lumens	: 13.73 cm^3
Length of module	: 30 cm
Wall thickness	: 450 µm
Pore size	: 0.64 µm
Outer surface area of lumens	: 381.5 cm^2
Total volume of glass tube	: 54.26cm^3
Surface area to volume ratio	: 22.23

The module was fabricated from a glass tube in which a bundle of 20 lumens were fixed and sealed by epoxy resin. Provision was made for recirculating the aqueous solution from inside lumens without mixing the organic solution of shell side. Prior to conducting the experiments, leak test was carried out using distilled water by circulating it inside the lumens.

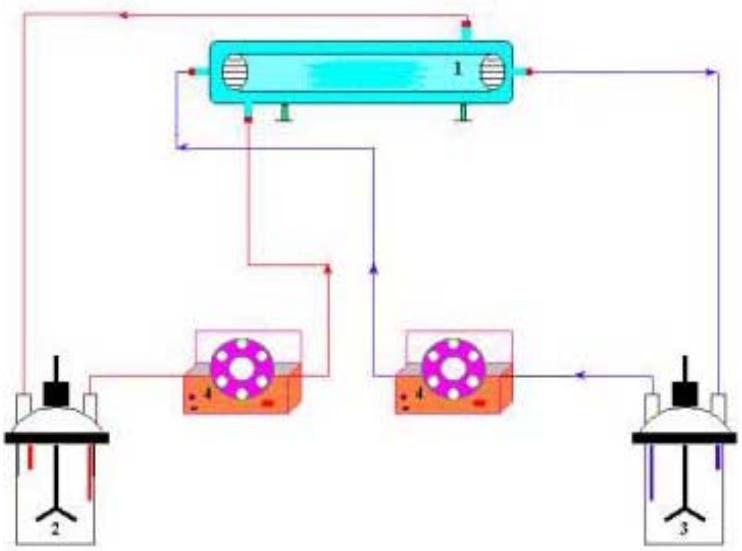

Fig. 1 Schematic diagram of dispersion free solvent extraction (DFSX) through hollow fiber contactor in recycle mode for recovery of Pu(IV):
1: hollow fiber contactor: 2.3: extractant and feed/strip reservoir

The non-dispersive membrane set-up

A schematic view of the membrane-based extraction process of Pu(IV) using a hollow fiber contactor in recirculation mode (using peristaltic pump) is shown in Fig.1. Both aqueous and organic phases were contacted in a hollow fiber module in a co-current or counter-current flow for extraction or stripping run under recirculating mode. In the extraction mode, the feed aqueous phase flowed through the lumen of the fibers at higher flow rate and organic phase flowed through the shell side with lesser flow rate as shown in Fig.2.a. While these conditions were maintained, the appearance of the organic phase on the aqueous side of membrane can be prevented if aqueous phase pressure is maintained at higher value than that of the organic phase pressure. In the stripping run, as shown in Fig.2.b, loaded organic extractant (Aliquat-Pu(IV) complex) flowed through the shell side at a flow rate of 1.66 $cm^3\ s^{-1}$ whereas strippants solution flowed through the tube side with the flow rate of 6.11 $cm^3\ s^{-1}$ in counter-current recirculation mode.

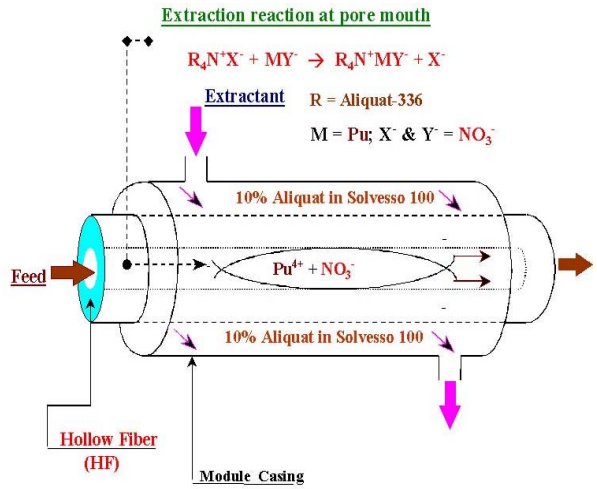

Fig.2a Extraction mechanism of Pu(IV) through hollow fiber contactor

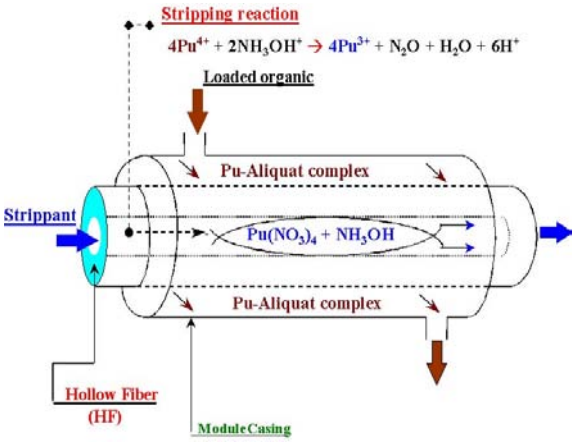

Fig.2b Stripping mechanism of Pu(IV) through hollow fiber contactor

The organic phase was ~ 200 cm^3 of Aliquat-336 diluted in Solvesso-100 solution with varying concentration of Aliquot-336. Also, ~200 cm^3 of aqueous feed solution of the desired concentration of Pu(IV) was used which was prepared by taking a suitable aliquot from tracer stock solution and diluting it with acid solutions of varying acidity of nitric acid. The solution of 0.5 M $NH_2OH.HCl$ in 0.3 M HNO_3 and 1 M CH_3COOH in 0.3 M HNO_3 were used as the stripping phase when back extraction of Pu(IV) was carried out.

The feed and organic solutions were re-circulated by means of calibrated peristaltic pumps. The measurement of transport of radionuclides through the hollow fiber membrane contactor was monitored by periodically sampling the feed/strip solution. Samples were analyzed for α using PLA make silver activated ZnS scintillation counter and for γ using NaI(Tl) scintillation counter.

Theoretical background

Extraction equilibrium

The extraction of Pu(IV) in Aliquat-336 is well studied [10]. The extraction mechanism of metal cation as an anionic species (MY^-) with quaternary amines (RMN^+X^-) e.g. Aliquat-336 (liquid ion exchanger) can be illustrated as follows:

$R_4N^+Cl^- + X^- \Leftrightarrow R_4N^+X^- + Cl^-$ ...(1)

$R_4N^+X^- + MY^- \Leftrightarrow R_4N^+MY^- + X^-$ ...(2)

Where X^- and Y^- are the ligands or anions. The capacity of this exchanger to act as extractant is related to its basicity: i.e. to the fact that their nitrogen atom has a mobile lone electron pair capable of forming co-ordinate bonds with molecules of other compounds [11].

Evaluation of Mass transfer coefficient

The mechanism of mass transfer in HFC can be explained as the diffusion of metal ions through the pores of the fibers from one phase to another without dispersion of the two contacting phases in one another. Evaluation of mass transfer coefficients is of importance because these determine the rate at which equilibrium is approached and decide the time required for a given separation, and therefore the size and the cost of equipment to be used. The mass transfer coefficients are evaluated by D´Elia, Cusslar et al.[12-14]. The key equation for the calculation of K_{Pu}^{E} or K_{Pu}^{S} for counter-current flow is,

$$\ln\left[\frac{\left(C_{e/s}^{0}/H - C_f^{0}\right)}{\left(C_{e/s}^{0}/H - C_f^{0}\right) + \left(V_f/HV_{e/s}\right)\left(C_f^{0} - C_f\right)}\right] = t\,\frac{\left[1-\exp\left(-4K_{Pu}^{E}V_m/d\left(1/Q_f - 1/Q_{e/s}H\right)\right)\right]\left[1/V_f + 1/V_{e/s}H\right]}{\frac{1}{Q_f} - \frac{1}{Q_{e/s}}\exp\left[-\frac{4K_{Pu}^{E}V_m}{d}\left(\frac{1}{Q_f} - \frac{1}{Q_{e/s}H}\right)\right]} \quad ...(3)$$

where Q_f and $Q_{e/s}$ are the feed and extractant strip flows; V_f and $V_{e/s}$ are the feed and extractant /strip volumes; C_f^0 and $C^0_{e/s}$ are the concentrations of the solute in the feed and in the extractant/strip solutions at time zero; C_f is the concentration of the solute in the feed at time t; V_m is the volume of all the hollow fibers; H is the distribution ratio of the metal; and d is the diameter of one fiber.

In DFSX systems, overall mass transfer coefficients are a weighted average of the individual mass transfer coefficients in the aqueous feed phase, across the membrane, and in the organic phase. The reciprocal of the overall mass transfer coefficient (the total resistance to mass transfer) can be described as the sum of mass transfer resistances inside the fiber (feed phase), across the fiber wall (membrane resistance) and outside the fiber (organic phase). Recent work shows that the main resistance to the solute transport lies in the membrane [15,16].

In the extraction of ionic species, it is assumed that chemical reactions are fast enough to be considered as instantaneous and hence the reacting species are present in equilibrium concentration throughout the interface.

The overall mass transfer coefficient for the module, which was used throughout the present study was calculated by slope analysis technique using equation (3).

Results and Discussion

The flow rates of the aqueous and organic phases were varied to see the intermixing of both the phases. The aqueous phase was passed through lumen side and organic through shell side, as shown in Fig.2.a.. The optimum flow rate of the aqueous phase and organic phase was found to be 5.83 $cm^3 s^{-1}$ and 1.53 $cm^3 s^{-1}$ respectively, in hydrophobic fibers. The aqueous phase pressure was maintained higher than the pressure of organic phase by keeping high flow rate of aqueous phase. If the pressure on the organic side exceeds the breakthrough pressure (Δ_P) [17,18], it will result in intermixing of these two phases. Since hollow fibers made from polypropylene are hydrophobic it cannot be expected that the boundary layers at the pore mouth of the fibers will decrease the diffusion path length at higher flow rate of aqueous phase. Higher flow rate of aqueous phase is to prevent intermixing of phases.

In case of typical liquid anion exchanger (LAE), e.g. Aliquat-336, values of D_{Pu} should increase with increasing HNO_3 concentration but nitric acid uptake by this amine particularly at higher molarity of acid caused metal extraction to be roughly constant or even low in some cases. The influence of NO_3^- concentration on transport can best be explained by considering the driving force for its transport to occur. The transport proceeds via the complexation of $Pu(NO_3)_4$ or $Pu(NO_3)_5^-$, $Pu(NO_3)_6^{--}$ species by LAE at the feed phase/membrane interface and formation of anion-pair type complex species, which dissolves in organic phase. The equilibrium constants and/or kinetics of interfacial reaction along with the membrane phase diffusion coefficient of the transporting species also affect the rate of transportation. The concentration of nitrate ions was increased, by increasing the nitric acid molarity in the aqueous feed solution. It is evident from Fig.3. that the percentage of Pu(IV) extraction from the feed at various feed HNO_3 concentrations lies in almost similarly shaped curves with the Aliquat-336/ Solvesso-100 systems and increases with molarity of HNO_3. Maximum 84% extraction was obtained in 105 min.

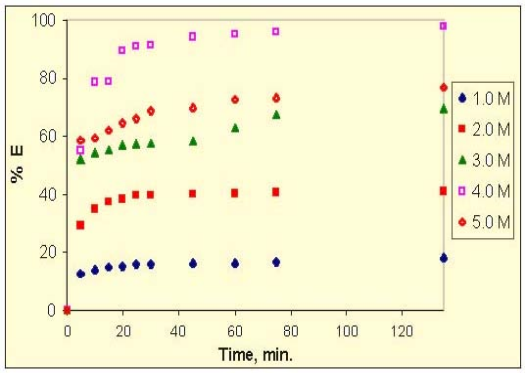

Fig.3. Influence of nitric acid molarity on 1% extraction of Pu: Feed H^+: Variable, Pu Conc.: 9.89 x 10^{-6} mol/L, Extractant conc.: 20% Aliquat-336 in Solvesso-100 (v/v), Aqueous flow rate: 5.83 $cm^3 s^{-1}$, Organic flow rate: 1.53 $cm^3 s^{-1}$, A/O ratio: 1.

As a representative case, the overall mass transfer coefficients (K_{Pu}^{E}) corresponding to 10% extractant concentration of Pu-Aliquat system have been determined from the slope of the straight lines from Fig.4, and has a value of K_w = 1.8 x 10^{-5} cm s^{-1}. Similar results have been observed for different extraction system by Babcoke et al. [19]. The extraction study of uranium with Alamine-336 shows an important decrease in the uranium flux for >30% extractant concentrations, which was attributed to significant increase in the viscosity of the organic phase. In an earlier work, the diffusivity (D_{eff}) of the chromate anion in the aqueous phase, was found to be 2.3 x 10^{-5} cm^2 s^{-1} [20] This value was estimated for working with a carrier concentration of 10%. Equation (2)

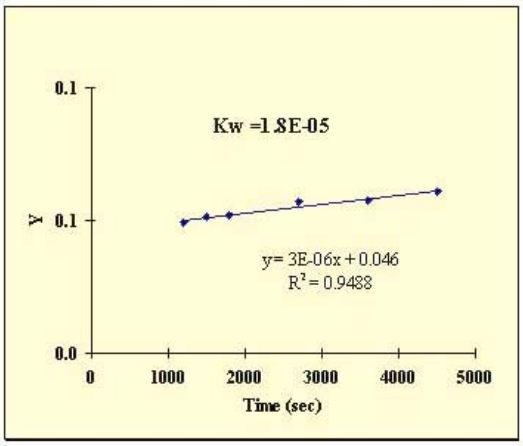

Fig.4. Overall mass transfer coefficient (K_W) for Pu-aliquat-336 in solvesso-100 system : Feed H^+: 4 M HNO_3, Pu Conc.: 9.89 x 10^{-6} mol/L, Extractant conc. : 10% Aliquat-336 in Solvesso-100, Aqueous flow rate: 5.83 cm^3 s^{-1}, Organic flow rate : 1.53 cm^3 s^{-1}, A/O ratio: 1.

$$y = \ln\left[\frac{\left(C^0_{e/s}/H - C^0_f\right)}{\left(C^0_{e/s}/H - C^0_f\right) + \left(V_f/HV_{e/s}\right)\left(C^0_f - C_f\right)}\right]$$

predicts that the extraction of Pu(IV) should vary linearly with total concentration of Aliquat-336. This relationship has been observed in solvent extraction studies [21]. To verify this relationship using hollow fiber in DFSX, 1x10^{-5} M $Pu(NO_3)_4$ solution was extracted with Aliquat-336 at 10% in the solvesso-100. Extraction studies were performed upto 50 % extractant concentration. Fig.5 shows that the %extraction of Pu(IV) increases with increase in extractant concentration. To enhance process economics and to get optimum viscosity, 20% Aliquat-336 was selected as carrier concentration to carry out further experiments.

In any practical chemical separation by solvent extraction it is necessary to be able to back-extract or 'strip' the metal ions from the organic phase after it has been initially extracted. Two different strippants were checked to determine their ability to strip Pu(IV) from loaded solutions of Aliquat-336. Since the value D_{Pu} with such extractant solution of Aliquat-336 is significant in

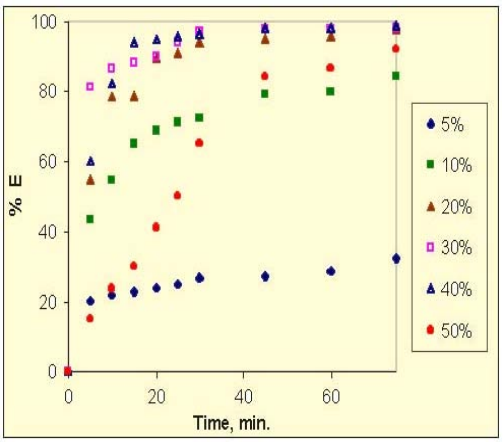

Fig. 5. Effect of extractant concentration on Pu(IV) extraction. Feed H^+: 4 M HNO_3, Pu Conc.: 9.89 x 10^{-6} mol/L, Extractant conc.: Variable, Aqueous flow rate : 5.83 $cm^3 s^{-1}$, organic flow rate : 1.53 cm^3 s^{-1} , A/O ratio: 1

dilute solution, its stripping from organic phase by varying the aqueous nitric acid molarity was not quantitative. As in HFC, due to the hydrophobic nature of the membrane, strippant was allowed to flow at faster rate as compared to organic flow rate to maintain higher pressure in aqueous side, and to avoid mixing of the two phases in contact. Hence stripping was comparatively slow [22]. Therefore, stripping of Pu(IV), by changing of valency or by complexing is preferred. The stripping experiments were performed in a single module using strippants such as 0.5 M $NH_2OH.HCl$ in 0.3 M HNO_3 and 1 M CH_3COOH in 0.3 M HNO_3 by flowing loaded organic solution (20% Aliquat-336 /Solvesso-100 loaded with Pu) in the shell side and strippant solutions from tube side. Results showed that stripping was very slow; less than 30% BEX was achieved in 315 minutes; the reason for this behavior may possibly be that a part of the organic being bypassed through the shell side; this may be avoided using densely packed hollow fiber modules or baffles in the shell side. Also, from Aliquat-336, stripping takes place by reduction of Pu(IV) ion, which makes the stripping difficult. Another alternative is to use hydrophilic membrane module which can improve the performance of Pu(IV) stripping as suggested by Cussler [23] and Kumar [24].

The extraction of Pu(IV) was not affected by the presence of fission products like ^{137}Cs, ^{106}Ru, and ^{154}Eu as there was no transport of Cs, Ru and Eu under similar conditions. This may be due to poor D values at this particular experimental condition in Aliquat/Solvesso-100 system for such fission products.

The same hollow fiber module was repeatedly used for all the experiments after washing with the solvent and distilled water. The flow rate of aqueous and organic phase was increased up to 9.72 $cm^3\ s^{-1}$ and 4.72 $cm^3\ s^{-1}$, respectively. The operation was continued for more than seven hour, no mixing of phases was observed which confirms its physical stability towards the rupture of polymeric membrane.

Conclusions

The experimental results revealed that the using higher flow rate of aqueous phase in hydrophobic membrane and with higher nitric acid and extractant concentrations rapid transport of plutonium ions takes place across the membrane. Thus hollow fiber contactor in DFSX mode with 20% aliquat-336 in solvesso-100 as extractant, could be successfully utilized for separation and concentration of Pu(IV) from dilute solutions as well as process waste streams. The stripping of Pu(IV) from organic phase took longer time which could be reduced by using hydrophilic micro porous hollow fiber lumens instead of hydrophobic fibers. The feasibility of this technique for separation of Pu(IV) from dilute solution even in presence of fission products from waste streams using 0.5 M $NH_2OH.HCl$ in 0.3 M HNO_3 solution as strippant was clearly established as an alternative to other conventional methods.

List of symbols

C	metal concentration (M)
V_M	volume of all the hollow fiber (cm^3)
A	effective surface area of the membrane (cm^2)
D_{eff}	effective membrane diffusion coefficient of the Pu(IV) containing organic species (cm^2/s)
K^E_{Pu}	overall membrane mass transfer coefficient for extraction (cm/s)
K^S_{Pu}	overall membrane mass transfer coefficient for stripping (cm/s)
D or H	distribution ratio
Δ_P	breakthrough pressure
t	time (second)
R	alkyl group

Subscripts

f and s	refer to feed and stripping solution respectively
e	extractant
s	strippant
aq	aqueous
org	organic
if	interface

Superscript

0	refer to concentration at time zero
n	number

Greek letter

η	viscosity

References

1. T.C. Lo, M.H.I. Baird and C. Hanson (Eds). Handbook of Solvent Extraction, Wiley, New York, NY, 1993 p.p. 275—507.
2. R.A. Leonard, D.G. Wygmans, M.J. McElwee, M.O. Wasserman, G.F. Vandergift, Sep. Sci. Technol., 28 (1993) 177-200.
3. P.R. Alexander, R.W. Callahan, J. Membr. Sci., 35 (1962) 546-549.
4. C.H. Yun, R. Prasad, A.H. Guha, K.K. Sirkar, Ind. Eng. Chem. Res. 32(1993) 1186-1195.
5. R. Prasad, K.K. Sirkar, J. Membr., Sci. 47(1989) 235-259.
6. Anil Kumar, R.Haddad, G. Benzal and A. M. Sastre, Ind. Eng. Chem. Res., 41 (2002) 613.
7. D.J. Kathios, G.D. Jarvinen, S.L. Yarbro, B.F J. Smith, Membr. Sci., 97(1994)251.
8. N.S. Rathore, J.V. Sonawane, Anil Kumar, A.K. Venugopalan, R.K. Singh, D.D. Bajpai, J.P. Shukla, J. Membr. Sci., 189 (2001) 119
9. D. E. Ryan, A.W. Wheelwright, USAEC Report No. HW- 55983 (1959).

10. J. V. Sonawane, Some Studies on Actinide Pertraction Through Liquid Membrane, Ph.D. thesis, University of Mumbai, 1999.
11. V.S. Shimidt, Amine Extraction, Israel Program for Scientific Translation, Jerusalem, (1971)
12. N.A. D' Elia, MS Thesis, University of Minnesota, Minneapolis, 1985.
13. L. Dahuron, E.L. Cussler, AIChE J., 34 (1988)130-136.
14. Yang Ming-Chien, E.L. Cussler, AIChE J., 32 (1986)1910-1916.
15. R. Prasad, K.K. Sirkar, J. Membr. Sci., 50, (1990)153-175.
16. M.E. Campderrós, A. Acosta, J. Marchese, Talanta, 47(1998)19.
17. R. Prasad, K.K. Ssirkar, AIChe J. 33(7) (1987) 1057-1066.
18. R. Prasad, K.K. Ssirkar, J. Membr. Sci. 50(1990)153-175.
19. W.C. Babcoke, R.W. Baker, E.D. Lachapelle, K.L. Smith, J. Membre. Sci., 7, (1980)89.
20. A.I. Alonso, A.M. Urtiaga,, A. Irabien, M.I. Ortiz, Chem. Eng. Sci., 49(1994)901.
21. J.P. Shukla and S.K. Mishra, J. Membr. Sci. 93 (1991) 64.
22. N.A. D´Elia, L. Dahuron and E.L. Cussler, *J. Memb[r. Sci.*, 29 (1986) 309.
23. E.L. Cussler, Hollow fiber contactors, in : J.G. Crespo, K.W. Boddeker (Eds.), Kluwer Academic Publishers, Netherlands (1995).
24. Anil Kumar Pabby and Ana-Maria Sastre, in *Ion Exchange and Solvent extraction*, Y. Marcus and A. Sen Gupta (Eds.), Marcel Dekker, New York,Vol.15, chapt.8 (2001) p 331.

This paper was adjudged as the Best Paper presented under Analytical and Environmental Section (AO-30) in 21st Annual Conference of Indian Council of Chemists, held at Rani Durgavati University, Jabalpur (M.P.) in October 24-26, 2002, and on this occasion, Dr N.S. Rathore was conferred the "Young Scientist Award".

About the authors ...

Mr S.K. Gupta, *after graduation from Rohilkhand University in the year 1992, worked in Camphor and Allied Products Ltd., Bareilly, Uttar Pradesh, for four years. In 1997, he joined PREFRE, BARC, Tarapur. He is engaged in the reconversion of plutonium. Also, he is associated with the research work of "actinides recovery using non dispersive solvent extraction (NDSX) technique utilizing hollow fiber contactor (HFC)" and has published about 10 papers.*

Dr N.S. Rathore *joined BARC after completing his M.Sc. (Chemistry) from Awadhesh Pratap Singh University, Rewa, (M.P.) in the year 1991 and has been working in the laboratory section of Power Reactor Fuel Reprocessing Plant at Tarapur. He is associated with analytical work related with process control and production of Plutonium. He was awarded the Ph.D. degree from University of Mumbai in 2002 for his thesis entitled, "Some Novel Chemical Methods For Nuclear Waste Decontamination" and has more than 26 research papers published to his credit. His area of research is Solvent Extraction, Ion Exchange and Liquid Membranes. He is the recipient of Dr Homi Bhabha Hindi Vigyan Lekh Pratiyogita award in 1998. He has received the "Young Scientist" award from the Indian Council of Chemists in 2002.*

Dr J.V. Sonawane, *(M.Sc. - Chemistry), Pune University, joined the laboratory section of PREFRE, BARC, Tarapur in 1981. He is engaged in the chemical processing of plutonium nitrate solutions to the final product plutonium dioxide. He was awarded Ph.D. degree by Mumbai University in 1999 for his thesis entitled, "Some Studies on Actinide Pertraction through Liquid Membranes". His major research interests include Non-dispersive Solvent Extraction using Hollow Fiber Membrane Contactors, Membrane/Metal Transport Processes (Liquid*

membrane processes) and Solvent Extraction Chemistry. He has published about 40 research papers in national and international journals.

***Dr Anil Kumar Pabby** is presently working in laboratory section of PREFRE Plant, BARC. After completing his Ph.D. from Mumbai University, Dr Pabby had carried out post-doctoral research work during 1997-1999 at Universitat Politecnica de Catalunya, Barcelona, Spain, under European Fellowships programme. Dr Kumar has more than 125 publications to his credit, published in national/international journals and symposia in addition to one Spanish Patent application. He has co-authorship of several book chapters in reputed book volumes published by international publishers such as Marcel Dekker, USA and American Chemical Society, USA etc. He is also serving as consultant to IAEA for preparing a technical document on "Membranes Technologies for Liquid Radioactive Waste Processing" which is to be published soon. Also, he was appointed leading investigtor in a collaborative programme on membrane technology between Universitat Politecnica de Catalunya and BARC. In addition, he is in the panel of experts for several international journals such as Industrial & Engineering Chemistry Research (American Chemical Soc., USA), Talanta (Elsevier USA), Analytica Chimica Acta (Elsevier USA), Journal of Membrane Science (Elsevier USA), Hydrometallurgy (Elsevier USA) and various others to evaluate referred research papers. Dr Pabby is also appointed as one of the Associate Editors of the International Journal, Journal of Radioanalytical and Nuclear Chemistry (Hungary), since 2002 .*

***Mr R.R. Singh** (B.Sc. Hons., Mumbai University) joined Fuel Reprocessing Division, BARC, Trombay in 1973 after graduation. Presently, he is working as a group leader in Plutonium reconversion area of PREFRE Plant. He is associated with the processing of plutonium nitrate to plutonium oxide from spent fuel of research and power reactors. His field of research is application of electrolytic process in fuel reprocessing and membrane processes. He is co-author of 21 research papers published in national and international journals and symposia.*

***Mr A.K. Venugopalan** joined Fuel Reprocessing Division in 1966 after graduation in chemistry. He is working in the laboratory section of PREFRE plant, Tarapur, from its inception. He is associated with several research activities like the development of electrochemical processes for the purification of plutonium, production of uranous nitrate, etc. He is co-author of about 35 research papers published in national and international journals and symposia.*

***Mr P.K. Dey** graduated in Chemical Engineering in 1970 from Jadavpur University, Kolkata. He then worked in Fertilizer Corporation of India Ltd., Sindri, for a year. In 1971, he joined BARC, Trombay, and was associated with reprocessing of spent fuel from research reactor at Trombay using solvent extraction technique. In 1973, he took the responsibility of erection and commissioning of country's first Power Reactor Spent Fuel Reprocessing Plant at Tarapur. The plant was successfully commissioned in 1975 and processed spent fuel from different Atomic Power Stations of the country. He has specialised in the planning of operation and maintenance of reprocessing plant and has incorporated various modifications in the process flow sheet to improve recovery, throughput and reduce the rate of generation of radioactive waste. Presently, he is responsible for operation of all the spent fuel reprocessing plants in the country in the capacity of Head, Fuel Reprocessing Division, BARC., Trombay. In 1996, he was deputed to St. Petersburg, Russia, for International Training Course on Implementation of State System of Accounting and Control of Nuclear Material, sponsored by International Atomic Agency, Vienna, Austria.*

***Dr B. Venkataramani** obtained his B.Sc. from the University of Madras and was awarded the Sri Pattabhi Ramireddi Medal II for standing FIRST in the University. He joined the Chemistry Division, BARC, in 1968, through the 11th batch of Training School (Homi Bhabha Awardee). He obtained his Ph.D. from University of Mumbai in 1975. He had worked in the Chemistry Department, S.C.K.-C.E.N., Mol, Belgium (1973-74) under the Indo-Belgian Collaboration Programme. He had attended the International Meeting on the Recovery of Uranium from Seawater (1983) and had delivered a Key Note Lecture at the International Conference on Ion Exchange (1995), both held in Japan. His fields of interest include, ion exchange, solvent extraction, water chemistry and chemistry of Uranium.*

Recovery of Reactive and Refractory Metals from their Respective Scrap

A.C. Bidaye and I.G. Sharma
Materials Processing Division
Bhabha Atomic Research Centre

Introduction

PROCESSING OF SCRAP, WASTE AND secondary resources not only fulfill the need of the hour but also impart multifacet benefits particularly in the case of reactive and refractory metals. This is so because the production processes, for metals like titanium, zirconium, molybdenum and vanadium from their primary resources, are complex and involve multi-step techniques which are both cost and energy intensive as well as occasionally generate voluminous hazardous wastes. The scrap, generated during metal production and use, and the wastes, create storage hazards and disposal problems. These, however, can serve as semi-processed sources of the metals and their processing will help overcome disposal problems. Thus, development of process flowsheets for recovery of reactive and refractory metals from their wastes/scrap/secondary sources is mandatory on both economic and environmental considerations. In this paper, efforts are focused towards development of processes/process schemes for the recovery of metal values from Ti, Zr and Mo scrap and V from Bayer's sludge.

Molybdenum

During the manufacture of tungsten filament for electric lamps, tungsten wire is double wound around molybdenum mandrel and the latter is separated from the coiled coil by dissolution of molybdenum in a mixture of nitric and sulphuric acids. This operation results in the generation of large volumes of spent acid containing dissolved molybdenum. A flowsheet for the recovery of the Mo values was developed and is depicted in Fig.1. The Mo powder analysed Fe<27, Ni, Mg, Pb, Ca<20, Cr, Al<100, Mn, Cu<10, Sn<200, all in ppm.

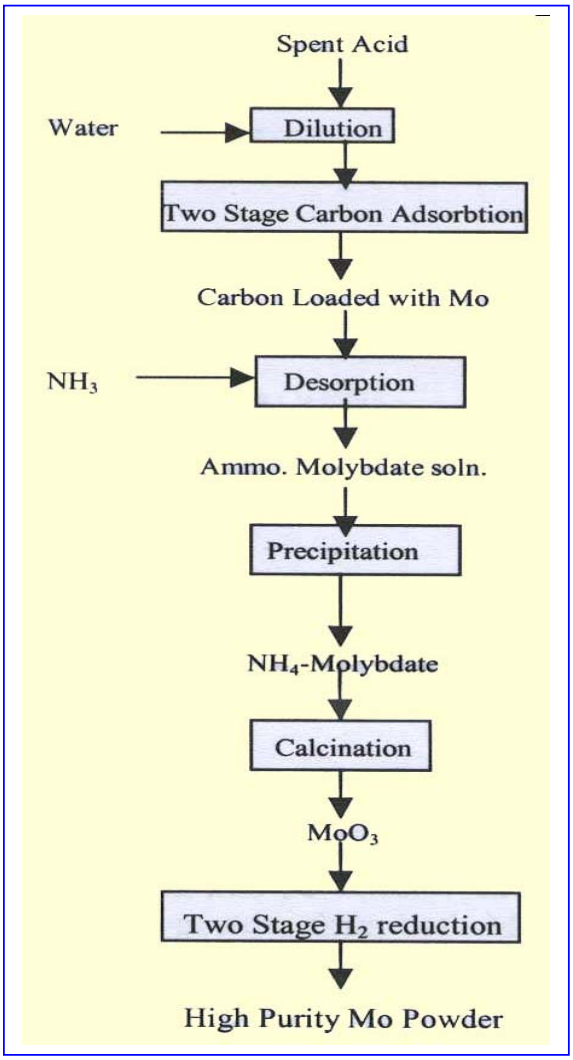

Fig. 1

In the furnace industry, Mo is principally used as heating elements and heat shields in high temperature resistance furnaces. During its fabrication and use, considerable amount of scrap is generated. A hydro-cum-pyro metallurgical route has been developed. It involves dissolution of the scrap in a mixture of nitric and sulphuric acids from which molybdic acid can be precipitated, which in turn can be calcined and subsequently H_2 reduced to get Mo powder. Alternately, the solution can be processed as in Fig. 1. The Mo powder analysed Fe<100, Ni, Cr, Al, Mn, Pb<20, Co<30, K, Mg<10, Sn<200, Cu<6, all in ppm.

Vanadium

During recycling of the depleted caustic leach liquor after aluminium hydroxide precipitation, significant level of V values present in the bauxite ores get co-extracted with Al in the Bayer Process. The V content in the recycled solution progressively builds up and beyond a certain limit it has to be separated. This is accomplished by fractional crystallization of a complex V-Na salt, familiarly known as Bayer's sludge, containing around 20% V_2O_5, 50% $Al_2O_3.3H_2O$ and 30% Na_2O. The process developed involves leaching of the sludge in hot water, followed by two stage carbon adsorbtion, desorption with ammonia, precipitation of vanadium cake and finally calcination to obtain pure V_2O_5, all processes being conducted under optimized conditions. The V_2O_5 analysed Fe<200, Ni, Cr<20, Al, Mg, Ca<25, Cu<10, Si<50, all in ppm. The oxide can be subjected to aluminothermic reduction, followed by arc consolidation to produce ferro-vanadium or other vanadium alloys, or the arc consolidation can be followed by molten salt electro-refining to obtain pure vanadium metal.

Titanium and Zirconium

During fabrication of finished products from Ti/Zr sponge, considerable amount of scrap is generated. The medium to heavy scrap, which is generally non-contaminated, goes for remelting, with or without blending. The light and generally contaminated scrap needs purification. A fused salt electrolytic process has been developed to treat this scrap. Optimum operating conditions and the results are depicted in Table 1.

Table 1: Electrolysis- Operating Conditions and Results

	Electrolyte	Soluble Ti/Zr (w/o)	Temp. (°C)	C.C.D (A/dm^2)	Current Efficiency (%)	Recovery (%)
Ti	NaCl-$TiCl_2$	2.76	830	71	85	75
Zr	NaCl-K_2ZrF_6	10.0	850	25.8	72	63

Chemical Analysis (in ppm) and Hardness values (VPN)

	O	N	C	Sn	Fe	Cr	Ni	Hardness
Ti scrap	3700	210	330	50	1850	225	355	230
Pure Ti	265	20	50	<10	<25	<2	<25	65
Zr scrap	1990	48	>1000	15000	1500	1000	640	250
Pure Zr	1080	<10	48	<110	50	15	15	135

Conclusions

High purity titanium and zirconium could be successfully recovered from their respective scrap by molten salt electro-refining technique.

A process flowsheet has been developed to prepare high purity V_2O_5, and its subsequent conversion into Fe-V, Al-V and vanadium. 3. Process schemes have been developed to prepare Mo powder from both Mo scrap and Mo bearing spent acid. Reproducibility of the findings has been confirmed on increasing the batch scale five-fold. 4. Carbon adsorbtion/ desorption step introduced in the flowsheet of spent acid treatment has resulted in substantial savings in terms of ammonia consumption.

This paper received the Best Paper award in Poster Session of Non-Ferrous Category at ATM of IIM-2002 held at Vadodara, during November 14-17, 2002

About the authors ...

Dr A.C. Bidaye *graduated in Metallurgical Engineering from the IIT, Bombay, in 1977, successfully completed orientation course of 21st batch of the Training School and joined the erstwhile Metallurgy Division in 1978. Since then, he has actively participated in various process metallurgy programmes involving preparation of metals and alloys by pyro and electrometallurgical routes, processing of secondary resources for recovery of metal values / metal intermediates and development of a novel, non-aqueous, eco-friendly flowsheet for effective separation of Hf from Zr. He was awarded the doctoral degree by IIT, Bombay, in 1996. Dr. Bidaye is currently involved in the programme on electrowinning of nickel and cobalt from the leach liquor generated during the processing of a variety of alternate resources and on the development and characterization of refractory metal based allovs.*

Mr I.G. Sharma *did his B.E. (Met. Engg.) in 1971 from Nagpur University and M.Tech. (by research), in 1980 from Mumbai University. He is from 15th batch of Training School, presently Head, Refractory Metals Development Section of Materials Processing Division and on the Editorial Board of Transactions of Indian Institute of Metals. Various fields of his interest and involvement are : (a) Metallothermic and hydrogen reduction of reactive and refractory metal oxides, (b) Molten salt and aqueous electrolysis, (c) Graphite and pyrolytic carbon coating on nuclear materials, (d) Processing of secondary resources, and (e) Preparation of low carbon specialty ferroalloys. Process know-how and technology of production of specialty ferroalloys has been transferred to a few private entrepreneurs. He has published about 60 technical papers in National and International journals. Presently, Mr Sharma is involved in the development of a non-conventional process scheme for the preparation of refractory metal based alloys which are promising candidates for the production of specification grade cobalt pellets and slugs for its ultimate conversion to* Co^{60} *isotopes.*

Synthesis and Sintering Behaviour of Lanthanum Strontium Manganite

A.Ghosh, A. K. Gulnar, D.D. Upadhyaya, Ram Prasad and A.K. Suri
Materials Processing Division
Bhabha Atomic Resesearch Centre

THE CO-PRECIPITATION METHOD WAS adopted for preparation of lanthanum strontium manganite ($La_{0.85}Sr_{0.15}MnO_{2.93}$), which will be used as a cathode element as well as support tube of a high temperature solid oxide fuel cell (SOFC). In this method, mixed nitrate solution of La^{3+}, Mn^{3+}, and Sr^{2+} are added in a precipitating bath at pH 8.0 in presence of carbonate ions. Precipitate, after washing and drying was calcined at temperature more than 1000^{O}C. Extensive ball milling ensured homogenisation of the powder before calcination. Calcined powder was characterized by X-ray diffraction technique, which confirmed the phase purity of the material. Dilatometric studies have been performed to determine the shrinkage behaviour of the material.

Table 1 : Effect of poreformer on densification behaviour of LSM

Poreformer (wt%)	Bulk density (%TD)	Open porosity (%)
0	96	0
2	92	2
7.5	82	17
10	60	40
15	53	46

Densification studies on pure as well as on powders with different concentration of poreformer have also been performed. Thermal expansion behaviour of 40% porous material has also been studied and values are in good agreement to that of yttria stabilised zirconia sintered body. Following the slip casting technique the feasibility has been demonstrated for fabrication of LSM tubes meeting the specifications of preliminary design of the fuel cell. Characterization of electrical conductivity as well as compatibility with the other cell elements has also been initiated.

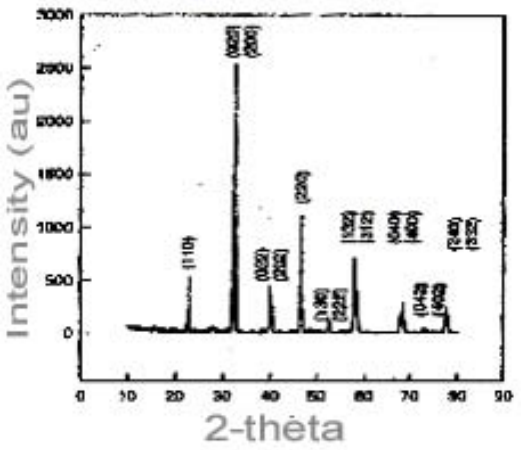

Fig 1 X-ray diffractogram of LSM

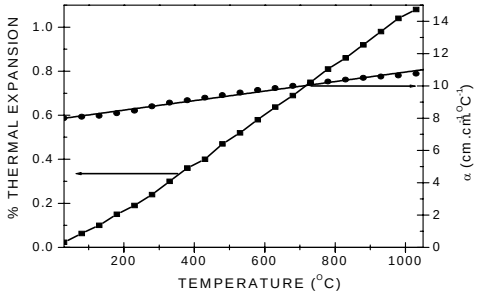

Thermal expansion behaviour of porous LSM

This paper received the second Best Paper award at ATM of IIM-2002 held at Vadodra during November 14-17, 2002

About the authors ...

Mr Abhijit Ghosh *received his B.Sc (Tech) in ceramics from University of Calcutta in 1995 and M. Tech (Ceramics) degree from IT-BHU in 1997 and joined Materials Processing Division, BARC, after completing 6th OCPGE in nuclear science. Since then, he is associated with R&D activity on advanced ceramics, especially structural and electrical ceramics. He is involved in the development of silicon carbide based ceramic, preparation and characterization of nano zirconia based materials, and development of solid oxide fuel cell devices. He has published more than 15 research papers in different journals and conference proceedings.*

Dr (Ms) Gulnar Abdul Karim *received her M.Sc (Chemistry) degree from Mumbai University in 1985. The Mumbai university awarded her doctorate degree in 1994 for her work in Synthesis and Characterization of new perovskite compounds. Since 1984, she has been actively pursuing R&D work on ceramics, especially superconductivity and structural ceramics. Her current research interests include the development of silicon carbide and materials for solid oxide fluid cells. She has published more than 20 research papers in different journals and conference proceedings.*

Dr D.D.Upadhyaya *joined BARC after completing the orientation course in nuclear science in 1968-69. He earned the Ph.D. degree in physics (1985) and published more than 80 research papers in different journals and conference proceedings. His fields of interest are in structure property correlation in electronic and engineering ceramics, lattice defect-structure characterization, and advanced synthesis and consolidation techniques. He visited Max-Planck Institute, Metals Research, Stuttgart, Germany, during 1987-89, under the Indo-German exchange programme.*

Mr Ram Prasad *joined Metallurgy Division in 1963 after completing BARC training school course in 6th batch. He was associated with the ceramic materials development programmes for nearly four decades. His main fields of interest have been electronic and magnetic ceramics, structural ceramics and bioceramics materials in which he has published more than 200 research papers. He retired from BARC on superannuation in Deccember 2002.*

Switchless Operation of a TEA Co_2 Laser

D. J. Biswas and J. P. Nilaya
Laser & Plasma Technology Division
Bhabha Atomic Research Centre

IN THE OPERATION OF A TEA CO_2 LASER, the main energy storage condenser normally discharges its energy into the load with the help of a spark gap or a thyratron both of which can close very fast and are also capable of withstanding high voltage and high current. In the repetitive operation thyratron is a better choice as spark gaps operate in the arc mode and suffer from recovery problem. Thyratrons, however, are expensive and have limited life. As a result there is now considerable interest in replacing these switches by all-solid-state-exciters (ASSE) in conjunction with magnetic pulse compression (MPC) [1]. Although such systems have long life and high degree of reliability, they suffer from low wall plug efficiency and bulkiness [1]. Effort has therefore been expended to eliminate the main discharge switch altogether in the operation of CO_2 lasers [2-4]. In this method the main discharge condenser is directly connected across the laser electrodes and is charged to a voltage well below the self-break down level of the laser gas mixture in the inter electrode volume. Automatic switching of this condenser occurs when the inter electrode volume is preconditioned by UV [2] or X-ray [3] photons or electrons from an external source [4]. In all these methods although the main discharge functions without a switch, the preconditioning of the inter-electrode volume is always initiated by a switch. We report here the operation of a UV preionised TEA CO_2 laser, which does not require the service of any external switch. The principle of operation of this scheme is described below.

In a typical UV preionised TEA CO_2 laser, the UV photons emanating from the spark channels placed along the length of the discharge precondition the inter-electrode region. In actual operation with a sequential spark type preioniser, all these spark channels are overvolted sequentially leading to their closure with the help of an external spark gap switch. The spark gap operates in arc mode and is itself a source of UV radiation when in conduction. Our intention was to make use of the UV radiation emanating from the spark gap itself for preconditioning the inter-electrode volume. We achieved this by segmenting the main spark gap into smaller adjustable gaps (see inset of Fig.1) and placing this integrated spark array along the length of the discharge as shown in Fig.1. A resistance (R) was connected across each of the gaps. We have successfully operated a mini TEA CO_2 laser where this spark array served the dual purpose of a switch as well as a source of uv photons for preconditioning of the inter-electrode volume.

The laser head comprised of a pair of cylindrical electrodes defining a discharge of cross-section 0.3 cm $\times$ 1.1 cm and of length 8.0 cm. The electrodes and the spark array were housed in a leak tight Perspex chamber, the two ends of which were O'ring sealed with a gold coated copper mirror (1 m ROC) and a 90% reflective ZnSe output mirror which also defined the resonator cavity of length 16.5 cm. The output energy and the power of the laser pulse were respectively monitored by a pyroelectric joule meter (Gentec, Model ED 200) and a fast room temperature detector (Photonic Solutions, Model PEM L3).

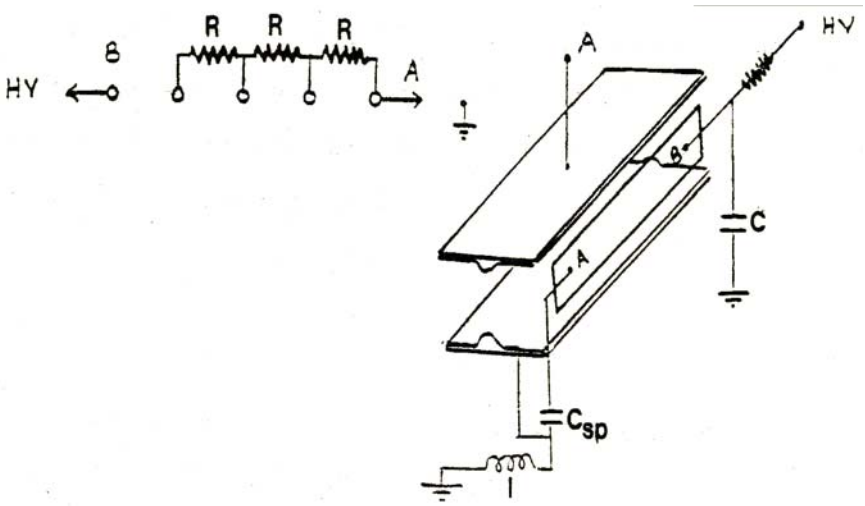

Fig. 1

The pulser circuit used for the excitation of the laser is also shown in fig. 1. A condenser C was resistively charged to a suitable voltage 'V'. The resistance 'R' ensured that the entire voltage 'V' appears across the first gap of the spark array leading to its closure. This resulted in the closure of the second gap and subsequently all the remaining gaps in sequence. The uv photons emanating from these sparks preconditioned the inter-electrode volume. Alongside preconditioning, the preionisation current also charged up the spiker capacitor 'C_{sp}' to an elevated voltage, which was impressed across the electrodes. This high voltage impulse caused the breakdown of the preconditioned gap. The inductance 'l' provided the required delay between the pre and the spiker discharges. The remaining energy in the condenser 'C', voltage across which was reduced, now appeared in the discharge at a rate decided by the value of 'l' causing its sustenance and efficient excitation.

The laser was initially operated with a gas mixture of CO_2:N_2:He::1:1:3 and the values of C, C_{sp}, and l were optimised respectively to 2.7 nF, 300 pF, and 3.3 μH by monitoring the output energy of the laser. While optimising the gas mixture we found that the operating voltage of the laser too changed. This is because the operating voltage of the laser is determined by the break down voltage of the first gap in the spark array and as the array is exposed to the gas mixture any change in its composition also changed the break down voltage and, in turn, the operating voltage. The most optimised and reliable performance in terms of energy (viz., 38mj @ 7 % electro-optic efficiency) occurred for a gas mixture of CO_2:N_2:He::1:1:2.5 for which the operating voltage was ~20 kV. The efficiency would be higher if the energy expended in preionisation is accounted for. By virtue of its short cavity length, the laser emission was expected to occur on SLM, which was corroborated by the absence of any beating at t_R in the temporal profile. In order to remove the dependence of the operating voltage on the gas composition we plan to isolate the preioniser cum switch from the laser head by making use of CaF_2 windows for coupling the uv radiation into the inter-electrode volume. Result of this investigation will be reported during the symposium.

References

1. H. Tanaka, H. Hatanaka, and M. Obara, Rev. Sci. Instrum. **61**, 2092 (1990)
2. A. Sylvan, P. K. Bhadani, and R. G. Harrison, Meas. Sci. Technol. **3**, 200 (1992)
3. K. Jayaram and A. J. Alcock, Appl. Phys. Lett. **46**, 636 (1985)
4. V. P. Singal, R. Vijayan, B. S. Narayan, D. J. Biswas, U. Nundy, Inf. Phys. Technol (2002, In Press)

This paper was selected for Poster award in the National Laser Symposium 2002 held at Thiruvananthapuram during November 14-16, 2002

About the authors ...

Dr Dhruba J. Biswas *received his M.Sc (Physics) degree from I.I.T Kharagpur in 1978 and joined the erstwhile MDRS, BARC, in 1979 after graduating from the 22nd training school batch. His experimental work on optical chaos fetched him the doctorate degree from the Heriot-Watt University, Edinburgh, in 1986 where he was on a two years' sabbatical. His current research interest includes physics and technology of mid-infrared gas lasers including optically pumped molecular lasers and laser induced physical processes. He has to his credit 65 scientific papers, including 5 review papers, in refereed international physical journals. He is a recognised Ph.D (physics) guide of Mumbai University. He is the recipient of the INSA young scientist medal (Physics, 1987), A. K. Bose Memorial award of INSA (Physical Science, 1989), N. S. Satyamurthy Memorial Award of IPA (1991), Associateship of International Centre for Theoretical Physics, Italy (1994-2001) and Senior-Associateship of ICTP (2003-2010).*

Dr J. Padma Nilaya *received her M. Sc (Physics) degree from Nagpur University in 1991 and joined the erstwhile MDRS, BARC, in 1992 after successfully graduating the 35th batch of the BARC training school. She is the recipient of the University gold medals for securing first position in the B. Sc and the M. Sc examinations. She received the Young Physicist Colloquium award of Indian Physical Society in 1999 and Indian Laser Association Best Ph.D. thesis award in 2001. Her field of research includes generation of coherent mid infra-red sources and their application to isotope separation. She has obtained her Ph. D from the University of Mumbai in 2002.*

Low Temperature Superconductor - Fabrication and Application

A.K. Singh, M. M. Hussain, S. P. Singh and V. G. Date
Atomic Fuels Division
Bhabha Atomic Research Centre

Introduction

THE DEVELOPMENT AND fabrication of superconductors for practical application is clearly connected with the physical properties required for the construction of high field magnets.

Important parameters which dictate conductor design and fabrication processes are:

(a) Critical temperature, T_c and upper critical field Bc_2. It depends mainly on alloy composition.
(b) Critical current density, J_c.
(c) Magnet size, i.e stored energy. It will decide the degree of stabilisation i.e the amount of high conductivity substrate.

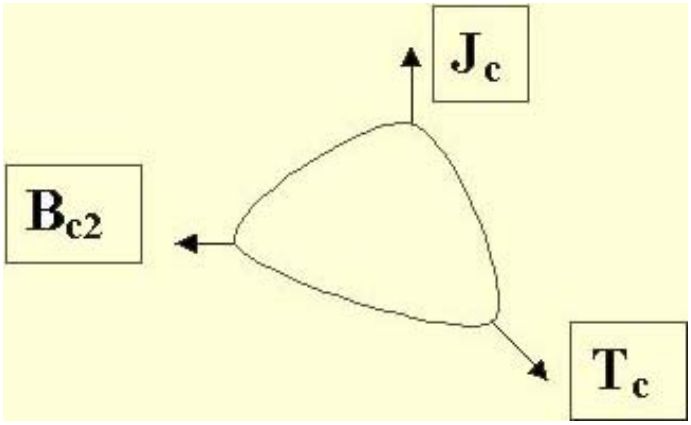

Sketch showing three critical parameters for a superconductor

Properties of Nb-Ti Alloys

In addition to the good superconducting properties of Nb-Ti alloys, the excellent combination of mechanical and metallurgical properties make this alloy one of the most important for various magnet applications. Nb-Ti alloy can be co-processed easily with different substrate materials such as Copper and Copper-Nickel etc.

The critical current density $J_{c,}$ one of the critical parameters shown in the sketch above, is a structure dependent and depends very strongly on the density, size and distribution of imperfection such as dislocations, grain boundaries and precipitates which act as flux pinners.

Multi-filamentary conductors are fabricated by extrusion technique. The main advantages of this technique are:

a) Radial stress field during area reduction.
b) Homogeneity of plastic flow.
c) High area reduction in a single step.

Since compressive forces are acting during the process very high packing density of the extrusion billet is required.

Assembly of Extrusion Billet

This is the first step of extrusion process. To achieve high packing density different methods are used. Depending on the force of the extrusion press and diameter of the extrusion container, OFHC (Cryogenic grade) copper sleeves are filled with an array of the following:

a) Straight lengths of hexagonally shaped Cu/Nb/Nb-Ti rods.

b) Straight lengths of hexagon copper rod fillers to arrive at required copper to superconductor area ratio.
c) Straight length of partial hexagons of copper.

Sealing of Billet

Residual gases are removed from the billet by evacuation and sealing is done under vacuum to prevent oxidation during preheat. Sealing techniques commonly used are Electron Beam welding and TIG welding.

Extrusion Temperature and Preheating

The choice of extrusion temperature is very important parameter. The upper limit of applicable temperature is decided by chemical reaction of stabilising copper with Nb-Ti which forms a brittle intermetallic compound $(NbTi)_2Cu$ causing wire breakage during drawing.

The lower limit is decided by the deformation resistance of the Nb-Ti alloy and precipitation of α-Ti below 600^{o}C. In addition to this, bonding is poor at lower temperature.

Cold Drawing and Intermediate Annealing

1. A high degree of cold work provides a structure with a high degree of imperfections. α-Ti nucleates only on small sub-bands of 200 – 500 Å width.
2. Annealing is required for precipitation of α-Ti.

Twisting

The eddy current losses can be reduced by introducing a twist pitch to the filament bundle which reduces the area of loop coupling with the changing magnetic field.

Experiment

High homogeneity Cu/Nb/Nb-47 wt %Ti alloy of 7mm dia in as drawn condition was used as input material. This rod was drawn to 6mm across flat (A/F) hexagon in several passes. OFHC copper partial hexagons of different shapes were fabricated by cold swaging. 6mm across flat Cu/Nb/Nb-Ti as well as OFHC copper hexagons were manually stacked using a special fixture in hexagonal geometry in 180mm dia OFHC copper sleeve. Partial hexagons were used to get a packing density of more than 99%.

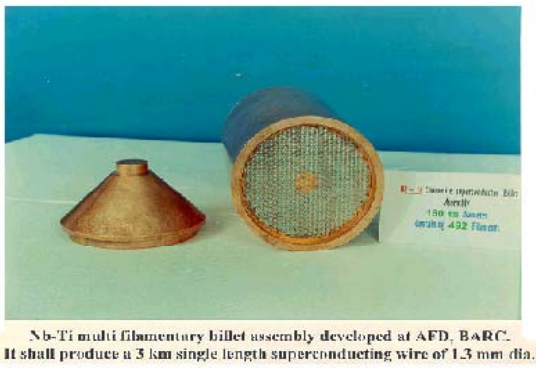

Fig. 1 Multi-filamentary billet assembly developed at AFD, BARC

Fig.1, shows the billet cross section. Both the ends were closed by OFHC copper end caps. This billet was sealed by electron beam welding to prevent oxidation. Helium leak testing was done to check the integrity of the weld.

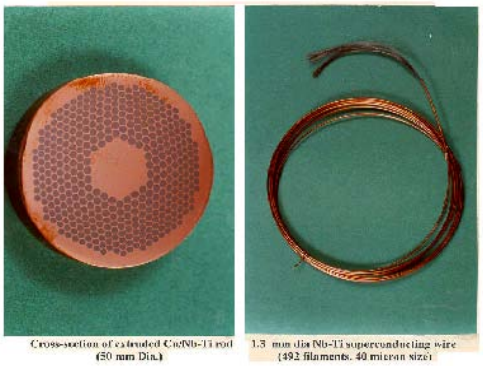

Fig. 2 Cross-section of extruded Cu/Nb/Nb-Ti rod (left) and 1.3 mm dia Nb-Ti super-conducting wire containing 492 filaments, each of 40 micron cross-section.

Extrusion was utilised to transform the assembled array of components into a composite structure. Hot extrusion was carried

out at 600^{0}C at slow ram speed followed by water quenching. The fig. 2, shows 50mm dia extruded rod cross section containing 492 Nb-Ti elements. Short samples were fabricated using three different thermomechanical treatments. Ageing treatment temperature was between 370^{0}C-420^{0}C with a soaking time of 6hrs-80hrs at different stages of cold reduction. 1.39mm dia wire was twisted and cold drawn to 1.37mm dia with a twist pitch of 12.4mm. The fig. 2, also shows 1.37mm dia wire containing 492 Nb-Ti filaments each of 40 micron size with Cu:SC ratio of 1.15:1.

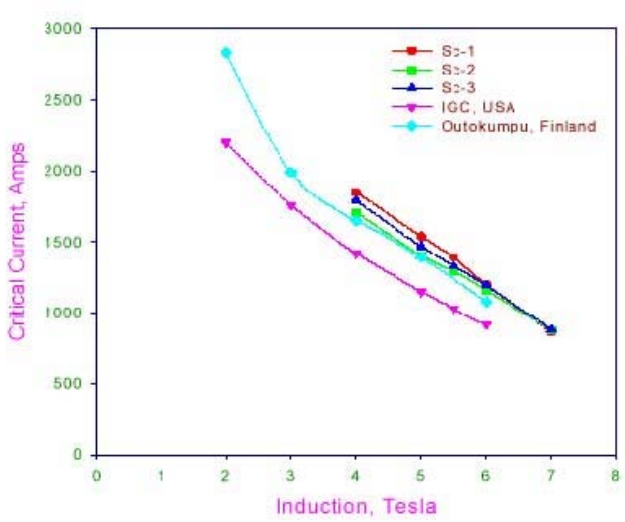

Fig.3 Comparison of critical current vs magnetic induction plots for Nb-Ti LTSC obtained from different sources. Sc-1, Sc-2 & Sc-3 represents the Nb-Ti LTSC Multifilamentary wires developed by Atomic Fuels Division, BARC

Results and Discussion

Short samples were tested for I_c (critical current) at the reputed Russian laboratory as well as at TPPED BARC. A critical transport current of 1294, 1330 and 1390 Amps was measured through sample-1, sample-2 and sample-3 respectively at 5.5 Tesla field and 4.2 K temperature (refer table 3). 'n' value i.e resistive transition index was observed to be 58. The maximum critical current density achieved in the wire is of the order of 2500Amps/mm^2 at 5.5 Tesla field and 4.2 K temperature. No filament breakage was observed in all the three samples. Metallography results have been shown in table 1. Residual Resistivity Ratio (ratio of resistance at 293^{o}K and resistance at 10^{o}K) for all the three samples have been shown in table 2 and mechanical properties are listed in table 4. Fig. 3, shows the comparison of critical current $^V/_S$ magnetic field induction plot for 1.37mm dia Nb-Ti wire obtained from different sources.

Test Results

1. **Metallography**

Table 1

Sample	Filament number	Filament diameter, µm	Spacing, µm	Cu:SC ratio	Note
Sc. I	492	40.6	6.3	1.2:1	Geometry of cross section is slightly distorted
Sc. II	492	40.6	6.3	1.17:1	Right geometry of cross section
Sc. III	492	35.5 (in central non-distorted zone)	7.6	1.18:1	Strong distortion of cross section geometry

2. Residual Resistivity Ratio

Table 2

Sample	$RRR_{293/10}$	
	As drawn	Annealed at 275°C for one hour
Sc. I	35	150
Sc. II	43	155
Sc. III	41	138

3. Critical Current versus B on untwisted wires, n value, critical current density

Table 3

I_c (0.1μV/cm), A/I_c (1.0μV/cm), A/n							
	Induction, T						
	4	5	5.5	6	7	8	9
Sc. I	1850/q*	1540/q	**1390/q**	1201/q	866/902/61	603/633/47	302/330/26
Sc. II	1710/q	1405/q	**1294/q**	1163/q	877/900/89	626/646/73	330/360/26
Sc. III	1790/q	1470/q	**1330/q**	1194/q	884/926/49	606/638/45	316/345/26
J_c (0.1 μV/cm), A/mm²							
Sc. I	3025	2518	**2273**	1964	1416	986	494
Sc. II	2796	2297	**2116**	1902	1434	1024	540
Sc. III	2901	2383	**2156**	1935	1433	982	512

Note: q* - quench

4. Mechanical Properties at Room Temperature

Table 4

No.	Sample	UTS, Kg/mm²	YS, Kg/mm²	δ, %	Note
1.	Sample I	95	58.0	1.2	Out of guage length
2.		95	48.0	2.3	
3.	Sample II	95	54.0	1.5	Out of guage length
4.		95	47.5	2.3	
5.	Sample III	94	45.0	2.4	
6.		96	46.0	2.4	

5. Filament breakage

No filaments broken were revealed.

Sr.No.	Application Areas	Devices
1.	Physical research	Detection and beam handling in high energy physics, RF cavities for particle accelerators, High field for solid state physics
2.	Measuring techniques	Superconductinelectron microscope, Josephson junction as low field detectors and measuring oscillators
3.	Energy technology	Superconducting eletric-generators (a.c. and d.c.), Superconducting magnetic energy storage system (SMES), Cryogenic power transmission, Fault limiter
4.	Processing technology	Magnetic ore separation, Particle accelerator for materials investigation
5.	Transportation	Levitation trains (MAGLEV), Electric motors for ship propulsion
6.	Telecommunication and computing	RF telecommunication cable, Josephson junction for computer logic, Ultra-high-performance filters, E-bomb
7.	Medicine	Particle accelerators for cancer therapy, MRI system and SQUID

Conclusion

Though no filament breakage was observed in all the three short samples but wire breakage was observed during cold drawing in route followed for sample 1. The thermomechanical treatment followed for sample 2 was better from fabrication point of view. This route was followed for fabrication of longer lengths of 1.37 mm dia wire containing 492 number of Nb-Ti filament each of 40 micron size with Cu:SC ratio of 1.15:1. This wire was soldered onto U-grooved rectangular OFHC copper channel which will be used for fabrication of magnets to be used in Superconducting cyclotron coming up at VECC, Kolkata. This wire is capable of carrying a critical current of 1330 Amps against VECC requirement of 1030 Amps at 5.5 Tesla field and 4.2 K Temperature.

References

1. H. Hillmann and I. Pfeiffer, A. f. Metallkde 58, 129 (1967).
2. I. Pfeiffer and H. Hillmann, Acta Met. 16, 1429 (1968).
3. D. C. Larbalestier, IEEE Trans. On Magnetics MAG-15, 209 (1972).
4. A. D. McInturff and G. Chase, JAP 44, 2378 (1973).
5. T. Luhman and D. Dew Hughes,"Treaties on Materials Science and Technology," 14 Academic Press (1979).
6. "Development and fabrication of superconductor for cyclotron magnet", by S.K. Gupta, M.M.Hussain, M.K.Malik and DSC Purushotham, DAE solid State Physics Symposium Calcutta, Dec. 27-31, 1995.
7. "Development and fabrication of Nb-Ti superconductor for cyclotron magnet", M. K. Malik, M. M. Hussain & A. K. Singh, ENSC – 2001, Nov. 21-23, NPL, New Delhi.

This paper won the Dr G.S. Tendulkar prize for the overall Best Oral Presentation at the 56th Annual Technical Meeting of Indian Institute of Metals held at Vadodara during November 14-17, 2002

About the authors ...

A. K. Singh, *B. E. in Metallurgical Engineering, joined Atomic Fuels Division, BARC, in 1998 after graduating from the 41st batch of Training School. He has been actively involved in development & fabrication of Low Temperature Superconducting wires and cables for various applications. He is also involved in extrusion of uranium metal and Al-alloy components for Dhruva fuel assembly.*

M. M. Hussain *joined Atomic Fuels Division, BARC, in 1985 through 28th batch of Training School. He completed his B. E. in 1983 from Ranchi University and M. Tech. (Met. Engg.) in 1994 from IIT, Bombay. His fields of expertise includes melting & casting, rolling, extrusion and heat treatment of uranium. He has been actively involved in development and fabrication of Low Temperature Superconducting wires and cables for various applications. He is life member of several professional bodies.*

S. P. Singh *is B. E. and M. Tech. in Metallurgical Engineering. He joined Atomic Fuels Division, BARC in 1970 through 13th batch of Training School. Initially, he worked on production of thorium metal and its fabrication into different shapes. He was deputed to KFA, Jurich, Germany, for a period of one and half years for carrying out metallurgical compatibility studies of thorium metal with different cladding materials under Indo-German joint collaboration program. Later on, he worked on development of powder metallurgical products for nuclear and non-nuclear applications. At present, he is Head, Metallic Section, AFD, mainly looking after melting and casting of uranium metal and alloys, mechanical working, heat treatment of various metals and alloys, and fabrication of Nb-Ti multifilamentary low temperature superconducting wires/cables for various applications. He is life member of various professional bodies.*

V. G. Date *is B. E. in Metallurgical Engineering from Pune College of Engineering. He joined Atomic Fuels Division, BARC, in 1964 after graduating from 7th batch of Training School. He worked on powder metallurgy of nuclear fuels, reactor control rods and welding of nuclear materials. He became Head, AFD, in April 2001 and retired on superannuation on 31st August 2002. He is life member of several professional bodies.*

Preparation of Plasma Sprayed Coatings of Yttria Stabilized Zirconia and Strontium Zirconate and Studies on Their Interaction with Graphite Substrate

K.P. Sreekumar, R.U. Satpute and P.V.Ananthapadmanabhan
Laser & Plasma Technology Division
Bhabha Atomic Research Centre

S. Ramanathan
Materials Science Division
Bhabha Atomic Research Centre

and

N. Venkatramani
Beam Technology Development Group
Bhabha Atomic Research Centre

Abstract

Plasma sprayed coatings are extensively used for high temperature chemical barrier applications. Thermal stability and interaction of the coating material with substrate materials are critical issues that decide coating performance. This paper reports preliminary results of high temperature interaction of plasma sprayed yttria stabilized zirconia and strontium zirconate coatings with graphite substrate.

Introduction

PLASMA SPRAY DEPOSITION OR PLASMA spraying is a process that combines particle melting, quenching and consolidation in a single operation. The process involves injection of powder particles(metallic, ceramic or cermet powders) into a plasma jet generated by heating an inert gas in an electric arc confined within a water-cooled nozzle. The temperature at the core of the plasma jet is 10,000-15,000 K. Metal or ceramic particles injected into the plasma undergo rapid melting and at the same time are accelerated. These molten droplets moving at high velocities, exceeding 100 metres/second, impact on the surfaces of the substrate forming adherent coating[1-3]. The coating is incrementally built up by the impact of successive particles by the processof flattening, cooling and solidification. By virtue of the high cooling rates, typically 10^5 to 10^6 K/sec., the resulting microstructures are fine-grained and homogeneous[3].

Plasma sprayed ceramic coatings are extensively used for thermal barrier, wear and corrosion resistant and chemical barrier applications. The use of ceramic coatings for thermal and chemical barrier applications is well established[4,5]. The choice of the specific ceramic material is decided by its thermal stability, chemical stability in the operating environment, etc. Table I gives some of the prospective ceramic coating materials for high temperature thermal barrier and chemical barrier applications[6,7]. Aluminium oxide, by virtue of

Table 1: Prospective ceramic coating materials for high temperature applications

Coating material	Melting point (K)	Remarks
Aluminium oxide	2327	Widely used ceramic coating for many applications
Yttrium oxide	2712	Stable in many reactive environments including carbon and molten metals
Yttria stabilized zirconia	~2600 K	Extensively used for TBC applications in aeroengine components
Calcium zirconate	2598 K	High melting point and suitable for many molten metal containment
Strontium zirconate	3000 K	High melting point and suitable for many molten metal containment

its reasonably high melting point (2300K) and chemically inert nature is the natural choice for thermal and chemical barrier applications. However, the main draw back of aluminina is its instability under reducing conditions. Above 1200^0C, alumina is reduced to its gaseous sub-oxides in presence of carbon, hydrogen and other reducing gases. By virtue of their higher melting points and better chemical stability in reducing atmospheres, yttria stabilized zirconia (YSZ) containing about 7 wt% yttrium oxide, $CaZrO_3$ and $SrZrO_3$ are expected to perform better in reducing environments. This report deals with the development and evaluation of high temperature stability of plasma sprayed YSZ and $SrZrO_3$ coatings on graphite substrates.

Plasma Spray Facility

The 20 kW atmospheric plasma spray system developed at the Laser&Plasma Technology Division was used for preparing the coatings. The system consists of a 20kW DC non-transferred arc plasma torch, DC power supply including RF igniter, powder feeder, plasma gas and cooling water systems. A photograph of the system with the powder laden plasma jet is shown in Figure 1.

Fig. 1A 20 kW Atmospheric Plasma Spray System

Fig. 1B Powder laden Plasma jet

$SrZrO_3$ and YSZ powders from CERAC Incorporated, USA were used for plasma spray deposition. Particle size distribution, by laser scattering technique showed narrow size distribution with about 60% of the particles having size in the range of 20-40 microns. A mixture of argon and nitrogen was used as the plasmagen gas. Input power to the plasma torch was varied from 10 kW to 18 kW by controlling the arc current. In the range of operating conditions used, the torch efficiency, determined by standard calorimetric method, was found to be 60%. Circular graphite coupons 40mm diameter and 10mm thickness were used as substrates. Experimental parameters are given in Table 2.

Table 2 : Operating Parameters of Plasma Spray Torch

Parameter	Range
Torch input power	10-18 kW
Plasma gas(Ar) flow rate	20 LPM
Secondary gas(N_2) flow rate	2 LPM
Powder feed rate	~10 g/min
Powder carrier gas flow rate	8 LPM
Torch to base distance	125 mm
Anode nozzle diameter	8 mm
Arc current	250-450 amperes
Powder injection	Radial injection through nozzle (near the exit)
Plasma gas injection	Vortex injection

Coating Characterization

The as-sprayed coatings were characterized by x-ray diffraction technique for identification of the phases. Optical microscopy was used for determining the microstructural and interface features. Reaction with graphite substrate was studied by heating the coated specimens at high temperatures in a specially designed plasma furnace.

Experimental Setup for Heat-Treatment Studies

High temperature reaction of the coatings with carbon was studied by subjecting the coated graphite specimens to thermal treatments in a plasma furnace. The furnace consists of a DC plasma torch mounted on a water-cooled stainless steel reaction chamber, DC power supply, gas train and control console. A close-fitting graphite tube 40 mm internal diameter, and 2 mm thick is inserted in the chamber. Specimens for thermal treatment are kept on a graphite rod, centrally located inside the graphite insert. The position of the specimen holder can be continuously varied with respect to the torch nozzle. Temperature at the top surface of the graphite rod was monitored by a Pt-Pt-Rh thermocouple. Figure 2 shows schematic of the experimental set-up.

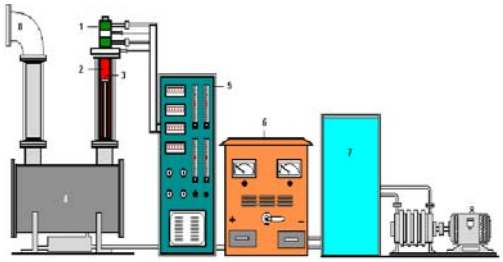

Fig. 2 Plasma heat treatment furnace

The plasma torch was ignited and the power was maintained constant at a specific level and the reactor was allowed to attain thermal equilibrium as indicated by the constant temperature at the surface of the graphite rod. The plasma power was varied and the equilibrium temperature at the surface of the graphite rod was recorded as before. The hot zone temperature can be varied by varying the plasma power, increasing the distance between the torch nozzle and the graphite rod and the gas flow rate. It was observed that for an input power of 12kW, when the specimen distance from the torch nozzle was 175mm, the equilibrium sample temperature was 1200 °C.

Sample temperature of 1400 C could be obtained at 10kW and 150mm.

Results and Discussion

Results of x-ray powder diffraction of as-sprayed coatings of YSZ using Ni-filtered Cu-Kα radiation showed the characteristic diffraction peaks of the cubic phase. $SrZrO_3$ coatings showed the diffraction peaks of cubic perovskite structure. Figure 3 shows typical optical micrograph of $SrZrO_3$ coating. Surface morphology of the coating shows molten and partially molten grains and intergranular porosity characteristic of plasma sprayed coatings.

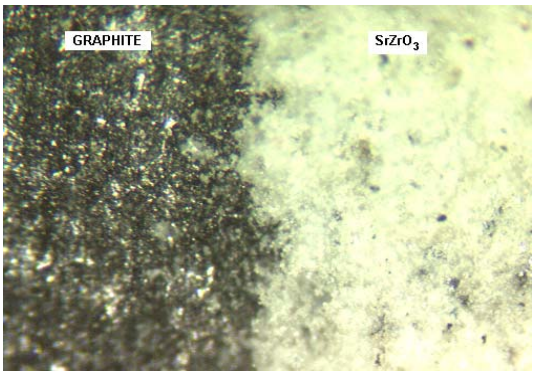

Fig. 3 Typical optical micrograph of Plasma sprayed $SrZrO_3$

Coating Interaction with Substrate

In order to study chemical interaction of $SrZrO_3$ and YSZ with carbon, thermodynamic analysis of the systems $SrZrO_3$-C and Y_2O_3-ZrO_2 –C have been studied. Free energy minimization plots for the systems $SrZrO_3$-C and Y_2O_3-ZrO_2 –C developed using CSIRO thermal package [8] are shown in Figures 4 and 5 respectively. The figures show the temperature regions of stability of the different phases. It is seen from Figure 4 that $SrZrO_3$ is stable only up to 2000K. The reaction of $SrZrO_3$ with carbon starts above 1750 K resulting in the formation of ZrC and SrO/Sr. This is undesirable as it can lead to delamination and coating failure. It is therefore necessary that the operating temperature should not exceed 1700 K. It is seen from Figure 5 that stabilized zirconia forms ZrC and Y_2O_3 above 1500 K. For better coating performance, it is recommended that the operating temperature does not exceed 1500 K.

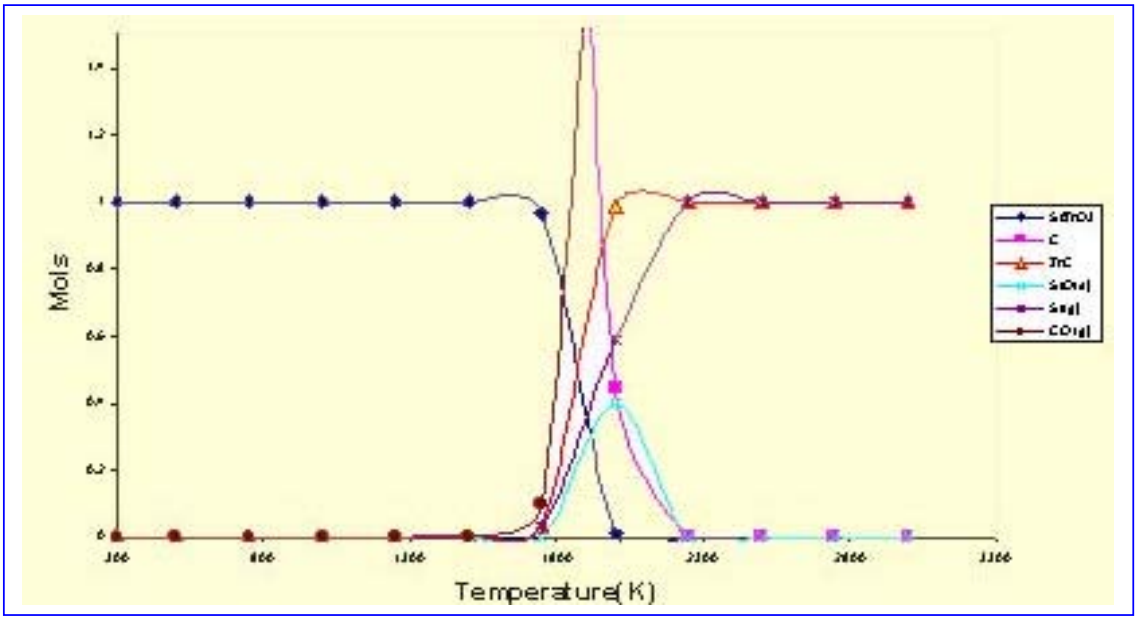

Fig. 4 Free Energy Minimization Plot for the system $SrZrO_3$-C

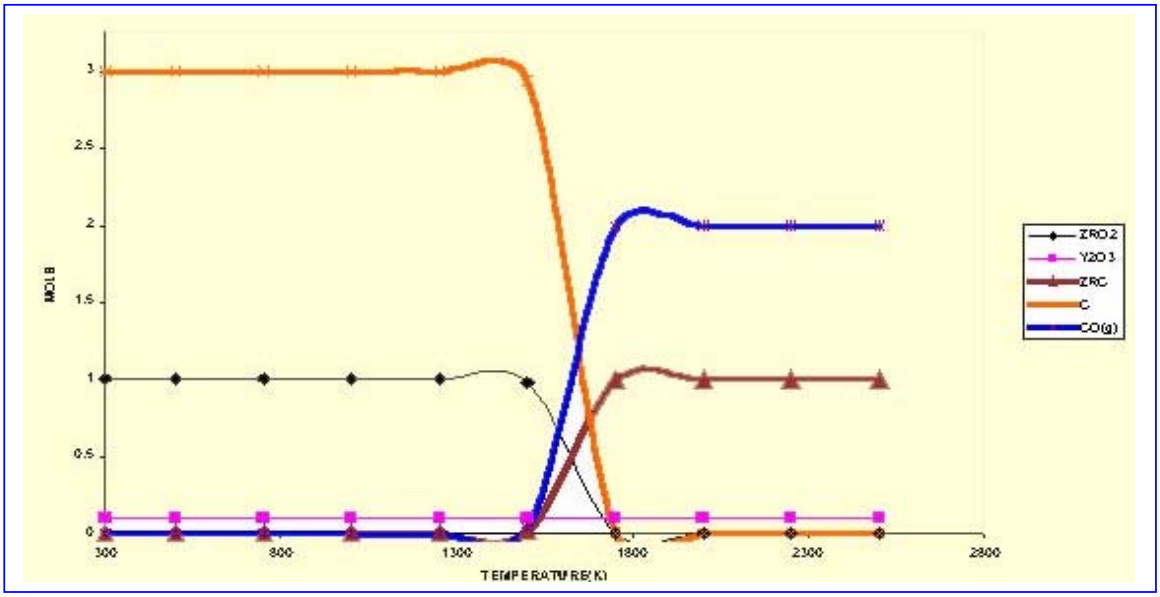

Fig. 5 Free Energy Minimization Plot for the system ZrO_2-Y_2O_3-C

Experiments on coating interaction with substrate were carried out by heating specimens of $SrZrO_3$ and YSZ coatings on graphite in the plasma furnace. The test specimens were kept on top of a graphite rod located centrally in the plasma furnace. The required sample temperature could be obtained by manipulating the input power and distance of sample from torch nozzle. Samples were heated to 1200 C and 1400C for 3 hours. Heating rate was controlled by slowly increasing the plasma power and the average heating rate was 15^0 /minute.

Results showed that coatings were stable at 1200C indicating no reaction of YSZ and $SrZrO_3$ with carbon. However, thermal treatment at 1400C led to coating delamination. The entire coating had separated from the graphite substrate, possibly due to interface stresses arising out of differential thermal expansion of the coating and graphite. However, there was no appreciable chemical reaction between carbon and $SrZrO_3$ as indicated by x-ray diffraction.

Conclusion

Plasma sprayed coatings of $SrZrO_3$ and Yttria stabilized zirconia have been deposited on graphite substrates. Thermal stability of the coatings on graphite substrates have been studied using a specially designed plasma furnace. Results of experiments show that there was no appreciable chemical interaction of the coatings with carbon up to 1400C. However, thermal treatment at 1400C led to complete delamination of the coatings. The coating adhesion can be improved by using iron as intermediate coating.

References

1. Robert B.Hiemann, Plasma-Spray Coating-Principles and Applications, VCH Publishers Inc., New York, NY, USA, 1996
2. D. Matejka and B. Benko, Plasma Spraying of Metallic and Ceramic Materials, John Wiley & Sons, Ltd., Chichester, UK, 1989.
3. Lech Pauloski, The Science and Engineering of Thermal Spray Coatings, John Wiley and Sons, 1995
4. C. Funke, J.C. MailandB. Siebert, R vassen and D. Stover, Surface &Coatings Technology, 94-95(1997), 106
5. R Vassen and D. Stover, in Functional Gradient Materials and Surface Layers Prepared by Fine Particles Technology (eds.) M.I. Baraton and I. Uvarova, Kluwer

Academic Publishers, Netherlands, 2001, p.199
6. Ihsan Barin and Gregor Platzki, Thermochemical Data of Pure Substances, VCH Publishers, Weinheim, Germany, 1995
7. M. Binniewies and E. Milke Thermochemical data of Elements and Compounds, Wiley-VCH, Weinheim, Germany, 2002
8. A. G. Turnbull and M. W. Wadsley, The CSIRO Thermochemistry System, Version 5, IMEC, Australia(1988)

This paper won the Best Paper award in the PLASMA 2002 symposium held at Bharathiar University, Coimbatore on December 19, 2002

About the authors ...

Mr K.P Sreekumar *is a senior scientist engaged in development of plasma sprayed ceramic/metallic/duplex coatings for various industrial and special research applications including strategic nuclear applications. His research work spanning 25 years in BARC includes design & development of plasma torches of various capacities for different plasma systems and building various thermal plasma equipments used for coating applications, mineral processing, aerosol generation, nano-particle synthesis, etc. He has more than 100 publications to his credit.*

Mr R.U. Satpute *is currently engaged in the development programmes of plasma spraying and plasma processing.*

Dr P.V. Ananthapadmanabhan *joined BARC after graduating from the 20th batch of the Training School in August 1977. He is engaged in Materials Processing by Thermal Plasma Technology. He has developed many novel materials and coatings for various specialized applications including strategic nuclear applications. His research interests include reactive plasma processing, high temperature materials, nano-particle synthesis, etc. He has also developed thermal plasma devices for mineral processing, aerosol generation, nano-particle synthesis, etc. He has more than 100 publications to his credit.*

Dr S. Ramanathan *joined BARC in 1976 through 19th batch of Training School and works on processing of advanced ceramic materials. He worked on the development of thoria-yttria solid oxide electrolyte for oxygen sensor applications and obtained PhD in Materials Science from IIT Mumbai. He worked on synthesis of controlled morphology sub-micron sized oxide powders by homogeneous precipitation technique and impervious oxidation resistant and porous catalytic coatings by sol-gel technique. Presently, he is working on the formation of ceramic shapes by liquid based fabrication technique (slip and tape casting). He has about forty-five publications to his credit.*

Dr N. Venkatramani *is Director of Beam Tecgnology Development Group in BARC. He is the architect of high power plasma, particle and laser beam research and development programmes in India. He has pioneered the thermal and non-thermal applications of these beams including some of the novel material processing techniques. He also directs nuclear and defense oriented projects like high power microwaves and industrially intensive beams.*

Transport and Magnetic Properties of HTS/CMR Multilayers

D.K. Aswal, Ajay Singh, S.K Gupta, J.V. Yakhmi and V.C. Sahni
Technical Physics and Prototype Engineering Division
Bhabha Atomic Research Centre

C.S. Viswanadham and G.L. Goswami
Atomic Fuels Division
Bhabha Atomic Research Centre

and

L.C. Gupta
Tata Institute of Fundamental Research, Mumbai

Abstract

We report magneto-transport and magnetization studies of heterostructures comprising of alternately stacked $YBa_2Cu_3O_{7-}$ (YBCO) and $La_{1-x}Pb_xMnO_3$ (LPMO) layers. The c*-axis oriented bi-layer and four-layer YBCO/LPMO heterostructures were prepared* in-situ *on (100) $SrTiO_3$ substrates using pulsed laser deposition. Zero-field cooled (ZFC) and field-cooled (FC) magnetization data show that in a four-layer structure the LPMO layers get antiferromagnetically coupled when the thermodynamic-fluctuation induced Cooper pairing begins in the YBCO layers, which is well supported by the magnetization versus applied field data. Evidence of antiferromagnetic coupling is also reflected in the temperature dependence of the magnetoresistance.*

Introduction

SUPERCONDUCTIVITY (SC) AND ferromagnetism (FM) are antagonistic orderings and investigation of their possible coexistence and mutual influence in tailor-made SC/FM multilayer structures has been an active area of theoretical as well as experimental research for last four decades [1]. The antagonism between SC and FM is understandable from the microscopic theory: SC requires an attractive interaction between electron pairs with antiparallel spins (i.e. formation of Cooper pairs), whereas for same electrons participation in magnetic ordering demands a parallel alignment of electron spins through an exchange interaction. Therefore, in a SC/FM heterostructure if exchange field of FM exceeds the condensation energy of Cooper pairs (measured in terms of energy gap, Δ) then destruction of superconductivity can take place due to paramagnetic effect. However, in SC/FM heterostructures both superconductivity and ferromagnetism can coexist. This is because proximity effect can induce a superconducting order parameter in FM layer; on the other hand, the neighboring pair of FM layers can interact with each other via the SC layer.

An important question is how superconductivity of a layered SC/FM structure is influenced by the presence of magnetic layers. The theoretical work of Radovic et al [2] predicted a phase difference $0<\phi<\pi$ between neighboring SC layers and an unusual oscillatory dependence of superconducting transition temperature (T_c) on the FM layer thickness (d_{FM}). However, the experimental reports on the evidence of π-phase

superconductivity and oscillations in T_c as a function of d_{FM} have been mixed [3-5]. For example, in V/Fe system some experiments showed oscillations in T_c-d_{FM} [3], while on same system other experiments showed a rapid decrease in T_c with increasing d_{FM} followed by a plateau [4]. Negative results were also published for Nb/Fe system [5].

Another important issue of SC/FM multilayers is how the magnetism of FM layers is influenced by the presence of SC layers. Theoretically it was shown that the singlet Cooper pairing of electrons in SC layers leads to a long-range antiferromagnetic interaction between FM layers due to Ruderman-Kittel-Kasuya-Yosida (RKKY) indirect exchange [1,6]. At present, however there is no experimentally known SC/FM heterostructure that shows magnetic coupling either above or below T_c. A recent experimental attempt in GdN/NbN/GdN trilayers failed to observe the magnetic coupling between the FM layers [7]. Sa de Melo theoretically showed that magnetic coupling in SC/FM heterostructures can be observed if the superconductor has higher T_c and ferromagnet has not so large pair breaking effect [8]. Thus, heterostructures comprising of high temperature oxide supercondcuctors and colossal magnetoresistance ferromagnets are considered to be good systems for such studies.

In this paper, we present some interesting experimental results of magneto-transport and magnetic studies carried out on $YBa_2Cu_3O_{7-\delta}/La_{1-x}Pb_xMnO_3$ (YBCO/LPMO) heterostructures fabricated using pulsed laser deposition technique. The results, for the first time, show that LPMO layers get antiferromagnetically coupled when the thermodynamic-fluctuation induced Cooper pairing begins in the YBCO layers.

Experimental

The bi-layer and four-layer YBCO/LPMO structures were fabricated on (100) $SrTiO_3$ (STO) single-crystal substrates by pulsed-laser ablation technique. The details of fabrication are described elsewhere [9]. Briefly, to fabricate YBCO/LPMO heterostructures a laser beam from a KrF excimer laser (wavelength 248 nm, pulse width 20 ns and repetition rate of 5 Hz) was alternately focused onto YBCO and LPMO targets. All the layers were deposited *in-situ* at substrate temperature of 730°C and oxygen pressure of 0.2 torr. In the present studies the thickness of YBCO layer was kept 100 nm, whereas the thickness of LPMO layer was varied between 25 and 100 nm.

X-ray diffraction (XRD) measurements were performed using CuK radiation to assess the orientation of the grown heterostructures. The surface morphology of samples was examined using atomic force microscopy (AFM). AFM measurements were carried out under ambient conditions using a scanning probe microscope (model-SPM Solver P47) in contact mode. Rectangular cantilevers of Si_3N_4 (length 200 μm and width 40 μm) having force constant of 3 N/m were employed for these measurements.

The electric resistance of the heterostructures was measured using a standard four-probe method in the temperature range between 50 and 300 K using a closed cycle helium cryostat (APD-make). The magnetoresistace of the heterostructures was determined by applying a field of 1T parallel to the plane of the substrates. The magnetic properties of the heterostructures were studied using a SQUID magnetometer (Quantum design MPMS model).

Results and Discussion

A typical XRD plot for [YBCO (100nm)/LPMO (50nm)]$_2$ heterostructure is shown in Fig. 1. The presence of only (00*l*) reflections suggests that both YBCO and LPMO layers have grown with *c*-axis perpendicular to substrate plane. In the expanded plot, as shown in the inset of Fig. 1, (002) LPMO, (200) STO and (006) YBCO peaks are clearly discernible. It is noted that the *c*-lattice parameter for LPMO in the heterostructure is 0.3909nm, which is same as that measured for a LPMO film directly grown on STO substrate. This suggests that crystallinity of LPMO layers is unaffected by the presence of YBCO layers. The *c*-lattice parameter of YBCO in

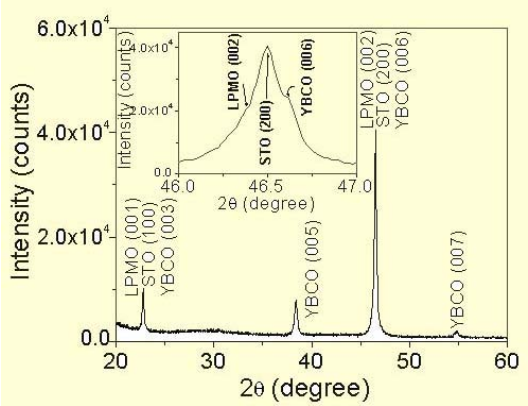

Fig. 1 XRD plot of a [YBCO(100nm)/LPMO(50nm)]$_2$ heterostructure. The inset shows the expanded plot in the 2θ range between 46 and 47°.

the heterostructure is determined to be 1.1673 nm. The oxygen content, (7-δ), of YBCO is computed using the empirical relation: (7-δ) = 74.49 – 57.87 *c*, where *c* is the *c*-lattice parameter in nm [10].The value of oxygen content, (7-δ), comes out to be 6.94, which suggests that YBCO layers are fully oxygenated.

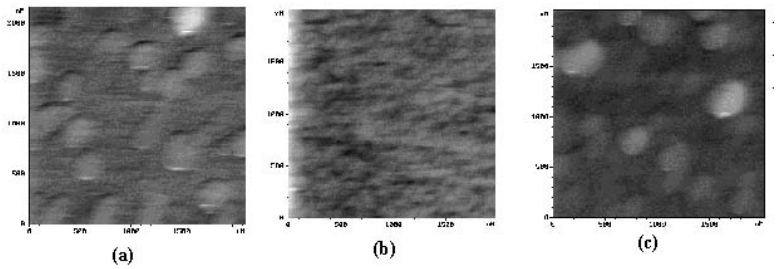

Fig. 2 2000 nm X 2000 nm AFM scans of (a) YBCO film on STO substrate, (b) LPMO film on STO substrate, and (c) YBCO(100nm)/ LPMO(50nm)]$_2$ heterostucture on STO substrate.

In Fig. 2 we show the AFM images of the top LPMO layer in [YBCO (100nm)/LPMO (50nm)]$_2$ heterostructure. For comparison, the surface morphologies of *c*-axis oriented YBCO and LPMO films grown on STO are also shown in Fig 2. YBCO film grows by 3D island growth, while LPMO film grows via 2D layer-by-layer growth. The surface morphology of top LPMO layer in a heterostructure exhibits a carpeting effect i.e. the morphology of LPMO is dictated by the morphology of the YBCO layer. These results along with XRD data suggest high quality of the grown heterostructures.

The temperature dependences of normalized resistance and magnetoresistance for a typical [YBCO(100nm)/LPMO(25nm)]$_2$ heterostructure are shown in Fig. 3. The magnetoresistance (MR) is expressed as $(R_0-R_H)/R_H$ X100, where R_0 and R_H are the resistance values under zero and 1 T magnetic fields. For comparison, the data of YBCO and LPMO films are also presented. From Fig. 3 we infer the following:

(i) For YBCO film, the resistance varies linearly between 140 and 300 K. Below 140 K (marked by T_{CP} in the Fig. 3 (a)), the resistance deviates from the linearity, which is well described in terms of thermodynamic-fluctuations induced formation of Cooper pairs [11]. Application of magnetic field did not yield any changes in the normal state resistivity, while T_c is suppressed marginally by ~1K.

(ii) The R(T) plot of LPMO film exhibits an insulator-to-metal transition (T_{IM}) at 235 K, which is a characteristic property of colossal magnetoresitive materials [12]. The T_{IM} corresponds to paramagnetic-ferromagnetic transition that occurs approximately simultaneously with insulator-to-metal transition. The temperature dependence of MR exhibits axial (peak) near T_{IM}. A common explanation of MR is usually provided in the framework of double-exchange mechanism, which is based on the assumption of the appearance of Mn^{+4} with the substitution of La^{+3} by a divalent cation (Pb^{+2}). It is believed that in this case ferromagnetism results from the strong ferromagnetic exchange between Mn^{+3} and Mn^{+4}.

(iii) The normal state behavior of [YBCO(100nm)/LPMO (25nm)]$_2$ structure is clearly influenced by both insulator-to-metal transition of LPMO layers at ~235 K and fluctuation conductivity of YBCO layers at

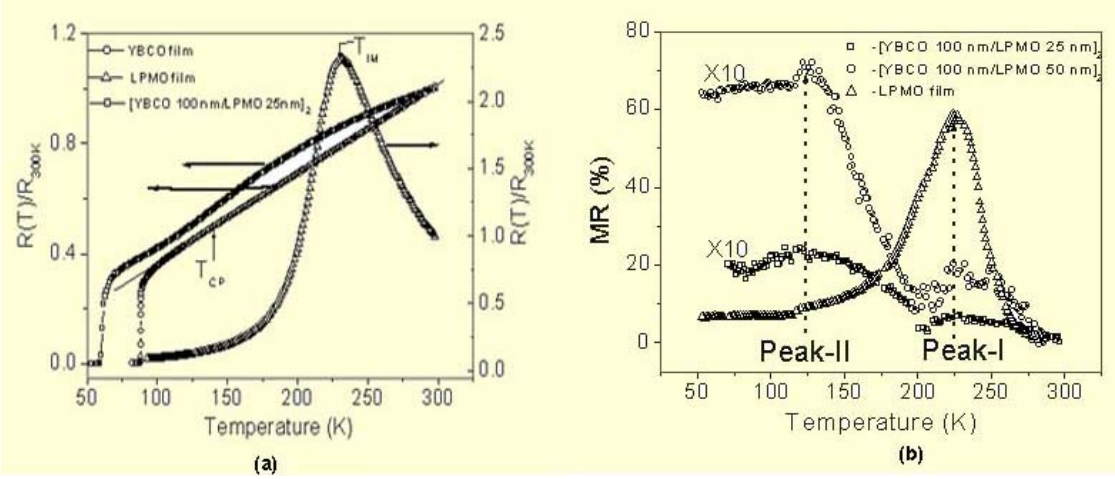

Fig. 3 (a) Normalized resistance as a function of temperature recorded for YBCO film. LPMO film and [YBCO(100nm)/LPMO(50nm)]$_2$ heterostructure. The straight line is linear fit to the normal state resistance data of YBCO film and T_{CP} corresponds to onset of fluctuation conductivity in YBCO film. T_{IM} represents the insulator-to-metal transition in LPMO film. (b) Temperature dependence of magnetoresistance (obtained at 1T magnetic field) for LPMO film, [YBCO(100nm)/LPMO(25nm)]$_2$ and [YBCO(100nm)/LPMO(50nm)]$_2$ heterostructures.

~140K. The heterostructure exhibits superconductivity at 59 K. The T_c of heterostructures was found to decrease monotonically with increasing the thickness of LPMO layers without any significant broadening of the transition width. This indicates that the suppression of T_c is not due to the chemical reaction between LPMO and YBCO. The suppressed superconductivity in the hetero-structure has been attributed to the self-injection of quasi-particles from YBCO to LPMO [13]. Due to d-wave symmetry of the order parameter in YBCO, there is a significant population of quasiparticle excitations. The ferromagnetic LPMO, having nearly perfect spin polarization, allows only those quasiparticles to diffuse across the YBCO/LPMO interface whose spins are parallel to those of LPMO. This induces further pair breaking in the YBCO and results in depressed T_c. Interestingly the temperature dependence of the MR exhibits two distinct peaks at temperatures 235 K (peak-I) and 130 K (peak-II), respectively. The magnitude of Peak-II being much larger as compared to that of Peak-I. The origin of Peak-I is obviously related to the CMR property of LPMO layers; while Peak-II appears to be correlated with T_{CP} and to investigate its origin we concentrate on the magnetic properties of the heterostructures.

In Fig. 4, we show the temperature dependence of the magnetization recorded in zero-field cooled (ZFC) and field cooled (FC) conditions. For a bi-layer structure two different transition regions can be identified: (i) a paramagnetic to ferromagnetic (FM) at ~240K and (ii) a ferromagnetic to diamagnetic transition at ~72 K. The ferromagnetic ordering at ~240 K corresponds to that observed for LPMO. It may be noted that in ferromagnetic state, the ZFC signal is lower than FC signal, and this indeed is the case with ferromagnetic materials. The diamagnetic transition at ~72 K indicates that the bi-layer structure has undergone a transition to superconducting state. In comparison, the four-layer structure shows two anomalous features: (i) antiferromagnetic (AF) ordering at 135 K (as revealed by FC data) and (ii) a larger ZFC signal as compared to FC signal in the temperature range 75-170 K. Since at 135 K the individual LPMO layers are expected to show FM ordering, therefore an AF ordering at this temperature in a four-layer structure can arise only if the spins of two LPMO layers, namely, F1

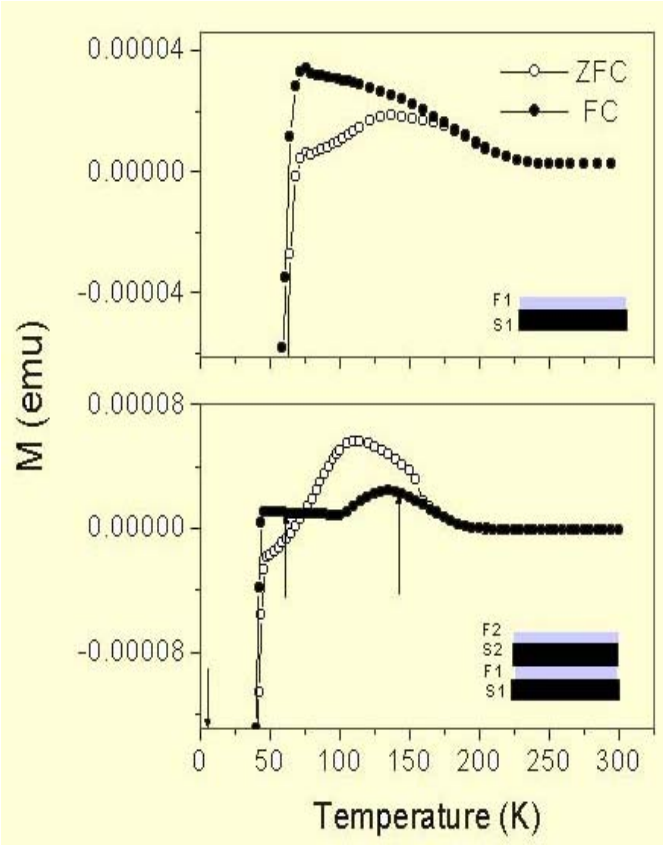

Fig. 4. Zero field cooled (ZFC) and field cooled (FC) magnetization as a function of temperature recorded for bi-layer YBCO(100nm)/LPMO(50nm) and four-layer [YBCO(100nm)/LPMO(50nm)]$_2$ heterostructures. The inset shows the schematic of the heterostructures: S1 and S2 are YBCO layers, and F1 and F2 are LPMO layers. Arrows marked at 140, 60 and 5K correspond to ferromagnetic, antiferromagnetic and diamagnetic states, respectively.

and F2, align in the opposite directions. It is interesting to note that AF ordering correlates with the formation of thermodynamic-fluctuations induced Cooper pairs in the YBCO layer. This suggests that AF coupling between CMR layers is prompted by the formation of Cooper pairs in the HTS layer.

A larger ZFC signal as compared to FC signal is a consequence of AF coupling between the two CMR layers i.e. F1 and F2, and is understood as follows. For the measurement of ZFC magnetization, the sample is first cooled to 5 K and then a field of 100 Gauss is applied parallel to the plane of the structure. The data is acquired during the warming cycle of the sample. At 5K, both YBCO layers i.e. S1 and S2 are in superconducting state and these layers would expel any applied field that is lower than lower critical field. Thus, magnetic layers F1 and F2, which are AF coupled, will have an additional magnetic flux that is expelled from S1 and S2 layers. The additional flux in F1 layer will have contributions from both S1 and S2 layers, while for F2 the additional flux would be only from S2. This would lead to a net positive magnetic moment as the temperature is increased above T_c. In the case of FC measurement, first a 100 G field is applied at room temperature and then magnetization is recorded during the cooling cycle of the sample. As field gets trapped at defects in S1 and S2 layers, the expelled field is almost negligible, which results in a temperature independent magnetization due to AF interaction between F1 and F2. However, at lower temperatures superconductivity dominates and the heterostructure shows a sharp diamagnetic transition.

In order to confirm the change in magnetic ordering i.e. ferromagnetic to antiferromagnetic to diamagnetic as a function of temperature in a four-layer structure, magnetization versus applied field (M-H) loops were recorded at three different temperatures belonging to different regimes of Fig. 4(b), which are marked by arrows. The obtained M-H loops are shown in Fig. 5. At 140 K the M-H loop is typical of a ferromagnetic state. However, at 60 K at low fields the magnetization varies less sharply with the field. In addition, the saturation magnetization decreases significantly, which confirms the occurring of antiferromagnetic coupling in the multilayer structure. At 5K, the M-H loop corresponds to a superconducting state.

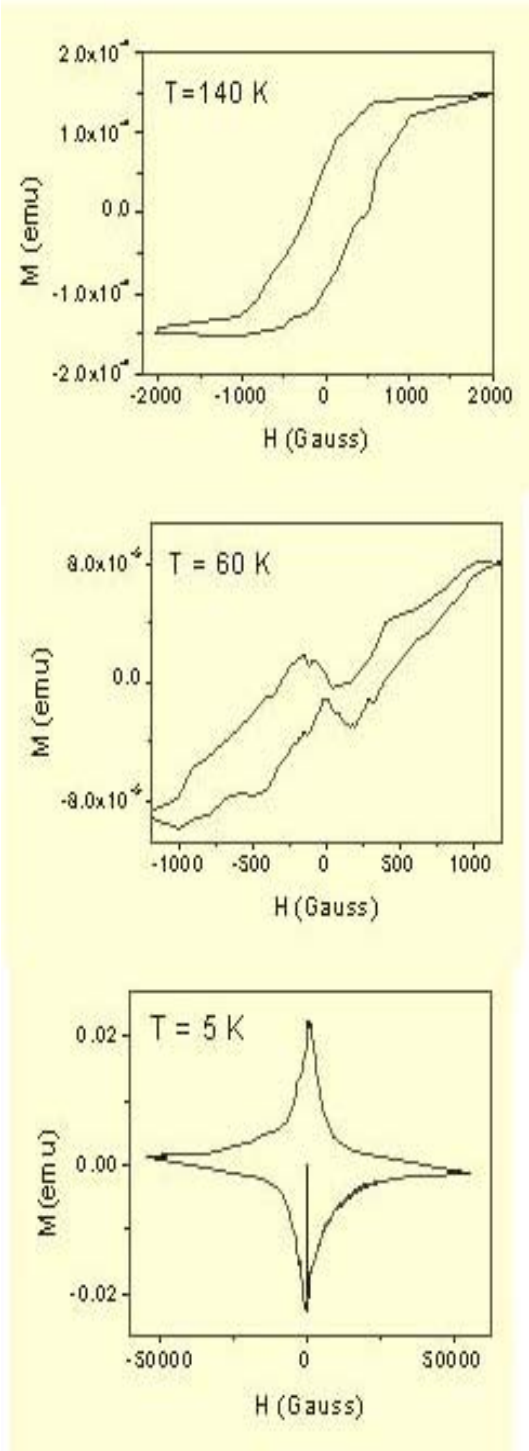

Fig. 5 Magnetization as a function of field applied parallel to the substrate-plane for [YBCO(100nm)/LPMO(50nm)]$_2$ heterostructure recorded at three different temperatures, namely 140 K, 60 K and 5K.

Interestingly the position of peak-II in temperature dependence of MR, Fig. 3(b), coincides with the AF coupling of CMR layers. This implies that the origin of peak-II is similar to that observed for magnetic/nonmagnetic GMR multilayers [14]. In the temperature region close to peak-II, F1 and F2 are AF coupled and therefore the resistance of the heterostructure is high due to spin-dependent scattering. On application of high magnetic field, F1 and F2 get ferromagnetically aligned resulting in the decrease of the resistance and hence a magnetorersistance.

The antiferromagnetic state in YBCO/LPMO heterostructures as revealed from magnetization and magnetoresistance data is therefore consistent with theoretical prediction whereby antiferromagnetic state arises due to long range RKKY exchange between neighboring FM layers through SC interlayer [1,6]. Recently, the coexistence of superconductivity and magnetisms has also been reported in a naturally layered $RuSr_2GdCu_2O_8$ compound [15,16] in which CuO layers are responsible for superconductivity while Gd layers are the magnetic layers. The Curie temperature and superconducting transition temperature for this compound are respectively 132 K and 46 K, respectively. This implies that superconducting state arises in a system that already has a magnetic ordering- a case similar to our YBCO/LPMO heterostructures. In $RuSr_2GdCu_2O_8$ compound, it has been experimentally shown that CuO layers show superconductivity, while in Gd layers a ferromagnetic ordering occurs in such a way that the magnetization of neighbouring layers are antiparallel i.e. the system exhibits a canted antiferromagnetim [16].

Conclusions

We have studied the magneto-transport and magnetic properties of YBCO/LPMO heterostructures. We have shown that these heterostrucutures exhibit both superconductivity and magnetism. Zero-field cooled (ZFC) and field-cooled (FC) magnetization data of a four-

layered YBCO/LPMO structure is complex and exhibit different magnetic states as the temperature is lowered i.e. paramagnetic, ferromagnetic, antiferromagnetic and diamagnetic states. The antiferromagnetic state is found to be correlated with thermodynamic-fluctuations induced Cooper pairing in YBCO. This suggests that Cooper pairing in YBCO leads to antiferromagnetic interaction between LPMO layers through RKKY indirect exchange. The temperature dependence of the magnetoresistance exhibits two peaks at temperatures 235 K and 130 K respectively. The magnetoresistance peak at 235 K corresponds to colossal magnetoresisitve property of LPMO layer; while peak at 130 K is a consequence of antiferromagnetic coupling of LPMO layers.

References

1. Yu A. Izyumov, Yu N. Proshin, M.G. Khusainov, Physics-Uspekhi **45**, 109 (2002), and references therein
2. Z. Radovic, M. ledvij, L. Dobrosavljevic, A.I. buzdin and J.R. Clem, Phys. Rev. B **44**, 759 (1991).
3. H.K. Wong, B.Y. Jin, H.Q. Yang, J.B. Ketterson, and J.E. Hillard, J. Low Temp. Phys. **63**, 307 (1986).
4. P. Koorevaar, Y. Suzuki, R. Coehoorn, and J. Aarts, Phys. Rev. B **49**, 441 (1994).
5. G. Verbanck, C.D. Potter, R. Schad, P. Belien, V.V. Moschalkov, and Y. Bruyseraede, Physica C **235-240**, 3295 (1994).
6. P.W. Anderson and H. Suhl, Phys. Rev. **116**, 898 (1959).
7. J.E. Mattson, C.D. Potter, M.J. Conover, C.H. Sowers and S.D. Bader, Phys. Rev. B **55**, 70 (1997).
8. C.a.R. Sa de Melo, Phys. Rev. Lett. **10**, 1933 (1997).
9. A. Singh, D.K. Aswal, S. Sen, C.S. Viswanadham, G.L. Goswami, L.C. Gupta, S.K. Gupta, J.V. Yakhmi, V.C. Sahni, J. Crystal Growth **243**, 134 (2002).
10. T.A. Venderah, C.K. Lowa-Ma, D.E. Blis, M.W. Decker, M.S. Osofsky and M.M. Miller, J. Crystal Growth **118**, 385 (1992).
11. D K Aswal, A. Singh, S. Sen, M. Kaur C. S. Viswanadham, G. L. Goswami, S.K. Gupta, J. Phys. Chem. Solids **63**,1797 (2002), and references therein.
12. J.M.D. Coey, M. Viret, and S. von Molnar, Adv. Phys. **48**, 167 (1999), and references therein
13. N.C. Yeh, R.P. Vasquez, C.C. Fu, A.V. Samoilov, Y. Li and K. Vakili, Phys. Rev. B **60**, 10522 (1999).
14. P.M. Levy, Solid State Physics, Vol. 47, Academic Press, 1994, p-367, and references therein
15. O. Chmaissem, J.D. Jorgensen, H. Shaked, P. Dollar and J.L. Tallon, Phys. Rev. B **61**, 6401 (2000) J.W. Lyn, B. Keimer, C. Ulrich, C. Bernhard and J.L. Tallon, Phys. Rev. B **61**, R14964 (2000).

This paper received the Best Poster Paper award at the International Symposium on "Recent Advances in Inorganic Materials," held at IIT, Bombay, during December 11-13, 2002

About the authors ...

Dr D.K. Aswal *joined TPPED (BARC) through 30th batch of Training School. He has made several contributions in the field of thin/thick films and single crystals of various high temperature superconductors and colossal magnetoresistive materials. He has also worked on recently discovered magnesium-di-boride superconductor. Presently, he is working on HTS/CMR multilayers, metallic-multilayers using molecular-beam-epitaxy and thermoelectric materials. Dr. D. K. Aswal is a recipient of prestigious JSPS fellowship during 1997-99 and was awarded Paraj-2000 prize for excellence in science. He has authored more than 120 scientific publications.*

Mr Ajay Singh *joined TPPED through 42nd batch of Training School. His area of research are development of thermoelectric devices and thin films & multilayer structures of high temperature superconductors and colossal magnetoresistive materials.*

Dr S.K. Gupta *joined BARC in 1975 and is presently Head of Thin Films Devices Section in TPPED. Over the years, he has worked on space quality silicon solar cells, high temperature superconductor thin films and single crystals, gas sensors and thermoelectric materials. He is a member of the National Academy of Sciences, India.*

Dr J.V. Yakhmi*, Head, Technical Physics and Prototype Engineering Division, BARC, has worked in BARC for the past 37 years on diverse areas of research in materials science, such as, high Tc systems, magnetic alloys, molecular materials, etc.*

Dr V.C. Sahni, *Director, Physics Group, BARC, joined BARC in1965. He has made important contributions in lattice dynamics of complex crystals, group theoretical methods as applied to solid state physics, Raman spectroscopy, measurement of electron momentum densities, quasi crystals, magnetization studies of many superconducting and several magnetic materials using SQUID magnetometer etc. Besides condensed matter physics, Dr. Sahni has specialized in the indigenous development of physics related instrumentation, particularly UHV based instruments and synchrotron radiation utilisation equipment for the storage ring INDUS-1 & upcoming ring INDUS-2 at Centre for Advanced Technology (CAT), Indore. Dr. Sahni is a Fellow of the National Academy of Sciences, India and an INSA Young Scientist Awardee. He has also been a Visiting Fellow at the Centre for Chemical Physics UWO, Ontario, Canada during 1981 -1982, INSA-USSR Academy Exchange Fellow in 1987 and INSA-Royal Society (UK) Exchange Fellow in 1993. Dr. Sahni has published over 250 scientific papers, coauthored the book "Dynamics of Perfect Crystals" and co-edited another book "Developments in Theoretical Physics".*

Mr Chebolu Subrahmanya Viswanadham*, M.Sc. (Physics), IIT Madras, 1980, is a physicist from the 24th batch of BARC Training School. He worked in different areas of materials science, including irradiation effects on nuclear fuels, fuel element behaviour modeling and material characterization. He is currently with the Laser Processing & Advanced Welding Section. His current research interests include pulsed laser deposition of thin films, UV laser micromachining, numerical modeling of laser material processing, and process monitoring using optical emission spectroscopy.*

Mr Gyanottam Lal Goswami, *B.E. Metallurgy, University of Roorkee,1970, is a metallurgist from the 14th batch of BARC training school. He worked on Nuclear fuel element fabrication., GTAW welding, Thermodynamics of nuclear materials and Laser materials processing. He has setup a Laser Material Processing laboratory at Trombay. He is currently Head, Laser Processing & Advanced Welding Section. His current research interests include laser material processing and system integration for laser processing.*

Prof. L.C. Gupta *has special intestest on the studies of phenomena such as ferroelectricity, magnetism, valence fluctuations and superconductivity applying microscopic techniques of NMR, NQR, Mossbauer and Mu-SR as well as bulk techniques. Subsequent to the discovery of supercondcuting quaternary borocarbide system Y-Ni-B-C (reported in Solid State Commun. 87, 413 (1993) and Phys. Rev. Letters 72, 274 (1994)), he has been particularly concerned with the identification of new intermetallic ternary and quaternary superconducting materials.*

A Novel Technique for Measurement of Atomic Data of Rare and Radioactive Isotopes: A Case Study in Gadolinium Isotopes

A. P. Marathe and B.N. Jagatap
Laser & Plasma Technology Division
Bhabha Atomic Research Centre

and

A. Venugopalan
Spectroscopy Division
Bhabha Atomic Research Centre

THERE HAS BEEN MUCH INTEREST IN high-resolution spectroscopy of rare and radioactive isotopes for measurement of isotope shifts (IS) and hyperfine structures (Hfs). These atomic parameters provide very useful information on the mean square charge radii and multipole moments of the nuclear ground and isomeric states. Such studies of nuclear physics via atomic physics have been immensely successful owing to the high sensitivity and high resolution afforded by the optical spectroscopic techniques [1,2]. In addition high-resolution spectroscopic data is indispensable in many other areas of interest, for example, in the ultra-trace analysis and development of laser selective processes.

A major difficulty in adapting a high-resolution spectroscopic technique for rare and radioactive isotopes is the sample size, which is limited by the low production yields and radiological safety considerations. A number of sophisticated laser spectroscopic techniques, which include laser induced fluorescence [3], resonance ionization spectroscopy [4], laser spectroscopy of trapped atoms and ions [5] and collinear fast beam methods [6], are used to this end. In this paper we report a technique of high-resolution spectroscopy based on recording Fabry-Perot optical spectrometer (REFPOS) and a novel design of a hollow cathode discharge lamp (HCDL), which works with microgram sample size. Using gadolinium isotopes, as an example, we show that the methodology can give excellent results at 10 μg sample size.

The basic equipment developed for this work is a liquid nitrogen cooled all metal HCDL [7]. The design is based on a hermetically sealed device, which can be conveniently loaded with a radioactive material in a radiologically protected facility and transported, without calling for any stringent safety requirements, to the inactive area that houses spectroscopic equipments. Operationally this concept is superior to many other techniques since the active material remains contained within the HCDL. This, however, represents an off-line technique, which makes it useful for isotopes having relatively long half life (> 1 day). The cathode of the HCDL is a copper cuvette, which holds the sample in the metal, oxide or nitrate form. To operate the discharge at microgram levels of charge, we use carriers, which provide suitable matrix for a stable emission lasting for a couple of hours [7,8]. Typically, graphite or a mixture of silver and tantalum powder provides an excellent matrix for lanthanides and actinides. The composition of the matrix is arrived at by a series of experiments, which optimise the

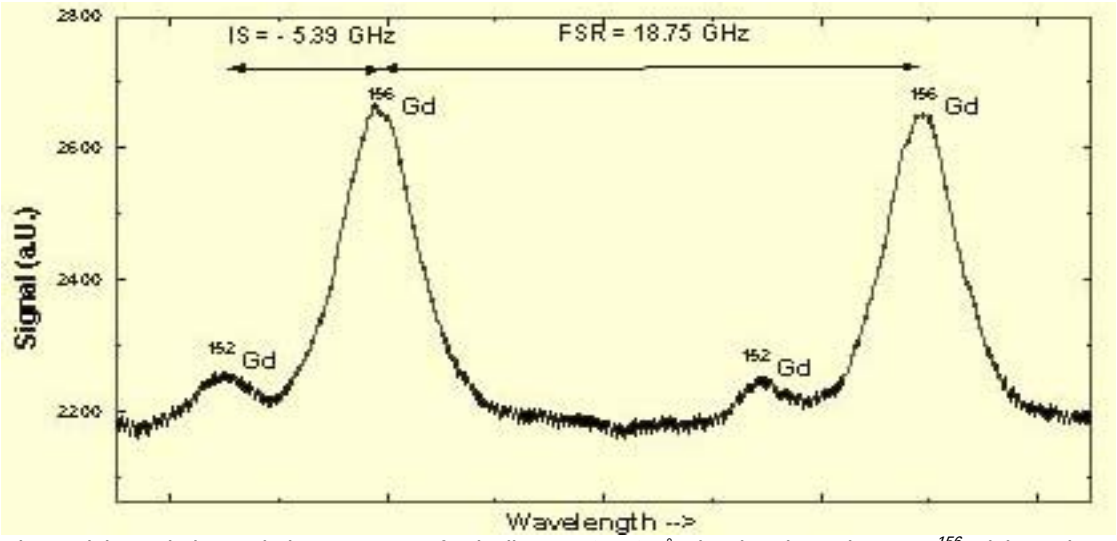

Fig. 1 High-resolution emission spectrum of Gd I line at 5015.04 Å showing the IS between ^{156}Gd (55 μg) and ^{152}Gd (10μg) recorded on the REFPOS.

throughput of the HCDL. The Doppler widths of the spectral lines from this source are in the range of 600-700 MHz, which are small compared to the typical IS (a few GHz) exhibited by lanthanides and actinides. High resolution spectroscopic studies are carried out using a home made REFPOS (FSR =18.75 GHz) set up that provides resolution typically ~ 10^6; sufficient for IS studies in lanthanides and actinides. For experiments on the gadolinium isotopes, we take a mixture of ~ 55 μg of ^{156}Gd and ~ 10 μg of ^{152}Gd and disperse it on the carrier (1 mg) coated on the inside surface of the cathode. The HCDL is operated with argon as buffer gas (2 torr) and current of 30-50 mA.

High-resolution spectrum of 5015.04 Å line of Gd I obtained by the procedure indicated above is shown in Fig.1. Since both these isotopes have zero nuclear spin, the spectra do not exhibit hyperfine structures. High S/N ratio enables us to obtain measurement of IS $\Delta\sigma$ (^{152}Gd - ^{156}Gd), which in the present case is - 5.39 GHz.

In conclusion, we have developed a method of performing high resolution spectroscopy of rare and radioactive elements by devising a new design of a HCDL and using this as an emission source for high resolution spectroscopy on REFPOS. The spectroscopic source can be used in conjunction with laser spectroscopic techniques [9], which can further reduce the requirement of the charge and give far better resolution. The results of these studies will be reported elsewhere.

References

1. E.W. Otten, Treatise on Heavy Ions Science 8, 519 (1989).
2. J. Billowes and P. Cambell, J. Phys. G Nucl. Part.Phys. 21 (1995) 707-739.
3. Yu. P. Gangrsky, B.K. Kul'dj'anov, K.P. Marinova, B.N. Markov and S.G. Zemlyanoi, Z.Phys. D 42,1 (1997).
4. G.D. Alkhazov, A.E. Barzakh, V.A. Bolshkov, V.P. Denisov, V.S. Ivanov, Yu. Ya. Sergeev, I.Ya. Chubukov, V.I. Tikhonov, V.S. Letokhov, V.I. Mishin, S.K. Sekatsky and V.N. Fedoseyev, Z. Phys. A 337, 257 (1990) 257.
5. G.D. Sprouse, J. Das, T. Lauritsen, J. Schecker, A. Berger, J. Billowes, C.H. Holbrow, H.-E. Mahnke, and S.L. Rolston, Phys.Rev.Lett., 63, 1463 (1989).

6. Schuessler H.A., Benck E.C., Buchinger F., Carter H.K., Nucl. Instru. And Methods in Phys. Res. A352, 583 (1995).
7. A.P. Marathe, A. Venugopalan, B.N. Jagatap, Ind. J. Phys. 76B, 483 (2002).
8. J.P Young., R.W.Shaw, C.M.Barshick, J.M.Ramsey, J. of Alloys and Compounds 273, 62 (1998).W.J. Childs, O.Poulsen and L.S. Goodman, Opt. Lett. 4, 35 (1979).

This paper was awarded third Best Prize in poster presentation at the DAE-BRNS Symposium on Nuclear Physics held at M.S. University, Tirunelveli, during December 26-30, 2002.

About the authors ...

Ms Asawari P. Marathe *graduated from the 40th batch of BARC Training School. She obtained her M.Sc.(Physics) from IIT Mumbai (1995). Her field of work is high-resolution spectroscopy and laser-ionisation spectroscopy.*

Dr B.N. Jagatap, *recipient of Homi Bhabha Award for Science & Technology (1999), graduated from the 20th batch of BARC Training School. He obtained his Ph.D. from Mumbai University (1988), Postdoctoral Fellow (1994-95) and was Visiting Scientist (1999) at the University of Western Ontario, Canada, and Senior Visiting Fellow (2000-01) at the Centre for Chemical Physics, UWO, Canada. His research interests are laser-atom/molecule interactions, high-resolution spectroscopy, laser cooling & trapping and physics of laser selective processes.*

Dr A. Venugopalan *of Spectroscopy Division, BARC, obtained his Ph.D. from Mumbai University (1982). He was research scientist (1986) at CERN and did his postdoctoral work (1990) at the University of Mainz. His research interest is high- resolution atomic spectroscopy.*

Radioprotecting Ability and Phytochemical Analysis of an Indian Medicinal Plant : *Terminalia chebula*

G. H. Naik, K. I. Priyadarsini and H. Mohan
Radiation Chemistry & Chemical Dynamics Division
Bhabha Atomic Research Centre

Abstract

Aqueous extract of a natural herb, Terminalia chebula was tested for potential antioxidant activity by examining its ability to inhibit γ-radiation induced lipid peroxidation in rat liver microsomes and damage to superoxide dismutase (SOD) enzyme in rat liver mitochondria. HPLC analysis of the extract showed the presence of compounds such as ascorbate, gallic acid and ellagic acid. This was also confirmed by cyclic voltammetry. The extract inhibits xanthine oxidase enzyme activity and is also an excellent scavenger of DPPH radicals. The rate at which the extract and its constituents scavenge the DPPH radical was studied by using stopped-flow kinetic spectrometer. Based on all these results it is concluded that the aqueous extract of Terminalia chebula acts as a potent antioxidant and since it is able to protect cellular organelles from the radiation induced damage, it may be considered as a probable radioprotector.

Introduction

OXIDATIVE STRESS OR EXCESSIVE production of reactive oxygen species (ROS) is being implicated in many diseases such as cancer, atherosclerosis, ageing, diabetics etc [1]. The potential targets for the ROS in cells are membrane lipids, DNA and proteins. External supplementation through antioxidants is recommended to protect cells from the deleterious effects of such oxidative stress conditions. In the search of novel antioxidant substances, the herbal extracts used in ayurvedic preparation received considerable attention due to their natural origin and lesser side effects [2,3]. *Terminalia chebula* popularly known as Harde, belongs to the family *Combretaceae*. It is used commonly in many Ayurvedic preparations as laxative, diuretic, cardiotonic [4]. In this paper we present in detail, different in vitro experiments, through which the antioxidant activity of the extract was tested and HPLC analysis of the extract by which we determined the active principles responsible for its activity. The kinetics of 2,2'-diphenyl-1-picrylhydrazyl (DPPH) radical scavenging ability of the extract was studied by using stopped flow spectrometer. Of late, there is also a considerable attention on the possibility of using some antioxidants as radio protectors, since exposure to high-energy radiation such as γ-rays can lead to the damage of cellular organelles by generating excessive ROS. Based on these results, possibility of using T*erminalia chebula* extract as a potent radio protector is also discussed.

Materials and Methods

The dry fruits of Terminalia chebula were extracted with distilled water at 70°C, filtered and the supernatant was concentrated and spray dried to get the dry powder of the extract. All the other chemicals were purchased from Aldrich/Sigma Chemicals. Nitrous oxide (N_2O) and oxygen (O_2) gases obtained from Indian Oxygen Ltd., Mumbai, were of IOLAR grade purity. Millipore water was used for preparation

of aqueous solutions. Freshly prepared solutions were used for each experiment. Rat liver mitochondria and microsomes were isolated from the liver of male albino wistar strain rats as described in reference [5]. γ-Radiation induced lipid peroxidation studies were carried in N_2O-purged rat liver microsomal solution in absence and presence of different concentration of the extract at physiological pH 7.4 (phosphate buffer). The detailed methodology used in the lipid peroxidation is given in our earlier reference [5].

SOD enzyme activity was studied in rat liver mitochondria The oxygenated buffer was used to adjust its protein concentration to 2 mg/ml. and was exposed to a total γ-dose of 240 Gy both in the presence and in the absence of the extract. SOD levels in the control and the irradiated samples were estimated according to the reported procedure [6].

HPLC and Cyclic Voltammetric Studies

HPLC analysis was carried out using C18 PCX 500 Dionex analytical column with 0.1M KCl, 0.05 M HCl and 32% acetonitrile as the mobile phase. The detection was carried out at 260 nm using UV detector. Peak areas were quantified by using external standards.

Cyclic voltammetric studies were performed on Ecochemie Auto Lab, PGSTAT 20 Model and by using a conventional three electrode system i.e glassy carbon working electrode, platinum wire as auxiliary electrode and Ag-AgCl reference electrode. Glassy carbon electrode was resurfaced with alumina. The electrochemical cell containing the aqueous solution 100 μg/ml of extract and 0.1M KCl buffer pH 7.4 was thermostatted at 25 ^{o}C. The cyclic voltammograms were recorded in the voltage range of –0.25 to 1.2 V at a scan rate 100 mV/s.

Radical Scavenging Assays

Xanthine-Oxidase Assay : 3 ml system consists of 38 mM tris-HCl buffer pH 7.4, 16 μM xanthine, 10 μM DCIP and about 0.02units/ml of xanthine oxidase enzyme. The decrease in absorbance of DCIP was monitored at 600 nm in the presence and the absence of the extract. (25 to 100 μg/ml).

DPPH Assay : 1 ml of 500 μM DPPH in methanol was mixed with equal volume of the extract solution in phosphate buffer (pH = 7.4). The mixture was slightly shaken and kept in dark for 20 minutes. The absorbance at 517 nm was monitored in presence and absence of different concentrations of the extract.

Stopped-Flow Studies : The kinetic measurements were made by using stopped-flow-spectrophotometer. The rate of disappearance of DPPH radical was followed separately by varying concentration of the extract, ascorbic acid, gallic acid and ellagic acid and monitoring its absorbance at 517 nm at 25 ^{o}C.

Results and Discussion

Lipid Peroxidation and SOD Enzyme Inhibition Studies : Peroxidation of lipids is a measure of damage to the membrane lipids caused by the attack of reactive oxygen species. Inhibition of lipid peroxidation by any external agent is often used to evaluate its antioxidant capacity. Studies on inhibition of γ-irradiation induced lipid peroxidation in presence and absence of the extract were carried out in rat liver microsomes and extent of lipid peroxidation was determined by TBARS method. when microsomes containing the aqueous extract of *Terminalia chebula* were exposed to a dose of 100 Gy to 600 Gy. considerable reduction in the extent of lipid peroxidation was observed as compared to control. At a fixed radiation dose of 270 Gy, the lipid peroxidation was studied at varying concentration (5 to 35 μg/ml) of the extract. From the figure 1, it can be seen that the extract shows protection ability at concentrations and at a concentration of 15 μg/ml of the extract the peroxidation is inhibited by 50% (IC_{50} value) .

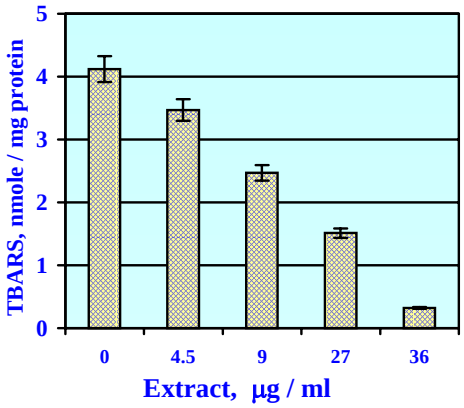

Fig.1: Inhibition of lipid peroxidation in rat liver microsomes exposed to γ-radiation in the presence of different concentration of extract

Superoxide dismutase (SOD) is an important cellular antioxidant enzyme, which converts superoxide radical into H_2O_2 and O_2 During the irradiation by γ-rays, the SOD activity initially increases to combat oxidative stress induced by γ-radiation, and further irradiation causes decrease in its activity due to its own consumption and damage by the excessive reactive oxygen species production. These studies have been carried out using rat liver mitochondria as they are rich in SOD enzyme and the aqueous mitochondrial samples were exposed to a radiation dose of 240 Gy in the absence and in the presence of the extract. In the absence of the extract, on irradiation the activity of enzyme decreased to 44 ± 5 % and in presence of 12 and 75 µg/ml extract the decrease in activity was 15 ± 3 % and 4 ± 1% respectively, thus restoring the activity of the enzyme to a great extent. These studies suggest that the extract of *Terminalia chebula* protects the antioxidant enzyme from the reactive oxygen species produced by γ-radiation.

HPLC & Cyclic Voltammetric Studies

The HPLC analysis of the extract was carried out to determine the polyphenols present in extract, as they are responsible for antioxidant activity and radical scavenging ability. The extract was dissolved in methanol or in aqueous buffer and the chromatograms were recorded at 260 nm using UV detector. The HPLC chromatogram showed three prominent peaks with retention time 3, 4.55 and 8.69 min corresponding to ascorbic acid, gallic acid and ellagic acid respectively as confirmed by injecting the standard solutions. Slight change in the retention times of these constituents in the extract may be either due to overlap of the peaks in the mixture or due to the fact that in the extract, these individual components are not in the free form but are bound as glycosides and other water soluble forms.

The Cyclic volammograms for the extract, ascorbic acid, gallic acid and ellagic acid were recorded The cycli voltammogram for the extract showed no clear reversible peaks but only gave a shoulder and a monotonously increasing peak. The initial shoulder is at a potential of 0.303 V and broad peak is at ~ 0.55 V corresponds to ascorbic acid and gallic acid respectively.

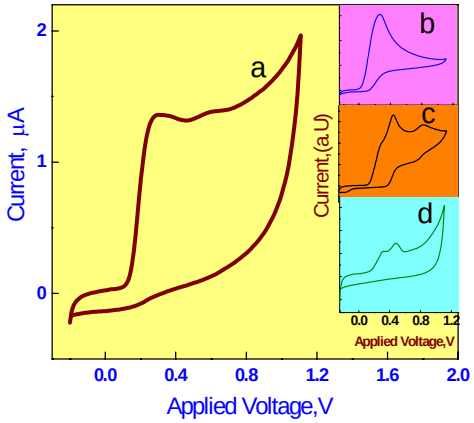

Fig.2 Cyclic voltammogramms of (a) aqueous extract of Terminalia chebula, (b) ascorbic acid, (c) gallic acid, and (d) ellagic acid

Ellagic acid peak in the extract may be merged due to the overlap of oxidation peaks of ascorbic acid and gallic acid. The chromatograms of Terminalia chebula and its constituents is as shown in figure 2.

Thus comparision of peak positions confirms the presence of the above determined products from HPLC analysis.

Radical Scavenging Assays

Both HPLC analysis and cyclic voltammetry confirmed that the extract contains phenolic compounds. Since these compounds are good scavengers of free radicals, we have studied the ability of the extract to neutralize the free radicals such as DPPH and superoxide radicals.

Superoxide radical was produced by Xanthine/ Xanthine oxidase system. The superoxide radical formed brings the reduction of DCIP dye as seen by its absorption at 600 nm. In the absence of the extract, reduction of DCIP dye takes place effectively. However in the prescence of different concentrations (24 to 100 μg/ml) of the extract a significant decrease in the reduction of dye was observed due to the scavenging of superoxide radical by the extract. The IC50 value for superoxide radical scavenging is found to be 50μg/ml.

DPPH is a stable free radical having a maximum absorption at 517 nm (ε_{max} = 9660 M^{-1} cm^{-1}) In the presence of compounds capable of donating a H atom or an electron, its free radical nature gets neutralized as seen by decrease in absorption at 517nm. The decrease in DPPH absorption in presence of varying concentration (3.5-23 μg/ml) of the extract has been monitored and it has been found that the absorbance due to DPPH decreases continuously up to 23 μg/ml and further increase in the concentration did not change the absorbance (probably due to its own absorption).

The concentration 12 ± 2 μg/ml at which it scavenges 50% of DPPH radical is given as IC_{50} value for the extract.

Kinetics of DPPH Reaction

Kinetics of the reaction of DPPH radical with the extract was followed by stopped-flow spectrometer. The extract was found to bleach the DPPH absorption in a few seconds,(figure 3).

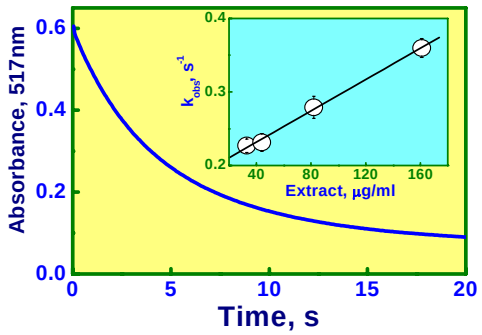

Fig.3 Absorption-time plot showing the decay of DPPH radical in presence of the extract. Inset : linear plot for the observed decay rate as a function of extract concentration.

The exponential fit to the decay of DPPH absorption with time gave a rate constant, which was found to increase linearly with increasing extract concentration (inset of figure 3). Thus at 66 μg/ml concentration, the extract showed a decay rate constant of 0.23 s^{-1}. This scavenging of the DPPH radical by the extract is mainly due to its constituents, viz., ascorbic acid, gallic acid and ellagic acid.

In order to understand this, the bimolecular rate constants of these compounds were independently determined by stopped-flow method as 140, 122 and 1000 $M^{-1}s^{-1}$ respectively. This confirms that all these three compounds present in the extract show very high reactivity towards DPPH radicals. Presence of these constituents either in free or bound form in the extract may therefore be responsible for the overall antiradical and antioxidant activity of Terminalia chebula extract.

Conclusions

The fruits of Indian medicinal plant *Terminalia chebula* are known for their pharmacological activity and in this paper it has been shown that it can be used as an effective antioxidant. The aqueous extract was found to be a very efficient inhibitor of radiation induced lipid peroxidation and damage to the superoxide enzyme. It is an excellent free radical scavenger, the property

arising mainly from the presence of well-known antioxidants like ascorbate, gallic acid and ellagic acid, as confirmed by the HPLC analysis. Presence of these potent antioxidants in significant levels either in free or bound form in the extract may therefore be responsible for the overall antiradical and antioxidant activity of *Terminalia chebula* extract. Thus our *in-vitro* studies coupled with the phytochemical analysis confirm that the extract possesses potential antioxidant activity. Since the extract protects various cellular organelles from radiation induced damage, we feel the extract can be used as a radioprotector, especially to protect humans from radiation induced damage. For such an activity, natural products with well established pharmacological history are best suited as they are gifted with lesser side effects.

Acknowledgements

The authors are thankful to M/S Ajanta Pharma Pvt Ltd., Mumbai for supplying the extract, Dr D. B. Naik, RC & CD divison for HPLC analysis and to Dr J. G. Satav, RB & HS Division, BARC, for providing the microsomes. Thanks are also due to Dr J. P. Mittal Director Chemistry & Isotope Group, BARC, and Dr T. Mukherjee, Head, RC & CD Division, BARC, for their support to this work.

References

1. Finkel, T., Holbrook, N. J, Oxidants, Oxidative stress and biology of ageing. Nature, 239-247,2000
2. Indian Pharmacopoeia, Government of India, Ministry of Health and Family Welfare, Published by the controller of publications, Delhi, Vol 1, 1996.
3. Chopra, R. N., Nayar, S. L., Chopra, I.C. Glossary of Indian Medicinal Plants, Council of Scientific and Industrial Research, New Delhi. 1956.
4. Jagtap, A.G., Karkera, S.G. Potential of the aqueous extracts of Terminalia chebula as an anticaries agent J. Ethnopharmacol., 68, 299-306, 1999.
5. Khopde, S.M., Priyadarsini, K.I., Mohan, H., Gawandi, V.B., Satav, J.G., Yakhmi,J.V., Banavaliker, M.M., Biyani, M.K., Mittal, J.P., Characterizing the antioxidant activity of amla (phyllanthus emblica) extract, Current Science 81, 185-190, 2001.
6. Naik, GH., Priyadarsini, K.I., Satav, J.G., Banavaliker, M.M., Biyani, Sohoni, DP, and H. Mohan. Comparative antioxidant activity of individual herbal components used in Ayurvedic medicine, Phytochemistry 63, 97-104, 2003.

This paper received the 'Dr. J.M. Dasgupta Award' in Organic and Bio Chemistry section at 39th Annual Convention of Chemists held at Nagarjuna University, Nagarjunanagar, during December 22-26, 2002

About the authors ...

Mr Ganesh Naik *has received his M.Sc degree in Organic Chemistry from Somaiya College, Mumbai University in 2000. He is a DAE fellow working in Radiation Chemistry and Chemical Dynamics Divison. He is persuing his Ph.D degree in the subject entitled, 'Study of Free radicals and Excited States of Some Important Biomolecules'.*

Dr Indira Priyadarsini *joined BARC in 1983. She obtained her Ph. D. in Radiation and photochemistry in 1990. She has co-authored more than 70 papers in international journals on radiation chemistry, photochemistry and radiation biology. Employing fast reaction techniques, she has been studying the free radical reactions involving antioxidants, radio protectors and radio sensitizers in model systems. She is currently working on the elucidation of mechanism of antioxidant action involving natural products and herbal extracts.*

Dr Hari Mohan *joined BARC in 1967. Since then, he has been actively involved in the study of fast reaction kinetics using accelerators and lasers. His current research interests include free radical reactions of halogenated and sulfur compounds and biomolecules of natural origin. He has co-authored more than 150 research papers in international journals. Presently, he is the Head, Radiation Chemistry Section of Radiation Chemistry & Chemical Dynamics Division, BARC.*

Chemical Properties of Transactinide Elements

P.K. Mohapatra
Radiochemistry Division
Bhabha Atomic Research Centre

Abstract

The chemical properties of transactinide elements viz. rutherfordium (Rf), dubnium (Db) and Seaborgium (Sg) are found to be similar to their homologs in the periodic table in group IV, V and VI respectively. Deviations are also predicted in many cases due to the relativistic effects which lead to unusual chemical properties. The chemical investigations in gas phase involve thermo chromatography and in aqueous phase using ARCA (Automated Rapid Chemistry Apparatus), MCT (Multi Column Technique), and SISAK (Short-lived Isotope Separation by AKUFVE). The radiochemical methods involved are fast separations followed by detection of correlated alphas of the daughter and grand daughter with those of the parent.

Introduction

THERE HAVE BEEN CONSIDERABLE efforts in recent years for expanding the periodic table beyond the actinides. The chemical studies involving the shortlived transactinides have, however, always been challenging, as it involves careful planning of the experiment at the 'one-atom-at-a-time' scale. This is due to the very short half-lives and extremely low production cross section of these elements. They often require fast radiochemical separations with very high transportation yield and efficient counting set-up.

As per the actinide concept brought out by Seaborg [1], the actinide series should end with lawrencium and a new 6d series should start with element 104 (Rf). Accordingly, the electronic configuration of Rf should be similar to the group IV elements. The early work on the chemical properties of Rf had indicated that it is tetravalent in nature and resembled, more often than not, the main group elements Zr and Hf. The chemical properties of element 105 also followed suit and resembled those of Nb and Ta. Early work on Sg too have indicated its resemblance to Mo and W. Based on these observations, the new set of transactinide elements occupy the periodic table as shown in Fig. 1.

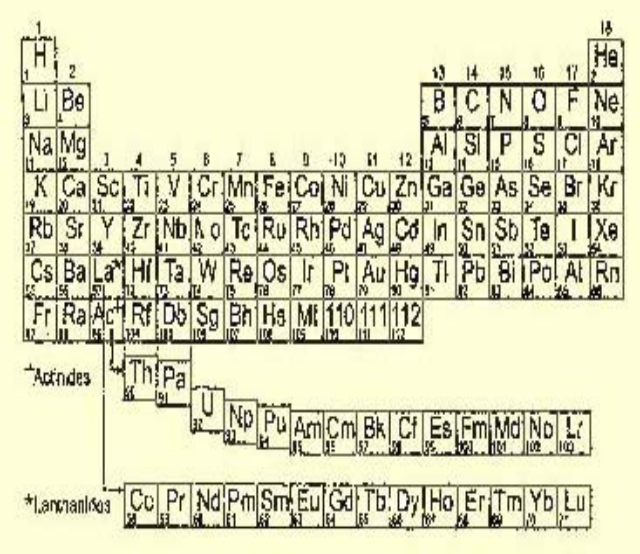

Fig. 1 Periodic table of elements including the transactinides

In spite of the parallels observed with the transactinides and their main group homologs, the chemical behaviour of the former is not as simple as one may expect and is full of surprises. The chemistry of Rf and Db, till recently the only transactinides whose chemical properties have been studied, have shown deviations from the chemical properties of their lighter homologs and often shown resemblances to their pseudo-homologs Th and Pa respectively. These have been attributed to the relativistic effect arising due to the stabilization of the 7 s and 7 $p_{1/2}$ orbitals [2]. This can destabilise and expand the d and f orbitals leading to unusual oxidations states and hence chemical properties.

One of the several challenges associated with the transactinide elements, is the rapidity with which the separations need to be carried out and the informations can be gathered thereafter. The chemical techniques often used in these fast radiochemical separations are ion-exchange chromatography, exraction chromatography, ermochromatography and solvent extraction using the AKUFVE. During the time period in which the entire process of transport, separation and detection is done in all probability most of the transactinide decay. Therefore, correlation of the gammas of the daughter and grand daughter is done to conclude that an event has taken place.

Synthesis of Transactinides

Transactinides are synthesized by nuclear fusion reactions with heavy ion projectiles [3]. These reactions have very low cross section and the production rates as well as half-lives decrease with increasing atomic number. Consequently, one deals with atom-at-a-time chemistry in these cases. Cold fusion reactions in which Ti-50, Cr-54, Fe-58, Ni-62,64 and Zn-70 are fused with Pb-208 and Bi-209 targets tend to give the highest possible cross sections. However, the n-deficient product nuclei have half lives less than one second and hence are not useful for any chemical studies. More n-rich and hence longer lived products are obtained in hot fusion reactions of O-18, Ne-22, Mg-26, S-34 targets with actinide targets. Recent chemical studies of rutherfordium deal with the 78-s ^{261}Rf produced in the ^{248}Cm (^{18}O, 5n) reaction which has a cross section of 5 nb. Due to reasonable half-life of ^{261}Rf (78 s), most chemical studies involve this route for the production of element 104. Recent studies on element 105 used 34-s ^{262}Db and 27-s ^{263}Db produced in 5n- and 4n- reactions of ^{18}O with ^{249}Bk targets with cross sections of 6 nb and 2 nb, respectively. Early works on the chemical studies on element 106 involved the 0.9 s ^{263}Sg produced at a 0.6 nb cross section by the ^{249}Cf(^{18}O, 4n) reaction. The recent discovery of the neutron rich ^{265}Sg and ^{266}Sg isotopes have longer half-lives (in the range of 3-30 s) but much reduced cross section of 260 pb and 60 pb for the ^{248}Cm(^{22}Ne, 5n) and ^{248}Cm(^{22}Ne, 4n) reactions respectively.

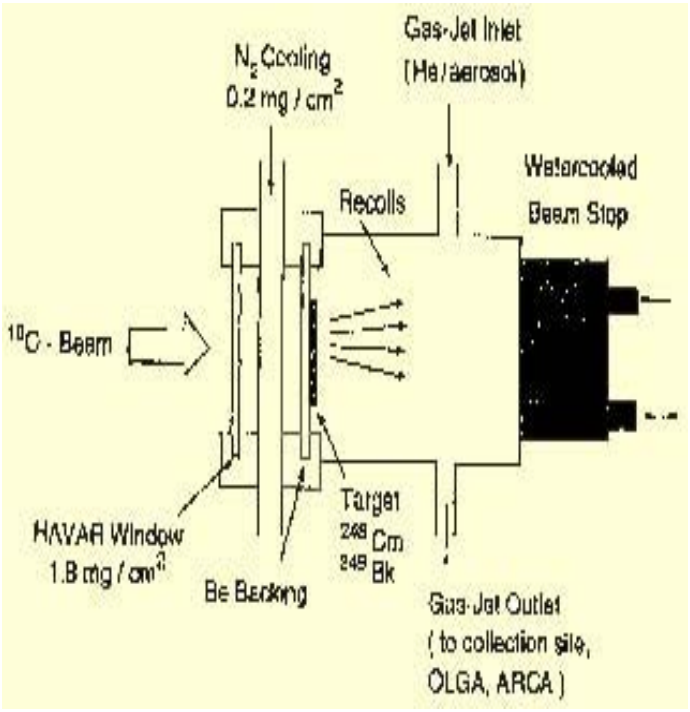

Fig. 2 Schematic diagram of the target and recoil chamber used for the production of transactinides

Experimental Techniques

As shown in Fig.2, the schematic of the target and recoil chamber clearly bring out the product in the recoil beam which is later thermalised and transported by a fine aerosol particles in He as the transport gas. The typical transport yield is about 50% over a distance of few tens of meters with the transport time being in the order of 2-5 s. The gas phase chemistry involves an isothermal on-line gas chemistry apparatus (OLGA) which enables the detection by the PIPS (Passivated Ion-implanted Planar Silicon) detectors. For the aqueous chemistry work involving ion-exchange as well as extraction chromatography, the automated rapid chemistry apparatus (ARCA) have been employed. It is a computer controlled apparatus for the fast HPLC based separations containing micro columns etched out in stainless steel magazines. The ARCA technique has been used for the study of elements up to 105. The ARCA studies with element 106 were not very encouraging and it needed another on-line chromatographic technique called the multi column technique.

The multi column technique (MCT) involves three columns in series. The first column (F) filters all the decay products coming from the accelerator along the KCl aerosol containing He jet. The second column (C) is the true chromatographic column where the element of interest experiences the retention time, t_R, which is of the order of its nuclear half-life which acts as an internal clock. The daughter nuclides that are formed during the passage of the mother through C are strongly retained on the third column (D). From the activity of the daughter in column D (A_D) and in the effluent (A_E) the retention time can be obtained as

$$t_R = (t_{1/2} / \ln 2). \ln[(A_D + A_E)/A_E] \quad (1)$$

and the K_d value can be given as

$$K_d = (t_R - t_0).V/m \quad (2)$$

where t_0 is the column hold up time due to the void volume, V, the flow rate of the mobile phase and m is the mass of the resin.

Gas Phase Chemistry

The gas phase chemistry has been studied by thermochromatography. The transported transactinide is allowed to react with HCl or Cl_2 / $SOCl_2$ mixture to give volatile chloride and oxychlorides respectively. Vapour pressure curves indicate the relative volatility of the chlorides and oxychlorides which can be calculated from the sublimation entropy as well as sublimation enthalpy data. However, as the gas phase chemistry of Rf, Db and Sg involves one-atom-at-a-time chemistry, it is reasonable to use the adsoption enthalpy data in place of the sublimation enthalpy based on which the relative yield vs temperature plots are generated. By a comparison with the relative yield vs temperature curves of the element of interest, homolog and pseudo-homolog, one gathers information on their chemical behaviour.

The first volatility experiments of Rf-chloride by Zvara et al. [4], have indicated that it has similar volatility to that of its analog Hf, which in turn is much higher as compared to the actinides. On the other hand, a recent experiment by OLGA (On-Line Gas chemistry Apparatus) has indicated much higher volatility for $RfCl_4$ as compared to $HfCl_4$ while comparable results were obtained with $ZrCl_4$. The gas phase chemistry studies of Db and its analogs Nb and Ta have been carried out with their respective bromides made from HBr and BBr_3 as the brominating agent. The volatility trend is Ta ~ Nb > Db which disagree with results from relativistic molecular calculations [5]. The respective chlorides were found to have higher volatility. The experimental data on the volatility of the oxychlorides of Sg and its analogs have shown the trend MoO_2Cl_2 > WO_2Cl_2 > SgO_2Cl_2 which agreed very well with the theoretical predictions based on DS DVM calculations [6]. On the other hand, the first experiments on Sg by the russian scientists at JINR, Dubna involved the 0.9-s ^{263}Sg and have shown an opposite trend in the volatility viz. SgO_2Cl_2 > WO_2Cl_2. The first gas phase chemistry of Hassium (element 108) was studied by the research group at Mainz, Germany recently [7]. Successful experiment with volatile HsO_4 was

deposited in a thin film of wet NaOH forming the salt $Na_2HsO_4(OH)_2$. This demonstrated that HsO_4 is an acid anhydride.

Solution Chemistry

The first separation of Rf in solution phase was performed on the cation exchange column using α-hydroxy isobutyric acid as the eluent, which showed that it eluted along with Zr and Hf while the trivalent actinides were strongly retained in the column [8]. Similarity in the chemical nature of Zr, Hf and Rf was also observed while investigating their anion exchange behaviour using Aliquat 336 as the extractant [9]. The extraction studies involving TTA have indicated that Rf is less readily hydrolysed as compared to Zr, Hf and Pu [10]. This is not in agreement with the results obtained by Bilewicz et al., who have reported the trend in the ease of hydrolysis as Rf > Zr > Hf. TBP extraction of Rf was studied by several groups who have reported solvated type of species being extracted into the organic phase the extraction sequence being Zr > Rf > Hf. Chloride complexation studies of Rf have indicated formation of species of the type $RfCl_6^{2-}$ and it formed stronger complexes than those with Zr, Hf and Th [11]. Strub et al., [12] have conclusively shown that Rf forms anionic complexes with fluoride ion. The continuous on-line studies involving the MCT were carried out by Mohapatra et al. [13], at 0.01M HF as well as at 0.1M HNO_3 + 0.5M HF which yielded K_d values of 234 and 2.1 respectively.

Gregorich et al., have performed the first studies on the chemistry of Db where its extraction into MIBK (methyl isobutyl ketone) was investigated from a mixture of 3.8 M HNO_3 + 1.1 M HF [14]. Under these conditions Db and Nb do not extract into MIBK while Ta gets quantitatively extracted suggesting the formation of anionic complexes with the former. The non Ta-like behaviour is further confirmed in the extraction of halide complexes with TiOA from an aqueous medium comprising of 12 M HCl + 0.03 M HF. The penta valency of Db was confirmed in an ARCA experiment using cation exchangers and alpha-hydroxy isobutyric acid as the eluent. Db, together with Nb and Ta were eluted promptly from the column while tri- and tetravalent ions were strongly sorbed on to the column [15].

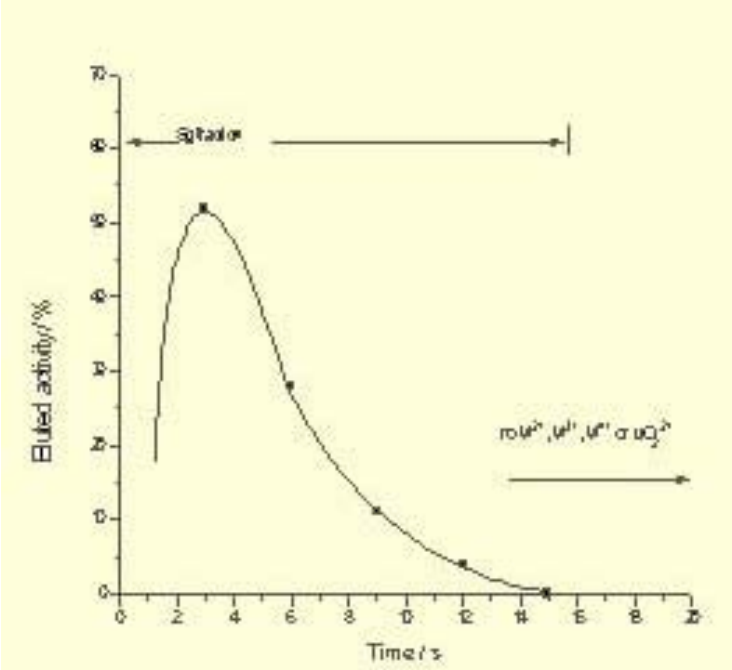

Fig. 3 Elution curve for W used as a model for Sg separation in ARCA using 0.1 M HNO_3 / 5x10^{-4}M HF [ref.16]

There is almost no solution chemistry data with Sg as the longest lived isotope till recently was the 0.9-s ^{263}Sg. The discovery of the 3-30 s ^{265}Sg and ^{266}Sg opened the possibility for the solution chemistry studies. Based on various models, theoretical predictions have been made on the chemical behaviour of Sg. For such calculations relativistic corrections are made which take into account the changes in the electronic configuration associated with the heavy elements. Based on the DS DVM calculations, the trend in the extractability of the group VI elements from HCl medium using tertiary /

quarternary amines follow the trend: U > Mo > W > Sg. However, no such experiments have actually been carried out with seaborgium.

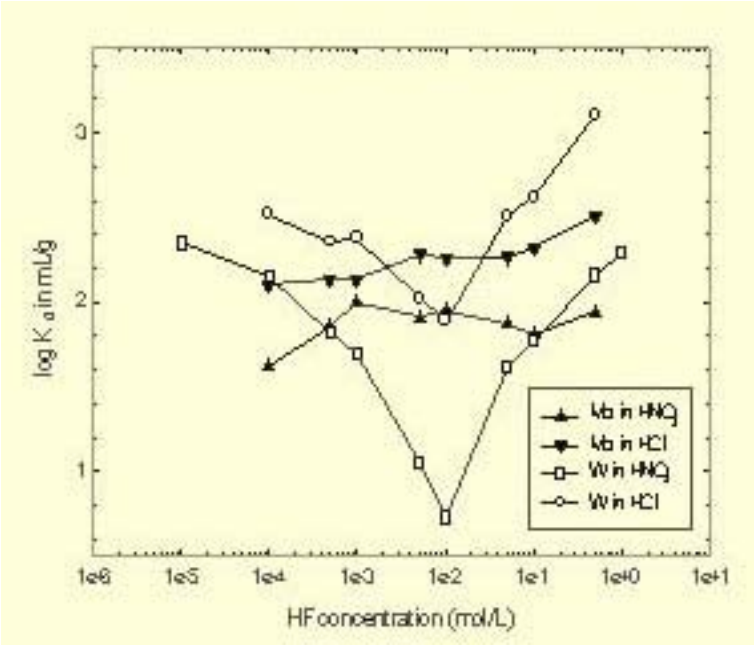

Fig. 4 Dependence of log K_d values of Mo and W on HF concentration at 0.1M HCl / HNO_3

The first aqueous chemistry of seaborgium [16] involved about 5000 identical chemical separations using ARCA. It was observed that in 0.1M HNO_3 / $5{\cdot}10^{-4}$ M HF, Sg forms neutral or anionic oxofluoro species, similar to W and Mo. This behaviour was in sharp contrast to the behaviour of uranyl ion which forms cationic species under similar conditions and could not be eluted from the column. As a trial run for the actual separation experiment, the homolgs of Sg, Rf and trivalent actinides along with W isotopes produced by the ^{20}Ne + ^{152}Gd reaction were used in an ARCA experiment (Fig.3). The behaviour of Sg was similar to that of W and the analogy was seen from 3 parent daughter correlations [17]. The profiles of ion exchange behaviour of Mo and W in HNO_3 + HF medium is depicted in Fig. 4. The trend in the K_d values are in the same line as their ability to form anionic complexes. Based on the theoretical complex formation trend: Mo > W > Sg, it is presumed that Sg may not form anionic complexes with low concentration of F^-.

Future Challenges

Though the studies on the chemical properties of Rf, Db and Sg have settled few questions such as their position in the periodic table, they have raised quite a few doubts too. More often than not, there is an uncertainity about their chemical speciation. In some cases Rf is found to mimic Zr and Hf, while in some other it behaved like Th or may be even like Pu. The chemical nature of these elements in atom-at-a-time scale is obviously expected to be very different from their bulk properties. Though the deviations from the chemical behaviour of their homologs are explained in terms of relativistic effects, much more studies are required to settle some of the unanswered questions.

Acknowledgement

The author thanks the Alexander von Humboldt Foundation, Germany, for financial assistance by granting a fellowship.

References

1. G.T. Seaborg; Chem. Engg. News **23**, 2190 (1945).
2. V. Pershina; Chem. Rev., **96**, 1977 (1996).
3. J.V. Kratz; in “Heavy Elements and Related New Phenomena”, W. Greiner and R.K. Gupta (Eds.), World Scientific, Singapore, pp. 129-193 (1999).
4. I. Zvara et al., Sov. Radiochemist. **11**, 161 (1969).
5. H. W. Gaeggeler; J. Radioanal. Nucl. Chem.., Articles, **183**, 261 (1994).

6. V. Pershina and B. Frike: J. Chem. Phys., **100**, 8748 (1996).
7. J.V. Kratz; Private communication.
8. R. J. Silva, et al., Inorg. Nucl. Chem. Lett, **6**, 871 (1970).
9. E.K. Hulet, et al., J. Inorg. Nucl. Chem., **42**, 79 (1980).
10. K.R. Czerwinski, Ph. D. Thesis, Univ. of California (1992).
11. D.C. Hoffman, in "The Robert A. Welch Foundation Conference on Chemical Research XXXIV Fifty Years with Transuranium Elements", Houston, Texas, 22-23 October 1990, p. 255, and Lawrence Berkely Report LBL-29815 (1990).
12. E. Strub, et al., Radiochim. Acta, **88**, 265 (2000).
13. A. Kronenberg, P.K. Mohapatra, et al., Radiochim. Acta (Communicated).
14. K.E. Gregorich, et al., Radiochim. Acta, **43**, 223 (1988).
15. M. Schaedel, et al., Radiochim. Acta, **57**, 85 (1992).
16. M. Schaedel, et al., Nature, **388**, 55 (1997).
17. M. Schaedel, et al., Radiochim. Acta, **77**, 149 (1997).

The author was conferred the Prof. R.C. Tripathy Award of the Orissa Chemical Society at Khalikote College, Berhampur, Orissa, in December 2002.

About the author ...

Dr P.K. Mohapatra *joined the Radiochemistry Division, BARC, in 1987 after completing his M.Sc. in Inorganic Chemistry from Utkal University and graduating from the 30th batch of the BARC Training School. He was awarded Ph.D. by Mumbai University in 1994. Dr Mohapatra did his Post-Doctoral research work at University of Liege, Belgium, under BOYSCAST Fellowship, DST (1998-1999) and at University of Mainz, Germany, under Humboldt Fellowship (1999-2000) on MRI contrast agents and chemistry of super heavy elements, respectively. His research interests include the chemistry of macrocyclic compounds and separation studies of actinides and fission products using novel extractants. Dr Mohapatra has to his credit over 50 publications in international journals and over 100 conference papers.*

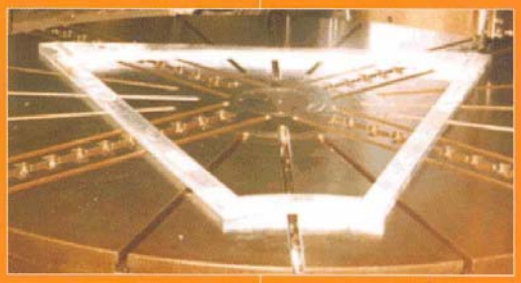

Edited and Published by Dr. Vijai Kumar, Head, Library & Information Services Division
Bhabha Atomic Research Centre, Trombay, Mumbai 400 085, India
(For private circulation)

Editorial Management : T. C. Balan. Computer Graphics, Design & Layout : P. A. S. Warrier
Available at URL : http\\www.barc.ernet.in